Mechanisms of Growth and Structural Properties of Di-indenoperylene on Metal, Dielectric, and Organic Surfaces

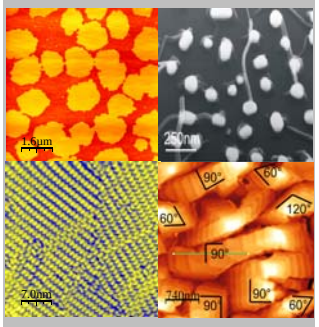

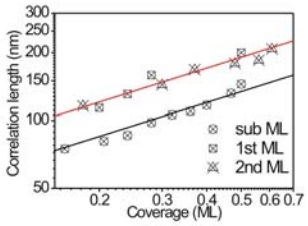

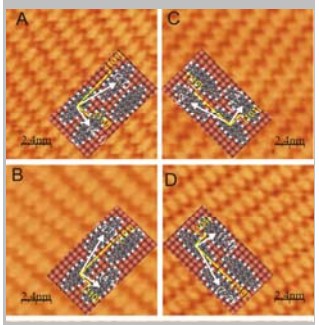

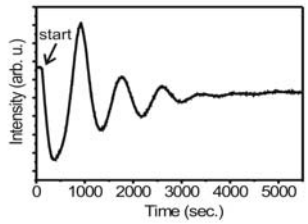

XueNa Zhang
Stuttgart, July 2008

Max-Planck-Institut
für Metallforschung
in Stuttgart

Institut für Theoretische
und Angewandte Physik
der Universität Stuttgart

Mechanisms of Growth and Structural Properties of Di-indenoperylene on Metal, Dielectric, and Organic Surfaces

Von der Fakultät für Mathematik und Physik der Universität Stuttgart
zur Erlangung der Würde eines Doktors
der Naturwissenschaften (Dr. rer. nat.) genehmigte Abhandlung

Vorgelegt von Xue Na Zhang aus China

Hauptberichter: Prof. Dr. H. Dosch
Mitberichter: Prof. Dr. J. Wrachtrup

Eingereicht am: 01.03.2008
Tag der Mündlichen Prüfung: 30.07.2008

Institut für Theoretische und Angewandte Physik der Universität Stuttgart

2008

To see a World in a Grain of Sand
and a Heaven in a Wild Flower,
Hold Infinity in the palm of your hand
and Eternity in an hour.....

From "Auguries of Innocence"

by William Blake

Contents

1 Deutsche Zusammenfassung v

1.1 Motivation v

1.2 Experimentelle Ergebnisse vi

1.2.1 Struktur und Wachstum von DIP-Schichten auf Siliziumdioxid vi

1.2.2 Dünne DIP Schichten auf Kopper vii

1.2.3 Dünne DIP Schichten auf selbstordnenden Monolagen (SAMs) viii

1.2.4 1D organische F_{16}CuPc Strukturen ix

1.2.5 Organisch-organische Heterostrukturen ix

2 Introduction 1

3 X ray scattering 5

3.1 Basic principle of X-ray Scattering 6

3.1.1 One electron scattering 7

3.1.2 One atom scattering 8

3.1.3 One molecule scattering 8

3.1.4 A crystal scattering 8

3.2 Specular reflectivity 9

3.3 Grazing incident X-ray diffraction 13

4 Scanning Probe microscopes 15

4.1 Atomic Force Microscope 15

4.1.1 Contact mode 18

4.1.2 Non-contact mode 20

4.1.3 Intermittent-contact mode 22

4.2 Scanning Tunneling Microscope 22

5 Organic semiconductors 26

5.1 Basic principles of organic semiconductors 26

5.2 Thin film growth 35

6 Experimental details 38

6.1 Preparation of Substrates and self assembled monolayers 38

6.2 UHV systems 40

6.2.1 Omicron MBE chamber 40

6.2.2 Portable MBE chamber 42

6.2.3 JEOL MBE chamber 42

6.3 Preparation of the organic thin films 42

6.4 The AFM, STM systems 43

6.4.1 Omicron UHV AFM/STM systems 43

6.4.2 Cervantes AFM system 43

6.4.3 Veeco MultiMode SPM system 44

6.5 X ray Sources 44

6.5.1 In-house X ray source 44

6.5.2 Synchrotron radiation 45

7 Growth behaviors of DIP on SiO_2: roughening, scaling and structural relaxation 49

7.1 Theory 50

7. 2 Morphology 56
7.2.1 Lateral concept of the 2D islands 60
7.2.2 Vertical revolution: roughness 68
7. 3 Structure 73
7.3.1 In-plane 73
7.3.2 Out-of-plane 76
7.4 Conclusions 80
8 Self assembly process of DIP on Cu(100) surface 82
8.1 Introduction 82
8.2 Self assembly process 83
8.2.1 Initial molecular self assembly 83
8.2.2 Submonolayer growth and molecular dynamics 85
8.2.3 Monolayer structure 92
8.3 Conclusions 97
9 Novel growth strategy for organic electronics 98
9.1 Growth of 1D organic structures 98
9.1.1 Introduction 99
9.1.2 Morphology of F_{16}CuPc grown on Au nanoparticle arrays 99
9.1.3 Inhibition of the 1D selective growth by SAMs 106
9.1.4 The growth behavior of F_{16}CuPc on other substrates 107
9.1.5 Conclusions 111
9.2 Growth of organic single crystals by SAMs 111
9.2.1 Introduction 111
9.2.2 Morphology and structure of DIP on APS SAMs 112
9.2.3 Conclusions 118
10 Architecture design of organic-organic heterostructure 120

10.1 Introduction 120
10.2 DIP and H_{16}CuPc heterostructure 121
10.3 F_{16}CuPc and H_{16}CuPc heterostructure 127
10.4 Pentacene and PTCDI heterostructure 133
10.4.1 On SiO_2 133
10.4.2 On Al_2O_3 142
10.5 Conclusions 149
11 Summary 151
List of figures 155
List of tables 163
Bibliography 165
Acknowledgements 179

Chapter 1

Deutsche Zusammenfassung

1.1 Motivation

In den vergangenen Jahren erfahren Organische Materialien mit Halbleitereigenschaften wachsende Aufmerksamkeit und immer größeres Interesse. Die Ursache dafür ist ihre Potential als Material in vielfältigen elektronischen und optoelektronischen Anwendungsmöglichkeiten. Organische Halbleiter werden zum Beispiel in organischen Feldeffekttransistoren (OFETs), organischen Leuchtdioden (OLEDs), Solarzellen, oder Photodetektoren, Photoelementen eingesetzt. Als praktische Anwendungen sind biegsamer Bildschirm, elektronisches Papier, hauchdünne, transparente Beschichtungen für Fenster und Wände oder auch einfach nur Lichtquelle denkbar und wahrscheinlich. Es gibt zwei Klassen von organischen Halbleitern: Polymere oder leichten Moleküle. Mit der Van der Waals Wechselwirkung verbindet man allgemein folgende Eigenschaften: Polymere haben ein großes Molekulargewicht, sind flexibel und bilden ungeordnete Strukturen. während die kleinen Moleküle starr sind und hochgeordnete Filme ausbilden können. Diese Arbeit konzentriert sich auf kleine, planare aromatische Moleküle. Ihre thermische Stabilität gegen Polymerisierung und Fragmentierung erlauben Sublimation unter UHV Bedingungen.

Eine kontrollierte Herstellung von dünnen, hochgeordneten organischen Schichten ist notwendig für Verständnis und Optimierung vieler Halbleiterbauelemente. Die Eigenschaften von dünnen Schichten kleiner Moleküle, u.a. ihr Wachstumsverhalten, ihre kristallographische Struktur und Ihre Morphologie sind direkt mit ihren elektrischen und optischen Eigenschaften verbunden.

In dieser Arbeit werden die Eigenschaften von organisch-anorganischen (z.B. organischen Halbleitern mit Metallen oder dielektrischem SiO_2) und organisch-organischen (z.B. organische Halbleiter mit organischen Halbleitern) Grenzflächen durch ergänzende Techniken wie Rasterkraft-Mikroskopie (AFM), Rastertunnelmikroskopie (STM), Rasterelektronenmikroskopie (SEM), so wie in-situ und ex-situ Röntgenbeugung (XRD) untergesucht. Die planare Moleküle n-Type $F_{16}CuPc$, PTCDI-C_8 kombiniert mit p-Type $H_{16}CuPc$, pentacene, DIP werden als Modellsysteme für organische Halbleiter ausgewählt. Al_2O_3(11-20) Au(100) Einkristalle und SiO_2 werden als Substrate für die organische Molekularstrahlepitaxie verwendet.

1.2 Experimentelle Ergebnisse

1.2.1 Struktur und Wachstum von DIP-Schichten auf Siliziumdioxid

Wir bestimmen die Struktur- und Morphologieeigenschaften organischer Filme des aromatischen Moleküls DIP auf Siliziumdioxid (SiO_2). Siliziumwafer mit einer SiO_2-Schicht werden üblicherweise bei der Anwendung in Feldeffekttransistoren benutzt. Es werden die Wachstumsbedingungen in Abhängigkeit der Substrattemperatur und der Schichtdicke untersucht. DIP wurde ausgewählt, da es ein vielversprechendes Material für die Herstellung von hochgeordneten Filme auf dielektrischen Materialien ist.

Die morphologischen Übergange der DIP Dünnschichten des Lage-auf-Lage Wachstums Modus zu einer schnellen Aufraunung mit Stranski-Krastanow-Wachstums Modus temperaturabhängig und schichtedickeabhängig beobachtet werden. Die van-der-Waals Kraft, also die Interaktion zwischen den DIP Molekülen und dem Substrat führen zu einem geschicheten Wachstums Modus. Im Lage-auf-Lage Wachstums Bereich werden die Größeverteilung und Gestalt so wie laterale Korrelation der zweidimensional Inseln sorgfältig untersucht um ihre Selbst-Affinität, Skalierung und fraktale Eigenschaften aufzudecken. Wir beobachten den Ostwald-Reifung Prozess der 2D-Inseln gewachsen bei Raumtemperatur. Die Variation der Diffusionlänge ist abhängig von Anzahn der Monolage.

Der Anfang des Übergang vom der Lage-auf-Lage zum 3D-Inseln Wachstums-Modus steigt mit zunehmender Substrattemperatur, ~ 3 ML bei RT, ~ 4 ML bei 90 °C und ~ 5 ML bei 120 °C. In Regime des schnellern Aufrauchens führt die Erhöhung der Temperatur Substrat zu einer Verschiebung des Skalenexponenten β zu niedrigeren Werten, nämlich von 0.84 bei RT, ~ 0.80 bei 90 °C, und ~ 0.77 bei 120 °C. Eine höhere Aufdampfen Rate führt zu einer niedriger Monolagen Anyahl und eienem höheren β Wert. Unter dem strukturellem Gerichtspekt bildet die erste DIP Monolage eine dichtere Schicht, trotz des amorphen Charakters der SiO_2 Oberfläche. Die erste DIP-Schicht wird unter einer Belastung Druckfestigkeit auf 96%-97% komprimiert des Gitter-Vektors *a* (bezogen auf die lockere Struktur von dünnen Filmen), während sie entlang Gitter-Vektor *b* auf nur 99.2% komprimiert wird.

Bei 120 °C entwickelt sich die In-plane-Struktur des gesamten Films entwickelt sich kontinuierlich, und erreicht eine entspannte In-plane-Struktur, während bei RT und 90 ° C die Struktur des Films einen abrupten Übergang zum entspannten Struktur erfährt. Bei 120 °C, ändert sich der Abstand zwischen verschiedenen Monolage von DIP-Filmen kontinuierlich von ~ 18 Å beginnt auf 16.732 Å. Der Übergang in die Morphologie von Lage-auf-Lage Modus zum schnelle Aufrauenung ist gleichzeitig mit dem Übergang in der Struktur aus einer komprimierten in-plane Struktur zu einer entspannten verbunden.

1.2.2 Dünne DIP Schichten auf Kupfer

Grenzflächen zwischen Metallen und organischen Materialien sind von besonderem Interesse. Diese Grenzflächen treten z.B. an den elektrischen Kontakten von OFETs auf. Dünne DIP Schichten auf Kupfer Einkristallen stellen ein ideales Modellsystem für organische Moleküle auf metallischen Oberflächen dar. Besonderes Interesse muß hierbei dem Wachstum der organischen Filme gelten, da dieses die Struktur sowie die Morphologie und somit auch alle anderen Eigenschaften der Schichten nachhaltig bestimmen. Hochgeordnete organische Dünnschichten der Moleküle DIP wurden auf der Cu(100) Oberfläche abgeschieden. Die Struktur der Schichten wurde mittels STM untersucht. Tunnelspektroskopiedaten wurden für Monolagen sowie Submonolagen von DIP aufgenommen. Das Wachstum der Submonolagen von DIP auf Cu(100) wurde von Raumtemperatur， 240 K und 150 K direkt in Echtzeit

beobachtet. Messungen an Submonolagen von DIP zeigen eindeutig, dass die Cluster Mobilität Merkmal für verschiedene Substrattemperaturen ist. Zudem wächst die erste Monolage DIP kommensurabel auf dem Metallsubstrat in chirale Domänen. Die Molekül-Substrat-Wechselwirkungen führen zu der beobachteten 2D-Anordernung und weitern das epitaktischen Wachstum der Vielfachschichten. Die 2D-Domänen von Monolagen sind metastabil, d.h. eine bessere Anordernung der Moleküle nach dem Ausheilen.

1.2.3 Dünne DIP Schichten auf selbstordnenden Monolagen (SAMs)

Wir haben die Bedeckungscharakteristiken von selbstordnenden Monolagen SAM's auf Siliziumoberflächen mit dem AFM untersucht. Das Wachstum einer Monoschicht aus APS auf Si(100) in Lösung wurde mittels ex-situ Rasterkraftmikroskopie untersucht. Die Höhe der Monoschicht liegt durchgängig bei etwa 1.7 nm wie Röntgenreflexionsspektroskopie Messungen yeigen. Das System APS auf Siliziumoxid bildet charakteristische atomische flache Monolagen aus. Auf diese nasschemisch abgeschiedenen organischen APS Filme werden im Ultrahochvakuum mittels Molekularstrahlepitaxie (MBE) dünne DIP Schichten (~ 15 nm) aufgedamft. Die DIP Schichte zeigen ein sehr unterschiedliches Wachstumsverhalten abhängig von den Substrattemperaturen. Die DIP-filme bedecken die APS mit einem geschlossenen Film auf niedriger Temperatur. Das System bildet Mikrometer Große Inselstrukturen bei höheren Substrattemperaturen. Die Temperatur von Übergang der 2D auf 3D Wachstum ist ~ 80 °C. Die Höhe der Inseln liegt durchgängig bei etwa 2.4 nm, woraus sich auf eine fast senkrechte Orientierung der Moleküle zur Oberfläche schließen lässt, woraus sich auf eine fast Molekulare auflöste Bilder zeigen, dass die Inseln mono-kristalline sind, mit möglichen Anwendungen in elektronischen Geräten. GIXD Messungen zeigen die gleiche Film Struktur bei verschiedenen Morphologien.

1.2.4 1D organische F_{16}CuPc Strukturen

Metallische Partikel mit Ausdehnungen im Nanometerbereich zeigen i.A. mit der Teilchengrösse stark veränderndte physikalische und chemische Eigenschaften. In dieser Arbeit werden Gold-Nanoteilchen mit wohldefinierter Teilchengröße und -abstand, welche durch ein spezielles chemisches Verfahren beruhend auf Gold-beladenen Mizellen in Kombination mit einem Plasmaprozeß grossflächig auf Bor-dotierten Diamantsubstraten deponiert wurden, als Schablone benutzt. Die Teilchengröße variatiert zwischen 2 und 50 nm. Auf diese Gold-Nanoteilchen Schablone werden im Ultrahochvakuum mittels OMBE dünne F_{16}CuPc Schichten (~ 15 nm) aufgedamft. F_{16}CuPc formiert einheitliche 1D Nanodrähte / Nanoröhren. Diese Nanodrähte / Nanoröhren zeigen keine Abhängigkeit von der Größe der Nanopartikel und haben einen universellen Durchmesser von 20-30 nm mit präziser Lokalisierung auf den Gold-Nanopartikeln. Die Packungsdichte der 1D Nanodrähte / Nanoröhren wird durch die Dichte der Gold-Nanopartikel bestimmt. Die Bildung der Nanodrähte / Nanoröhrchen hat eine sensibles Selektivität von Substrat Temperatur und die Größe der Au Nanopartikel.

1.2.5 Organisch-organische Heteroschichten

Organisch-organische Heteroschichten sind für zukünftige elektronische und opto-elektronische Bauteile von großem Interesse, z.B. für Leuchtdioden, Transistoren, Informationsspeicher, oder photovoltaischen Zellen. An den Grenzflächen zwischen einzelnen organischen Schichten innerhalb der Bauteile kann optisch induzierte Ladungstrennung stattfinden, was zu einer lokalisierten Dipolschicht führt. In der vorliegenden Arbeit soll mit Hilfe einer XRD-Messung die Ausbildung einer Licht-induzierten Dipolschicht verfolgt, und quantitativ erfasst werden. Der besondere Vorteil dieser Methode im Verglich zu anderen ist, dass man rechzeitig die Struktur Veränderung beobachten.

Wir untersuchen die Struktur, die Eigenschaften und die Anorderung von organischen-organische Heterostrukturen. Wir haben folgende Dünnschicht Struktur der untersuchten Systeme festgestellt: i) DIP/H_{16}CuPc Heterostruktur zeigt einen Wachstum Übergang von der

LBL (RT) zum SK (130 °C). Die Struktur der bedeckenden H_{16}CuPc Lage bleibt gleich unter die Ablagerung von dünnen DIP Filmen. DIP dünnen Filme zeigen strukturelle Veränderungen mit dem Schichtdecke, die auch bei der Heterostruktur DIP/F_{16}CuPc und DIP/SiO_2 beobachtet wird. ii) Die Struktur und die Anorderung von F_{16}CuPc/H_{16}CuPc und H_{16}CuPc/F_{16}CuPc Heterostrukturen sind stark mit der Reihenfolge der abgelagerten Schichtdicke der Pufferschicht korreliert. Wir schlagen vor, dass der Aufbau einer Grenzschicht die Eigenschaften der Struktur und die Anorderung von Auflage beeinflusst. Die vorliegenden Ergebnisse zeigen, dass eine dünne F_{16}CuPc Schichte als PufferSchicht zu den besten der Orderung der Heterostruktur Struktur führt und werden als PufferSchicht in der Design-Ebene gewählt wird. iii) Die pentacene/PTCDI und PTCDI/pentacene Heterostruktur-Seriess auf SiO_2 order Al_2O_3 zeigen komplexere Szenarien. Pentacen (RT) / PTCDI(RT)/SiO_2 zeigt wenig in der in-plane-Orderung und keine Out-of-Plane Orderung von pentacene Auflage. Im Gegensatz dazu zeigen die Heterostrukturen pentacene(RT)/ PTCDI(150 °C)/SiO_2 hervorragende strukturelle Orderung von pentacene Auflage sowie gut definierter Monolage Höhe aufgrund der besseren schabloner LBL Morphologie und höhere strukturelle Orderung des PTCDI Puffer-Schicht gewachsen bei 150 °C. Die Heterostruktur von PTCDI(RT)/pentacene(RT)/SiO_2 Exponate zeigt große strukturelle Orderung. Pentacene (RT) / PTCDI (RT) / Al_2O_3 zeigt wenig In-plane-Orderung, sondern Out-of-Plane-Orderung von pentacene Auflage. Die Pentacene(RT)/PTCDI(150°C)/Al_2O_3 Heterostrukturen zeigen große Struktur Orderung und bessere Ausrichtung des pentacene dünn Films senkrectbar Bezug das Substrat Oberfläche. Die Heterostruktur von PTCDI (RT)/pentacene (RT)/Al_2O_3 zeigt wenig in der In-Plane Anordernung und keine Out-of-Plane Anordernung des PTCDI Auflage.

Chapter 2

Introduction

An organic semiconductor is any organic material that has semiconductor properties. In contrast to inorganic materials (covalence bond), the solid state structure of organic semiconductors is based on weak interactions, principally van der Waals and dipole-dipole interactions, between neighboring molecules/polymer chains. Organic semiconductors offer remarkable potential as active elements in new generations of organic electronics. They possess a number of advantages over conventional inorganic Si and Ge semiconductor devices: high brightness and contrast, wide viewing angle, low power consumption and light weight. Such devices are expected to be ultimately incorporated, for instance, into large area all-plastic integrated circuits for low-end and cheap electronics. The technological promise of these unique characteristics puts organic semiconductors to the forefront of research efforts and enormous progress has been made in both experimental and theoretical investigations. Breakthrough products employed in commercial technologies include organic field effect-transistors (OFETs) showing promise as their efficiencies are being rapidly improved [1-8], organic light-emitting diodes (OLEDs) used in displays for car radios [9-15] and organic photovoltaic cells and solar cells also employ conducting polymers for a number of applications [16-20].

Respect to organic semiconducting materials, there are two classes are actively investigated for organic electronic applications: π-conjugated polymers and "small" semiconducting oligomers. Organic semiconducting polymers include intrinsically conductive polymers (ICPs) and light emitting polymers (LEPs) possessing electronic band gaps that allow for the emission of visible light. Organic polymers contain long chain block bone which normally gives rise to disordered structures. In contrast, small organic molecules

possess extended π-conjugation that can form well-ordered crystalline structures and thus allow for the preparation of high purity, highly ordered thin films by sublimation techniques. Some oligomers may be processable by solution techniques. Although it is not yet clear which class of organic materials will dominate future organic electronics, the devices that have so far reached the market are mainly made from oligomers. In addition, the high-quality films of oligomers can serve as model systems that will ultimately make it possible to also understand the properties of polymers, in particular the mechanisms governing charge transport. The frequently used small organic semiconductors include pentacene, anthracene, rubrene, Alq_3, and sexithiophene, etc. The close packing of the molecules in the solid enhances the π-orbital overlap in the material, origin of its semiconducting and transport properties.

Charge-carrier injection from a metal electrode into an organic thin film or from one organic thin film into another, and charge-carrier transport within the organic thin films, all are important parameters for device operation. Thus, organic electronic performance relies largely on the morphology, structure, ordering and thermal stability of the thin films and the properties of the interfacial layers. For instance, thin films showing highly ordered structure and high crystallinity normally have a better performance. For the morphological respect, the thin films exhibiting large domains and less grain boundaries have higher charge mobility. The organic/dielectric interface is a must of all organic devices. The metal-organic interfaces occur, e.g., at the metal contacts of OFETs where they influence the charge carrier injection in the organic film. In some devices, such as organic solar cells, or OLEDs, or ambiplolar transistors, organic-organic heterojunctions are basic elements, thus a comprehensive survey of the organic-organic interface is crucial for technological applications.

The aim of this thesis was to systematically investigate the complex interplay and interconnection between morphology, structure and ordering of the organic thin films and the organic/inorganic and organic/organic interfacial properties by performing X-ray diffraction and AFM/STM measurements. The compounds under investigation include n-type organic semiconductors: di-indenoperylene (DIP), PTCDI-C_8, F_{16}CuPc and p-type organic semiconductors: H_{16}CuPc and pentacene.

The first part of this thesis is organized as follows. Chapter 3 and 4 present a theoretical introduction to X-ray and AFM/STM. In chapter 5, some general aspects of thin film growth

and in more detail the specific techniques of organic molecular beam deposition (OMBD). The experimental methods for the preparation of the organic and the different experimental techniques used within this thesis are described in chapter 6.

The MBE growth is a non-equilibrium procedure. Recently there is considerable effort in the development and analysis of appropriate non-equilibrium models for epitaxial growth to extract detailed information about the underlying atomistic processes and their energetics, more beyond, to gain sufficient insight to control and manipulate the thin film morphology and structure to achieve desired properties. The most widely used models include: at the level of classical mechanics, molecular dynamics; stochastic atomistic lattice-gas models, which are typically analyzed by kinetic Monte Carlo simulation; or a continuum approaches. In addition, the self affine nature and scaling properties of the thin film is of great interest. Here we use thin film growth of DIP on SiO_2 as a model system to study the growth process of organic molecules on dielectric surfaces to (addressed in chapter 7). To shed light on the underlying physical mechanisms, we performed a complete structural and morphological characterization of the DIP grown on SiO_2 from initial sub-monolayer regime to 3D growth regime at a various substrate temperature and deposition rate. The temperature ranges from non-equilibrium (at room temperature) to near-equilibrium state (120 °C).

In organics-based (opto)electronic devices, the interface properties have remarkable impact on the barrier for charge injection between the metal electrodes and the active organic layers, as dipoles form at the organic/metal interfaces. Detail knowledge of the interfacial properties of the organic-metal interface is of crucial importance. Scanning tunneling microscopy (STM) imaging has proven to be a powerful tool to access the local morphology with resolution on the nanometer scale. Moreover, real time STM investigation provides a unique pathway to study the initial formation of the organic molecules on the metal surface. Therefore, chapter 8 is devoted to study the interfacial properties and self assembly process of DIP on transition metal surface Cu investigated by STM.

Chapter 9 present two alternative approaches of the controlled fabrication of organic semiconducting structures for the new electronic devices: the selective growth of one dimensional organic nanowires/nanotubes of by using metal nanoparticle templates; growth of large micrometer size DIP single crystals by functionalizing the surface using self-assembled monolayer.

Organic-organic heterostructures have recently received much attention due to their application in OLEDs or OFETs with ambipolar characteristics. However, to improve stability and increase the lifetime of real devices remains an important challenge. Organic-on-organic epitaxy is a very promising strategy to obtain well-ordered heterostructures of active organic molecules. In Chapter 10, we discuss the experimental results of the structural and ordering investigations organic-organic heterostructure.

Finally, we summarize the results in the last part of the thesis, i.e. chapter 11.

Chapter 3

X Ray Scattering

X-rays were discovered by a German physicist Wilhelm C. Röntgen (figure 3.1) in 1895. X-gamma rays. As the wavelength scale is comparable to the size of atoms, X rays are ideally suited to probe the structural arrangement of atoms and molecules in a wide range of materials. X-ray diffraction, discovered by Max von Laue (1912), is a powerful well-established method for study of the structural properties; especially the penetration depth makes it useful for investigations of buried solid-liquid and solid-solid interfaces. For more detailed information about the basic principles of X-rays, the reader is referred to [21-26].

Discovery of X ray, Mr. Röntgen Mrs. Röntgen's hand under X ray

Figure 3.1: A photo of W.C. Röntgen, who discovered X ray (left). The first X ray radiation graph (right).

3.1 Basic principle of X-ray Scattering

If one considers an X-ray beam as a monochromatic plane wave, then the spatial and temporal variation of the X ray wave propagating along $\vec{r}$ direction can be expressed as

$$\vec{E}_{in}(\vec{r},t) = \hat{\varepsilon}E_0 e^{i(\vec{k}_i \cdot \vec{r} - \omega t)}, \tag{3.1}$$

where $\hat{\varepsilon}$ is the unit vector, $\vec{k}_i$ is the wave vector, $\hat{\varepsilon} \cdot \vec{k}_i = 0$ since the transverse character of electromagnetic waves, t is the time. An X-ray photon can either be scattered or absorbed when it interacts with a medium. The scattering process involves both $\vec{k}_i$ and the scattered wave $\vec{k}_f$. The momentum transfer $\vec{q}$ is given by

$$\vec{q} = \vec{k}_i - \vec{k}_f . \tag{3.2}$$

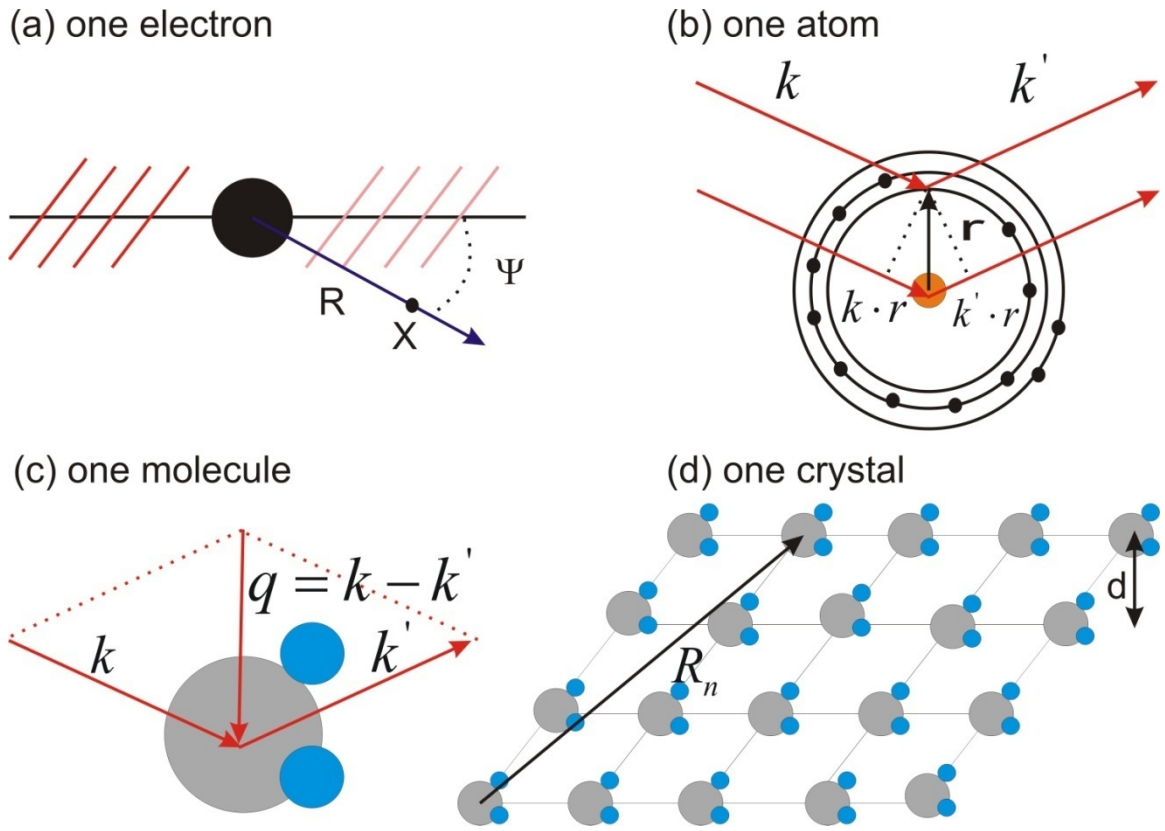

Figure 3.2: The scattering from (a) an electron, (b) an atom, (c) a molecule and (d) a molecular crystal.

3.1.1 One electron scattering

Electron is the elementary scattering unit for X-rays. In the classical description of the scattering process, an electron will be forced to vibrate when it weakly interacts with an X-ray and radiates as a second source, as illustrated in figure 3.3 (a). The magnitude of the radiated field is,

$$\vec{E}_{rad}(\vec{R},t) = -r_e \frac{e^{i\vec{k}\cdot\vec{R}}}{|R|}\cos\psi \cdot \vec{E}_{in} \tag{3.3}$$

where ψ is the angle with respect to the direction of the incident beam and $\vec{R}$ is the distance from the scattering point to an observation point X, and r_e is the classical electron radius:

$$r_e = \frac{e^2}{4\pi\varepsilon_0 mc^2} = 2.82\times10^{-5}\ \text{Å}, \tag{3.4}$$

where e is the electron charge, m is the mass of the electron and c is the speed of the light. The minus sign in Eq. 3.3 indicates that the radiation field is 180° out of phase with the incident field. The intensity of the field radiated by an electron illuminated by an X ray source is therefore,

$$I \propto \left|E_{rad}\right|^2 = \left(\frac{r_e^2}{R^2}\right)\left\langle E_{in}^2\right\rangle P \tag{3.5}$$

where P is the polarization factor dependent on the source; for an unpolarized source, $P = \frac{1}{2}(1+\cos^2\psi)$, and for synchrotron radiation, $P = 1$ or $P = \cos^2\psi$ depending on the scattering plane.

If $d\Omega$ is taken as be the solid angle subtended by the X-ray detector and $d\sigma$ the number of X-rays scattered per second into $d\Omega$, we can define the differential cross section as $\frac{d\sigma}{d\Omega}$. For elastic scattering of a free electron (Thomson scattering), the differential cross section is,

$$\left(\frac{d\sigma}{d\Omega}\right) = r_e^2 P \tag{3.6}$$

3.1.2 One atom scattering

In an atom composed of Z electrons, the electrons are considered to be continuously distributed in the atom and can be described by the electron density function $\rho(r)$. The scattered radiation field is now due to a superposition of contributions from this charge distribution. To evaluate this superposition, we assume that the incident wave interacts with the volume element at the origin 0 and the position $\vec{r}$ respectively, shown in figure 3.2 (b).

To describe the response of the atom to X-ray, we introduce the atomic form factor

$$\hat{f}(\vec{q},\hbar\omega) = f^0(\vec{q}) + \hat{f}'(\hbar\omega) + i\hat{f}''(\hbar\omega) \tag{3.7}$$

where f^0 is an isotropic, non-resonant term. $\hat{f}'$ and $\hat{f}''$, known as the dispersion or anomalous corrections, are (3x3) tensors of the resonant contributions dominated by tightly bound inner-shell electrons.

3.1.3 One molecule scattering

We proceed to consider the scattering from a molecule composed of numbers of atoms (figure 3.2 (c)). The form factor of molecule can be extended to the molecule by considering the atomic form factors of the consisting atoms (labeled as j atom) and their positions inside the molecule r_j,

$$F^{mol}(\vec{q}) = \sum_{r_j} f_j(\vec{q}) e^{i\vec{q}\cdot\vec{r}_j} \tag{3.8}$$

where $f_j(\vec{q})$ is the atomic form factor of the j th atom in the molecule.

3.1.4 A crystal scattering

The scattering of X-rays from a crystalline material periodic in space fulfills Bragg's law under the condition that the reflected waves interfere constructively (Laue condition). Applying the Laue condition and taking d as the spacing of the reflection planes, the Bragg law is defined as

$$m\lambda = 2d\sin\alpha_i\,, \tag{3.9}$$

where m is the integer number.

If $\vec{R}_n$ is the vector that defines the lattice and $\vec{r}_j$ the position vector of the atoms, then the position of any atom can be described by $\vec{R}_n + \vec{r}_j$. The unit cell structure factor is

$$F^{crystal}(q) = \sum_{r_j} f_j(q) e^{iq\cdot r_j} \sum_{R_n} e^{iq\cdot R_n} \tag{3.10}$$

where the first term is the unit cell structure and the second term is a sum over all lattice positions. The lattice vectors $\vec{R}_n$ have the form of $\vec{R}_n = n_1\vec{a}_1 + n_2\vec{a}_2 + n_3\vec{a}_3$, where $(\vec{a}_1, \vec{a}_2, \vec{a}_3)$ are the basis vectors of the lattice and (n_1, n_2, n_3) are integers.

If one defines reciprocal lattice basis,

$$\vec{a}_1^{\,*} = 2\pi\frac{\vec{a}_2\times\vec{a}_3}{\vec{a}_1\cdot(\vec{a}_2\times\vec{a}_3)},\ \vec{a}_2^{\,*} = 2\pi\frac{\vec{a}_3\times\vec{a}_1}{\vec{a}_1\cdot(\vec{a}_2\times\vec{a}_3)},\ \vec{a}_3^{\,*} = 2\pi\frac{\vec{a}_1\times\vec{a}_2}{\vec{a}_1\cdot(\vec{a}_2\times\vec{a}_3)}, \tag{3.11}$$

then any lattice site in reciprocal space is given by,

$$\vec{G} = h\vec{a}_1^{\,*} + k\vec{a}_2^{\,*} + l\vec{a}_3^{\,*}\,, \tag{3.12}$$

where (h,k,l) are all integers. The lattice sum in Eq. (3.10) will be an integer number if the scattering vector $\vec{q} = \vec{G}$; this is the Laue condition for diffraction from a lattice which is equivalent to Bragg's law.

3.2 Specular reflectivity

We consider the specular reflectivity of flat surfaces, a process which does not involve loss of energy of the impinging radiation, i.e. elastic scattering. For a flat surface, the reflected specular intensity will be confined to a direction symmetric from the incident beam, the scattered and incident wave have the same wavelength and the incident angle α_i and the scattered angle α_f are identical, so $|\vec{k}_i| = |\vec{k}_f|$ and $\vec{q}$ is along the surface normal,

$$|\vec{q}| = 2|k|\sin\alpha_i = \frac{4\pi}{\lambda}\sin\alpha_i\,. \tag{3.13}$$

We introduce the index of the refraction, n, to describe the reflection and refraction of X-

rays,

$$n = 1 - \delta + i\beta, \tag{3.14}$$

where δ and β are the dispersion and absorption of the material, respectively. Usually, δ is of order of 10^{-5} in solid materials and the imaginary part β is normally two magnitudes smaller than δ. In the limit of small angles of incidence as the refractive index n is close to unity, thus and the electron density can be considered as continuous. In this approximation, the reflection can be treated as a classical problem of reflection of an electromagnetic wave at an interface. The reflected amplitude is obtained by writing the continuity equation of the electric field and of the magnetic field at the interface. This leads to the classical Fresnel reflectivity of r, amplitude reflectivity and t, transmittivity [27-28]:

$$r = \frac{k_{i,z} - k_{t,z}}{k_{i,z} + k_{t,z}} \tag{3.15}$$

and

$$t = \frac{2k_{i,z}}{k_{i,z} + k_{t,z}} \tag{3.16}$$

where $k_{i,z}$ and $k_{t,z}$ are vertical components of incident and transmitted wave respectively.

When the medium presents regions of different electron densities, assuming that the medium consists of n boxes for which each box has a homogenous electron density, then the Fresnel coefficient calculation is performed by applying the boundary conditions of the electric and magnetic fields at each interface. This corresponds to a multilayered film structure consisting of n layers with the total number of interfaces involved being $n+1$. Starting from the air/film interface (the film surface), these interfaces are labeled successively as interface 0, 1… j, n (Fig. 3.3). If α_j is defined as the incidence angle with respect to the interface j, then α_j equals to α_0 the incidence angle with respect to the film surface. Also, the refractive index with respect to the vacuum for the layer j is defined as n_j given by

$$n_j = 1 - \delta_j + i\beta_j \tag{3.17}$$

The Fresnel reflection coefficient of interface j is given by

$$r_j = \frac{k_{j,z} - k_{j+1,z}}{k_{j,z} + k_{j+1,z}} \tag{3.18}$$

with $k_j = 4\pi\sqrt{\alpha_c^2 - 2\delta_j - 2i\beta_j}\,/\,\lambda$.

To calculate the specular X-ray reflectivity intensity at interface j, one can use the recursive algorithm introduced by Parratt (Parratt-formalism) [26,29],

$$X_j = \frac{r_j}{t_j} = e^{-2ik_{z,j}z_j}\,\frac{r_{j,j+1} + X_{j+1}e^{2ik_{z,j+1}z_j}}{1 + r_{j,j+1}X_{j+1}e^{2ik_{z,j+1}z_j}} \tag{3.19}$$

with boundary conditions that $X_{n+1} = 0$ (no reflection from the substrate) and $T_1 = 1$ (the vacuum layer is totally transmitted).

The typical features of reflectivity curve of a multilayer are Bragg peaks separated by Kiessig fringes. The distance between two Bragg peaks is inversely proportional to the periodicity of the multilayer and the one between Kiessig fringes gives the total thickness of the multilayer d via $\frac{2\pi}{d}$.

Real surfaces or interfaces of multilayers are never ideally flat as assumed in above formalism. X-ray techniques are extremely sensitive to any defects in flatness and a significant part of the intensity is scattered off-specularly in the diffuse regime (figure 3.2). According to the so called kinematical theory, the roughness σ of the surface is considered. The definition of σ is,

$$\sigma^2 = \left\langle (z(x,y) - \bar{z}^2 \right\rangle, \tag{3.20}$$

where $z(x,y)$ is the height positioned at (x,y), and $\bar{z}$ denotes average height.

Surface roughness reduces the specular reflectivity by Debye–Waller like factor. In the assumaption of small correlation length of the height fluctuations, one can take

$$r^{rough} = r^{flat}e^{-2k_{i,z}k_{t,z}\sigma^2} \tag{3.21}$$

For multilayers, a term of $e^{-2k_{Z,j}k_{z,j+1}\sigma_{j,j+1}^2}$ to account for the roughness of each interface should be included into each Fresnel reflection coefficient.

The reflectivity of an arbitrary electron density profile, $\rho(z)$, can be described by the "Master-Formula" under the semi-kinematical approximation:

$$I(q_z) = R_F(q_z)\left|\frac{1}{\rho}\int_{-\infty}^{\infty}\frac{d\rho(z)}{dz}e^{iq_z z}dz\right|^2 . \qquad (3.22)$$

While this formalism in general does not properly take into account effects around the critical angle, it is fairly good for higher angles and has the important advantage of a closed-form equation. Apparently from the definition only points with non-zero density derivative contribute to the Fourier transform.

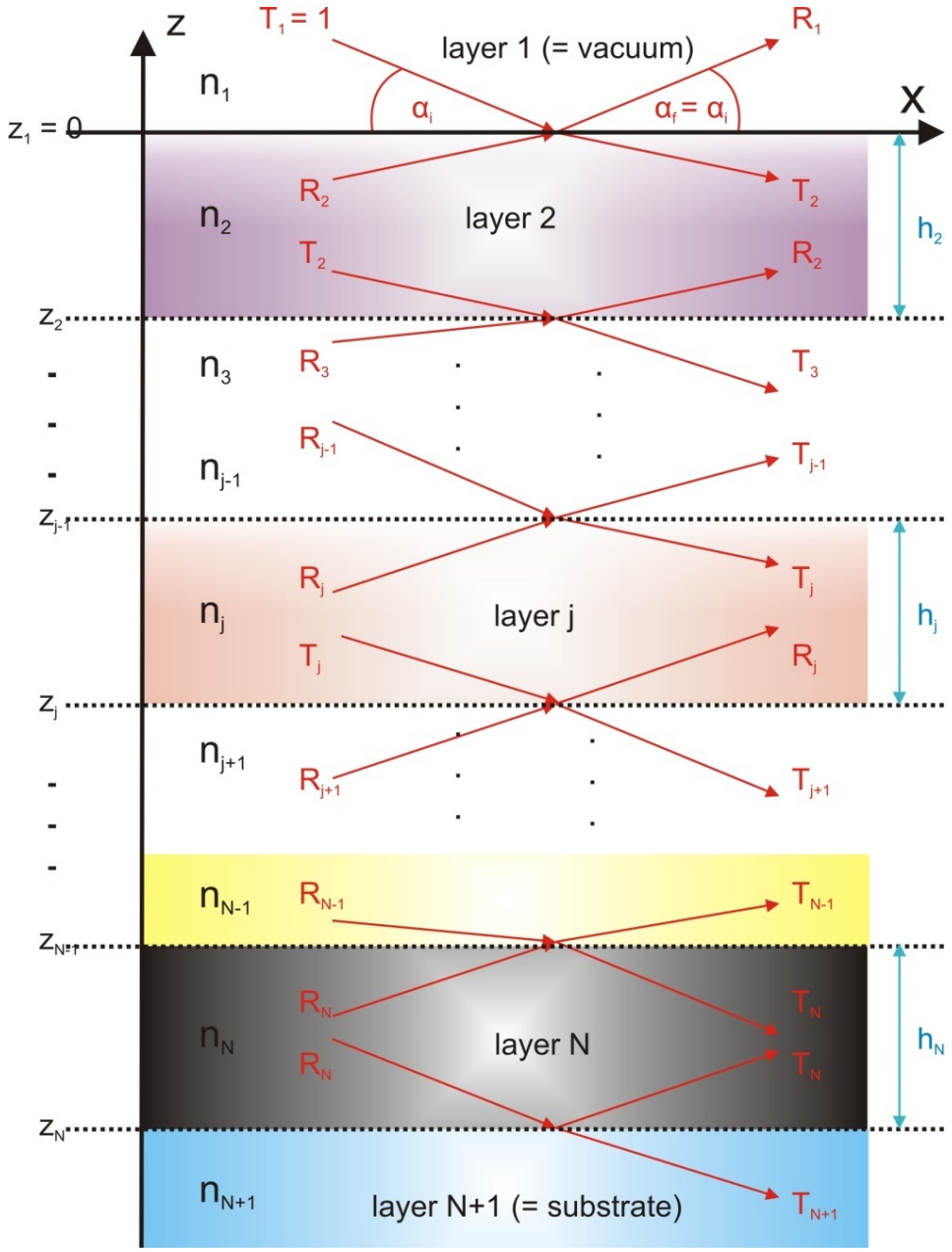

Figure 3.3: Schematic of the refraction of a multilayer.

3.3 Grazing incident X-ray diffraction

For X-rays, solid materials are less refractive than vacuum (defined as having refractive index of 1) resulting in a refractive index smaller than unity. Consequently, there exists a *critical angle* of incidence, α_c, below which X-rays undergo total reflection. Neglecting the absorption ($\beta = 0$), the critical angle α_c relates to the dispersion term δ by

$$\alpha = \alpha_{criticcal} = \sqrt{2\delta} = \sqrt{\frac{\lambda^2 r_e \rho_e}{\pi}} . \tag{3.23}$$

The refracted wave (called in this case evanescent wave) propagates parallel to the interface while its amplitude damps exponentially below the interface. A specimen can be probed with X-rays through its thickness by variation of the angle of incidence to modify the penetration depth. However, critical angle reflection is not well defined for heavily absorbing materials, as reflection is not constant at the critical angle, but a function of β / δ.

If the incident angle of the X-ray wave is set to be at an angle at or smaller than α_c so that the phenomenon of external reflection from the surface can be achieved, the system is said to be in grazing incident geometry. The incident wave is totally reflected while the refracted evanescent wave traveling along the surface. The electromagnetic field can be expressed as

$$E \sim e^{i\vec{q}_{xy} \cdot r_{xy}} e^{-z/\Lambda} \tag{3.24}$$

where $\vec{q}_{xy}$ denotes the wave vector parallel to the surface and the plane parallel to the surface, z represents the direction normal to the surface and Λ is the penetration depth of the X-ray into the system and typically in a range of a few nanometers. The scattering of X-rays from the substrate is minimized (through slightly non-zero k_z) and the surface selectivity is tunable by changing the incident angle of X ray.

If there exists lateral ordering at the surface, the evanescent wave may be diffracted with sufficient intensity to be detected as peaks. The two dimensional lattice points in real space corresponds to two dimensional lattice rods in reciprocal space parallel to q_z. Bragg law of the 2D system can be defined as

$$\vec{q}_{xy} = 2\pi(h\vec{a}^* + k\vec{b}^*) \tag{3.25}$$

As most of the incoming X-ray beam is wasted at grazing angle, the GIXD is performed by

using synchrotron sources which fulfill this purpose and provide highly intense X ray beams.

The organic thin films are two dimensional powders in-plane with randomly oriented crystalline domains. The GIXD measurements were performed by detector scans (δ-scan) to probe polycrystalline rings. In reciprocal space, a δ-scan corresponds to the line profile of the Ewald sphere.

Chapter 4

Scanning Probe Microscopes

Scanning Probe Microscopy is a general term, used to describe a growing number of techniques that use a sharp probe to scan over a surface and measure some property of that surface. Some examples are STM (scanning tunneling microscopy), AFM (atomic force microscopy), and NSOM (Near-Field Scanning Optical Microscopy).

By using such a probe, surfaces can be imaged at the nanometer scale, resolving individual atoms and taking true 3-D maps of surfaces. With this powerful technique, conductive (by STM) or non-conductive materials (by AFM, SNOM), oxides and even biological materials, such as DNA, can be investigated on the sub-nanometer scale. By now, there is a family of some twenty different types of microscopes. They are used both as standard analysis tools and as high-level research instruments and can be found in many academic and industrial laboratories of physics, chemistry and biology.

4.1 Atomic Force Microscope

AFM, invented in 1986 by Gerd Binnig, Calvin F. Quate and Christopher Herber, is one of the foremost tools for imaging, measuring and manipulating matter at the nanoscale. AFM operates by measuring attractive or repulsive forces between a tip attached to a tiny leaf spring (cantilever) and the sample [30-34]. Probing the tip-sample interaction, AFM can apply on conductive and non-conductive samples.

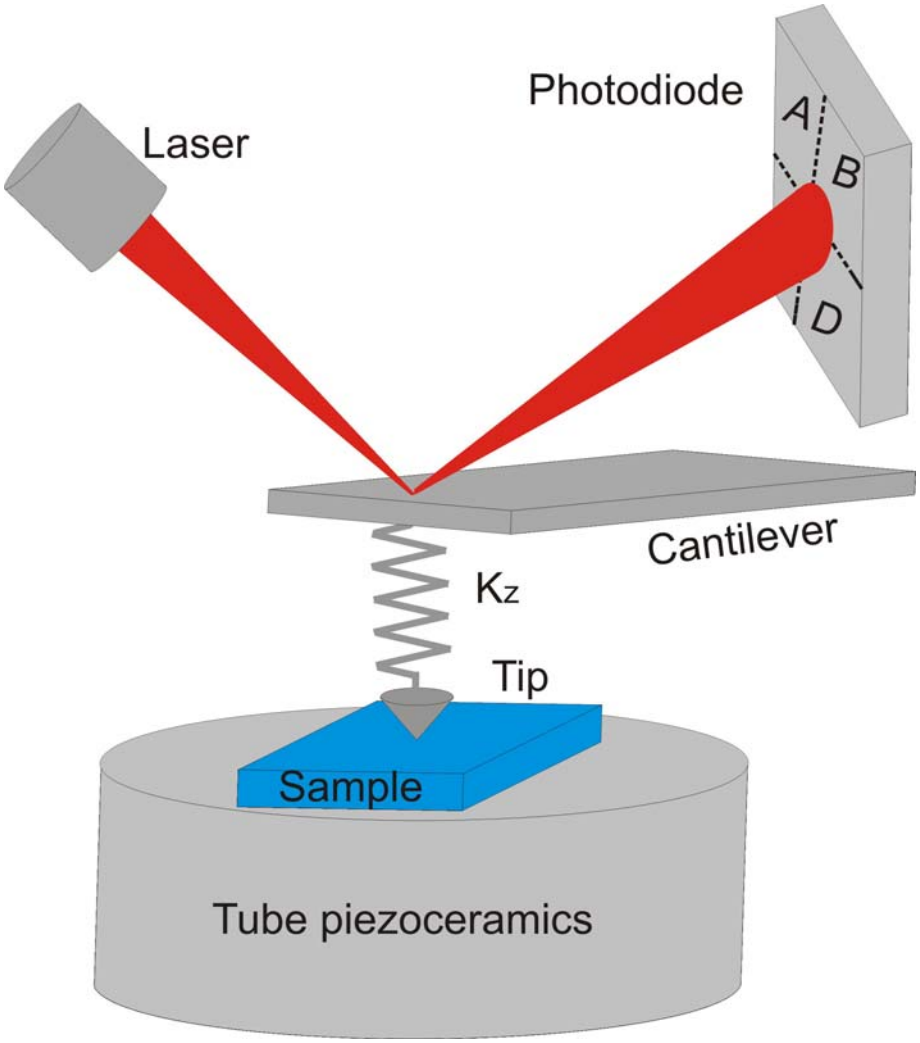

Figure 4.1: A schematic illustration of working principle of AFM: The cantilever visualizes as a coil spring with its spring constant k directly affects the downward force exerted on the sample, which is positioned by tube piezo-ceramics position with high resolution. The laser is reflected by the cantilever to the photodiode to detect the deflection.

The optical lever (figure 4.1) operates by reflecting a laser beam from the cantilever. Angular deflection of the cantilever causes a twofold larger angular deflection of the laser beam making this technique very sensitive to small fluctuation in the surface topography. The reflected laser beam strikes a position-sensitive photo-detector consisting of four segmented photodiodes. The difference between the photodiode signals indicates the position of the laser spot on the detector (the angular deflection of the cantilever) [35-36]:

$$\Delta I_{vertical} = I_A + I_B - (I_C + I_D) \tag{4.1}$$

and

$$\Delta I_{horizontal} = (I_D + I_B) - (I_C + I_A)\,. \tag{4.2}$$

The angular deflection of the cantilever can be correlated with the tip-surface forces by Hooke's law, assuming spring-like behavior of the cantilever: $F = k_z \cdot \Delta Z$, where k is the characteristic spring constant of the cantilever, and ΔZ is its deflection. The movement of the sample is realized by using a piezo-electronic tube of length l, wall thickness h and inner diameter d. The sensitivity is enhanced due to the large l to d ratio and forces as small as a few pico-Newton up to a few nano-Newton can be detected. The concept of resolution in AFM is different from that radiation based microscopies: the former primarily limited by apical probe and sample geometries and the latter by diffraction. The lateral resolution for AFM is defined by the ability to distinguish two separate points on an image.

AFM operation can be qualitatively explained in term of van der Waals forces [37-38]. The interaction of two atoms, located at a distance r from each other, is approximated by Lennard-Jones potential (a schematically represented in figure 4.2) [39]:

$$U(r) = 4\mathrm{E}[-(\left(\frac{\sigma}{r}\right)^6 + \left(\frac{\sigma}{r}\right)^{12}] \tag{4.3}$$

where E is the depth of the potential well and σ is the finite distance at which the interparticle force is zero. The first term describes the “long” range attraction through dipole-dipole interaction of the atoms. The second term represents the short-range repulsion force resulting from overlapping electron orbitals (Pauli repulsion). At relatively large separation, as the atoms are gradually brought together, van de Waals interaction leads to a negative interaction potential and they first weakly attract to each other. This attraction increases until the atoms are so close together that their electron clouds begin to repulse each other electro-statically. This electrostatic repulsion progressively weakens the attractive force as the interatomic separation continues to decrease. The force goes to zero when the distance between the atoms reaches a few Ångstroms, about the length of a chemical bond. When the total van der Waals force becomes positive (repulsive), the atoms are in contact. Upon further approaching, the interatomic interactions lead to a continuous increasing repulsion. In this regime the probe penetrates the sample, first leading to elastic and finally inelastic deformation.

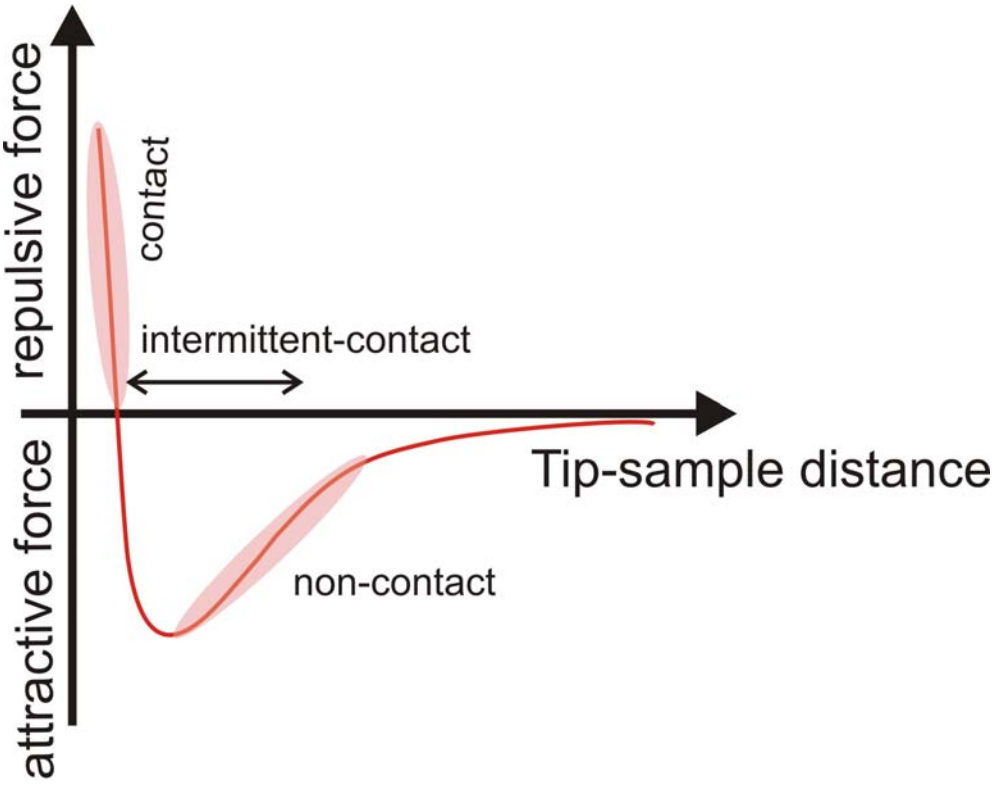

Figure 4.2: A schematic describes the Lennard-Jones force vs tip-sample distance. Depending on the interaction regime, there are normally 3 different operation modes which are marked in figure 4.2: contact mode, non-contact mode and tapping mode (intermittent-contact).

4.1.1 Contact mode

In contact mode, also known as repulsive mode, the apex of the AFM tip is in direct contact with the surface. The elasticity force of the cantilever is counterbalanced by the tip-sample interaction forces. During acquisition, the force between the tip and the surface is kept constant during scanning by maintaining a constant deflection. Due to the steep slope of the van der Waals curve in the contact regime, the repulsive van der Waals force balances almost any force that attempts to push the atoms closer together. In AFM, this means that as the cantilever pushes the tip against the sample, the cantilever bends rather than forcing the tip atoms closer to the sample atoms. In this way, the probe sums over the surface, topological changes are detected be vertical defections of the cantilever. Cantilevers used in contact

mode normally have relatively small stiffness coefficients to provide high sensitivity and to avoid undesirable influence of a tip on a sample. The force exerted between the tip and the sample in contact mode is on the order of about 0.1-1000 nN. Under ambient conditions, two other forces are present besides van der Waals interactions: capillary force from a thin layer of water in the atmosphere and the mechanical force from the cantilever itself. The capillary force causes the AFM tip to stick to the sample surface and its magnitude varies with the tip-sample distance and the ambient humidity. In a liquid, such as water drop on the surface, the large capillary force is isotropic, therefore the total force that the tip exerts on the sample can be reduced to some extent. The mechanical force resulting from the cantilever is similar to the force of a compressed spring and its magnitude and sign (repulsive or attractive) is dependent on the cantilever deflection and the spring constant. Consequently, in contact mode AFM, the repulsive van der Waals forces arising for the AFM tip-sample interaction must balance the sum of the forces arising from the capillary force plus the mechanical force from the cantilever.

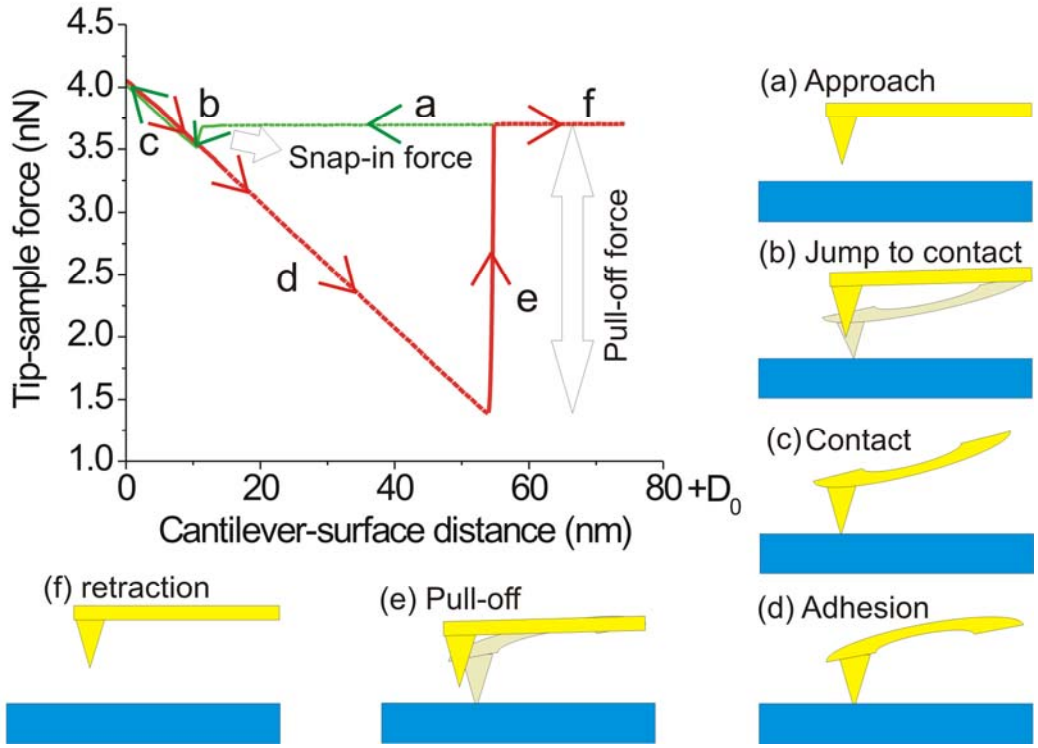

Figure 4.3: A graph of a force-distance curve measured with AFM of DIP film on SiO_2 by using a Si_3N_4 cantilever with force constant of 0.1 nN/nm. (a) to (e) corresponds to the approach and retraction procedure.

With the help of the so-called force-distance curve, the features of local force interactions and the properties of a surface can be measured. As an example, figure 4.3 shows a measurement performed during a cantilever with force constant 0.1nN/nm from a DIP thin film surface. The whole approach-retract procedure is described schematically: (a) the tip approaches to the surface without detecting any force. (b) At a smaller vertical tip-surface distance, the cantilever jumps down into contact due to the attractive tip-surface force. (c) The tip-sample keeps in contact upon a further approach. (d) While retracting, the tip remains in contact with the surface due to the counterbalance of the adhesion force. (e) At a vertical distance, when the force gradient exceeds the cantilever spring constant, the tip "pulls-off". (f) With further retraction, tip moves out of the surface without detecting any force.

During contact mode AFM, as the probe scans over the surface, excepting vertical deflections, surface friction and topologic slope changes can twist the cantilever and give rise to lateral forces on the cantilever. Thus a lateral force image is formed simultaneously with topological images. Lateral forces exhibit minor part of topology and pronounced variations in the chemical composition of the surface. Lateral force microscopy (LFM) can provide important information on local variations in chemical composition.

4.1.2 Non-contact mode

Non-Contact AFM (NC-AFM) works via the principle of amplitude modulation detection [39-43]. The spacing between the tip and the sample is on the order of tens to hundreds of angstroms, which is indicated in Figure 3.2 as the non-contact regime. In NC mode, the probe is kept at a fixed height from the surface and the topographical changes are gathered through changes in oscillation of the cantilever. The non-contact mode has the advantage that the tip never makes contact with the surface, and, therefore avoids disturbing or destroying the sample. This is particularly important in measuring of soft materials, for instance, organic thin films or biological cells.

An oscillating cantilever can be approximated by an effective mass m^* with a resonance frequency of f and a spring constant of k. When the cantilever moves across the surface with friction coefficient c and is subject to a non-linear interaction force between the

cantilever and the sample $F(z)$, the resulting equation of motion is

$$m^* \frac{d^2 z}{dt^2} + c\frac{dz}{dt} + (k - \frac{dF}{dz})z = 0 \tag{4.4}$$

For large z, $F = 0$. By reducing z down to the nanometer range, F >0 and imaging is possible by measuring the change in the amplitude and frequency of the oscillation of a cantilever. As the c value is normally negligible; the NC-AFM mechanism can be understood in terms of a force-gradient model. According to this model in the limit of small amplitude, when a cantilever approaches a sample, its resonant frequency experiences a shift in spring constant from its intrinsic spring constant. This is called the effective spring constant (k_{eff}) and the following equation holds [44]:

$$k_{eff} = k - \frac{\partial F}{\partial z} \tag{4.5}$$

The corresponding effective resonance frequency is

$$f_{eff} = \frac{1}{2\pi}\sqrt{\frac{k_{eff}}{m^*}} \tag{4.6}$$

As the change of force is much smaller that the spring constant, $\frac{\partial F}{\partial z} << k$, we have

$$\Delta f = -\frac{f\frac{\partial F}{\partial z}}{2k} \tag{4.7}$$

i.e an attractive force leads to a larger resonance frequency while a repulsive force a smaller one.

There are normally three control parameters in the NC-AFM mode: (1) the driving frequency, f, chosen close to resonance value, (2) the vibration the amplitude A corresponding to zero F (or large z) and (3) the desired vibration amplitude A_{set}. To obtain a NC-AFM image, the cantilever approaches the sample surface until its instantaneous oscillation amplitude drops to the initially chosen set point A_{set}. The set point is chosen such that $A_{set} < A_{f_{set}}$ at the user-defined driving frequency f_{set}. The scans are collected under the condition of A = A_{set}. In essence, from the above model, the NC-AFM image may be considered to be a map of constant interaction-force gradient, i.e. the *stiffness* $\frac{\partial F}{\partial z}$,

experienced by the tip due to the sample. Therefore, scanning at a given amplitude set-point is equivalent to keeping a constant *stiffness*, or force gradient.

4.1.3 Intermittent-contact mode

In intermittent-contact mode or tapping mode, the probe oscillates close enough to the surface, such that there is only intermittent contact between probe and sample during each oscillation period [45-46]. It combines the positive aspects of both non-contact and contact modes: it is mainly nondestructive yet bears the potential for high spatial resolution. Intermittent-contact mode can be realized by keeping the average probe position sufficiently far away from the sample surface and meanwhile sufficiently large driving amplitudes up to hundreds of nm. As a consequence, the small-amplitude approximation is no longer valid and the tip experiences the full variation of the probe-sample interaction potential, described in figure 4.3. The large amplitude establishes the intermittent contact as part of oscillation extends into the repulsive regime. The repulsive forces experienced by the cantilever during intermittent contact lower the oscillation amplitude. This yields a highly surface-sensitive signal that can be used for feedback support. To avoid the tip sticking in the water layer and remaining in contact with the surface, very stiff cantilevers are normally chosen. The main advantage of tapping mode is the improved lateral resolution on soft samples with minimal sample damage.

4.2 Scanning Tunneling Microscope

The scanning tunneling microscope (STM) invented by Binnig and Rohrer [47-51] has become a fundamental experimental technique for the surface science and nanotechnology.
The operation of a STM relies on the tunneling of electrons between a finely sharpened tip (conductive, normally made of tungsten or platinum-iridium wires) and the sample in very close proximity. The electron wave functions of the tip and sample can be expressed in one dimension by quantum mechanics equation as:

$$\psi = Ce^{-2\sqrt{2m(\phi-E)}(d/\hbar)} \tag{4.8}$$

where C is a constant, ϕ is the work function, d is the distance to surface and E is the

energy measured with respect to the Fermi level. When the tip and sample are far apart, Fig. 4.4 (a), they have different Fermi levels E_{Fermi} (work functions ϕ_s for sample and ϕ_T for tip respectively) but equal vacuum levels. When the tip is brought within two nanometers of the sample surface by a piezoelectric transducer, at this small separation, the orbital overlap of tip and sample wavefunctions tend to align Fermi levels as shown in Fig. 4.4 (b). In this equilibrium state, the electrons have equal probability of tunneling from the tip to the sample or vice versa. When a voltage V is applied to sample, the energy levels will be rigidly shifted upward or downward depending on the polarity of the applied voltage by amount of eV, in turn, a net tunneling current arises, flowing through the vacuum gap in the direction of the bias, (Fig. 4.4 (c) and (d)).

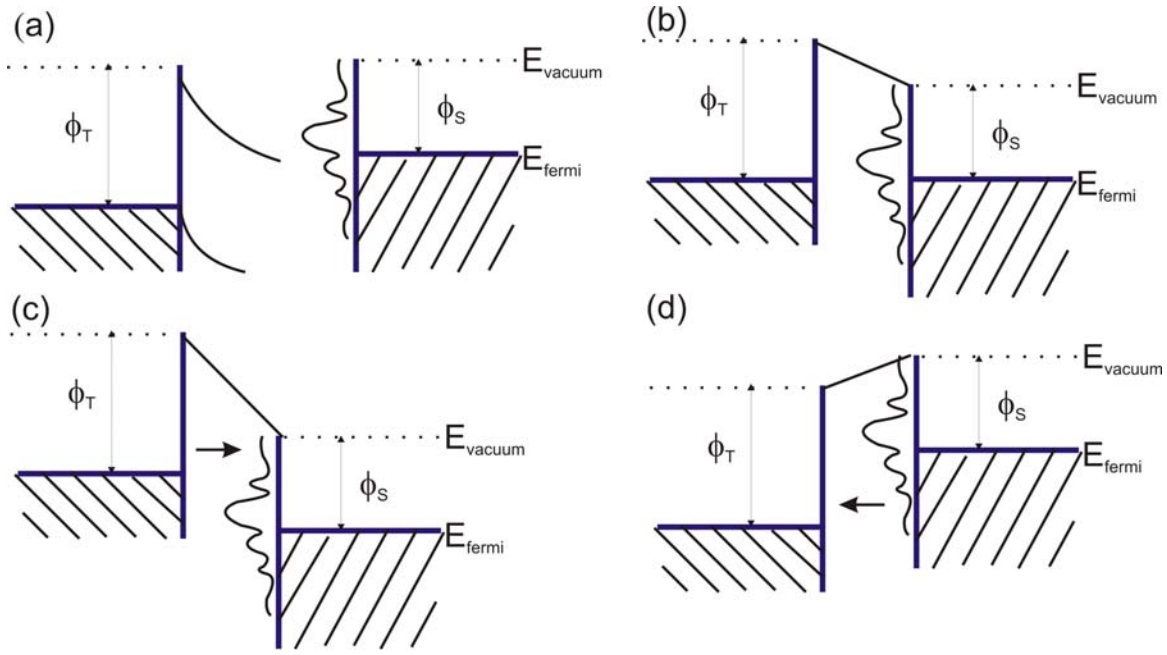

Figure 4.4: Energy level diagram for sample and tip. (a) Independent sample and tip. (b) Sample and tip at equilibrium, separated by small vacuum gap. (c) Positively biased sample: electrons tunnel from tip to sample. (d) Negatively biased sample: electrons tunnel from sample to tip.

The tunneling current I can be written based on the perturbative-transfer Hamiltonian approach of Bardeen [52]:

$$I = \frac{e}{\hbar}\sum_{S,T}\left|M_{ST}\right|^2 \delta(E_S - E_T)[f(E_S) - f(E_T + eV)] \tag{4.9}$$

where $$M_{ST} = \frac{\hbar}{2m}\int dS(\psi_S^* \nabla \psi_T - \psi_T^* \nabla \psi_S) \tag{4.10}$$

is the tunnel matrix elements considering the convolution of the tip and sample states, $f(E)$ is Fermi-Dirac function. As tunneling can only occur from filled states into empty states, an δ-function bases on elastic tunneling approximation: the electrons tunnel without losing energy. The energy shift eV is a result of the applied bias voltage V The tunneling current depends on the overlap between the wave functions of tip and sample in the tunneling barrier and decays exponentially with the distance between the tip and sample. This property of the tunneling current is used to operate scanning tunneling microscopy.

A complete description of the tunneling current requires full knowledge of the electronic states of the sample and tip. For a tip ideally terminated with a single atom, the tunneling current is confined laterally to a radius of a few tenths of a nanometer. The remarkable spatial resolution of the STM derives from this lateral confinement of the current. However, the sharpness and the shape of STM tip are difficult to control. There are various ways to describe the tip shape in the theory of STM. Terso and Hamann [53-54] proposed a model to describe the outermost tip atom as an atomic s-wave function which is rather simple and gives good explanation of STM images. In this approach, the tip is treated structuralless as a spherical *s*-wave. The density of states (DOS) is taken as constant. With this assumption, the tunnel matrix in equation 4.10 is simplified and the tunneling current can be taken as proportional to the charge density at the surface:

$$I(R) \propto \sum_{E_F - eV \le E_n \le E_F} \left|\psi_S(R, E_n)\right|^2. \tag{4.11}$$

Thus, the density of states (DOS) above the sample surface in vacuum at the tip position determines the appearance of STM image. Within this model, it is estimated that a change in the tip-surface distance by one Ångstrom results in a variation of a factor of ten in the tunneling current.

One of the basic modes of STM operation is constant-current mode. The bias voltage and current set-point of the feedback loop circuit are two main control parameters. First, the tip is moved towards the surface, until a tunneling current is established. Then the feedback loop is

activated to stabilize the tunneling current at the set-point value. At very low bias voltages, which are commonly used on metallic surfaces, the constant current STM image is governed by the energy integrated local density of states (LDOS) of the sample surface under the Terso-Hamann approximation. In this thesis, however, larger bias voltages (typically on the order of 1V) and higher temperatures (room temperature) are employed for imaging self assembly of organic molecules on metal surface. Thus the energy range of surface states involved in tunneling expands and the molecular orbitals must be taken into account when considering the DOS of the overall system. In this thesis, we study organic semiconductor DIP, which exhibits a moderate HOMO-LUMO gap on Cu (100) surface. Thus, when the surface adsorbate exhibits electronic states near the Fermi level, then individual molecular orbitals may dominate in the mediation of the electron transmission. HOMO of the adsorbate dominantly mediates the process of current tunneling for negative sample bias by the, if the HOMO is situated near the Fermi level. Conversely, the LUMO may play a dominant role in this case of positive sample bias if it is located near the Fermi level. Thus, by appropriately chosing bias voltages, STM images can reveal the shape of individual molecular orbitals [55].

In the spectroscopic mode, the local differential conductivity $\frac{\partial I}{\partial V}$ is measured which is proportional to the LDOS. In practice, the $\frac{\partial I}{\partial V}$ signal is measured by adding to the dc-bias a small ac-bias voltage with an amplitude of a few to a few tens mV. The modulation of the tunneling current due to the change of the bias voltage is extracted by a lock-in amplifier.

Chapter 5

Organic semiconductors

In this chapter we focus on organic molecules with semiconducting properties and the mechanism of organic thin film growth. We first give, in section 1, a review of the basic concepts of organic semiconductors and introduce the organic semiconductors investigated in this thesis. In section 2, we summarize the main processes involved in thin film growth from the vapor deposition and the influence of the growth parameters.

5.1 Basic principles of organic semiconductors

Semiconducting materials based on organic molecules and polymers have been the focus of intense investigation in the past decades [56-58]. These novel materials can be used to make lightweight flexible opto-electronic devices such as displays, solar cells, organic thin film transistors and lasers. Organic semiconductors can be broadly classified into two groups based on their molecular weight: heterocyclic long-chain polymers and conjugated small weight molecules. Polymers are normally soluble in organic solvents and easy to form thin films with large surface area but establish amorphous character. In contrast, small molecules are more facile control of charge transport by modification of various molecular parameters. For example, the ability of these molecules to pack into well ordered polycrystalline films leads to higher mobility compared to polymeric semiconductors. Moreover, organic chemistry offers tools for tailoring materials' functional properties via modifications of the molecular/monomeric units, opening new possibilities for inexpensive device manufacturing. In this thesis, we focus on the growth of thin films formed by oligomers with complementary p- and n-type semiconducting behaviors, which are promising candidates for practical

organic electronic devices.

Organic semiconductors consist of aromatic backbones with feature of 'π-conjugated bonds'. The carbon atom forms three sp^2 hybrids with 120° to each other in a plane and the remaining p-orbital is perpendicular to this plane. A σ-bond between two carbons forms by overlapping of two sp^2-orbitals and sideways overlap of p orbitals gives rise to formation of π bond. Figure 5.1 depicts the orbitals and bonds for two sp^2 hybridised carbon atoms. If carbon atoms form larger molecules, typically with benzene rings as the basic units, the π-bonds become delocalized and form a π -system which often extends over the molecule. The band gap for organic semiconductors corresponds to the energy difference between the highest occupied molecular orbital (HOMO) and the lowest unoccupied molecular orbital (LUMO), which greatly impacts the optical and electrical properties.

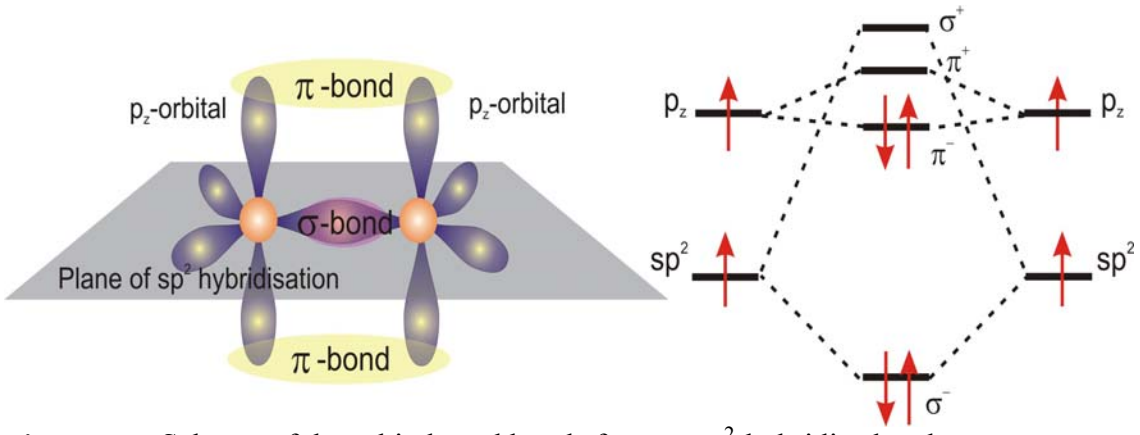

Figure 5.1: Scheme of the orbitals and bonds for two sp^2-hybridised carbon atoms.

Unlike inorganic semiconductors, the structure arrangement of organic semiconductors is based on weak van der Waals and dipole-dipole interactions. The electronic transport includes an intramolecular and an intermolecular transport. The transport within the molecule is very efficient due to the conjugated electrons but limits to small distances. The intermolecular charge hopping between adjacent molecules is slower and depends drastically on efficient intermolecular π orbital overlap.

Di-indenoperylene (DIP)

Di-indeno-perylene (DIP) is a perylene-derivate with two indeno units connected to the

central perylene core (chemical formula $C_{32}H_{16}$). It is known as a red dye "periflanthene" and first synthesized in 1934 by von Braun [59]. DIP is a planar molecule with dimension of 18.4 Å x 7 Å by taking account of van der Waals radii and a molecular weight of 400.48 g/mol, its molecular structure and dimension are illustrated in figure 4.3. DIP has weak solubility in most organic solvents due to its non-polar construction; therefore it is suitable for physical deposition between sublimation temperature 350 °C and decomposition temperature 540 °C [60]. It shows p-type semiconducting behavior in combination with metal contacts.

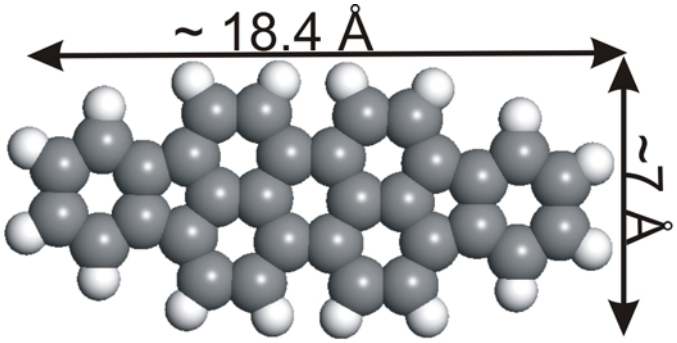

Figure 5.2: Molecular structure and dimension of di-indeno-perylene.

The bulk crystal of DIP has triclinic structure with four molecules in the unit cell, space group P $\bar{1}$ and density of 1.354 g/cm^3 [61]. DIP exhibits various thin film structures depending on specific substrates. On weak inert substrates, for instance, single crystal of NaCl, perylene, a-plane Al_2O_3, or silicon with native or thermal oxide layer, DIP molecules adopt basically upright-standing configuration [62-65]. On the other hand, DIP molecules adopt lying-down configuration on the metal surfaces, for example, on graphite (HOPG), Ag(111) [66] and polycrystalline gold [67] due to strong molecule-substrate coupling. The detailed lattice parameters are listed in Table 5.1.

Unit cell	Single crystal [60]	DIP on SiO_2 [64]	DIP on NaCl [62]	DIP on perylene [62]
a (Å)	11.59	8.55	8.67	11.0
b (Å)	13.97	7.09	6.96	10.6
b (Å)	14.88	16.66	18.55	17.5
α (°)	98.11	--	90.0	90.0
β (°)	98.10	--	93.5	106.0
γ (°)	114.43	90.00	90.0	90
structure	triclinic	rectangular	monoclinic	monoclinic

Table 5.1: DIP lattice parameters of single crystals or thin films.

DIP deposited on amorphous silicon substrates displayed an exceptionally high degree of crystallinity. The XRD measurements showed that a lattice spacing of 16.66 Å. The AFM measurements of the DIP films showed a strong increase in roughness with increasing film thickness referred to as 'rapid roughening' phenomenon. On stepped a-plane sapphire the DIP molecules showed an anisotropic in-plane orientation, in some cases the growth with screw dislocations.

The critical influence of the structural order on the performance of DIP-based organic thin-film transistors has been highlighted in a work by Karl et al.[68-69], where a drastic enhancement of the field-effect mobility could be measured by reducing the mosaicity of the films. In addition, an increase of the charge charier mobility due to the ambient water vapor was reported [70].

Copper-phthalocyanine (F_{16}CuPc and H_{16}CuPc)

Metal phthalocyanines are very well known dye pigments having similarity in structure with biological molecules chlorophyll and haemoglobin. Copper phthalocyanine dyes find extensive use in various areas of textile dyeing, for spin dyeing and in the paper industry. Owing to its semiconductor properties, more importantly high chemical and thermal stability, they become one of the most frequent used molecules for the new organic electronic industry: light emitting diodes (LEDs), solar cells and field-effect transistors, etc [71-73]. H_{16}CuPc shows p type semiconducting behavior observed for when combined with typical contact materials such as Au. For F_{16}CuPc, the fluorine increases the electron affinity of the molecules and favors an efficient electron injection into the empty LUMO states, thus showing n-type semiconducting behavior.

Copper pthalocyanine is a planar molecule, the perfluorinated one (F_{16}CuPc: $C_{32}F_{16}N_8Cu$) has dimension of 14.5 Å x 14.5 Å and a molecular weight of 863.9 g/mol; the normal one (H_{16}CuPc: $C_{32}H_{16}N_8Cu$) has a molecular weight of 576.07 g/mol. The structures of two molecules are illustrated in Fig. 5.3.

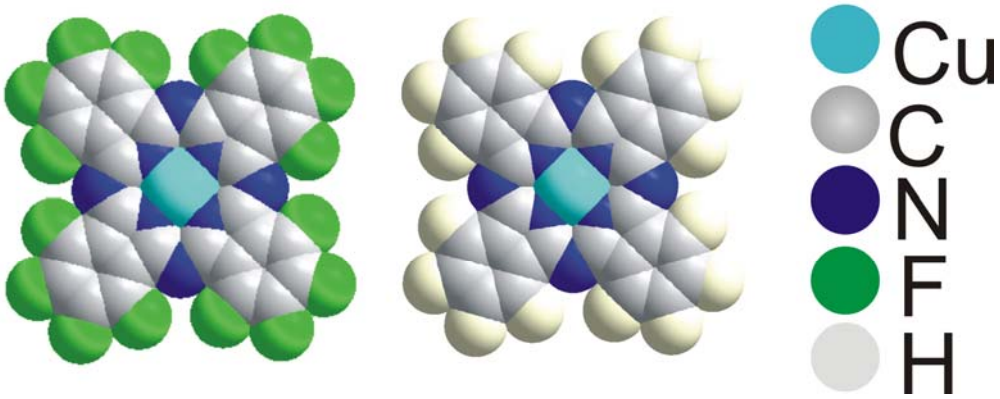

Figure 5.3: Molecular structure of H_{16}CuPc and F_{16}CuPc.

H_{16}CuPc is reported to have polymorphic forms: α-, β-, γ-, δ-, ε-, π-, τ-, and χ-forms [74-79], an example of their crystal structures is listed in Table 5.3. Among the various polymorphs, the metastable α form and the stable β form are the best known and most thoroughly studied forms. In both crystalline forms the phthalocyanine units are positioned in columnar stacks with the ring tilted with respect to the stacking axis (tilt angle), which cohere to form the molecular crystal. The two forms consist of molecular columns, with a herringbone-type arrangement between the columns. One of the significant differences between the α- and β-modifications is the overlapping of neighboring molecules within a molecular column; the α-modification has a larger overlap and hence a smaller lattice constant b along the column direction. Furthermore their lattice parameters are different as well metal-metal distance. The different structure of α and β phase is shown in figure 5.4. The thin film structure of H_{16}CuPc grown epitaxically on different substrates, for example mica (ashida,1966), KCl, KBr, SiO_2 and polycrystalline gold have been investigated, however different literature reported different crystal structures and the data are often not agreeable and the reader is referred to specific literatures for details [80-82].

The bulk structure of F_{16}CuPc has been explored by X-ray powder diffraction with two molecules in the unit cell. However, the detailed structure of F_{16}CuPc thin films on SiO_2 shows much more complex scenario [83]: F_{16}CuPc first forms a low density disordered interfactial layer, then subsequently ~ 2 monolayer thick the so called $\beta_{bilayer}$ phase, then arranged $\beta_{bilayer}$ structure, finally stabilized with β phase structure, the detailed crystal structure is listed in Table 5.3.

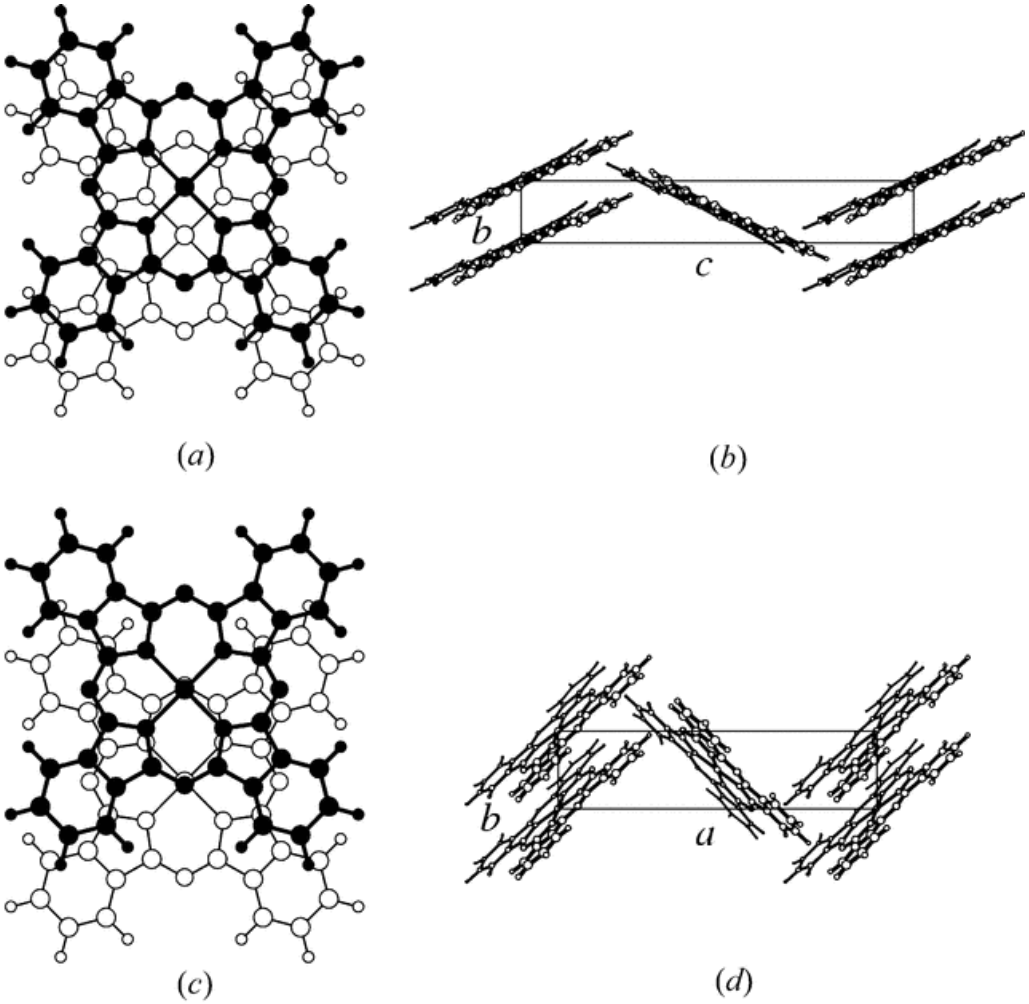

Figure 5.4: Typical crystal structures of planar phthalocyanines: (a) and (b) the α-modification; (c) and (d) the β-modification. (a) and (c) represent the overlapping of neighbouring molecules within a molecular column. Both structures have herringbone type molecular packings (from Hoshino et al.).

	α phase	β phase	γ phase	ε phase
a (Å)	13.886	21.822	17.388	26.591
b (Å)	3.769	4.694	8.6483	3.590
c (Å)	13.061	13.493	11.074	20.225
α (°)	96.2	--	--	--
β (°)	90.6	123.477	113.56	124.352
γ (°)	90.3			
structure	monoclinic	monoclinic		

Table 5.2: $H_{16}CuPc$ lattice parameters of single crystals or thin films.

$F_{16}CuPc$	bulk	β phase	$\beta_{bilayer}$	β-phase
a (Å)	20.018	19.407	14.61	20.26
b (Å)	5.106	4.79	3.31	4.87
c (Å)	15.326	14.628	--	--
α (°)	90	90	--	--
β (°)	111.83	120.56	--	--
γ (°)	90	90	90	84.1
Layer spacing (Å)	15.3	--	14.1	14.3

Table 5.3: $F_{16}CuPc$ lattice parameters of single crystal or thin films on SiO_2.

Pentacene

Pentacene ($C_{22}H_{14}$) is a linear planar oligoacene consisting of five fused benzene rings, see figure 5.5 for molecular structure. It has emerged as a viable p type semiconducting candidate as the active layer in organic thin film transistors (OTFTs), which exhibit high hole mobilities as high as 0.237 $cm^2(Vs)^{-1}$ and high I_{on}/I_{off} ratios [84-88].

The first bulk structure determination of pentacene showed that pentacene has the triclinic structure ($P\bar{1}$) with two molecules in the unit cell and a density of 1.32 g/cm^3. The molecules are arranged in a herringbone packing motif with an interlayer spacing of 14.5 Å [89]. A smaller *d* spacing of 14.1 Å was recently reported for single crystals grown by vapour transport and from solution [90-91]. The detailed structure listed in Table 5.4.

The structures of pentacene thin films, however, differ from the bulk, are attributed to "thin film phases" when deposited on amorphous silicon or other substrates. The "thin film phases" have different *d* spacings, for instance, 15.0 Å, 15.5 Å and 15.4 Å [92-96]. The selectivity of different phases governes by a variety of factors including substrate material, substrate temperature during deposition, rate of deposition, and film thickness. The two-phase coexistence was observed in a few literatures [97-98]. Research efforts have also been extended to the structures of pentacene grown on other various substrates like carbon, kapton and NaCl [99-100].

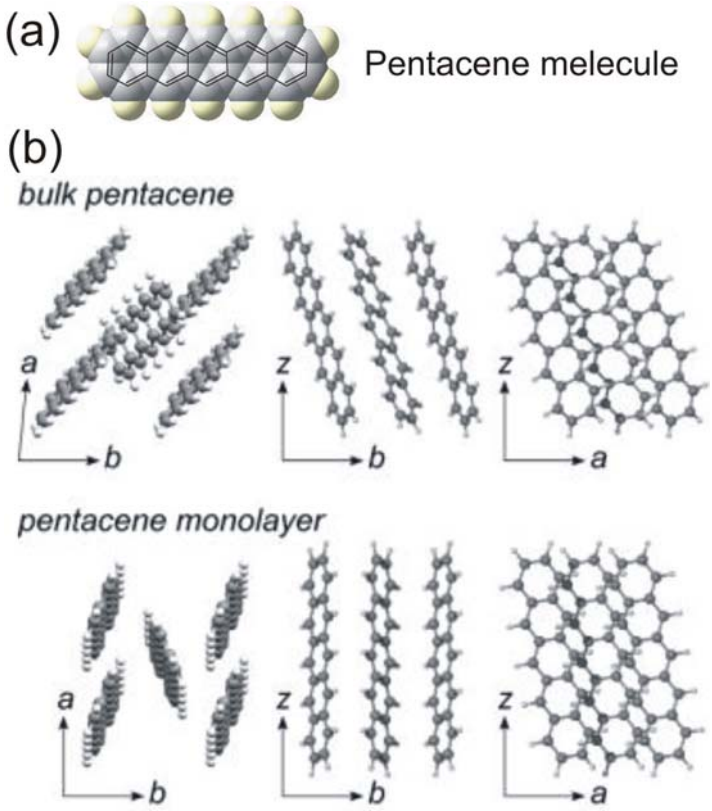

Figure 5.5: (a) Molecular structure of pentacene (b) up: crystal structure of bulk pentacene. down: The thin film structure of pentacene [97].

Pentacene	single	single	single	On SiO_2		
a (Å)	7.93	6.28	6.27	6.37	6.49	5.77
b (Å)	6.14	7.71	7.78	7.53	7.41	7.49
c (Å)	16.03	14.44	14.53	15.1	14.75	17.2
α (°)	101.9	76.75	76.48	71.37	77.25	73.5
β (°)	113.6	88.01	87.68	90.6	85.72	75.3
γ (°)	85.8	84.52	84.68	87.1	80.92	91.2
dspacing	14.4	14.1	14.12	14.4	14.37	15.5

Table 5.4: Lattice parameters of pentacene single crystal and thin film structure of pentacene on SiO_2 [89-96].

PTCDI-C_8

PTCDI-C_8 (N,N*-dioctyl-3,4,9,10-perylene tetracarboxylic diimide) is a planar organic molecule with molecular formula $C_{40}H_{42}O_4N_3$. PTCDI-C_8 is an n-type material (in combination with gold electrodes) and soluble due to its long alkyl chains, the chemical

structure and dimensions are shown in Fig. 5.6. The thin film structure of PTCDI-C8 were investigated by Malenfant et al. using x-ray diffraction and they revealed a d spacing of ~ 20 Å [101]. Krauss et al. revealed an oblique unit cell with lattice parameters of a = 9.1 Å, b = 4.8 Å, c= 20.36 Å and α = 67° by AFM and GIXD [102]. Malenfant et al. employed PTCDI-C_8 thin films into organic thin-film field-effect transistors and measured a mobility of 0.6 $cm^2V^{-1}s^{-1}$ [103].

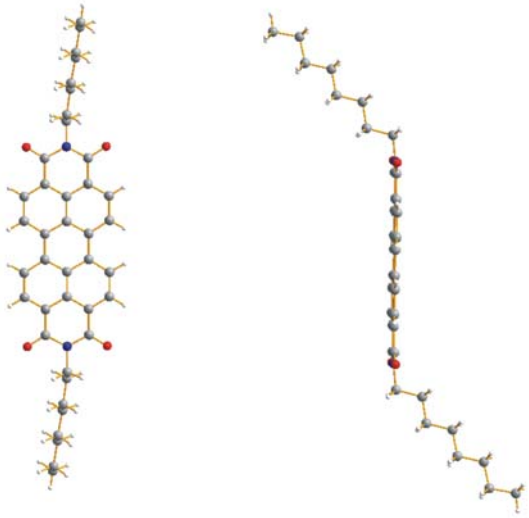

Figure 5.6: Schematic of the structure and dimension of PTCDI-C_8.

The close analog of PTCDI-C_8, PTCDI-C_5, which consists of shorter alkyl chain is studied by Chesterfield et al. focused on polycrystalline thin films of PTCDI-C_5 and bulk structure by E. Hädicke et al., revealed a triclinic structure with one molecule per unit cell with lattice parameters, a=4.754 Å, b=8.479 Å, c=16.296 Å, α=86.88° β=83.50° and δ=83.68° [104]. Struijk et al. focused on studies of the structure and morphology of PTCDI-C_{18} deposited on quartz slides (SiO_2/Si) by applying x-ray diffraction [105]. They calculated a monoclinic unit cell with the parameters a = 10.3 Å, b = 3.6 Å, c = 40.1 Å and β = 81.7°. In addition, they observed phase transitions from crystalline phases to highly ordered liquid crystalline phases and isotropic phases.

5.2 Thin film growth

Crystal and thin film growth are rich subjects with many different facets and enormously theoretical approaches. Basically, the morphology of the growth is governed by the surface energetics to minimize the surface free energy on one hand, and on the other hand by the dynamics, i.e. kinetics of the atomistic processes. The growth taking place under the equilibrium condition is determined mainly by energetic factors. Kinetic aspects however are more important for the growth far from the equilibrium. Crystal growth experiments proceed normally close to equilibrium with high substrate and deposit temperature. Under such growth conditions, only the optimum binding sites of the crystal are stable binding sites. In contrast, in thin film deposition, normally carried out far from the equilibrium, even metastable sites can act as nucleation sites due to the large chemical potential difference. In the following, we would focus on the important concepts related to thin film growth by molecular beam epitaxy (MBE). For the basic concept of the thin film growth, the reader refers to [106-110].

Thin film growth by inorganic molecular beam epitaxy (MBE) and organic molecular beam deposition (OMBD) bear many similarities and some fundamental differences. In MBE, the substrate is a clean single crystal and the adsorbates are usually single atoms or dimmers with isotropic so that the orientation of the adatom relative to the substrate or to other atoms is irrelevant for the strength of the interaction. The adsorbates are chemically absorbed on the substrate with strong covalent or ionic bonds, thus lattice matching is a requisite to avoid the buildup of stress. In contrast, the organic intermolecular bonding is van der Waals in nature and the individual molecules have anisotropy shape, which are responsible for the main difference in the growth mechanism between MBE and OMBE.

Growth modes

In general, growth of thin films is classified into three modes by considering the energy difference among substrate and film surface energies (γ_s, γ_f) and the interface energy (γ_i):

$$\Delta\gamma = \gamma_f + \gamma_i - \gamma_s \tag{5.1}$$

Figure 5.7 illustrates these growth modes: layer-by-layer (Frank-van der Merwe mode),

layer-plus-island (Stranski-Krastanov mode) and island mode (Volmer-Weber mode).

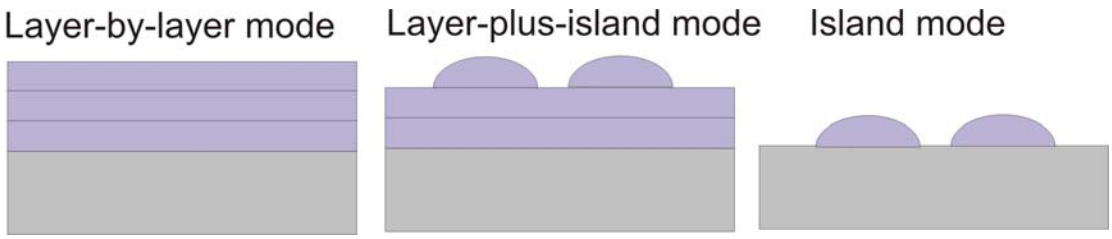

Figure 5.7: Three Growth modes: layer-by-layer, layer-plus-island and island mode.

The layer-by-layer mode ($\Delta\gamma = 0$) occurs when the deposit atoms are more strongly bonded to the substrate than to themselves, thus the formation of islands is energetically unfavorable due to the enlargement of surface. Under this condition a layer tends to complete before the new one starts and the substrate is completed wetting equivalent to a high surface energy of the substrate.

The layer-plus-island mode ($\Delta\gamma < 0$) occurs whenever the layer formation becomes less favorable and the islands develop after formation of one or more wetting layers to lower surface free energy. This growth mode is often observed for lattice mismatched inorganic systems.

The island mode ($\Delta\gamma > 0$) occurs when the interactions within the adsorbates are stronger than to the substrate, forming three-dimensional (3D) islands. In the case of inorganic systems, this mode is typical observed for highly mismatched systems and dissimilar materials.

In the case of organic molecular crystals, the interactions between molecules in the crystal are weak van der Waals interactions. Furthermore the strength of the molecule-molecule and molecule-substrate interactions (and so the free energy of the system) depends on the shape and relative orientation of the molecules.

Nucleation and growth

The elementary processes of nucleation and growth of a thin film grown are schematized in Fig. 5.8. The molecule beam faces the substrate at a flux of F . Considering a unit sticking coefficient, the single atoms on the substrate diffuse with a hopping rate

$$h = \nu \exp(-E_d / k_B T) \tag{5.2}$$

where E_d is the activation barrier for diffusion, k_B is the Boltzmann constant and ν is the attempt frequency for hopping. The diffusion constant D relates to h for two dimensional growth $D = 1/4a^2 h$, where a is the effective hopping distance between sites. In the transient regime, the adatom density builds up following $N_1 \sim Ft$ leading to nucleation of far-separated islands, t is the deposition time and N_1 is the adatom density. Nucleation of the islands occurs upon formation of the stable clusters of adatoms. We assume a well defined critical size i, the island consisting of $i+1$ molecules is stable against dissociation and effectively immobile. In the subsequent steady-state regime, newly deposited atoms will stick to the existing island rather than nucleate new islands. Let N_s denotes the nucleation density (per site) of islands of s atoms, the density of the stable islands is given by $N = \sum_{s>i} N_s$ and the layer coverage $\theta = \sum_{s\geq 1} sN_s = Ft$. The nucleation and formation of the islands can be understood from atomistic kinetic rate equations,

$$\frac{dN_1}{dt} \approx F(1-\theta) - (s+1)K_{nuc} - K_{agg} \tag{5.3}$$

$$\frac{dN_s}{dt} \approx K_{nuc} \tag{5.4}$$

K_{nuc} is the nucleation rate given by $K_{nuc} = \sigma_s h N_1 N_s$, where the capture number is σ_s describing the propensity for capture of diffusion adatoms by islands of size s to form stable island. The aggregation rate is $K_{agg} = \sigma_{av} h N_1 N$, where σ_{av} is the mean capture number for stable islands.

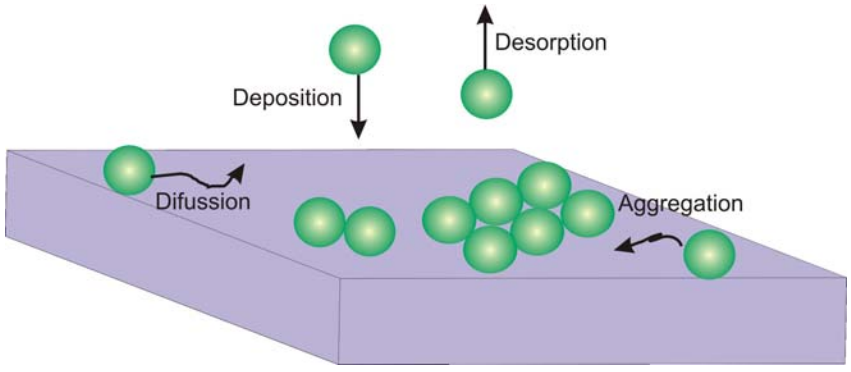

Figure 5.8: Schematic of atomistic process of thin film growth.

Chapter 6

Experimental details

This chapter devotes to introduce experimental preparation of organic thin films and describe the technical details employed for growth and characterization of the organic thin films. After a standard cleaning procedure of the substrates, organic thin films depositions were carried out by means of organic molecular beam deposition (OMBD) under ultra high vacuum (UHV) condition. The structure and morphology properties were investigated by combination of x-ray diffraction, atomic force microscopy, STM and SEM. Synchrotron radiation was used to obtained in-plane structural properties of the organic thin films.

6.1 Preparation of Substrates and self assembled monolayers

For the deposition of the organic films, four different types of substrates have been used, namely inert substrates: oxidized silicon wafers and single-crystalline sapphiresAl_2O_3, which interact weakly with organic thin films by van der Waals force; metal single crystal substrates: Cu (100) and Au (111), which domistrate much stronger interaction when interact with organic molecules.

Native oxidized Si (100) wafers: The silicon wafers have (100)-orientation with a miscut less than 0.5°. The oxide layer has a thickness of ~ 15 Å. There are two cleaning procedures of the Si wafers depending on specific need of the experiments 1) Three circles of successive ultrasonic baths with acetone and ethanol for about ten minutes. 2) The substrates were first cleaned with freshly prepared piranha (98% H_2SO_4, 35% H_2O_2

V:V=7:3) for around 15 min, then rinsed with ultra-pure water. To avoid resident chemicals, the substrates afterwards were ultrasonated with ultra-pure water as last cycle. After that the substrates were immediately dried in a nitrogen stream. Prior to deposition of the organic materials, the substrates were heated in UHV above 400 °C for a minimum of 12 hours to desorb of the rests of organic contaminants and condensed water.

Sapphire (A-plane) substrates: Single crystal Al_2O_3 $(11\bar{2}0)$ platelets (10 mm x 10 mm x 0.5 mm, polished on one side, with a deliberate surface miscut of 0.1°) were used as substrates for some samples (Crystal GmbH, Berlin). A normal surface preparation process was performed as follows: (i) degreased with ultrasonic cleaning in acetone and ethanol each for 10 min, (ii) UHV heating at 400 °C for 2 h. This procedure results in clean, well-defined, and unreconstructed substrates.

Cu (100) and Au (111) substrates: The single crystal Au (111) and Cu (100) substrates were prepared in a standard procedure by consecutive sputter and annealing cycles. For Cu (100) substrate, the sputtering performed at an Ar gas (99.9995% in purity) pressure of 1.8 x 10^{-2} Pa with I_{em}= 30 mA, V= 600 eV for 30 min and the subsequent annealing was at 600 °C for ~ 1h under JEOL UHV system. The Au (111) substrate was sputtered at Ar gas pressure of 1.3 x 10^{-5} mbar with I_{ion}= 10 mA, V=800 eV for 30 min. The annealing temperature was held at T = 700 °C under Omicron UHV system. The formation of large terraces confirmed a good substrate quality by AFM or STM.

The self assembly of 3-aminopropyltriethoxysilane (APS, $(CH_3CH_2O)_3Si(CH_2)_3NH_2$) film was formed by immerging the substrates into the freshly prepared APS solution (1mM APS in absolute toluene solution) for 10 min. Then, the samples were treated in an ethanol and de-ionized water ultrasound bath for around 60 min. This rinsing protocol results in the formation of the flattest and most homogenous APS films among all recipes reported in literature since the quality of the APS monolayer strongly depends on the rinsing process. The freshly-prepared substrates were transferred into the ultra high vacuum chamber and annealed above 100 ºC for 2 hours and then set to the growth temperature.

6.2 UHV systems

Three MBE systems have been used for the sample preparation and the in situ analysis: (1) a stationary Omicron MBE system (in the following called OMBE for organic MBE), (2) a portable MBE chamber optimized for in situ X-ray diffraction experiments, and (3) a commercial JEOL MBE system.

6.2.1 Omicron MBE chamber [111]

The OMBE chamber consists of three parts: load lock, growth chamber and analysis chamber with base pressure of 10^{-7} mbar, 10^{-10} mbar and 10^{-11} mbar respectively.

A small fast entry load-lock chamber works as pathway for introduction and extraction of samples to ambiance or the growth chamber. This chamber is equipped with 4 sample storage stages, one of which provides a heating station for degassing the substrates. A transfer rod allows transferring the samples to the deposition section without breaking the vacuum.

The growth chamber is equipped with a quadrupole mass spectrometer (QMS) for controlling the state of organic melecules, a quartz crystal microbalance (QCM) for monitoring the film thickness and four Knudsen cells for evaporating organic materials and metal. The manipulator allows flexible transferring sample accompanied with a heating and cooling stages. K-type or C-type thermocouples are used for the temperature measurement, and the heating current is regulated by Eurotherm PID controllers. During deposition, the vacuum is in the order of 1×10^{-9} mbar.

In the analysis chamber, LEED, Auger electron spectroscopy (AES), and a combined room temperature AFM and STM are available allowing in situ characterization of the films.

The pressure of the whole system is mounted by an oil-free vorpump, a turbo-molecular pump with additional two ion-pumps and two titanium sublimation pumps. Ion gauges monitor the pressure of the chambers.

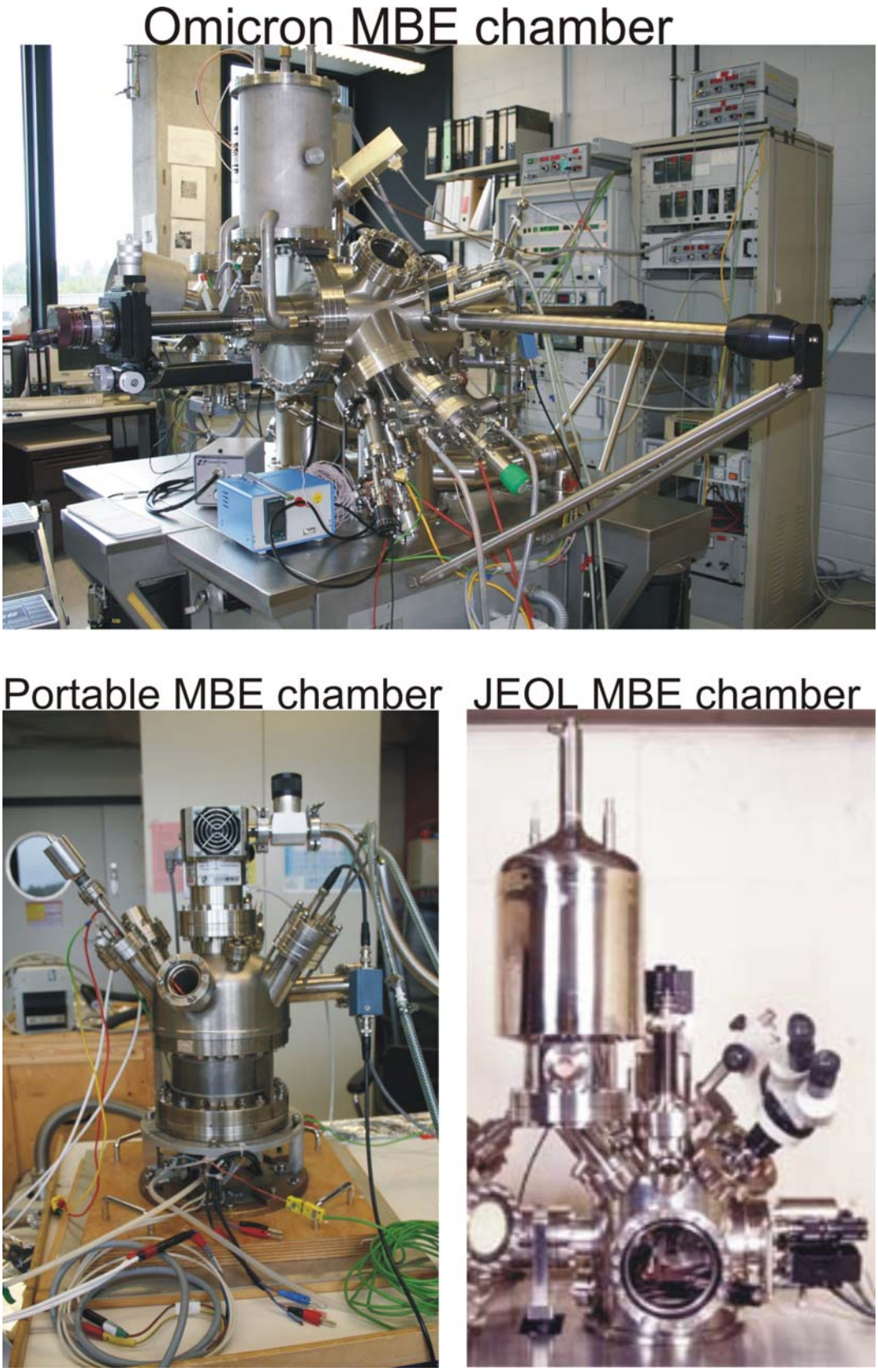

Figure 6.1: Three different MBE-UHV systems.

6.2.2 Portable MBE chamber

The portable MBE chamber has a sample heating stage, a sputter gun, up to 3 evaporation sources and a QCM. The pumping system consists of an external Membrium pump, a turbo-molecular pump and an ion pump. The chamber is special designed to fulfill the need of in situ, real-time X-ray diffraction measurements. It is portable and can be directly mounted on X-ray diffractometer. A beryllium window ensures the penetration of X-ray for probing the samples. The shutters and the temperatures of the evaporation cells and the substrates can be controlled remotely during the X ray measurements.

6.2.3 JEOL MBE chamber (SPM-4500M) [112]

The JEOL system has three individually chambers: lord lock, deposition chamber and SPM chamber. The system is operated at a base pressure of 1 x 10^{-8} Pa. Deposition chamber has a sputtering gun and up to 2 Knudsen-cells can be mounted. The SPM chamber has a STM and a Knudsen cell for in-situ real time deposition-characterization measurements. A cooling stage is mounted top-side of the SPM chamber to carry out low temperature STM measurements. However, as there are no temperature control units for evaporation cells, the temperature is calibrated externally and controlled by setting current of the power supplies. As there is no QCM available, the thickness of the film is calibrated before the experiment and controlled by deposition time at specific deposition temperature. The JSPM-4500 UHV SPM is designed for the high resolution study of surfaces. Atomic scale imaging with STM mode is available. Variable temperature options allow imaging with sample temperatures from less than 20K to above 1500K. STM modes include CITS, I-V, S-V, and I-S.

6.3 Preparation of the organic thin films

In the experiments, organic semiconductor molecules diindenoperylene (DIP) and F_{16}CuPc, H_{16}CuPc, pentancene commercially from Aldrich was used. PTCDI-C_8 were

synthesized at the institute of organic chemistry, university of Würzburg. All the molecules were further purified twice via gradient sublimation in the 'Kristallabor' of the third physical institute at Stuttgart University. The evaporation temperature and the deposition rate are described in detail in each chapter. During the deposition, the substrates were facing normal to the evaporation cells to ensure a homogenous growth.

6.4 The AFM, STM systems

The AFM measurement were performed in air either in contact mode with cantilevers with spring constant of 0.03 N/m) or in amplitude modulation mode (Tapping-AFM) with a Digital Instruments NanoScope III SPM (cantilevers with a spring constant of K~40 N/m were used). Image processing was performed using WxSM free software (Nanotec, Spain). The samples presented the same morphology after a few months.

6.4.1 Omicron UHV AFM/STM systems [111]

The Omicron combined UHV AFM/STM is an extraordinarily versatile scanning probe microscope for imaging various types of surfaces, non-conducting, conducting, hard or soft, etc. It combines various STM and AFM measurement modes including contact mode AFM with simultaneous lateral force (friction) detection and non-contact mode AFM in a single instrument. In addition, simultaneous STM and AFM imaging is possible. Electrostatic, magnetic force imaging

6.4.2 Cervantes AFM system [113]

Cervantes AFM system from "Nanotec" [s1] is an AFM system for characterizing and performing experiments on samples at the nanoscale in ambient or liquid environments. The flexibile and unique design allows data acquisition under remarkable choice of modes: contact mode, tapping mode, 3d modes, jumping mode. It is multifunctional and can be also used as Kelvin Probe Microscopy, Magnetic Force Microscopy plane scan, lithography, etc. Cervantes implements innovative modifications that allow you to

add new features to your existing experiments.

6.4.3 Veeco MultiMode SPM system [114]

The MultiMode scanning probe microscope from Veeco is the world's best-selling SPM. It performs a complete range for charactering surface properties like topography, elasticity, friction, adhesion, and electrical/magnetic fields. The data are easily acquired from micro- to atomic-scale images with a single piezo stage. In addition, the MultiMode SPM provides sample heating and cooling stage for temperature dependence study.

Figure 6.2: AFM and STM systems: omicron UHV AFM/STM, Veeco Multimode SPM, Nanotec cervanters AFM/STM (from left to right).

6.5 X ray Sources

6.5.1 In-house X ray source

Part of the specular X ray diffraction measurements were performed by using an in-house 6-circle high resolution X ray diffractometer, see figure 4.3. A standard rotating water-cooled anode generator produces a routine power of 3 kW/60 kV/80 mA. By using Cu/Ge as monochrometer, Cu k_α radiation resulting from transitions between an L and K shell of Cu atom with wave length of 1.54 Å is selected.

Figure 6.3: In-house 6 circle high resolution X-ray diffractometer.

6.5.2 Synchrotron radiation

Synchrotron radiation as light was seen for the first time at the General Electric in the USA in 1947. Within the facility, electrons are accelerated almost to the speed of light and fly in a closed orbit inside a stainless steel tube. Large electromagnets are positioned at regular intervals along this so-called storage ring, to guide the electrons around the curves and keep them focused in the center of the tube. As the electrons fly around the curves through the magnetic field, they emit electromagnetic radiation. Predicted by Einstein's relativity theory, the emitted light is intense, highly focused and extremely broadband, covering the entire spectral range from hard x-rays to the far infrared and terahertz ranges. The combination of brilliance and broad spectral range makes

synchrotrons the most powerful light source known to science. Many experiments involving x-ray and infrared analytical techniques are only possible when a synchrotron is used as the light source. Due to the high flux of the 3rd generation of the high flux synchrotron X ray source, the measurement time can reduce to several seconds or minutes per data point.

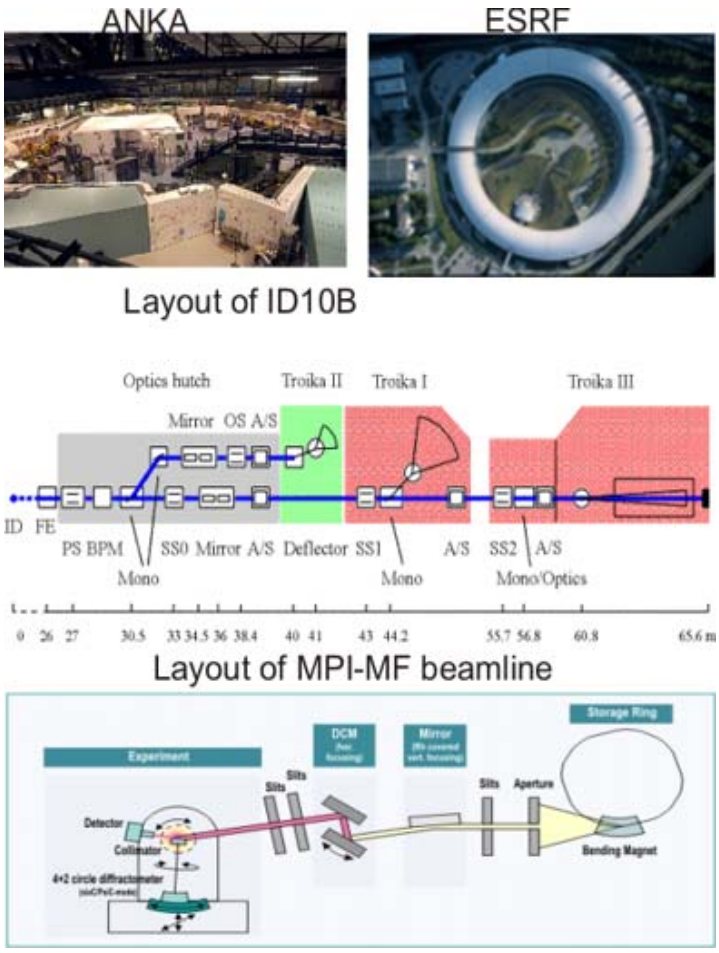

Figure 6.4. The synchrotron radiation facility at ANKA and ESRF.

In this thesis, two different X ray sources were used. Most part of X ray diffraction measurements were performed at surface diffraction beamline of MPI-MF located at synchrotron radiation Angström Quelle Karlsruhe (ANKA). Parts of measurements were carried out in ESRF, gronoble, beamline ID10B. The program SPEC is used for controlling diffractometer. The incident and exit angles were fixed to the critical angle of the substrate.

MPI-MF, ANKA [115]

The synchrotron radiation facility ANKA located at the Research Center Karlsruhe (FZK) is a third-generation style electron storage ring with energy between 1.9 and 3.5 GeV, an initial electron beam current of 180 mA and beam life time ~ 20 hours. The MPI-MF-beamline is dedicated to study the in-situ structural characteristics of materials in reduced dimensions, like surfaces, interfaces, thin films, and nano-crystalline compound materials. The beamline can either be operated in monochromatic, pink or white beam mode. The polychromatic photon beam is produced by a 1.5 T dipole bending magnet (EC = 6 keV, 0.3 mrad horizontal,0.03 mrad vertical) and fed through the optical elements of the beamline, which consists of a ruthenium coated silicon mirror and a double-crystal monochromater. The mirror allows cutting the energy spectrum of the incident photons at its higher end to suppress the harmonic content in the monochromatic beam. In addition it is used to focus the beam in the vertical direction. The DCM consists of a flat Si (111) single crystal and a Si (111) crystal bender for horizontal focusing. The position of the incident X-ray beam is traced by a blade beam position monitor in front of the optics.

The outgoing beam can be monitored by the insertion of a fluorescence screen at the end of the optics. Two pairs of horizontal and vertical slits allow pre-selecting the beam size on the sample. The energy of the X ray beam is tunable from 5 to 20 keV, corresponding to the wavelength rang between 0.5 to 3.1 Å with resolution ~$2x10^{-4}$ $\Delta E/E$.

ESRF ID10B [116-117]

Located in Gronoble, France, European Synchrotron Radiation Facility (ESRF) is one of the largest synchrotron facilities in the world with high spectral flux and high spectral brilliance beamlines. The electron beam in the storage ring has energy of 8.02 GeV and maximum electron current of 200 mA. Combined grazing-incidence diffraction (GID), X-ray reflectivity (XRR), and grazing-incidence small-angle scattering (GISAXS) techniques in a single instrument, ID10B in ESRF is a multi-purpose, high-brilliance undulator beamline for high resolution X-ray scattering and surface diffraction on liquid and solid interfaces. ID10B is an independent branch of the TROIKA beamline. The energy is tunable from 8 keV to13 keV for a diamond (111) crystal monochromator or

from 13 keV to 22 keV for a diamond (220) crystal monochromator with energy resolution $\Delta E/E$: $5.9*10^{-5}$ and $3.3*10^{-5}$, respectively. Scattering experiments can be performed in both horizontal and in vertical scattering geometry with a 6-circle diffractometer. High-resolution studies are possible in both scattering geometries via the use of crystal analyzer stages in different orientations. Scattering profiles can be taken with either a 0-D detector or a 1-D detector.

Chapter 7

Growth behaviours of DIP on SiO_2: roughening, scaling and structural relaxation

In the last decades we have witnessed an increase number of studies aimed at understanding the growth of ordered organic films on inorganic substrates and their structure-performance relationships. A vast number of growth studies have chosen silicon oxide as substrate because this is the dielectric material generally employed for OFETs [118-125]. Organic molecules generally orient with their aromatic plane perpendicular to the surface or with a tilting angle with respect to the vertical direction of SiO_2 due to the weak vertical interaction between molecule and substrate. Small conjugated organic molecules often develop more complex growth scenarios than inorganic materials due to their anisotropic shape and their weaker intermolecular interaction (van der Waals). It has been reported that the carry charge transport occurs within the first a few monolayers of the thin film, thus the physical properties of this very thin layer strongly influences the performance of organic-based devices [126-130]. Very recently it has been high lighted that the geometrical arrangement of first layers of pentacene determines the threshold of increase of charge mobility. Thus, to understand the nucleation and growth mechanisms in the early stage of the organic thin film growth is essential for the prediction of structure-performance relationships and further improvement in mobility for a better design of the organic architectures.

In this chapter we present a complete structural and morphological characterization of the DIP grown on SiO_2 from initial sub-monolayer to 3D growth regime at a wide temperature range: from non-equilibrium (at room temperature), a moderate temperature

(T = 90 ºC), to near-equilibrium state (T = 120 ºC). The morphology characterization in the concepts of roughening, fractal and scaling is discussed in detail. We report also the observed structural transition monitored by in-situ X ray diffraction.

The cleaning and growth procedures are described in chapter 6.1. It is necessary to point out that the cleanliness of the substrates is of utmost importance to avoid 3D heterogeneous nucleation initiated by surface impurities, which in turn alter the growth modes dramatically and give artifacts. All X-ray and AFM measurements were performed on DIP films grown under similar conditions and on the small pieces of Si cutting from same Si wafer. Grazing incidence X-ray diffraction (GIXD) measurements were performed in-situ at the synchrotron source ANKA in Karlsruhe (λ=1.23984 Å). The interruption of the growth had no effect on the observed in-plane structure: X-ray measurements in 5 ML DIP thin film at T_{sub}= 120 °C grown in a single step and multi-step gave similar results. For the AFM measurements, a set of samples were grown with desirable different thicknesses and substrate temperature in OMBE chamber (base pressure of 10^{-10} mbar).

7.1 Theory

All rough surfaces exhibit perpendicular and lateral fluctuations. Lateral roughness (parallel to the interface plane) can be characterized as a very basic level by examing if the term $z(x,y)-z'(x,y)$ is a Guassian random variable whose distribution only depends on the relative coordinates $(X,Y)\equiv(x'-x,y'-y)$, where $z(x,y)=h(x,y)-<h(x,y)>$ with $h(x,y)$ being height function and $<\cdots>$ the spatial average. Vertical fluctuation can be characterized by a statistical mean square roughness (RMS)

$$\sigma =< z(x,y)^2 >^{1/2} \tag{7.1}$$

with $z(x,y)=h(x,y)-<h(x,y)>$. For a self-affine roughness $\sigma(L)$ increases with the horizontal length L as

$$\sigma(L)\propto L^H , \tag{7.2}$$

where $0<H<1$ is referred to as the “roughness exponent”. The height correlation function

$$g(R) = < [z(x', y') - z(x, y)]^2 > \tag{7.3}$$

scales as

$$g(R) \propto R^{2H} \tag{7.4}$$

with $R = \sqrt{(X^2 + Y^2)}$.

Considering film growth phenomena, the time evolution of surface roughness must be accounted besides the spatial properties. Family and Vicsek introduced the "dynamic scaling" to incorporate both temporal and spatial scaling behaviours [151]. The spatial and temporal scaling behaviours of films grown under nonequilibrium conditions can then be combined into the dynamic scaling form,

$$\sigma(L,t) = L^H F(t / L^{H/\beta}) \tag{7.5}$$

where

$$\sigma(L) \propto L^H \text{ for } t / L^{H/\beta} \to \infty \tag{7.6}$$

and

$$\sigma(t) \propto t^{\beta} \text{ for } t / L^{H/\beta} \to 0. \tag{7.7}$$

Within the context, the evolution of the saturated RMS with deposition time t is characterized by "growth exponent" β.

If the correlation length increases with time as

$$\xi \propto t^{1/z} \tag{7.8}$$

, we have

$$z = H / \beta \tag{7.9}$$

and z is referred as scaling exponent.

One can introduce quantitative measures of the surface roughness evolution for mounds (3D layering) growth. Suppose the layer coverage θ_n with n counting the layers and θ_0 = 1 represents the substrate, then the total coverage,

$$\Theta = \sum_{n=1}^{n=\max} \theta_n = Ft \tag{7.10}$$

And the exposed area of layer n is

$$p_n = \theta_n - \theta_{n+1} \tag{7.11}$$

with $\sum p_n = 1$ and $\Theta = \sum n p_n = n_{av}$. The roughness is therefore can be simplified as,

$$\sigma^2 = \sum (n - n_{av})^2 p_n \tag{7.12}$$

For the statistics limit, a growth with time in the absence of interlayer transport, the exposed coverage follows Poisson distribution with

$$p_n = \frac{e^{-\Theta}\Theta^n}{n!}, \tag{7.13}$$

and therefore $\sigma = \sqrt{\Theta}$, giving β=0.5. All the growth phenomena with β>0.5 refer to "rapid roughening".

For an ideal layer-by-layer growth on a perfectly flat substrate, a specific case of 3D layering growth, only the top layer is incomplete as any given time, then the evolution of the roughness yields

$$\sigma = \sqrt{(1-\delta\theta)(\delta\theta)} * h \tag{7.14}$$

where $\delta\theta$ is the relative coverage of the last layer and h is the layer height. Instead of a scaling law of $\sigma(t) \propto t^{\beta}$, the saturated RMS σ is periodic oscillation function of deposition time t (figure 7.1 (a)). In addition, figure 7.1 (b) illustrates the evolution of $\sigma(L)$ with the horizontal length L in LBL growth feature. The roughness $\sigma(L)$ displays damped oscillation (instead of $\sigma(L) \propto L^H$ for self-affine growth) with $L \to \infty$, $\sigma \to \sqrt{(1-\delta\theta)(\delta\theta)} * h$.

In the microscopic view, in the early stage of the islands growth, the molecules arrive and accommodate on the surface (condensation) and migrate along the surface (diffusion) and finally aggregate into 2D adatom islands (nucleation). A simple consideration separates the 2D islands growth into three regimes: the growth regime in which and the number of islands increases, indicating that nucleation of new islands is occurring; the aggregation regime (steady state regime), the island density is approximately constant, the islands only grow laterally without new islands formation; coalescence regime, in which the island density decreases rapidly. Upon this assumption, for correlation length $\xi(t)$ as a function of t , (figure 7.1 (c)), ξ initial equals infinity as no nucleation sites, with increasing nucleation sites, ξ decreases rapidly in nucleation regime. In the steady state regime, where the 2D islands grow

laterally, ξ keeps constant. In the coalescence regime, the continuous filled vacancy islands lead to a rapid increasing of ξ.

For coverage before coalescence, island density N_{ND} is inverse proportional to ξ by

$$\theta = \sum_a N_a \frac{a}{L^2} = \frac{N\overline{A}}{L^2} = \overline{A} \cdot N_{ID} = \overline{A} / \xi^2 , \tag{7.15}$$

where a is the island size, L is the linear length scale (L^2 then is the image size), N_a is the number of the islands of size a, N is the total number of the islands in the image and N_{ID} is the islands density. In the above mentioned steady state regime,

$$\xi = \text{constant}, \quad \overline{A} \propto \theta . \tag{7.16}$$

However, in most cases, it was reported that the adlayers typically coarsen in a self-similar fashion for long time in the submonolayer regime. Therefore the lateral structure is characterized by a single length scale, $L(t)$, which increases asymptotically to algebraic dynamic scaling law,

$$L(t) \propto t^n \text{ [131].} \tag{7.17}$$

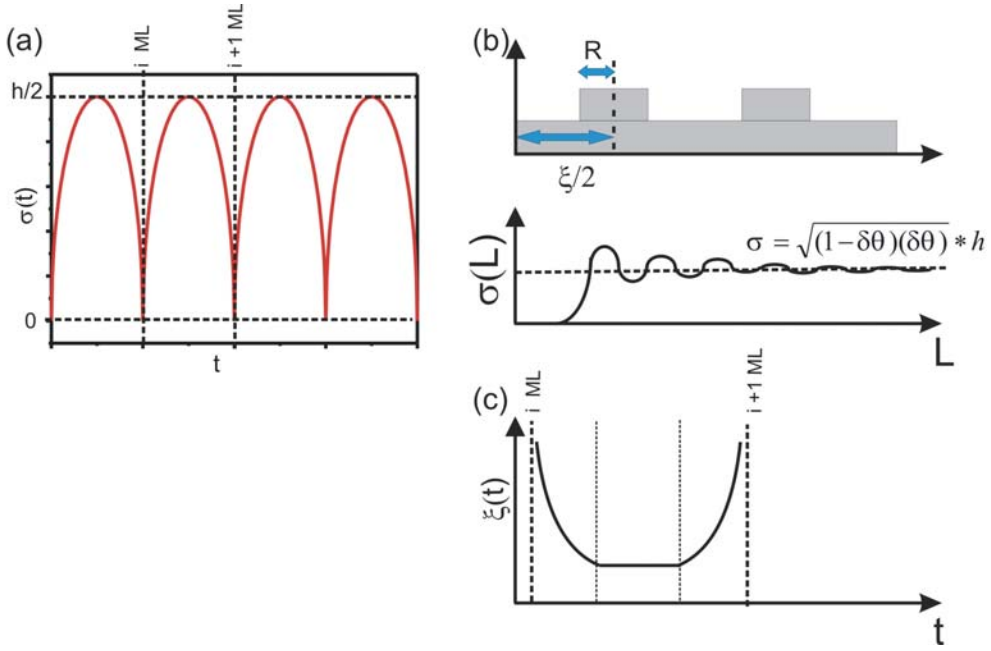

Figure 7.1: The typical features of (a) roughness σ as a function of t and (b) σ as a function of L and (c) ξ as a function of t for a layer-by-layer growth.

The coarsening can occur via "Ostwald ripening". Oswald ripening process is characterized by dissolving of material from small islands to fee the growth or ripening of large islands, and consequently the initially larger islands will grow at the expense of the smaller ones. For the attachment-limited kinetics, the evolution of the individual islands depending strongly on the average islands size, gives $n = 0.5$. For 2D islands growth, $L(t) = \xi(t)$, we have

$$\xi \propto \theta^{1/2} \text{ and } \overline{A} \propto \theta^{2} \ . \tag{7.18}$$

For diffusion-limited kinetics, the island revolution depends on the relative sizes of the neighbouring islands, one finds $n = 1/3$, thus,

$$\xi \propto \theta^{1/3} \text{ and } \overline{A} \propto \theta^{5/3} . \tag{7.19}$$

The coarsening can also occur via "Smoluchowski ripening", the diffusion and subsequent coalescence of large 2D islands. In this case, the coarsening exponent $n = 1/(2 + 2\alpha)$ depends on the scaling of the cluster diffusion coefficient,

$$D_a \propto a^{-\alpha} , \tag{7.20}$$

where a is the islands size and α is the diffusion scaling exponent, and

$$\xi \propto \theta^{1/(2+2\alpha)} , \ \overline{A} \propto \theta^{(2+\alpha)/(1+\alpha)} . \tag{7.21}$$

Therefore, by analysis the correlation length and average islands size dependence as a function of increasing fraction coverage, one can gain insight into the precise growth ripening process.

The 2D islands size distribution and shape revolution are determined by delicate interplay between diffusion, substrate temperature and other factors. In the fundamental concept of dynamic scaling assumption, at a given stage of growth, there is only a single length scale in the problem. If the islands are self affine in nature, then scaling the island size distribution, one measures the same island size distribution. In other words, the island size distribution can be factored into two parts—one which contains all dependence on coverage and length scale, and another which is a scale-invariant fundamental distribution function. Define a normalized island size density function

$$\int f(\frac{a}{\overline{A}}) = 1 \text{ and } \int \frac{a}{\overline{A}} f(\frac{a}{\overline{A}}) = 1 , \tag{7.22}$$

then their discrete corresponds are $\frac{N_a}{N}$, which $\sum_a \frac{N_a}{N} = 1$ and $\sum_a \frac{a \cdot N_a}{N \cdot \overline{A}} = 1$. The number density function $N_a(\theta)$ is

$$N_a(\theta) = \theta \overline{A}^{-2} f(a/\overline{A}), \tag{7.23}$$

where a is the island size.

The island size distribution function with increasing coverage moves gradually to larger island size with considerably broadens of distribution. The dynamic scaling properties of 2D islands are extensively studied by Amar and Family, which assume in the asymptotic large D/F limit, the island-size distribution centers at the average islands size and behaves as $(a/\overline{A})^i$ for $(a/\overline{A}) < 1$ and an exponential decay for $(a/\overline{A}) \geq 1$, therefore a general scaling form for $i \geq 1$ is

$$f_i\left(\frac{a}{\overline{A}}\right) = C_i \left(\frac{a}{\overline{A}}\right)^i e^{-ia_i\left(\frac{a}{\overline{A}}\right)^{1/a_i}}, \tag{7.24}$$

where the constants C_i and a_i fulfill

$$\frac{\Gamma[(i+2)a_i]}{\Gamma[(i=1)a_i]} = (ia_i)^{a_i},\ C_i = \frac{(ia_i)^{(i+1)a_i}}{a_i \Gamma[(i+1)a_i]}. \tag{7.25}$$

The i value here is the critcal cluster size.

The evolution of the islands shape, which is always of utmost fundamental interests, gives rise to the 2D roughening. For an isolated two dimensional island, the shape is a result of competition between two kinetic processes: periphery diffusion and adatom incorporation.

In the initial stage of growth on a flat surface, if F is fixed, the value of D determines the average distance of which an adatom will have to travel before finding/joining an existing island or meeting another adatom to create the possibility of nucleating a new island. As nucleation continues, this distance decreases and eventually becomes constant. By meeting an island, periphery diffusion characterizes the time at which an organic molecule takes to diffuse along the island boundary to find an energetically favorable binding site. Monomer incorporation is characterized by the average time interval between two successive monomer incorporation events. In island growth, the effect of frequent monomer incorporation is opposite to that of periphery diffusion. The monomer incorporation and periphery diffusion

together determine the island shape, if monomer incorporation is faster than periphery diffusion, leading to growth instabilities and fractal island shapes, for instance, diffusion limited aggregation (DLA), a "hit and stick mechanism" in essence, which gives rise to formation of thin branches (ramified islands) islands in with a fractal dimension of 1.67. On the other hand, compact islands form if monomer incorporation is slower than periphery diffusion with a fractal dimension of 2.0. The "coastlines" of 2D islands can be self-affine fractal with dimension

$$D=d-1-H, \tag{7.26}$$

where d is the spatial embedding dimension and H is the roughness exponent. The area-perimeter method is a classic method to access the quantitative estimation/evaluation of islands shape in lateral direction, in which the perimeters P and areas A are plotted on a log-log graph

$$P \propto A^{\rho} \tag{7.27}$$

and the shape scaling exponent (perimeter to area ratio) ρ can be determined. ρ =0.5 corresponds to the compact islands without fractal. Consider the kinetics of the diffusion process, the diffusion coefficient $D_{diffuse}$ is related to the islands density by

$$N_{ID} \propto (D_{diffusion} / F)^{\chi}, \tag{7.28}$$

where the exponent χ is related to the critical island size i by $\chi = i/(i+2)$.

7. 2 Morphology

Figure 7.2 displays a series of AFM images of DIP thin film grown on SiO_2 at RT with increasing film thickness. The morphologies of the thin film present two different stages of the growth process: initially, the DIP thin film exhibits a layer-by-layer feature; at an onset thickness of D ~ 3 ML, the growth mode transfers into a 3D mound formation (formation of multilayers stacks of 2D islands). The 3D islanding gives rise to a rapid growth of the roughness exponent β larger than 0.5, therefore refers to the so called "rapid roughening". DIP islands adopt a height of 17.0 $\pm$ 1.0 Å showing that the molecules adopt a nearly upright configuration from the initial stage with a tilting angle of about 22º. Within the error bar of AFM images, DIP films are considered to reveal similar terrace height in subsequent layers

upon further deposition. Figure 7.3 and 7.4 show DIP thin films grown on SiO_2 at 90 °C and 120 °C, from which we disclosed essentially the same morphological transition from LBL growth to 3D islanding at a critical thickness of ~ 4 ML and ~ 5 ML respectively. At T_{sub} = 90 °C, by decreasing the deposition rate from 3.5 Å/min to 0.5 Å/min, $D_{critical}$ shifts from ~ 3 ML to ~ 5 ML.

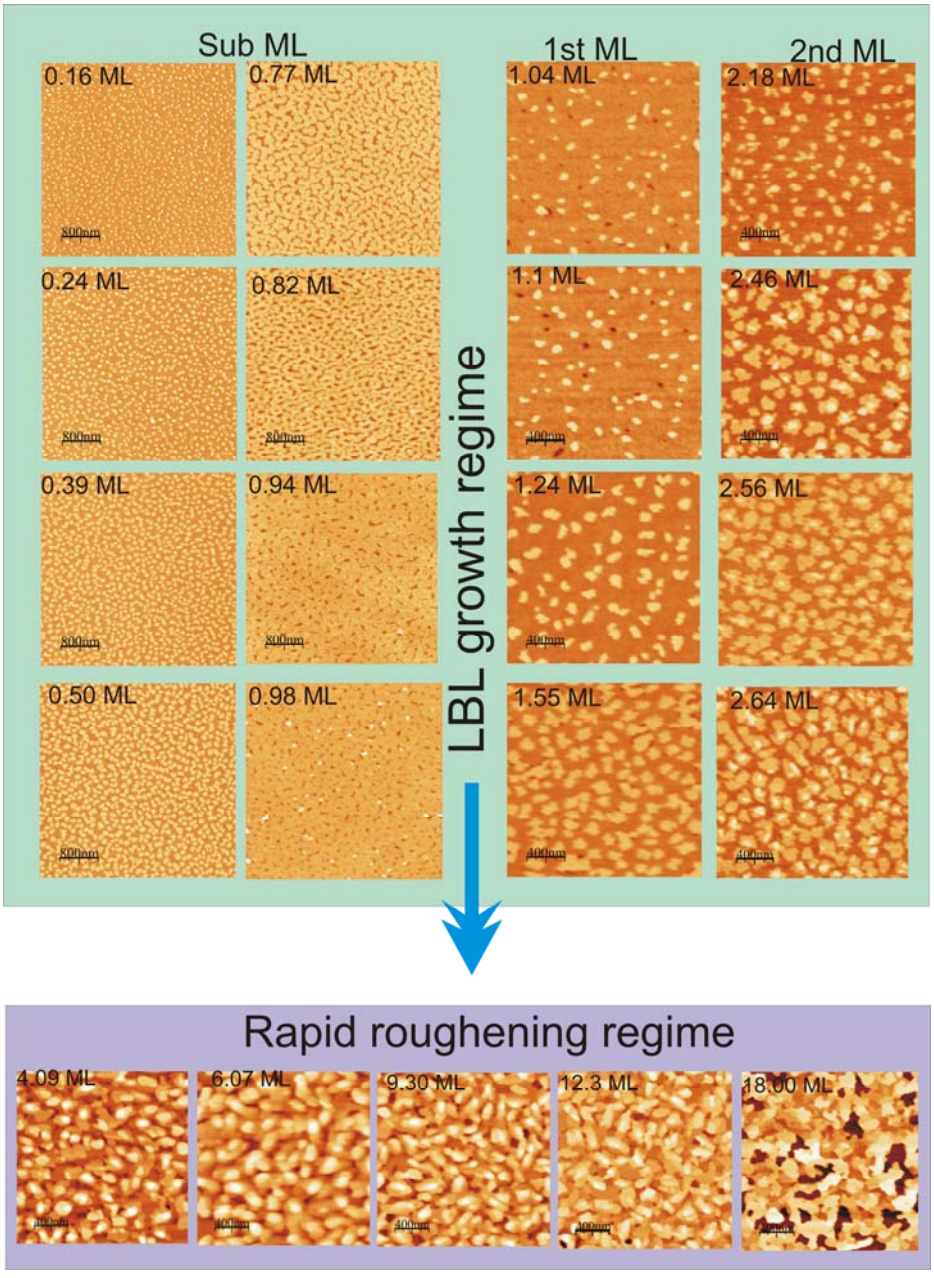

Figure 7.2: Morphology of DIP thin film deposited on SiO_2 at RT. A layer-by-layer to 3D islanding is clear identified at a critical thickness of ~ 3 ML.

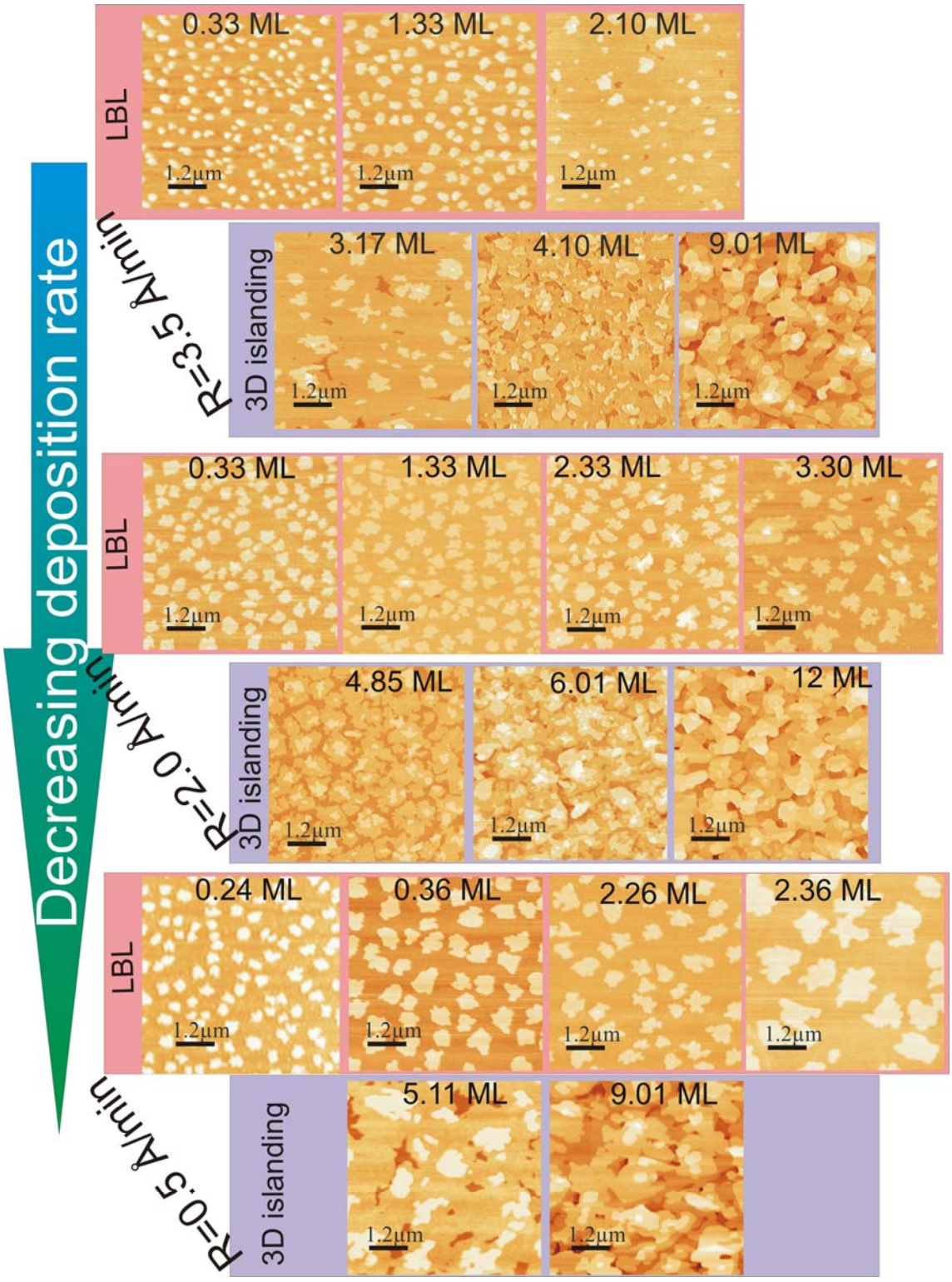

Figure 7.3: Morphological revolution of organic semiconductor DIP as a function of coverage grown at the 90 °C with deposition rate of 0.5, 2.0 and 3.5 Å/min.

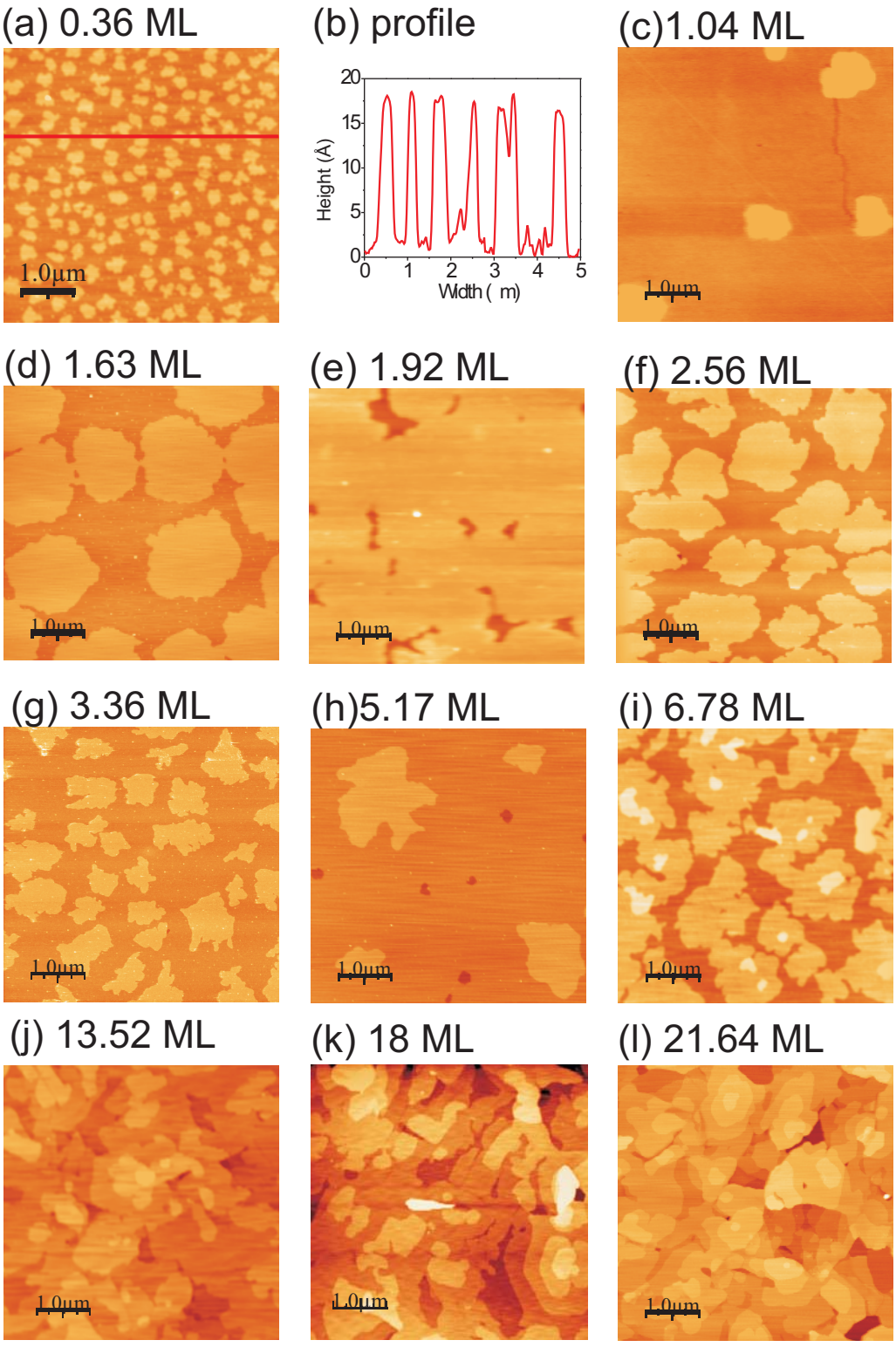

Figure 7.4: AFM images of morphological revolution as a function of coverage at 120 °C.

7.2.1 Lateral concept of the 2D islands

At RT

We focus first on the morphology of DIP thin film in the initial layer-by-layer growth regime. Grown at room temperature, with increasing film coverage from 0.16 ML to 0.50 ML, the DIP island density (N_{ID}, number of islands per area,) has decreased remarkably, which can be ascribed as a ripening process. At coverage of 0.8 ML, the 2D island growth is in coalescence regime, there are no individual islands rather than interconnected into one net. With further increasing coverage to 0.94 ML, the coalescence continuous develops and the submonolayer is almost complete with only a few pinholes left. Notice at this coverage, we observe the formation of 2nd layer islands, thus it is considered as the threshold for the growth of the 2nd layer. At a coverage of 0.98 ML, the islands density of the 2nd layer increase rapidly, meanwhile continuously filling of the submonolayer. At a coverage of ~ 1.24 ML, the first layer is completed covered.

And the lateral separation distribution (correlation length) is determined by surface diffusion and deposition rate. The correlation length of different layers displayed in figure 7.5 gives clear evidence of the different growth regimes. As described in figure 7.1, for the second layer, with the coverage smaller than ~ 0.18 ML, the correlation length decreases rapidly characterizing the nucleation regime; for the submonolayer, with the coverage larger than ~ 0.8 ML, the correlation length increases again characterizing the coalescence regime. In the ripening regime, the correlation length continuous increases despite the increasing coverage. By plotting correlation length vs fraction coverage in a log-log diagram, an obvious linear behavior in the ripening regime is observed. Fitting the curves with equation 7.17, $\xi = k\theta^n$, we get the same n value of 0.5 ± 0.04 for all the layers, and $k = 270 \pm 6$ for 2nd , 3rd layers and $k = 190 \pm 5$ for the first layer (2nd and 3rd layers were fitted with one formula due to their similar behavior). A smaller k value of the submonolayer indicates a smaller diffusion length compare to the subsequent layers at certain coverage, in turn, a stronger interaction between DIP and SiO_2 than intermolecular interaction between DIP

molecules. From the obtained *n* value, we suggest the ripening process occurs via the "Ostwald ripening".

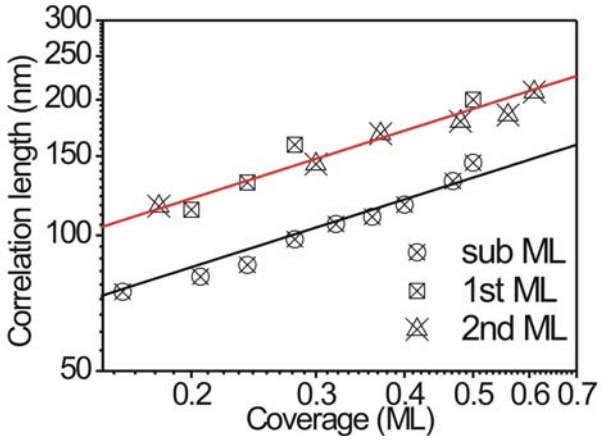

Figure 7.5: The correlation length as a function of fraction layer coverage of DIP thin film grown at RT.

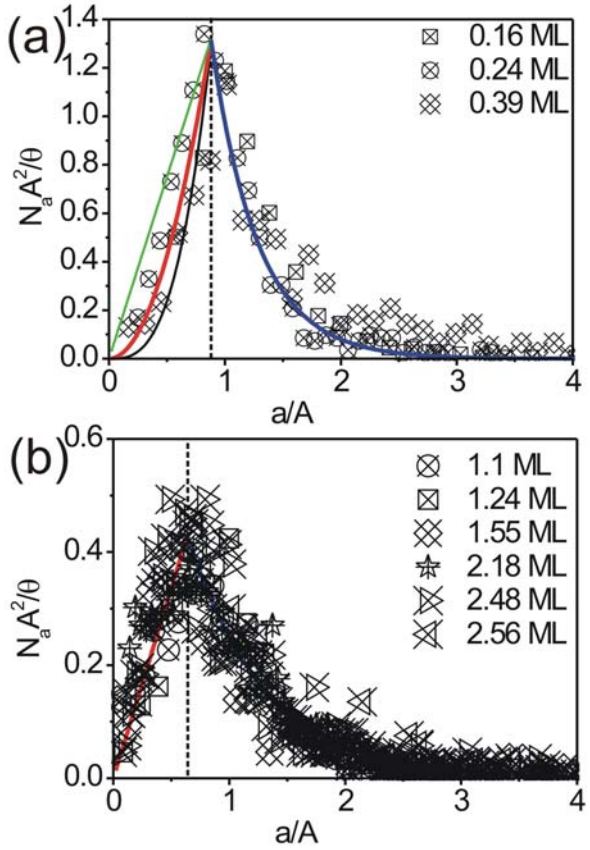

Figure 7.6: Normalization of the island size distribution by the average size of the islands of DIP thin films grown at room temperature.

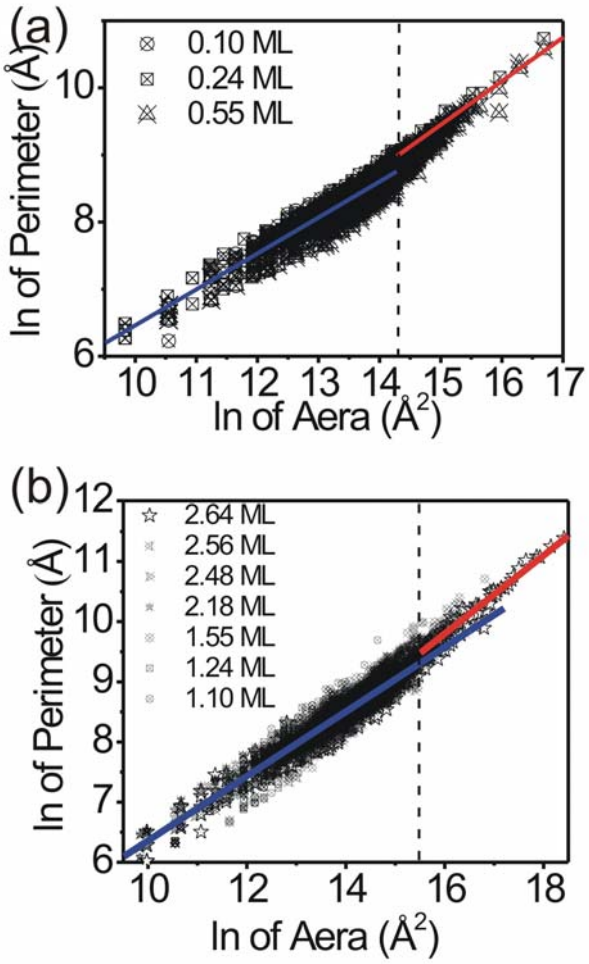

Figure 7.7: Fractal analysis for DIP islands on SiO_2 at room temperature, in which plots (a) and (b) show the data of ~2000-3000 islands. The islands shape transition takes place at the critical area size of lnA ~ 14.2 $Å^2$ for the submonolayer and lnA ~ 15.5 $Å^2$ for the second and third layers.

For the fraction coverage between 0.5-0.7, the growth is almost in a steady state regime, all the new coming molecule contribute to the lateral growth of the existing 2D islands without forming new islands, which is characterized by similar island density in this regime.

We analyze further the size distributions obtained from the AFM images and quantitatively demonstrate self-affine of the island size distributions. Figure 7.6 shows island size distributions normalized by $\overline{A}$ in the ripening regime, which shows all the curves of different layers scale into a single curve. In our case, the peak positions of scaled size distribution of

all the layers shift to lower $(a/\overline{A})$ instead of $(a/\overline{A})$ =1, for the 1st layer $f(\frac{a}{\overline{A}})$ centered at $\frac{a}{\overline{A}} = 0.88$, for the 2nd and 3rd layer at $\frac{a}{\overline{A}}$ = 0.64 due to the ripening process. Adopting previous mentioned prediction, we fit $(a/\overline{A})^i$ for $(a/\overline{A}) \le (a/\overline{A})_{\max inum}$ and exponential decay for $(a/\overline{A}) \ge (a/\overline{A})_{\max inum}$ according to equation 7.24 and 7.25. The scaling function for the island size distribution differs for 1st layer (DIP-SiO_2) and subsequent layers (DIP-DIP), which suggests of a change in critical size of nucleation for 1st layer, $i = 2$ gives the best fit, while for the 2nd and the 3rd layer $f(\frac{a}{\overline{A}})$ can be fitted with identical function which gives $i = 1$ (the fitting curves are shown together with the experimental data).

Figure 7.7 describes the islands shape distribution at room temperature. In the initial stage growth of the first DIP layer (coverage of 0.22 ML), islands of compact-like shape form with ρ ~0.537. Notice that DIP molecules interact rather different vertically: an organic-inorganic interface (DIP on SiO_2) in the submonolayer regime and organic-organic interface (DIP on DIP) in the multilayer regime, but similar laterally (DIP-DIP) and the shape is mainly deterimined by a lateral inter-molecular interaction related parameters rather than determined by vertically molecule substrate interaction, it is reasonable that similar ρ is observed on the second layer (DIP on DIP surface) and the submonolayer (DIP on SiO_2) surface. In the sub-monolayer regimes, with increasing the coverage, the islands shape undergoes a transition from compact-like islands to less dense branch ones with a ρ value of ~ 0.65. The shape transition is essentially due to the coalescence. The fractal analysis discloses a critical size of lnA=14.2 $Å^2$ for islands shape transition, which corresponds to island of size $A_{critical}$ ~14688 nm^2. For the 1st and 2nd layer, astonishingly, the same islands shape are observed but at a higher $A_{critical}$ of lnA=15.5 $Å^2$ and this onset of island area is exp(15.5-14.2) ~ 3 times larger than that of the submonolayer.

At 90 °C

The morphology of the DIP thin films grown at 90 °C is displayed in figure 7.2. We study the 2D islands of different layers at the fraction coverage of ~ 0.33 ML at R ~ 2 Å/min. From the fractal analysis, we reveal the identical islands shape of the islands on individual

layers with ρ = 0.60 ± 0.01, see figure 7.8 for clarity. The island size distribution of different layers scales into a single function of $f(\frac{a}{\bar{A}})$, by fitting the curve we got $i = 2$. At a fraction coverage of 0.33 ML, with the increasing layer number from first to the fourth layer, the correlation length ξ continuous increases from ~ 420 nm to ~ 650 nm, thus a continuous increasing of $D_{diffusion}$. This clearly evidenced a strong interaction with the substrate.

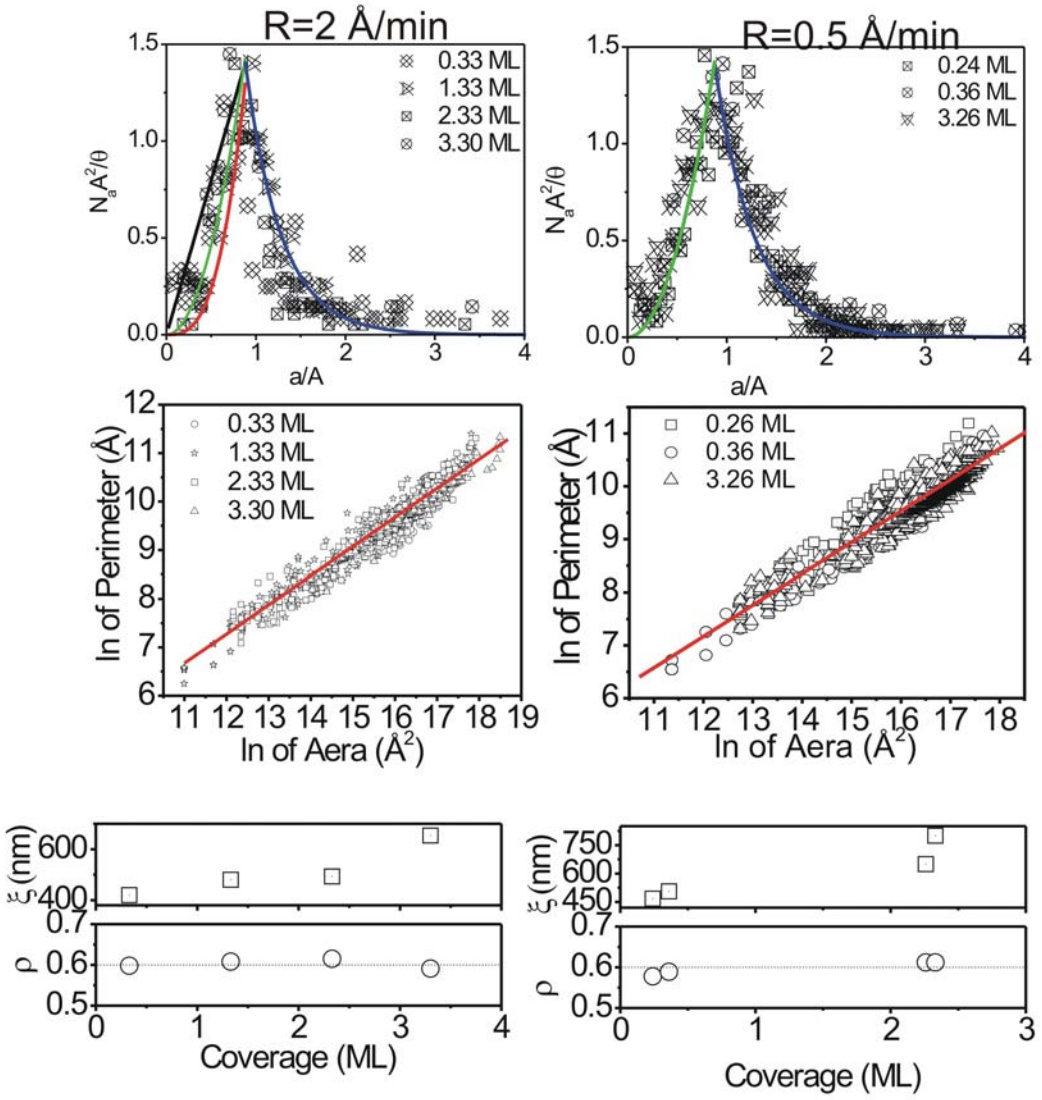

Figure 7.8: The island size distribution, the islands shape and the correlation length and ρ of DIP thin films grown at 90 °C with deposition rate of 0.5 Å/min and 2 Å/min.

Surprisingly, the area-perimeter relationship at R ~ 2 Å/min and R ~ 0.5 Å/min is very similar that all the curves can scale into one single function. Remarkably, we reveal the same scaling behaviour of islands size distribution, the identical equations can be used to fit $f(\frac{a}{\overline{A}})$ at R ~ 0.5 Å/min. The different deposition rate only results in different islands density, a lower deposition rate always results in a lower islands density.

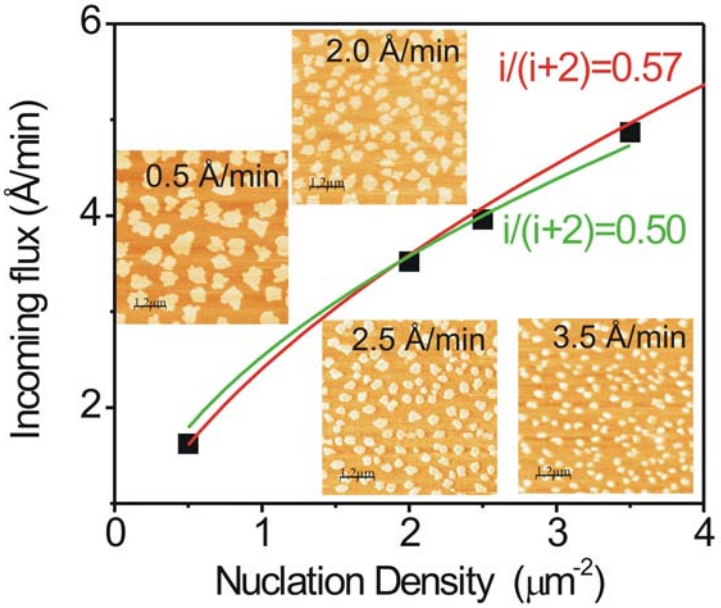

Figure 7.9: The incoming flux as a function of the nucleation density of DIP films with 0.33 ML coverage, the red curve is best fit and the green curve is the fitting by fixing i=2.

By changing R, the islands density N_{ID} changes. Islands composing molecules larger than i are stable against dissociation. Figure 7.9 displays the incoming flux as a function of the nucleation density, the best fit gives i ~ 2, thus suggests that at 90 °C, stable cluster size is 2.

At 120 °C

At 120 °C, near the equilibrium condition, the islands shape displays a more complex scenario. Compare to lower temperature, the islands of same coverage exhibit larger sizes due to the increased diffusion length. In the submonolayer regime, at a low coverage of 0.36 ML, the DIP islands exhibit more fractal shape of the average size of $\overline{A}$ ~ 5087 nm^2. To access a quantitive aspect of the fractal dimension, the slope of log-log plot of perimeter vs area gives ρ ~ 0.64. By increasing the coverage to 0.48 ML, the DIP islands display larger

size of $\overline{A}$ ~ 37219 nm^2 , i.e. ~ 6 times larger than the islands of coverage of 0.36 ML and translating to a 2D compact shape with ρ ~ 0.53. The comparison of the films of 0.36 and 0.48 ML thickness is shown in Figure 7.10. The transition from fractal shape to compact shape is also observed in pentacene, which it is contributed to the molecules diffuse and fill the holes between braches as a matter of fact thicken braches and drive the shape transition [132]. In metal-on-metal epitaxial growth, island shape transition from dendritic shapes at the early stage of growth to compact shapes at higher coverage before island coalescence was observed in both experiments and simulations [133]. Whereas the fractal-dendritic to compact shape transition for the homoexpitaxial growth like Pt islands on Pt(111) or Al islands on Al(111) were attributed to the general scenario that the active step adatom migration or adatom transport around the corner [134-135]. Deposition directly between the fractal arms, as well as interlayer transport (down the step edge), induce the transition, since both mechanisms help to widen the island branches, and slow down the lateral growth rate. However, the "nature" is not that simple. The compact shape of the islands is observed for the coverage from the 2nd monolayer and the third monolayer with the fractal scope varies 0.52 ± 0.05. On the deposition of the fourth monolayer however, the fractal shape is observed ~ 0.6. Transition of island shape from a compact one to fractal-like is caused by rising temperature, lowering coverage or deposition flux. The films' physical properties will very much depend on the smoothness or roughness of the final growth front that will form the interface to the adjacent material or the surface that interacts with the environment.

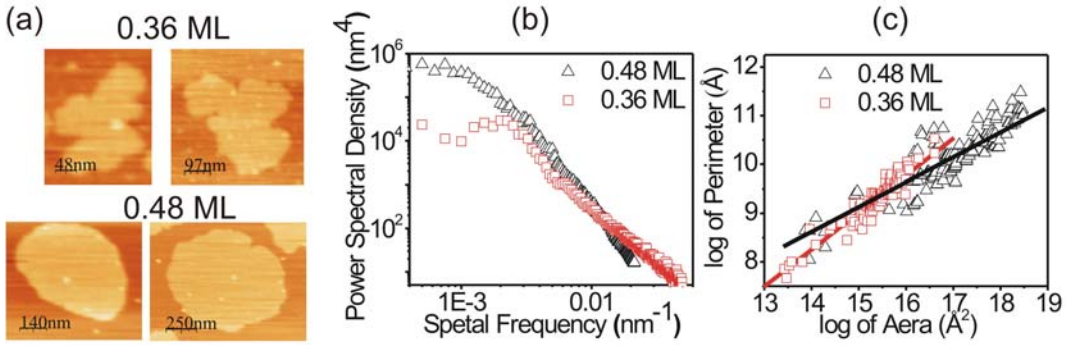

Figure 7.10: (a) The selective islands images of coverage of 0.36 ML, 0.48 ML. (b) The PSD analysis, which shows different correlation length, roughness and roughness exponents of the two films. (c) The different fractal shape of the two films.

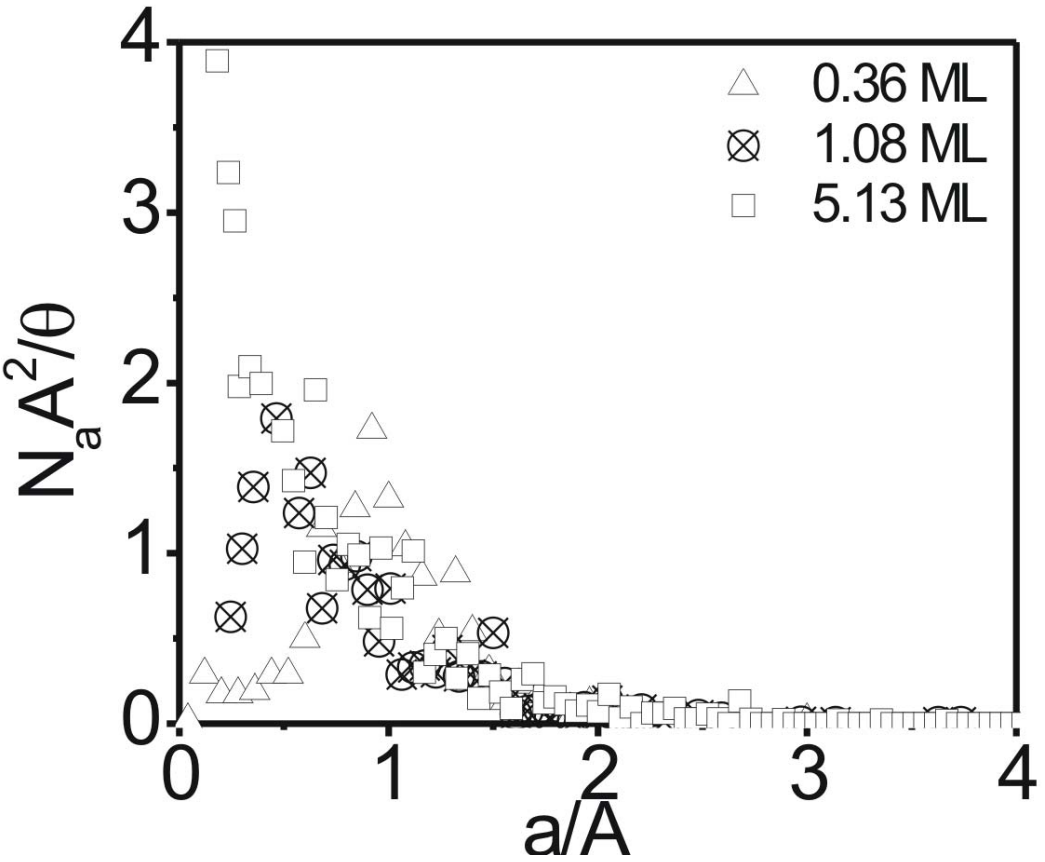

Figure 7.11: (a) and (b) the decreasing nucleation density with increasing coverage indicating a characteristic Oswald ripening regime.

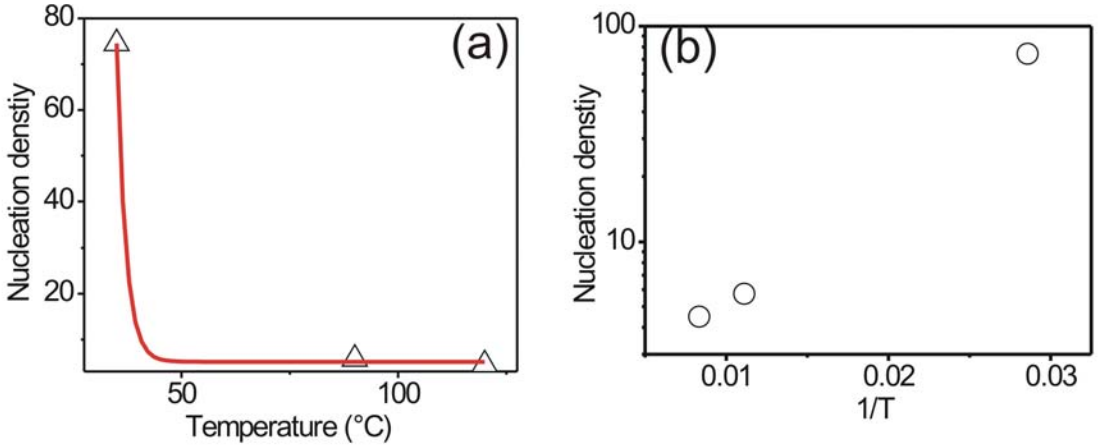

Figure 7.12: The islands density as a function of the substrate temperature for $\theta \sim 0.33$ ML.

In addition, at 120 °C, the island size distribution function shows no scaling feature, as an example, the $f(a/\overline{A})$ of film thickness of 0.36 ML, 1.08 ML and 5.17 ML is shown in figure 7.11.

Another important issue is the islands density dependence of the substrate temperature. Comparing the coverage of 0.33 ML, at room temperature the correlation length is ~ 108 nm, ξ increases from 420 nm to 1200 nm with increasing substrate temperature from 90 °C to 120 °C. On the other hand, the island density continuously decreases according to equation 7.15. Figure 7.12 shows N_{ID} as a function of T_{sub} at coverage of 0.33 ML plotted either in linear (a) and logarithmus scale.

7.2.2 Vertical revolution: roughness

We now focus on the vertical morphology revolution of DIP thin films. At RT, the growth of the first and second layer is a perfect layer-by-layer feature. At 3 monolayer coverage, the formation of the 4th layer islands on top of the 3rd layer can be observed, indentifying a slow growth mode transition to 3D islanding. Note for the idea layer-by-layer growth, there is 100% interlayer mass transfer, i.e. all the molecules deposited on the islands will travel down. On the other hand, random deposition is 0 % (without) interlayer mass transfer. To trace this process, we calculate the fraction coverage of 3rd and 4th layers with increasing coverage and compare with the case of random deposition, the results are summarized in table 7.1. The calculated percentages of the 4th layer are always larger and 3rd layer are smaller than the experimental observation, which indicates an apparent mass transfer from the 4th layer to the 3rd layer. This moderate case indicates built-up of a finite Edward barrier. Meanwhile from almost identical nuclear density of the 2.48 ML and 2.64 ML coverage, the newly coming molecules contribute to the growth of 4th monolayer forming new islands, and lateral growth of the former 3rd layer islands.

The degree of this imperfection can also be clearly manifested in the evolution of the layer coverage versus coverage θ calculated from the AFM images (figure 7.13 (a)), from which the degree of the imperfection is related to how much the slope value of the 2nd ML derivative from 1. The films grown at 90 °C show less dominant imperfection effect as a

function of the layer coverage (Fig. 7.13 (b)). At 120 °C, the DIP thin film exhibits a more idea layer-by-layer growth mode. To give a clear view of the growth, we rely on roughness σ, which displays an oscillatory behavior with period of one layer thickness (h ~ 16.64 Å) in agreement with a perfect layer-by-layer growth (figure 7.13(c)). The dotted line plots the theoretical evolution of the surface width.

Thickness (Å)	2.18	2.42	2.56	2.64	2.71
3nd layer (real)	17.0%	37%	48%	55%	61%
4th layer (real)	0.8%	5%	7%	9%	10%
3rd layer (cal)	----	37%	46%	51%	58%
4th layer (cal)	----	5%	10%	13%	12%

Table 7.1: The layer coverage percentage of the 3rd layer and the 4th layer of DIP grown at room temperature.

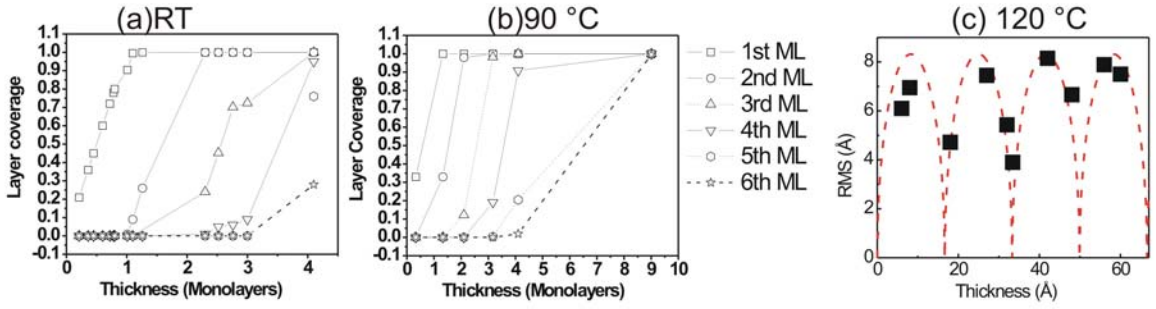

Figure 7.13: Layer coverage as a function of film thickness in the 2D growth mode regime (a) at room temperature, (b) at 90 °C and (c) The roughness σ as a function of the film thickness in the 2D growth mode regime. The dotted line represents the behaviour of an ideal layer-by-layer growth.

With increasing coverage, the morphology of DIP thin film undergoes a general transition from layer-by-layer growth to multilayer growth. At room temperature, the transition takes place until the completion of the third layer. For coverage exceeding this critical thickness (θ_{crit} ~3 ML), a morphological transition to an apparent 3D growth mode occurs, as observed in the simultaneous nucleation and growth of several layers (see figure 7.1 for detail). The appearance of 3D transition shifts to higher layer coverage with increasing substrate temperature, ~ 4 ML at 90 °C and ~ 5 ML at 120 °C. By fitting the curves of σ (θ)

accordingly to the power-scaling law $\sigma \propto (\theta - \theta_{crit})^{\beta}$ where β is the growth exponent, taking a critical thickness of morphology transition, from the slopes we get the β=0.84 at RT and β=0.80 at 90 °C and β= 0.77 at 120 °C respectively. The results are summarized in figure 7.14 together with the fits. Figure 7.15 plots $\sigma(\theta)$ at different deposition rate, as we can see, a higher deposition rate results in a rougher surface.

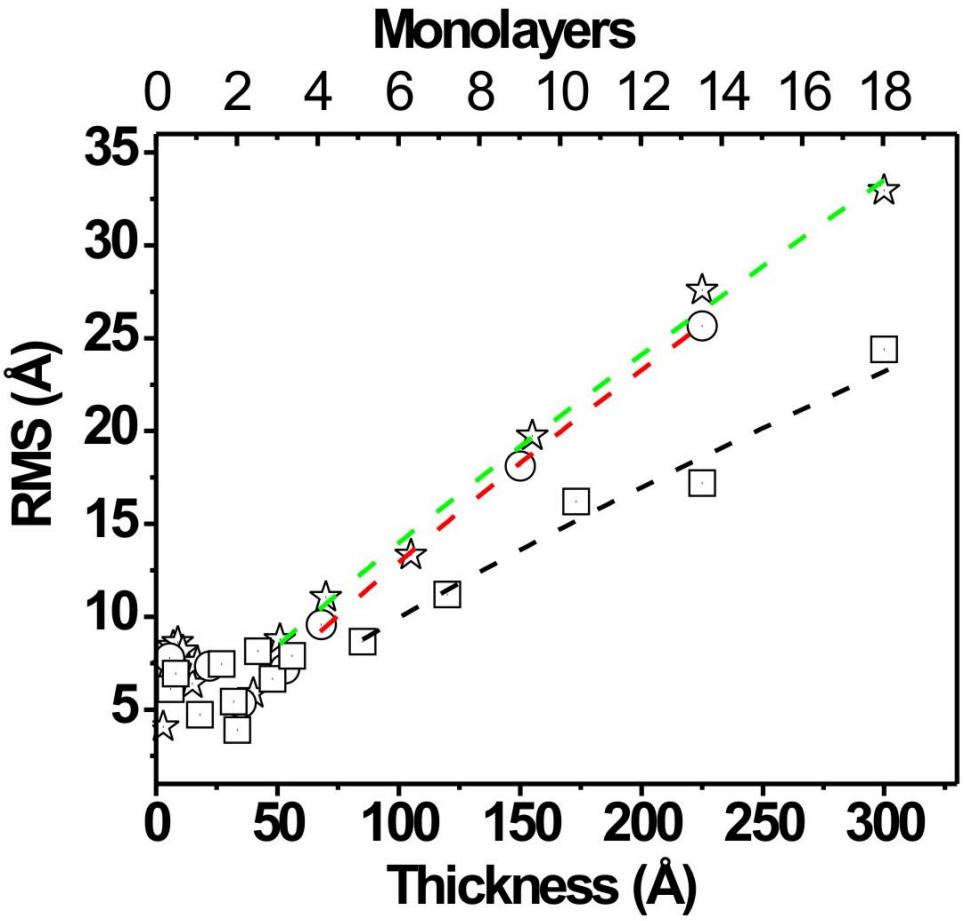

Figure 7.14: σ as a function of the film thickness. The square data are from room temperature, and the circle data for 90 °C and the star data for 120 °C. Two regimes can be observed below and above a certain threshold thickness, θ_{crit} ~ 3 ML for RT, ~ 4 ML for 90 °C and ~ 5 ML for 120 °C. When the coverage exceeds the threshold thickness, a 3D growth mode regime is observed exhibiting a rapid roughening of the surface. The dash lines are the fits according to the scaling-law $\sigma \alpha (\theta - \theta_{crit})^{\beta}$, ($\beta$=0.84 at RT and β=0.80 at 90 and β= 0.77 at 120 °C respectively).

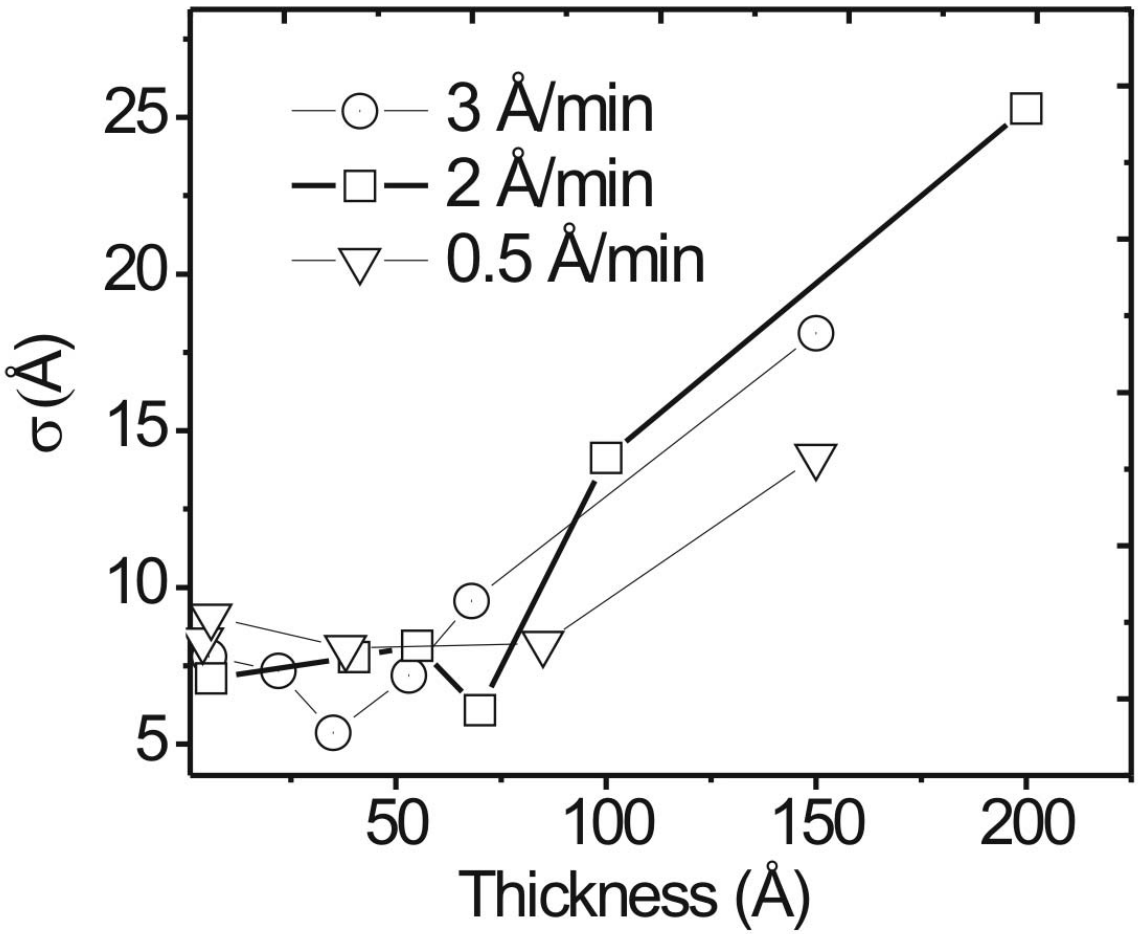

Figure 7.15: σ as a function of the film thickness at 90 °C for different deposition rate.

The growth exponent larger than Poisson exponent $\beta = 0.5$ is called "rapid roughening". The anomalous rapid roughening phenomena are observed for several inorganic semiconductor systems and metals [136-139]. However the reports of rapid roughening of organic thin films are rare and the growth mechanism is largely unexplained. The growth exponent of $\beta = 0.772 \pm 0.031$ obtained at 120 °C is in agreement with the growth scaling exponent previously reported for DIP on thermally oxidized SiO_2 for thicknesses up to 540 ML [63]. In that study, the observed rapid roughening had been tentatively attributed to lateral inhomogenities emerging from the coalescence of two-dimensional domains

presenting different tilt orientations. Because this tilting is also present during the layer-by-layer growth of the first layers, the existence of tilt domains can not account for the onset of the rapid roughening. Moreover tilting domains are general feature exhibiting during the growth of organic thin film on inert substrates.

The morphology of a multilayer film is determined by the intralayer transport (transport of the molecules within a molecular layer) and interlayer transport (transport of the molecules between different layers). Nucleation of islands on the original surface together with inhibited interlayer transport leads to mound formation, which in turn leads to a steadily growing number of exposed molecular layers and increase in roughness growth front. However growth exponent in this case should be smaller than the random deposition since the interlayer transport always acts a factor to smooth the surface. It is unlikely to understand the observed rapid roughening without any vertical driving force. The transition from LBL growth to mound formation is invoked by step edge barrier. The normal agreement of transition from LBL to mound growth is that lowering temperature makes the barrier more efficient and enhances the nucleation probability on top of the islands and initiates mound formation. The multilayer evolution of unfold as a function of temperature is governed by the activation of the molecular processes which enable the exchange of the molecules between molecular layers. Despite a lot of unclearness, clear evidence shows that the morphology transition is more dynamical factor determined than kinetics. The kinetic actability results in a higher roughness at lower substrate temperature with the same thickness. This is due to a decreasing diffusion length. There might be a significant drop in interlayer transport. Several factors may contribute to this decreased transport such as faster nucleation, a decreased diffusion, and an increased Schwoebel barrier for thicker films. In the section 7.3, we will discuss the rapid roughnening in terms of structural change.

From a thermodynamics point of view, the system for thin film growth tends to form an energetically most favourable configuration, while kinetics determines the growth behaviour of the film. It is generally believed that the surface roughness developed during film growth is a result of competition between two opposite effects: roughening and smoothing. The film surfaces growing under this competing effect often evolve into self-affine fractal patterns with the roughness being interpreted by a scaling theory. Depending on the roughening and smoothing mechanisms involved, the film surface growth may fall into different growth

models with each having a different set of scaling exponents. Thus, quantitative analysis of the film surfaces, especially determining the scaling exponents, can help us understand the mechanisms of surface growth.

7.3 Structure

7.3.1 In-plane

The evolution of the in-plane structure with coverage has been monitored in-situ during DIP growth by GIXD. Because the organic crystalline domains on SiO_2 are randomly azimuthally distributed, in-plane Bragg reflections were measured by performing a detector scan. Figure 7.16 depicts a scheme of the in-situ GIXD measurement data of in-plane structure revolution at different substrate temperatures same as AFM measurements. The in-plane reflections have been labelled accordingly to the DIP thin-phase structure consisting of a rectangular lattice with two molecules in the unit cell (depicted in chapter 5). The corresponding evolution of the in-plane lattice parameters, *a* and *b,* with coverage are plotted on the right sides. The coverage is also given in fraction of ML of standing molecules (related to the equivalent thickness D (Å) through D/16.6 (Å)). At room temperature and 90 °C, these GIXD results disclose a compressive strain along the *b* lattice vector in the first a few DIP layers relative to the lattice dimensions of DIP thin films. The structural transition occurs within a very narrow range of the coverage, at around 3 ML at room temperature and ~ 4 ML at 90 °C, the compressive strain are released. Notice that larger changes are observed for the *b* lattice parameter, namely -3.4 % and -3.0 % at room temperature and 90 °C, while *a* a lattice parameter shows little change, only -0.3 % and -0.8 % respectively.

At 120 °C, a noticeable shift in the peaks position is observed with increasing thickness up to the fifth layer which is indicative of significant changes in the in-plane structure. The compressive strain is dynamically relieved upon formation of subsequent DIP layers. These GIXD results disclose a compressive strain of 4 % along the *b* lattice vector in the first DIP layer (coverage of 0.6 ML) relative to the lattice dimensions of DIP thin films. Thus, in spite of the amorphous character of the SiO_2 surface and consequently without any shear stress imposed by lattice matching, molecular interaction with the substrate leads to a denser DIP layer.

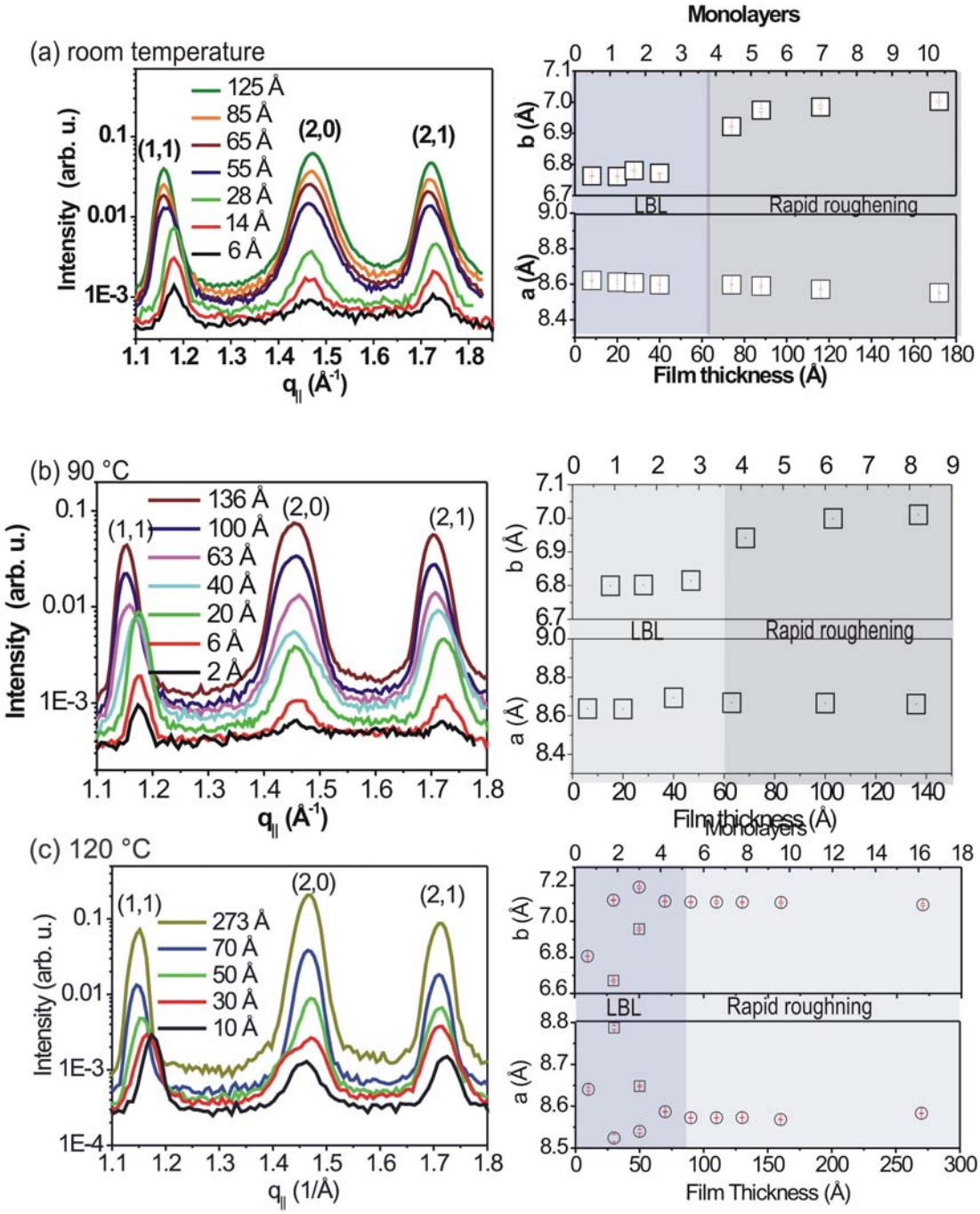

Figure 7.16: The GIXD measurements of DIP at (a) RT, (b) 90 °C and (c) 120 °C. On the right, the calculated lattice parameters *a* and *b* are plotted as a function of the layer coverage. The shadows mark the morphology evolution separation of LBL growth and rapid roughening regimes, which take place accompanied with the strain relaxation at the same critical thickness.

The compressive strain is dynamically relieved upon formation of subsequent DIP layers. Thus, it is observed that the in-plane structure of the DIP first layer changes upon further DIP growth. Upon the deposition of 1.2 DIP layers more (total coverage is 1.8 ML) two structures are observed: a strained structure which is -5.9% compressed along the *b* lattice vector and 2.3% expanded along *a* lattice vector (squares in figure 7.17 (c)) coexisting with an almost relaxed structure (circles in figure 7.17 (c)). From the integrated intensity (assuming no significant changes in the structure factor), it is estimated that each structure occupies about the half of the total coverage. Thus, it is conceivable that strained and nearly-relaxed structures correspond to the first and second layer, respectively, although this can not be directly concluded from the data. The deposition of one more layer leads to a considerable strain relief in the whole film (< 2%). The structure is relaxed beyond 5th ML.

T (°C)	β	$D_{Critical}$	$a_{initial}$ (Å)	$b_{initial}$ (Å)	δ a (%)[1]	δ b (%)[2]	a_{final} (Å)	b_{final} (Å)
35	0.84	~3 ML	8.621	7.763	-0.8	-3.4	8.552	7.003
90	0.80	~4 ML	8.638	7.800	0.3	-3.0	8.6610	7.010
120	0.77	~5 ML	8.640	7.807	0.7	-4.0	8.580	7.090

Table 7.2: In-plane lattice parameters and calculated strain as a function of the coverage. [1]$\delta a = \Delta a/a*100\%$ and [2]$\delta b = \Delta b/b*100\%$ calculated relative to the lattice parameters for a DIP film with highest coverage.

The data are summarized in the table 7.2. Although the deviations of the in-plane lattice parameters are given according to the standard definition of *strain*, it should be kept in mind that the concept of strain is not appropriately defined for organic molecular systems because it ignores the larger degrees of freedom due to their anisotropy. The strain, rather than continuous, relieves during the transition. Although the deviations of the in-plane lattice parameters are given according to the standard definition of *strain*, it should be kept in mind that the concept of strain is not appropriately defined for organic molecular systems because it ignores the larger degrees of freedom due to their anisotropy. In spite of the amorphous character of the SiO_2 surface and consequently without any shear stress imposed by lattice matching, molecular interaction with the substrate leads to a denser DIP layer.

7.3.2 Out-of-plane

The out-of-plane structure of the organic thin films was investigated by X-ray diffraction measurements. Figure 7.17 shows specular X-ray reflectivity curves of DIP films at different substrate temperatures with similar film thickness of ~ 135 Å. By fitting the curves with Parratt formalism, the film thicknesses and roughness can be extracted, the results are summarized in Table 7.3. The obtained film thickness is consistent with the calibration deposition value from QCM. The DIP film exhibits increasing roughness with decreasing substrate temperature coinciding of the AFM measurements. At 120 °C, the roughness of ~ 8 Å is derived, while the roughness increases to ~ 28 Å at room temperature. The distance between Kiessig interference fringes which reflects the total film thickness almost equalizes to that of the Laue oscillations around the first order DIP Bragg reflection, which indicates that the DIP films are coherently ordered over their entire thickness. The Bragg peaks of DIP show small position difference at different substrate temperatures. The rocking widths of the film are in the range of ~ 0.006° confirming the high crystalline order of the films in the out-of-plane direction.

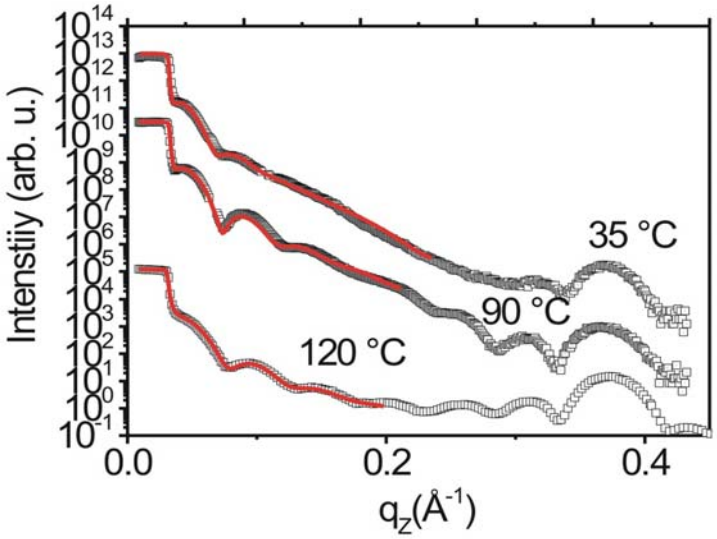

Figure 7.17: Specular X-ray reflectivity of three DIP films at different substrate temperature on SiO_2. The red curves are the fitting results by using Parratt formula.

T_{sub} (°C)	D (Å)	ρ (e^{-1}/ Å^3)	σ (Å)	d (Å)	VD (Å)	Rocking
35	140.12	0.448	27.556	16.989	231	0.00685
90	133.84	0.427	18.167	17.103	201	0.00674
120	133.06	0.4556	7.948	16.869	207	0.00604

Table 7.3: The thickness, deposition rate, electron density and roughness of DIP films prepared at different substrate temperatures, from fitting the XRD curves by the Parratt algorithm.

We performed extensive X ray diffraction measurements with increasing film thickness at 120 °C to monitor the revolution of the out of plane ordering. The well defined Kiessig and Laue oscillations reveal coherent ordering of the film. The Bragg peaks were observed to shift to higher q value, i.e. smaller lattice spacing, with increasing film thickness (shown in figure 7.18 (a), the arrows are guided to eyes). By fitting the Bragg peaks with Gaussian equation, we derived the exact locations and halfwidths. The results are listed in Table 7.4. The lattice spacing of DIP film of 50 Å thicknesses is ~ 18 Å, while a thick film of thickness of 270 Å the Bragg peak decreases to 16.732 Å, the tilting angle of the DIP molecule respect to the substrate surface is plotted in figure 7.18 (b) and the corresponding layer spacing in 7.18 (c).

D	1st Brag peak			2nd Bragg peak			d_z (Å)	VD (Å)
	q_z	ω_{HW}	rocking	q_z	ω_{HW}	rocking		
50	0.351	0.067	0.00612	0.700	0.075	0.0060	17.951	95
70	0.364	0.046	0.00606	0.733	0.048	0.0065	17.149	136
90	0.368	0.039	0.00597	0.740	0.041	0.0063	16.984	159
110	0.371	0.035	0.00596	0.744	0.0352	0.0061	16.901	180
130	0.372	0.030	0.00604	0.746	0.031	0.0062	16.839	206
160	0.374	0.024	--	0.748	0.025	--	16.797	257
270	0.376	0.015	0.00633	0.751	0.015	0.0064	16.723	431

Table 7.4: The fitting results of the first Bragg reflectivity and the second Bragg reflectivity by using Gaussian formula. The mociacity is given by the half-width of the rocking curve

fitted by Gaussian formula. The d-spacing is calculated by using the position of the second Bragg peak and the average domain size by its half-width of the second Bragg peak.

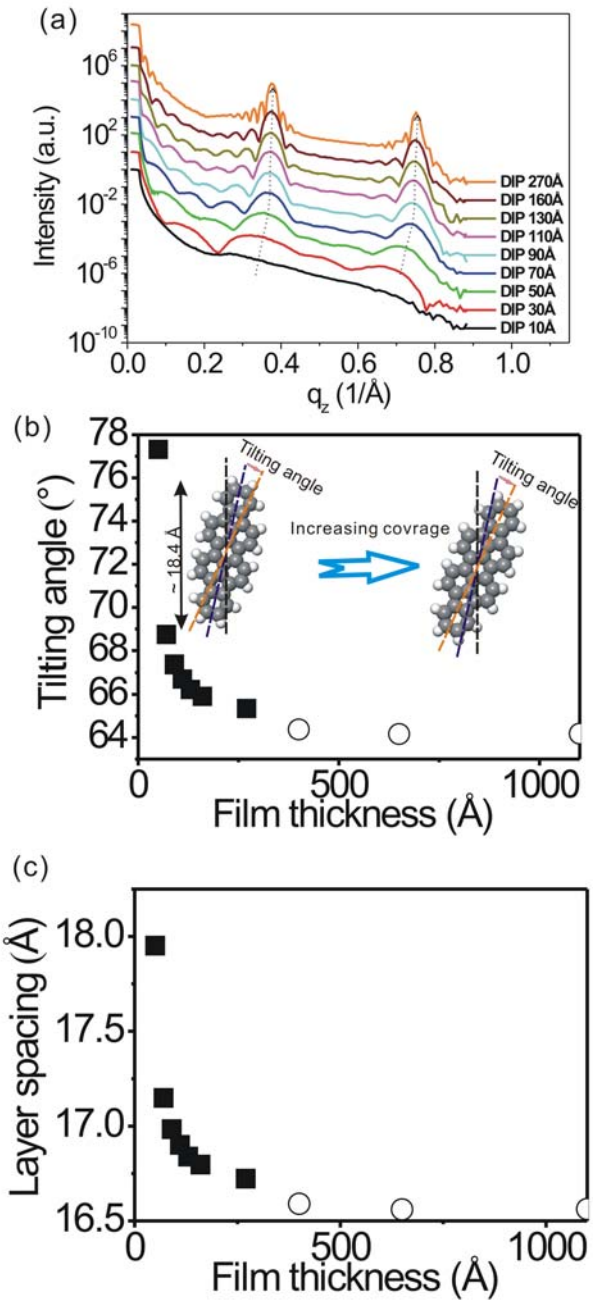

Figure 7.18: Specular X-ray reflectivity of the DIP films as a function of increasing film thickness at the substrate temperature of 120 °C on SiO_2. The dashed arrows red curves are guided for depicting the shifts of the Bragg peak positions (circles data cited from [64]).

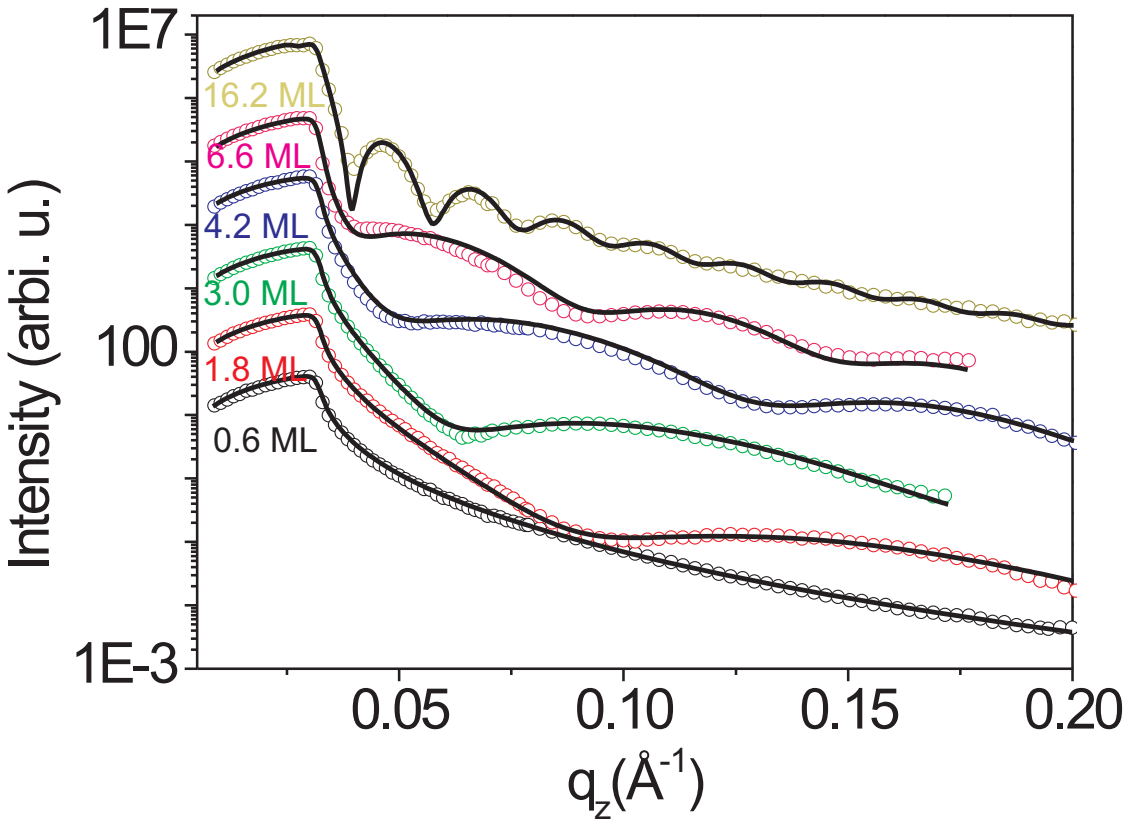

Figure 7.19: Specular X-ray reflectivity of DIP films on SiO_2 as a function of coverage at substrate temperature of 120 C. The black curves are the fitting results by using Parratt formula, while the colored lines are XRD data, the curves are shifted for the clarity sake.

D (ML)	0.6	1.8	3.0	4.2	7.6	9.6	17.2
ρ (e^{-1}/ $Å^3$)	0.665	0.479	0.489	0.542	0.484	0.468	0.409
σ (Å)	4.56	5.49	3.8	4.48	5.50	8.70	25.71
D (fitted) (Å)	11.35	33.3	50.8	71.0	107.29	157.76	271.6

Table 7.5: The fitting results of the X ray reflectivity data, the fit is with 3 box model including a thin film layer and a layer of SiO_2 and bulk Si.

The continuous change of the out of plane structure is accompanied by the changing of the in-plane structure discussed before. The mosaicity over the whole film thickness is ~ 0.006° disclosing high crystallinity of the DIP films. Notice this value is same as rocking scan got at

different substrate temperatures, the high crystallinity character holds unaffected by film thickness and different substrate temperatures. Figure 7.19 shows the selective reflectivity curves fitted by Parratt and the corresponding electron density profile. From the electron density curve we notice two basic tendencies with increasing film coverage: first, the electron density of the DIP film increases slightly with the increasing coverage, this is consistent with the decreasing Bragg spacing indicating a denser layer forms. Second is the continuous increasing roughness, which is physically reasonable and in coincide with AFM observation. The results data are listed in Table 7.5.

7.4 Conclusions

Combining AFM and in-situ GIXD, we provide a direct insight into the evolution of the in-plane structure and morphology in the early stages of DIP film growth on SiO_2. We show that the morphological transition from layer-by-layer growth to rapid roughening of DIP films is a general phenomenon of the DIP thin film growth, ranging from far from equilibrium state to near equilibrium state.

Despite the "weak" val der Waals force, the interaction with the substrate favours a layered growth. At the layer-by-layer growth regime, we studied the lateral correlation, scaling and fractal properties of the 2D islands. Respect to the growth process, we reveal an Ostwald ripening process and a fast coalescence regime.

In the rapid roughening regime, increasing of substrate temperature leads to a shifting of $\theta_{critical}$ to higher layer thickness and higher β value, namely, $\beta \sim 0.84$ and $\theta_{critical} \sim 3$ ML at RT, $\beta \sim 0.80$ and $\theta_{critical} \sim 4$ ML at 90 °C, and $\theta_{critical} \sim 5$ ML and $\beta \sim 0.77$ at 120 °C. A higher deposition rate results in a shifting to higher $\theta_{critical}$ and β value.

For the structural respect, SiO_2 causes the formation of a denser first layers. In spite of amorphous character of the SiO_2 surface, the first DIP layer is under a compressive strain of ~ 3 %-4 % along *a* lattice vector (relative to the relaxed structure of thin films). Upon further deposition the structure of the whole film evolves continuously until a relaxed in-plane structure is achieved at a critical coverage. This is concomitant with a transition from perfect-layer-by layer to rapid kinetic roughening.

The two transitions, in morphology and structure, are coincidently at same critical thickness: (i) from layer-by-layer growth mode to rapid roughening. (ii) from a compressed in-plane structure to relaxed structure. However the connection between these two phenomena is not clear yet. In terms of kinetics, thickness-dependence strain could result in variations on diffusion length with the monolayer number. In a thermodynamic description, a dependence of the elastic and surface energy with thickness may be expected. To date these issues have largely remained unexplored for organic growth. Thus a comprehensive understanding of this work demands further theoretical and experimental studies. It is reasonable to hypostasize that the layer-by-layer to rapid roughening transition observed for DIP might be in essence Stranski-Krastanov growth as result from the energetic interplay with thickness.

Chapter 8

Self-assembly process of DIP on Cu(100) surface

In this chapter we report the self-assembly behavior of single molecules and (supra) molecular adsorbed at Cu (100) surface by performing scanning tunneling microscopy measurements in ultra-high vacuum conditions. We first focus on the growth process of DIP molecules at surface. An alternative step-by-step scenario was proposed involving formation of DIP 1D chains on the step edges and subsequent nucleation of two dimensional supramolecular nanostructures. In section 8.2, we focus on the dynamics of the molecular clusters in percolation regime for which we revealed an orientation preference nucleation of the organic molecules respect to the substrate orientation. We illustrated and elucidated supramolecular nanostructures, which is denoted to section 8.3. The annealing effect on the 2 D monolayer structure of DIP is discussed in section 8.4. Finally we describe briefly the formation of multilayer structure.

8.1 Introduction

The fabrication methods of the microelectronics industry have been refined to produce smaller and smaller devices, but will soon reach their fundamental limits of quantum mechanics. An alternative and promising way to produce nanostructures is the self assembly of atoms and molecules on atomically well-defined surfaces. Molecular self-assembly is the spontaneous association of molecules under equilibrium conditions into stable, structurally

well defined aggregates governed by non-covalent bonds [141-143]. Understanding the mechanisms the self-ordering phenomena is of critical importance of controlling the self-assembly and growth processes to create a wide range of surface nanostructures and it also provides important clues for optimizing the performance of organic devices. The deposition of organic molecules by sublimation or evaporation on atomically clean substrate allows for individual identification and tracking, which is prerequisite for the assembly and operation of molecules in single molecular devices.

8.2 Self assembly process

8.2.1 Initial molecular self assembly

The copper substrate has a cubic close packed crystal structure with lattice parameter a=3.6149 Å. Cu (100) surface shows a square unit structure with Cu-Cu distance of 2.55 Å. The bulk copper substrate Cu (100) has two high symmetry directions, namely [011] and [01-1]. The STM scanning direction is 45° respect to these high symmetric directions of the substrate.

The preparation of the Cu (100) was described in chapter 5. The depositions were carried out at a low deposition rate of ~ 17 min per monolayer. The controlling of the deposition rate was by setting the Knudsen cell current. The resulted structure of the DIP molecules is supposed to be in thermodynamic equilibrium. The STM measurements (JEOL Ltd., SPM-4500M) were performed at room temperature or lower (down to 150 K). The early stages of assembly process start from the continuous decoration of the organic molecules on the monatomic/multiatomic surface edges. The STM image in figure 8.1 (a) together with high resolution images of (b) and (c) indicates that at a deposition time of 3 min (17 min of deposition corresponding to full monolayer coverage) the deposited molecules are preferentially adsorbed along the Cu step edges forming chains composed of a single row of molecules. The molecules appear with ellipsoid shapes. Three types of absorption can be distinguished: some DIP molecules with standing up configuration (side by side) align with the well defined straight step edge coast line with an average separation of ~ 8.4 Å, while

others exhibit a rotating angle respect to surface normal of Cu (100) and on the kinks or edges or on random sites DIP molecules adopt random disordered orientation. In essence, the shape of coast lines of the step edges defines the ordering of the one dimensional organic chains.

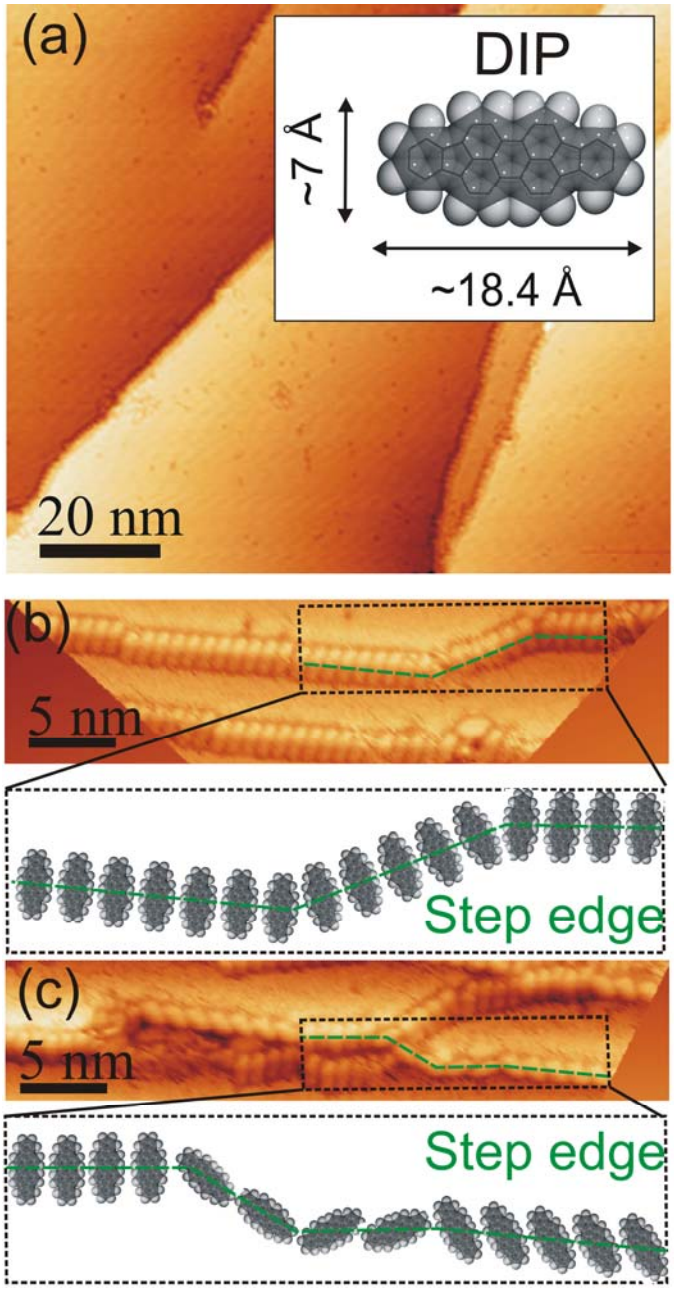

Figure 8.1: STM image of the initial stage of DIP deposition with a deposition time of ~ 3 min (17 min for full layer coverage). The molecules are preferentially adsorbed along the step edges forming single-row chains.

8.2.2 Submonolayer growth and molecular dynamics

The submonolayer coverage in percolation regime offers a unique pathway to study the initial formation of molecular aggregates and molecular dynamics on the surfaces. At a deposition of 0.35 ML, molecular clusters nucleate on the copper surface. The organic clusters nucleate either from the step edges at the substrate surface or on the large terraces. High resolution STM images revealed that the DIP molecules adopt a flat-lying orientation, i.e. the planar molecular plane is parallel to the surface of the Cu(100) substrate. This orientation results from the strong interaction between the electron-rich metal surface of the Cu(100) and π-electron orbitals of the DIP molecules similar to the observation of DIP adsorbed on Cu(111) and Au(111) surfaces [144]. In addition, figure 8.2 highlights that the step edges decorated with DIP molecules acting as nucleation sites for further aggregations, which then adopt a preferential direction with their molecular long axis *l* along the substrate high symmetry direction of either [011] or [01-1]. The schematics in figure 8.2 under each image illustrate this observation. The coordination number difference between upper and lower step edges (more preferred) is screened by the DIP chains decorating the step edge, so that no obvious favoring of nucleation on the lower step edges was observed.

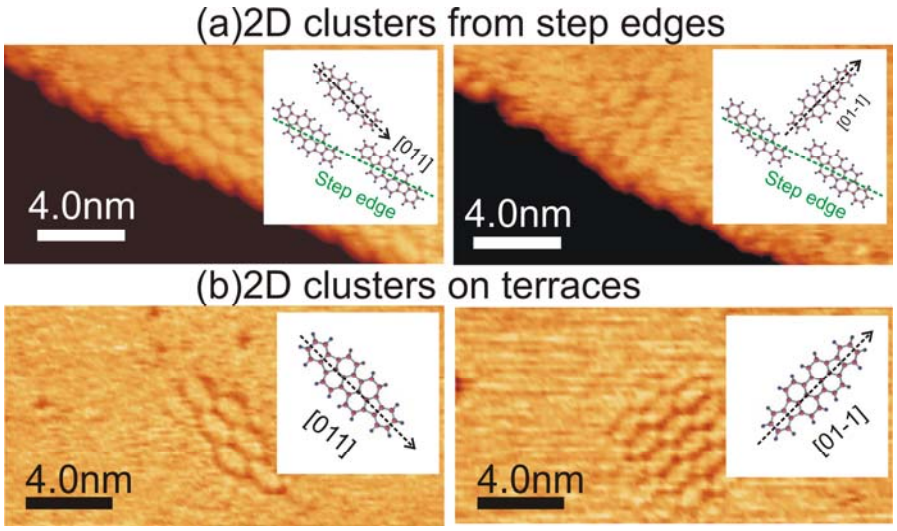

Figure 8.2: (a) Molecular clusters starting from the upper and lower step edges. (b) Small molecular clusters on the large terraces.

High resolution STM images allowed us to monitor in-situ dynamics of supramolecular self assembly. Here we discuss the dynamical behavior of the DIP molecules in two separate parts in terms of the substrate topography: isolated organic clusters on large terraces or those organic clusters starting from the Cu step edges.

DIP clusters on the large Cu terraces

On the large terraces, single molecules exhibit preference for specific sites and specific orientation.

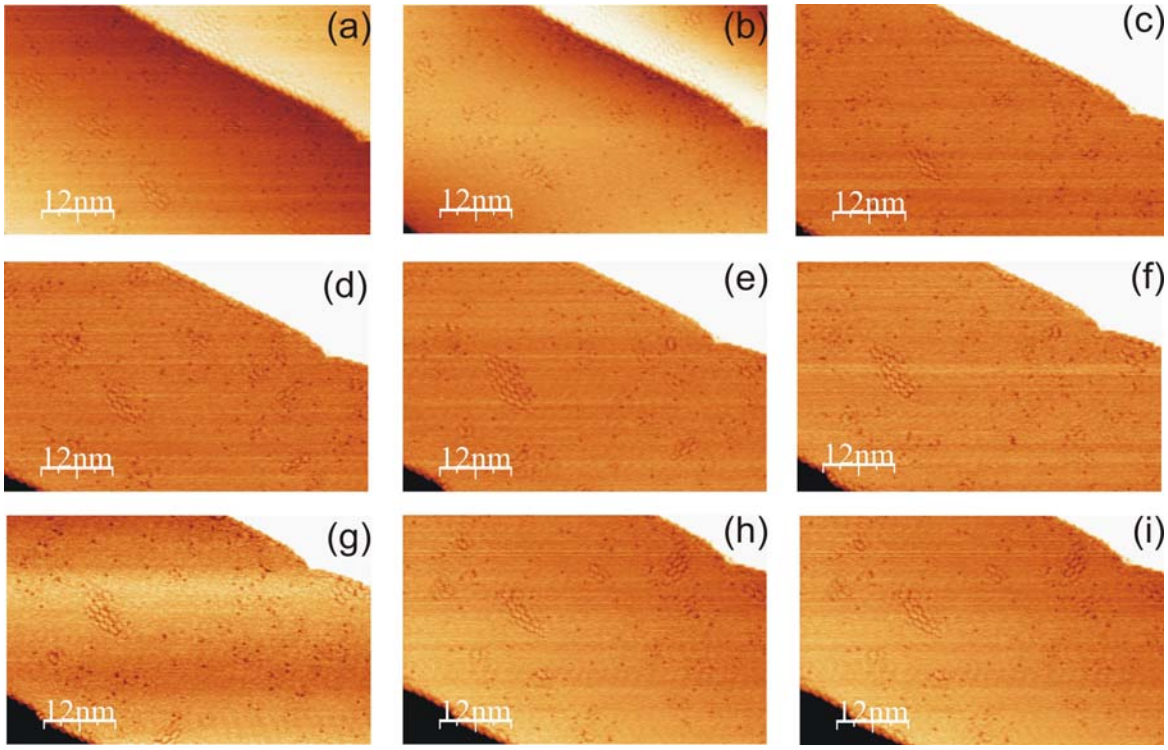

Figure 8.3: (a)-(i) STM images of dynamical behavior of organic clusters on the same area of one of large terrace of Cu (100) at room temperature (continuous scan with time interval of ~ 1 min).

Figure 8.3 shows a series of STM images of molecular aggregates isolated on one of the large terrace at room temperature. All the images were recorded continuously with an interval time of ~ 1 min. At room temperature, these molecular clusters were very mobile and rarely keep their position with time and can change their shape and rearrange their internal

structure easily. They consisted of much less molecules comparing to those clusters starting from the step edges. Single molecules, dimers or trimmers were observed to condense on the surface. The molecules tracking at the place of the point defects of the Cu surface appear to be much less mobile. Though small in size, the organic clusters try to arrange themselves into ordered arrays and show obvious facets.

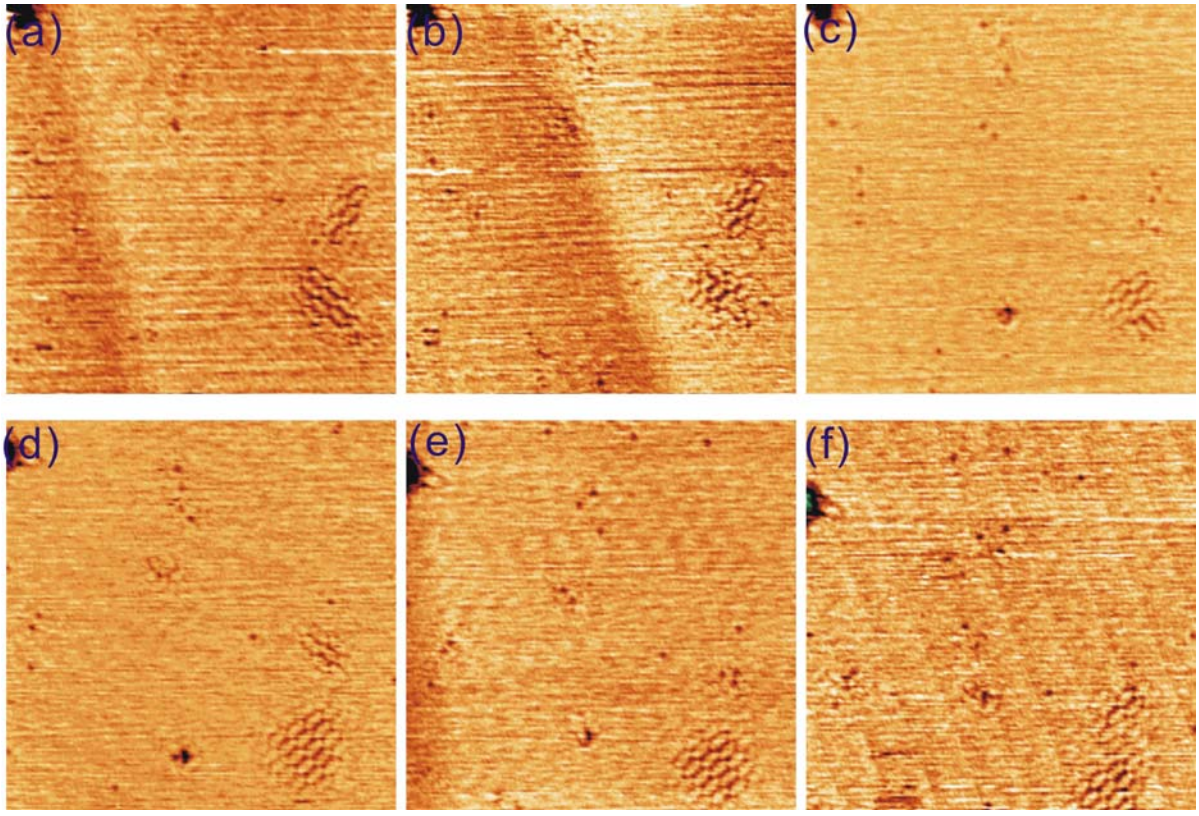

Figure 8.4: (a)-(f) STM images of dynamical behavior of organic clusters on the same area of one of large terrace of Cu (100) at 240 K. The images have a size of 32 nm*32 nm. (Continuous scan on the same area, the interval time is 1 min per scan).

We performed our experiment further by cooling the substrate at different temperatures. Figure 8.4 represents the dynamic behavior of the DIP molecules at the temperature of 240 K, from which similar robust way of molecular movements was observed. Cooling the substrate down to 150 K (the basic temperature of our experimental setup by cooling with liquid nitrogen), all molecules are still mobile indicating weakly corrugated substrate–adsorbate interaction, i.e. a very low diffusion barrier, see figure 8.5 for details. With cooling down

procedure, we disclosed the increasing average cluster size from the statistical counting. The average cluster size is 5.1 molecules per cluster at room temperature. Most observed clusters, however, consisted of four molecules, in turn, that can be taken as the stable cluster size at room temperature. A larger average cluster size of 8.6 molecules per cluster at 240 K and 11.5 molecules per cluster at 150 K was observed. Namely, lowing substrate temperature helps to reduce the activity of clusters, reflecting from decrease of $\overline{\left(\frac{\Delta i(t)}{i(t)}\right)}$, from ~0.7 at RT to ~0.2 at 240 K and 150 K, note the $\overline{\Delta i(t)}$~5.5 at 150 K is larger than $\overline{\Delta i(t)}$~1.8 at 240 K due to its relative larger cluster size. The static and dynamic characterization of the clusters are summarized in Table 8.1.

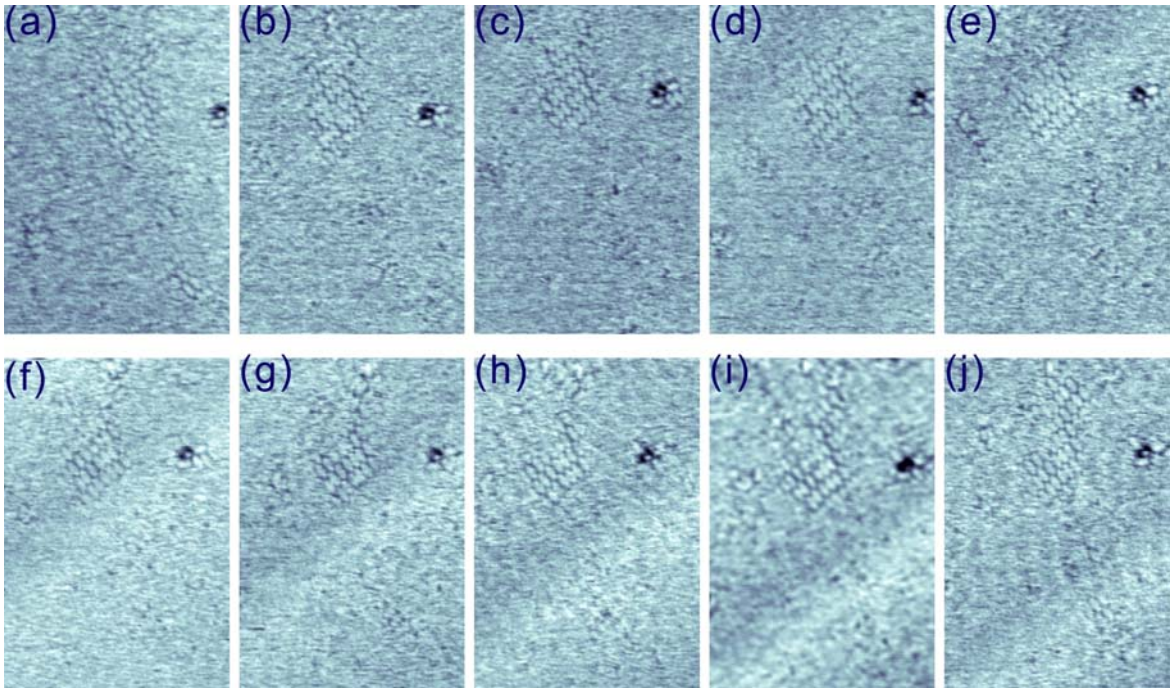

Figure 8.5: (a)-(j) STM images of dynamical behavior of organic clusters on the same area of one of large terrace of Cu (100) at temperature of 150 K. (Continuous scan on the same area, the interval time is 1 min per scan). The images have a size dimension of 25 nm *37 nm.

The cluster size at a give temperature is determined by two physical surface quantities, surface diffusion and adatom binding energy. Decreasing the substrate temperature leads to a

depression of the diffusion length of the molecules by $D \propto \exp(-E/k_B T)$, where E is the energy barrier from site to site and k_B the Boltzmann constant. From the observed cluster size, a rough value of 640 meV can be deduced for the activation energy. The cluster size distribution exhibits an asymmetric shape with a peak position smaller than the average cluster size $\overline{A}$. This is due to the coexistence of small clusters and the formation of large ones due to coalescence, in turn shifts $\overline{A}$ to a higher cluster-size. The cluster-size distribution is summarized in figure 8.6.

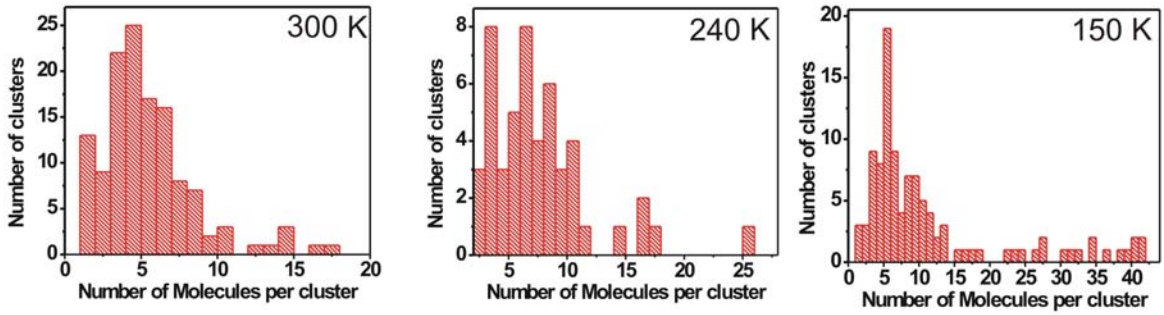

Figure 8.6: The plots of the cluster sizes vs the statistical number of the clusters along different orientations of the substrate (a) at 300 K (b) at 240 K and (c) at 150 K.

Temperature	dynamical (single cluster)			static (average over> 50 clusters)		
	$\overline{i(t)}$	$\overline{\Delta i(t)}$	$\overline{\left(\frac{\Delta i(t)}{i(t)}\right)}$	$\bar{i}$	$n(i)\|_{max}$	σ
300 K	8	10	1.8	5.1	4	11.1
240 K	10	1.8	0.2	7.6	4.6	5.4
150 K	27.4	5.5	0.2	11.5	6	3.4

Table 8.1: The dynamical and static characterization of clusters at substrate temperature of 300K, 240 K and 150K. $\overline{i(t)}$ means average size of a single cluster size fluctuate with time, $\overline{\Delta i(t)}$ is average cluster size change per min; $\bar{i}$ is the average cluster size, σ is its derivative.

DIP clusters starting from the step edges

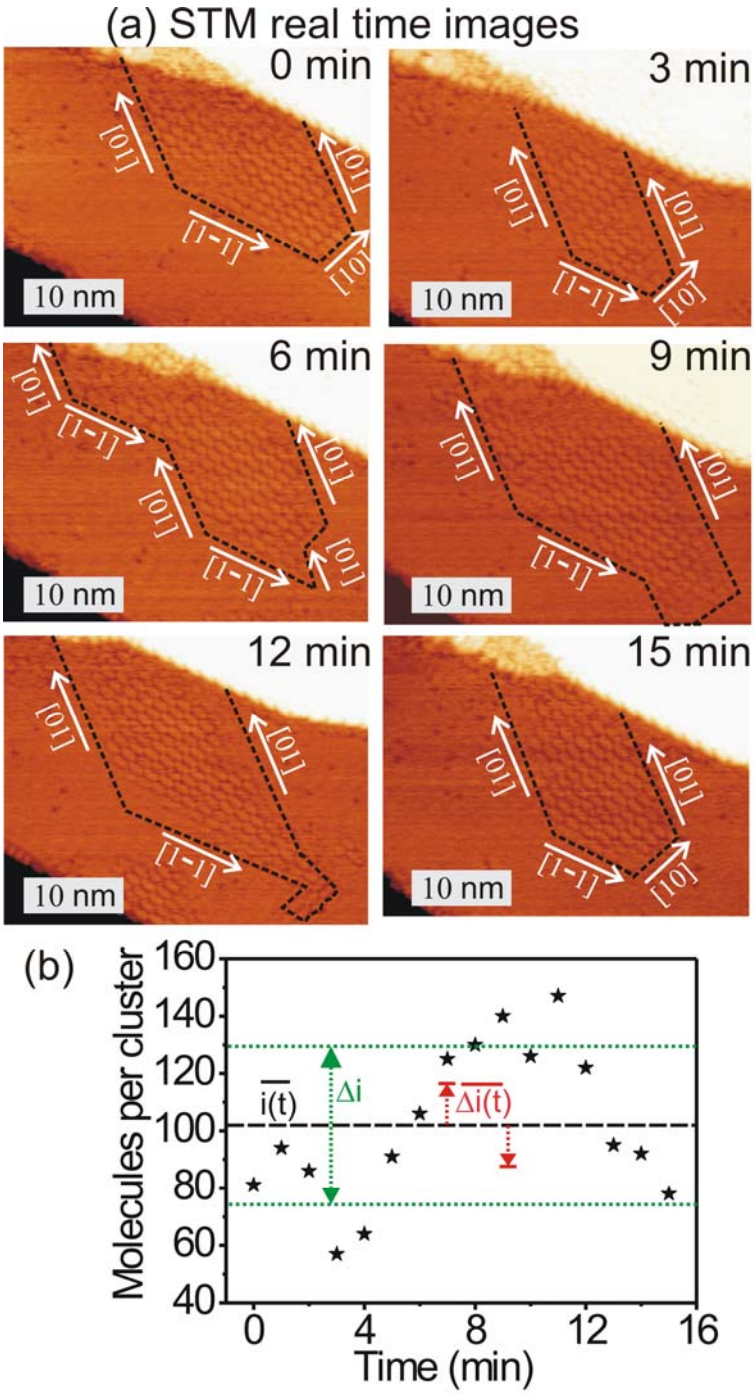

Figure 8.7: Initial stage of DIP deposition with a deposition time of ~ 3 min (17 min for full layer coverage). The STM image shows large flat terraces without molecules, while the molecules are preferentially adsorbed along the step edges. (b) and (c) High resolution STM images of 1D molecular chains with illustrations showing the molecular orientations.

A series of the images displayed in figure 8.7(a) shows the temporal evolution of the large aggregates emerging from the same coverage. A large island started to separate into two islands from its less ordered part, the relatively smaller one continuous shrunk and finally disappeared. The larger one survived but remained changing its shape dynamically through exchange the outermost molecules with the so called "liquid" phase while the internal structure is rarely affected. The so called "liquid" refers to the fast moving organic molecules with a speed significant higher than the STM scanning speed, therefore their shapes can not be resolved by performing STM measurements and characterized as random noise like feature but mountain the same height. The molecular condensed island exhibited well defined crystallographic faces, nevertheless the molecule facets of the island along the molecular [0,1], [1,-1] or [1,0] directions and the newly desorbed or aggregated molecules adopt one of the above mentioned direction.

Fig. 8.7(b) gives detailed cluster size changing with time according to images in 8.7(a); a statistics analysis over a time period of 15 min gives average cluster size $\overline{i(t)}$ ~ 102.1±26.9 molecules/cluster (illustrate as black dashed line and greens dashed lines respectively). To trace the cluster activity, we need to look at how far the cluster size derives from its previous value with time, this is given by $\Delta i(t) = i_{t+1} - i_t$, describing the cluster size changing per minute with time t. We get $\overline{\Delta i(t)}$ ~ 14.5, meaning there are around 14.5 of molecules coming or leaving this 2D island per minute (as red dashed arrows in figure), quantitatively correspond to ~17% of unstable molecules in the island.

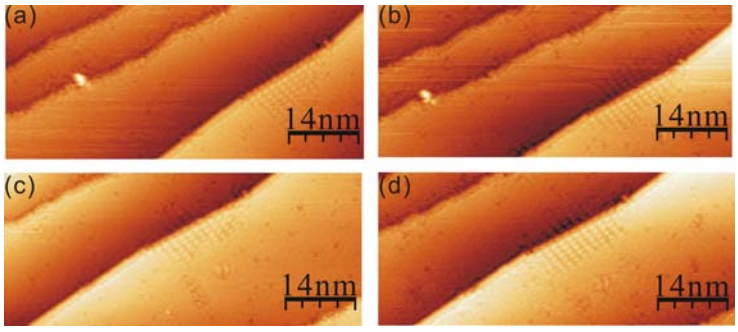

Figure 8.8: (a)-(d) STM images of dynamical behavior of organic clusters on the same area of one of large terrace of Cu (100) at temperature of 150 K.

Figure 8.8 and figure 8.9 describe the similar dynamical behaviors at substrate temperature of 150 K and 220 K and no obvious slow-down of the mobility of islands was observed.

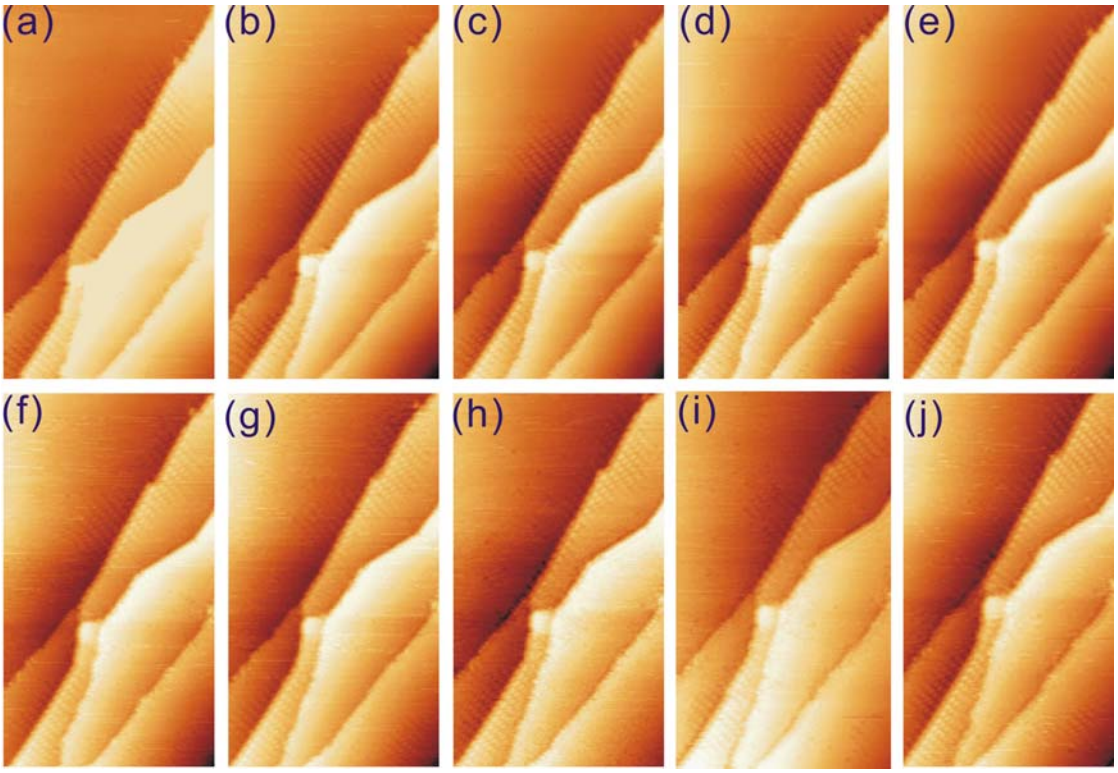

Figure 8.9: (a)-(j) STM images of dynamical behavior of organic clusters on the same area of one of large terrace of Cu (100) at 220 K. (Continuous scan on the same area, the interval time is 1 min per scan). The images have a size dimension of 40*80 nm.

8.2.3 Monolayer structure of DIP

Figure 8.11 depicts the formation progress of the monolayer structure DIP on Cu (100), from which we observed the "liquid" phase of the organic DIP molecules and solid ordered DIP molecules. We noticed the liquid phase locate among the domain boundaries of the ordered solid phases. Figure 8.10 (b) was recorded 2 min later than (a), from which we witness a fast transformation from liquid phase to solid phase. Figure 8.10 (c) and (d) show the subsequent

images of the final stage transition from coexistence to a totally ordered solid nanostructures, from which final ordered domains have a loose packing differing from all the surrounding orientations. In fact, the recording of these coexistence phases was rare, which means a fast ordering and a stable phase of ordering nano-structural arrays. Other observed less ordered DIP molecule packing always exists among the domain boundaries.

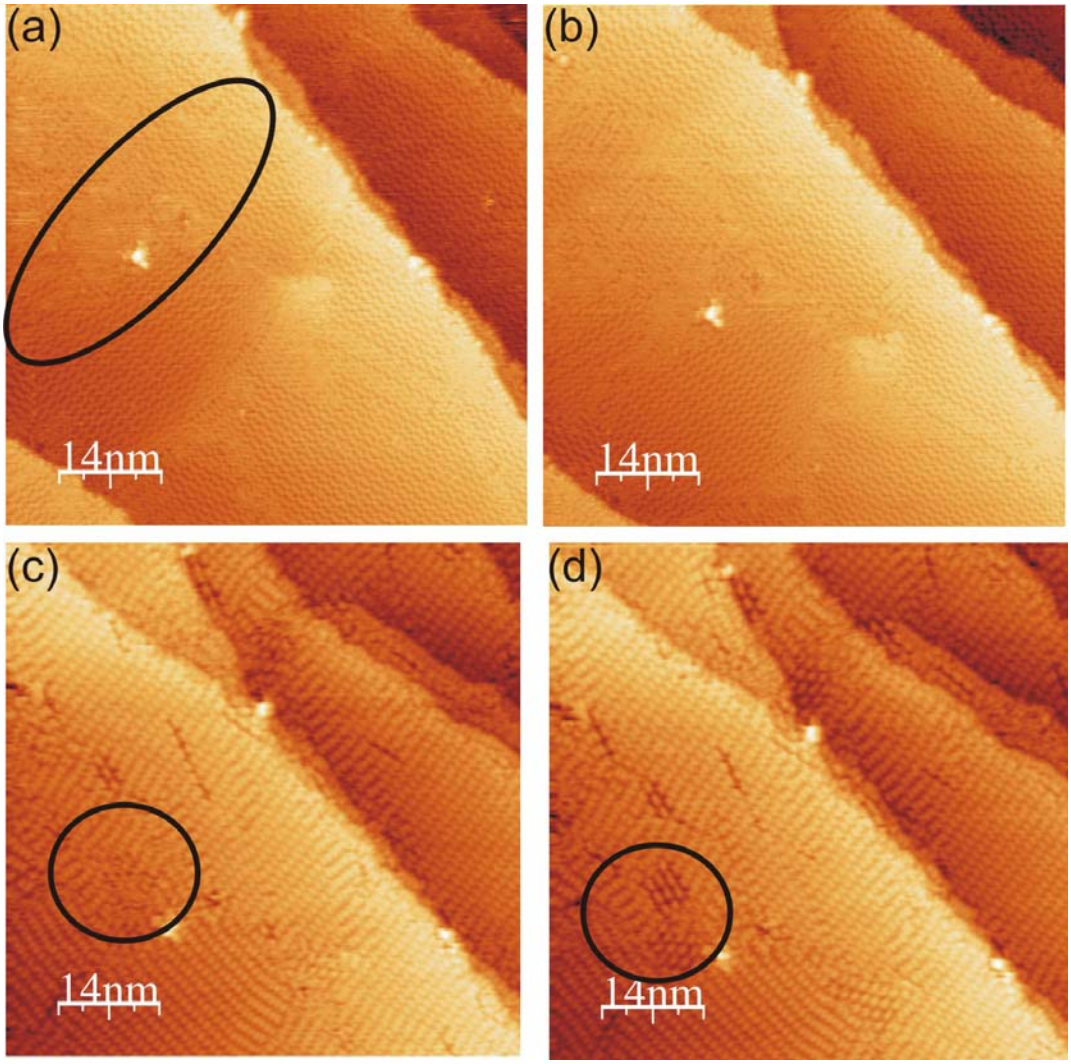

Figure 8.10: (a) to (d) STM images showing the coexistence of liquid phase and solid phase of DIP and the continuous shrink of the liquid phase to solid phase, the black open circles mark the noticeable changing sites. The time interval from (a) to (c) is two minutes and from (c) to (d) is 1 min.

Figure 8.11 shows STM images of the highly ordered layer structure resulting from full

monolayer deposition of DIP on Cu (100). With respect to the molecular packing, adjacent DIP molecules are parallel to each other side by side with each end-group pointing to the center of the joint place of next row. Figure 8.11 (a) shows the typical morphological patterns of well ordered organic molecular arrays on the large copper terraces. The first image in figure 8.11 (a) shows well distinguish domain boundaries, the second image gives a more mixed domains, while a third one exhibits a slightly "snake" zigzag feature of the ordering. Several domains coexist within one image with distinct orientation differences.

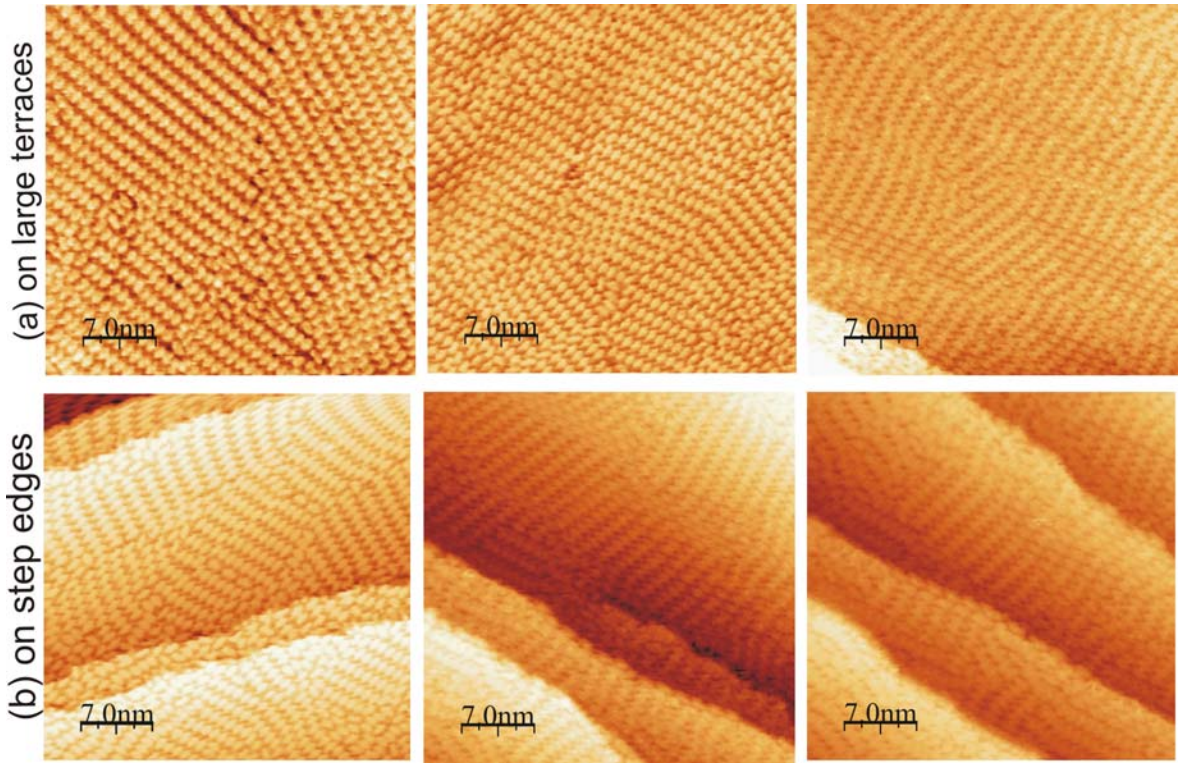

Figure 8.11: Monolayer coverage of DIP on Cu (100) (a) on large terraces (b) on step edges.

The organic clusters try to arrange themselves into ordered arrays and show obvious facets. The molecular clusters condensed with long axis *l* along the substrate high symmetric direction of either [011] or [01-1] with equivalent probability due to the substrate isotropy. A more detailed examination reveals the presence of two chiral domains for each of the two molecular orientations, thus the formation of four equivalent domains, which might due to four fold symmetric character of the substrate surfaces. These four equivalent domains are

shown in figure 5(a) with label "A","B" chiral along [011] direction and "C", "D" along [01-1] direction. The associated unit cell is commensurate with the underlying substrate, characterized by the epitaxial matrixes of "A": $\begin{bmatrix}\vec{A}_1\\ \vec{A}_2\end{bmatrix}=\begin{bmatrix}4 & -1\\ 2 & 7\end{bmatrix}\begin{bmatrix}\vec{x}\\ \vec{y}\end{bmatrix}$, "B": $\begin{bmatrix}\vec{B}_1\\ \vec{B}_2\end{bmatrix}=\begin{bmatrix}-4 & -1\\ -2 & 7\end{bmatrix}\begin{bmatrix}\vec{x}\\ \vec{y}\end{bmatrix}$, "C": $\begin{bmatrix}\vec{C}_1\\ \vec{C}_2\end{bmatrix}=\begin{bmatrix}-1 & 4\\ -7 & -2\end{bmatrix}\begin{bmatrix}\vec{x}\\ \vec{y}\end{bmatrix}$ and "D": $\begin{bmatrix}\vec{D}_1\\ \vec{D}_2\end{bmatrix}=\begin{bmatrix}1 & 4\\ 7 & -2\end{bmatrix}\begin{bmatrix}\vec{x}\\ \vec{y}\end{bmatrix}$, where $\begin{bmatrix}\vec{A}_1\\ \vec{A}_2\end{bmatrix}$, $\begin{bmatrix}\vec{B}_1\\ \vec{B}_2\end{bmatrix}$, $\begin{bmatrix}\vec{C}_1\\ \vec{C}_2\end{bmatrix}$ and $\begin{bmatrix}\vec{D}_1\\ \vec{D}_2\end{bmatrix}$ are the lattice parameters of DIP 2D crystals and $\begin{bmatrix}\vec{x}\\ \vec{y}\end{bmatrix}=\begin{bmatrix}\vec{a}_{0-11}\\ \vec{a}_{011}\end{bmatrix}$ are the Cu substrate lattice parameters along [011] and [01-1] directions (summarized in Table 8.2).

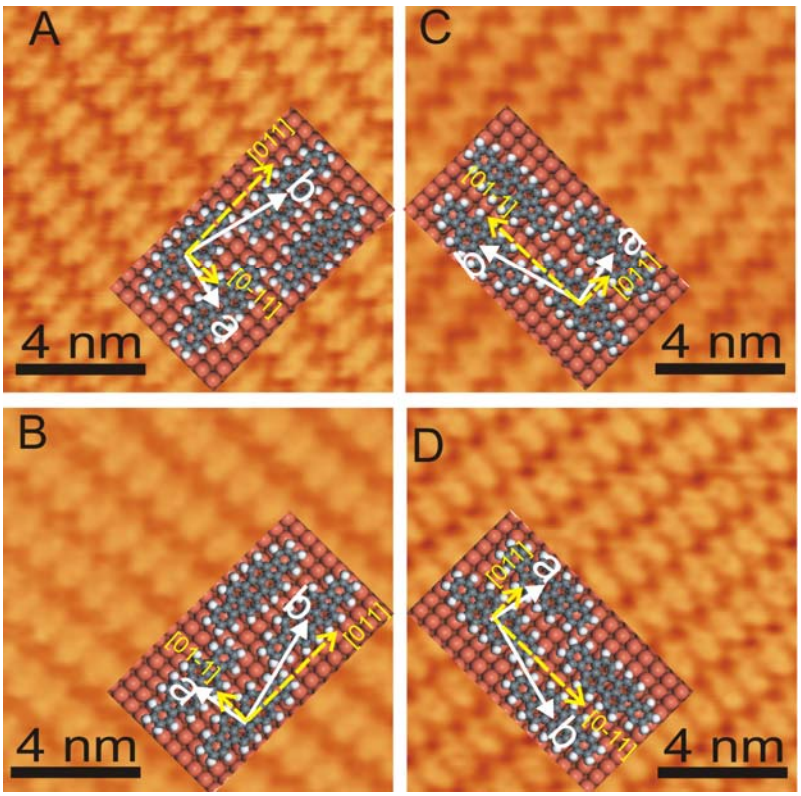

Figure 8.12: The four different domain orientations labeled as "A","B","C" and "D" with a full layer coverage of DIP on Cu (100) on large terraces (deposition time is 17 min). The insects show the schematics of real space model of the corresponding adsorption geometry.

A real space schematic model structures (optimized) of DIP are shown as the insets of figure. In this model, we consider the van der Waals force interaction among the molecules and all the molecules are assumed to center at the bridge site of the copper molecules as has been calculated by DFT for its building block perylene[23,24]. This model is in consistent with the molecular packing and the resulted domain orientations we observed in the STM data, thus strengthens the chiral character and epitaxial matrix of DIP monolayer in theory.

domains	A	B	C	D
matrix	$\begin{bmatrix} 4 & -1 \\ 2 & 7 \end{bmatrix}$	$\begin{bmatrix} -4 & -1 \\ -2 & 7 \end{bmatrix}$	$\begin{bmatrix} -1 & 4 \\ -7 & 2 \end{bmatrix}$	$\begin{bmatrix} 1 & 4 \\ 7 & -2 \end{bmatrix}$

Table 8.2: The matrixes of four typical domains of DIP correspond to lattice parameters $\begin{bmatrix} \vec{a}_{0-11} \\ \vec{a}_{011} \end{bmatrix}$ of Cu substrate.

The adsorption of monolayer of DIP organic molecule on Cu (100) is metastable: annealing the monolayer at higher temperature leads to rearrangements of the molecule to form larger domains as indicated by the unidirectional rows over such a large-scale image and across step edges by rearrangement of molecule orientation of the domain walls, see figure 8.14 (a) and (b). A key requirement for the formation of this highly ordered structure during annealing appears to be free or loose packing of molecules at the domain boundaries. Such molecules then can fluctuate between neighboring grains due to the exceed kinetic energy and the free rotation of the molecules along their long axis direction on the Cu(100) surface to attain the appropriate molecular arrangement to form a large 2D network. Alternatively, larger grains can grow at the expense of smaller ones by Ostwald ripening.

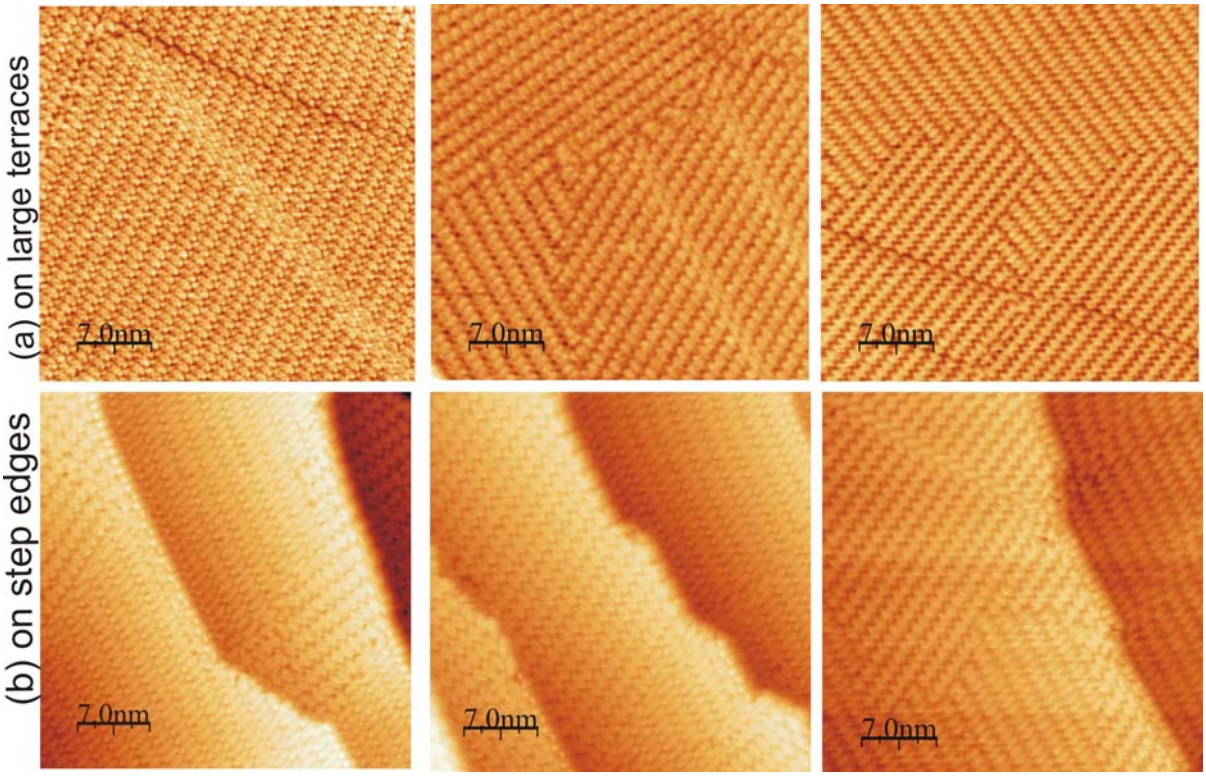

Figure 8.13: The arrangement of organic DIP on Cu (100) surface after annealing at 50 °C for 3 hours (a) on large terraces (b) on step edges.

8.3 Conclusion

In summary, we examined microscopically the growth process of organic molecule DIP on Cu(100) surface. We observed 2D ordering patterns mediated by substrate-molecule interaction, resulting in the epitaxial grown multilayers. The cluster revolution at early stage of growth suggest strongly mobile at different temperatures. While the adsorbate-substrate interaction guides the orientation of the 2D pattering, the adsorbate-adsorbate lateral spacing is governed by weak van der Waals interactions. The organic molecules are commensurate with the substrate and assemble into chiral domains, which can be modified by subsequent annealing resulting in more ordered domains.

Chapter 9

Novel growth strategy for organic electronics

This chapter is devoted to provide a gateway towards the practical fabrications of organic electronics by the novel design of the growth of the organic semiconductors. Two alternative approaches for the application of organic electronics were investigated. In the first section, we present the realization of selective growth of one dimensional organic semiconductor nanowires/nanotubes of F_{16}CuPc by using Au nanoparticle arrays templates. This approach shed light on a technologically simple and inexpensive organic semiconducting nanowire fabrication with precise control of their location and packing density. The delicate dependence of the growth of these organic nanowires/nanotubes on substrate temperature and on gold nanoparticle size was exploited. In the second section, we show the powerful tunability of the self assembled monolayers on the growth of the organic thin film by changing the surface energy. Large micrometer size DIP single crystals were successfully synthesized through this functionality. Organic semiconductor single crystals provide defect free channel for charge transport in terms of a single crystal OFET, thereby improving charge mobility in magnitude range. We studied the kinetic controlling parameter on the transition from thin film morphology towards a single crystal. The structure properties and the driving force underneath are further exploited.

9.1 Growth behaviour of F_{16}CuPc on Au nanoparticle arrays

9.1.1 Introduction

The controlled fabrication of one-dimensional (1D) inorganic semiconducting structures has opened new promising avenues for new nanoscale electronic devices such as optoelectronic devices and sensors [145-146]. The vapor-liquid-solid (VLS) process is used to describe the formation of 1D nanostructures, or nanowires (NWs): liquid metal (catalyst) droplets act as absorption sites for gas-phase reactants and guide the growth of inorganic materials into nanostructures or nanowires [147]. The diameters of the catalysts limit or control the sizes of these nanowires.

The novel properties of inorganic materials has motivated extensive research in the synthesis of similar 1D architectures composed of organic molecules. However, the controlled growth of organic semiconducting nanostructures is rarely reported in literature and the synthesis approach remains experimental challenges. So far two synthesis strategies have been pursued: the use of nanoporous membranes as templates and self-assembly in solution. Whereas the first is more advantageous to produce large arrays of uniform nanotubes, the latter promises spatially control of bottom-up organization. The self-assembly of nanotubes from solution has been reported, however, provides little control over the spatial arrangement, the morphology and the aspect ratios of the nanostructures [148]. We investigated the vertical growth of organic F_{16}CuPc nanowires directed by templates of gold nanoparticles arrays. The growth occurs via vapour-phase transport, whereby the gold nanoparticles act as nucleation sites for the F_{16}CuPc molecules and direct their anisotropic growth. In contrast to the inorganic semiconductor growth, F_{16}CuPc nanowire shows no dependence on nanoparticle size and adopts a universal diameter of 20-30 nm.

9.1.2 Morphology of F_{16}CuPc grown on Au nanoparticle arrays

We employed micellar nanolithography, a self assembly technique, to pattern native oxidized Si (100) substrates with gold (Au) nanoparticles. The feasibility of this technique in controlling nanoparticle size (D) and separation (L) has been extensively demonstrated in previous studies. This method has further been optimized for selective deposition of metals such as Au or Ag by an electro-less deposition step to enlarge particle sizes beyond the capability of the micellar technique [149]. The sample morphologies have been characterized

with a field emission scanning electron microscope (SEM) in back-scattered electron (BSE) imaging mode. Figure 9.1 shows a SEM image of the nanoparticle arrays with particle size D ~ 10 nm and separation L ~ 100 nm. The SEM image displays a homogenous pattern of Au nanoparticles over a large area and shows that the Au nanoparticles adopt hexagonal structure on Si surface.

Before the growth, the Au nanoparticle patterned surfaces were heated up to 450 °C under ultra high vacuum conditions for two hours to avoid remnant impurities and contaminations. One must be aware that a longer annealing time or a higher desorption temperature bear the risk of melting and desorbing of the Au nanoparticles. For all the templates considered, only part of the substrate is covered with Au nanoparticle arrays, the other part of bare SiO_2 substrate acts as reference for monitoring the nominal coverage.

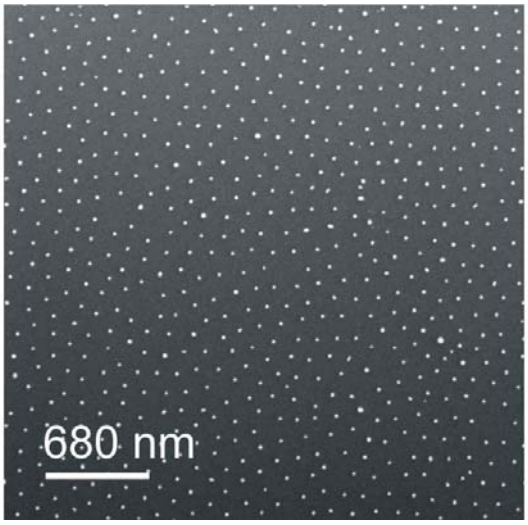

Figure 9.1: SEM image of the Au nanoparticle array on bare SiO_2. The separation L between the gold nanoparticles and the particle size D are external control parameters. The gold nanoparticles adopt a hexagonal pattern on the surface.

The deposition of $F_{16}CuPc$ is performed at different substrate temperature but at a constant low deposition rate of ~ 1 Å/min. All samples discussed here have a film thickness of ~ 10 nm. We noticed that the deposition rate rarely has effects on the formation of the nanowires, while a higher deposition mass helps to form longer wires. Figure 9.2 (a) illustrates the schematic of the deposition process in OMBE. The morphology of a $F_{16}CuPc$ thin film at a boundary region between the patterned and unpatterned areas is shown in figure 9.2 (b). The

thin film of F_{16}CuPc on the unpatterned side (flat SiO_2 substrate) exhibits continuous smooth feathers. On the patterned side of the silicon surface, Au nanoparticles instigate nanowire structures associating with an underneath F_{16}CuPc wetting layer. The Au nanoparticles act as nucleation sites for the F_{16}CuPc molecules and promote their wire-like growth.

The F_{16}CuPc nanowires are initially grown vertically on top of Au nanoparticles. However during the SEM scanning procedure, these soft nanostructures were bent down to the substrate surface. This makes the observation of the vertical growth of the F_{16}CuPc nanowires rather difficult; nevertheless figure 9.3 gives an example of the standing wires. Most frequently, SEM images show uniform F_{16}CuPc nanowires connecting the Au nanoparticles and forming a network. We attribute this behaviour to electrostatic forces between the Au nanoparticles and the organic nanowires, which are negatively charged by the electron beam. This would in fact suggest that the growth direction of one single nanowire could be controlled by applying an electric field between nano-structured gold electrodes. These organic nanostructures are stable after several weeks of storage in air but can get amorphous under ultra moisture condition, for instance pure water.

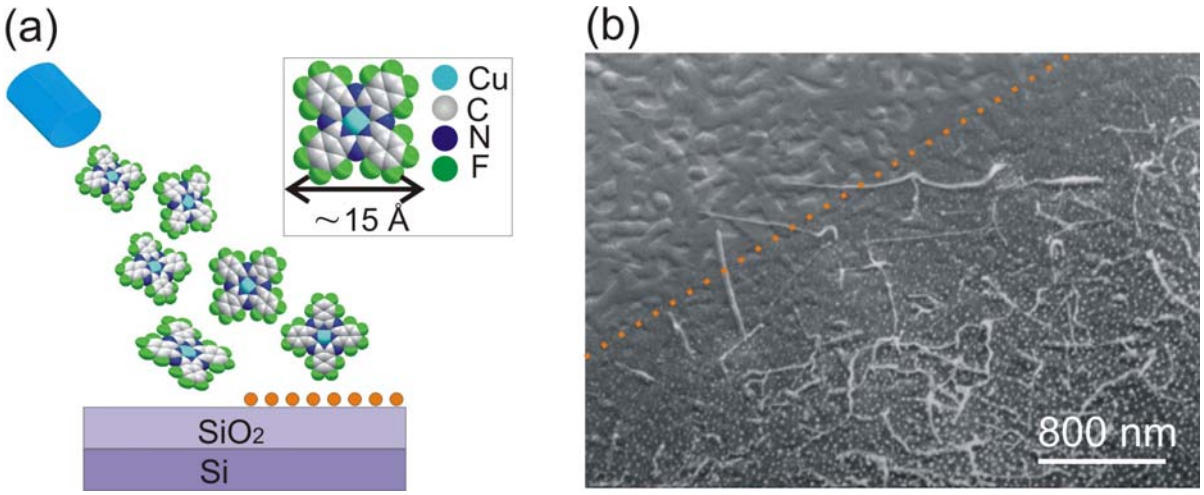

Figure 9.2: (a) This schematic figure illustrates the growth procedure of organic semiconductor F_{16}CuPc molecules on the template of gold nanoparticle arrays. The part of substrate without Au nanoparticle arrays is used as reference. (b) SEM image taken on the boundary (orange dotted line) between the gold template and bare SiO_2 showing the high selective growth of nanowires.

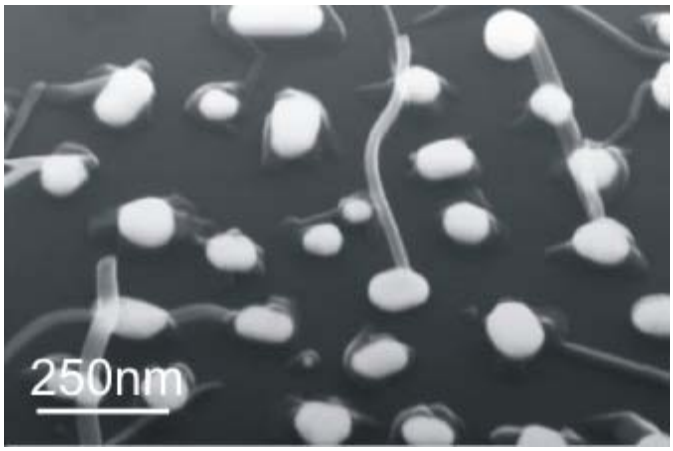

Figure 9.3: SEM image illustrating the vertical growth of $F_{16}CuPc$ wires on top of the gold nanoparticles with a diameter of 20-25 nm.

The distance L between the nanodots enables us to control the packing density of the $F_{16}CuPc$ nanowires. Figure 9.4 shows $F_{16}CuPc$ nanowires grown at T_{sub} = 120 °C. The organic $F_{16}CuPc$ nanowires have a uniform diameter of D = 20-25 nm. The Au nanoparticle size D plays an essential role in the organic nanostructure growth. There exists a critical particle size D* as a threshold to induce $F_{16}CuPc$ nanowire formation. Templates with an Au nanoparticle size smaller than D* lead to the growth of a smooth thin film like that on bare SiO_2. Figure 9.4 (a) and 9.4 (b) show the morphology of $F_{16}CuPc$ onto templates with Au nanoparticles of size D = 10 nm but various L, in which a smooth growth of the film was observed. Beyond this threshold, the $F_{16}CuPc$ nanowires possess a fixed diameter (D = 20-25 nm) regardless of the Au nanodot size D (figure 9.4 (c)-(f)). Single nanowires emerge (from each Au particle) when the size of the nanoparticle exceeds a critical linear dimension of D* = 20 nm (which is in good approximation the diameter of the $F_{16}CuPc$ nanowires) implying that the nanowire formation is only possible when the nanodot size exceeds the intrinsic diameter of the $F_{16}CuPc$ nanowires. The ratio of Au nanoparticle to organic nanowire is close to 1:1 at the moderate Au particle size D ~ 35 nm. For larger particle diameters, multiple organic nanowires form from one single Au nanoparticle (figure 9.4 (d)-(f) for clarity). In figure 9.4 (f), we observed that $F_{16}CuPc$ enveloped the Au particle forming large bubbles and the multiple organic nanowires are short in length (~ 100 nm).

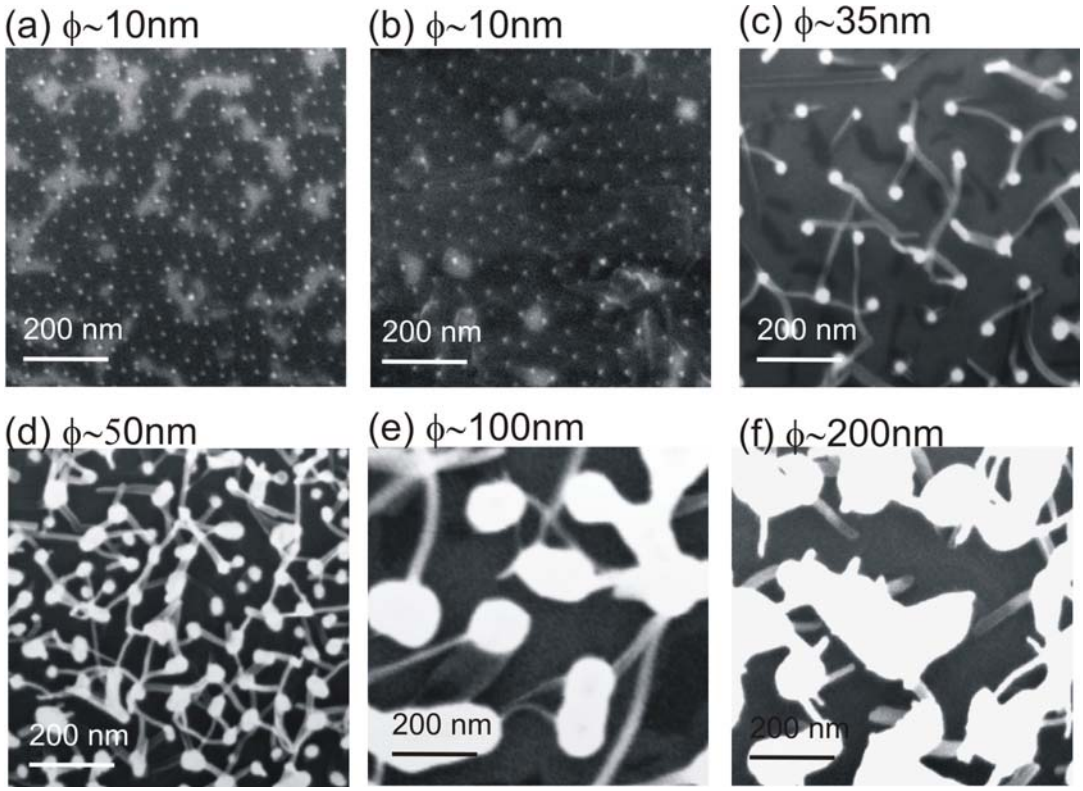

Figure 9.4: SEM images illustrating the influence of the Au particle size on the nanowire formation. Single nanowires emerge from Au nanoparticles when the size exceeds a critical diameter of D* = 20 nm. The width of the $F_{16}CuPc$ wires is independent of the particle size. The substrate temperature is 120 °C.

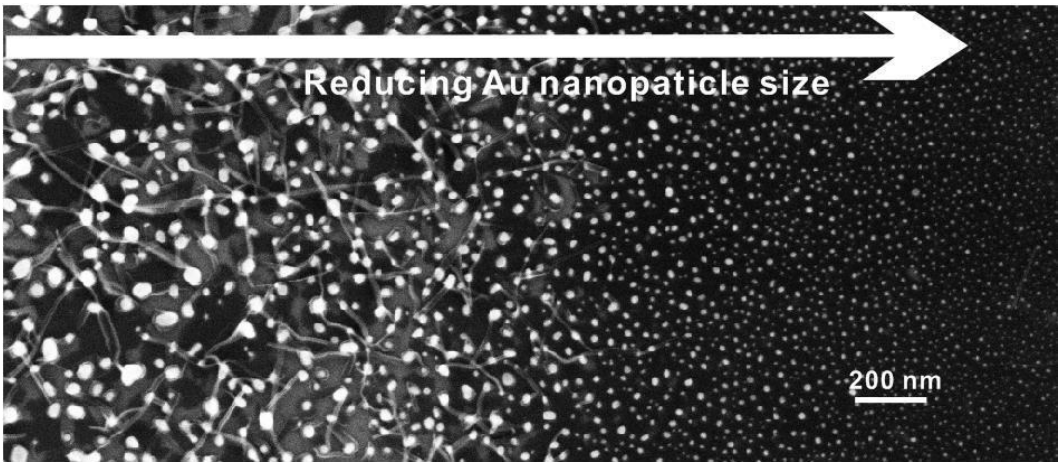

Figure 9.5: SEM image depicts the Au nano-particle size effect of the formation of the organic $F_{16}CuPc$ wires (T_{sub} = 120 °C).

Figure 9.5 gives a clear view of this selective growth evolution of the $F_{16}CuPc$ nanowires on the Au nanoparticle size. The origin for the selection of this length scale is not clear however it is in striking contrast to the formation of inorganic nanowires which adopt a diameter dictated by the size of the metallic seed.

The substrate temperature plays a critical role for the nanowire formation. In figure 9.6 we show SEM images for samples grown at room temperature with increasing Au nano-particle size. When the $F_{16}CuPc$ deposition performed at room temperature, the morphology is very similar to that on bare SiO_2 substrates, i.e. a wetting layer in essence. None or only very short wires (maximum lengths of 40 nm) are observed to grow on the Au nanoparticles (Fig 9.6 (c)).

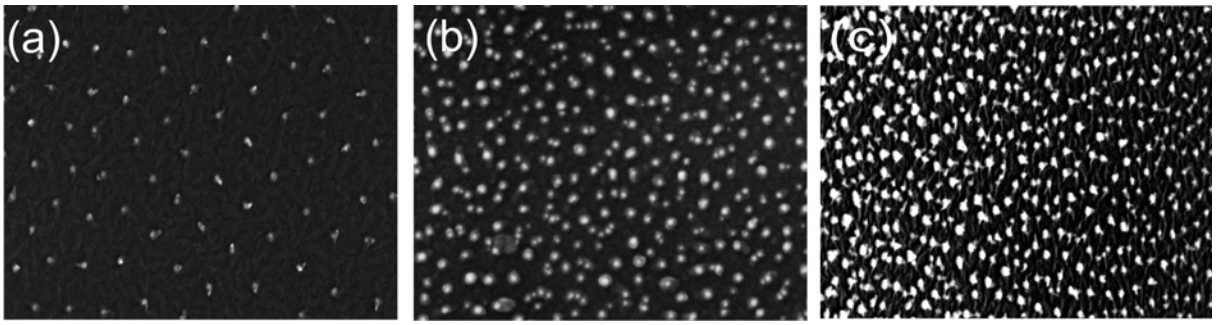

Figure 9.6: SEM images illustrating the growth of organic $F_{16}CuPc$ on Au nanoparticle arrays at room temperature, despite of increasing nanoparticle size, the formation of organic $F_{16}CuPc$ nanowires is rarely observed. The images have a dimension of 600 nm x 1000 nm.

A higher substrate temperature at 140 °C leads to the formation of organic nanowires restrained within a selective size range of Au nanoparticles. Figure 9.7 (a) and 9.7 (d) show the SEM images of Au nanoparticle with size smaller than 15 nm and larger than 35 nm, respectively, on which no nanowire formation was observed. The nanowires grew within a narrow Au particle size 20 nm <D< 30 nm, figure 9.7 (b) and (c). The higher substrate temperature promotes the growth of longer but by far less dense wires: a length of nanowires up to 900 nm can be observed.

At a substrate temperature of around 160 ºC, the high selective growth of organic nanowires on Au nanoparticle size is still dominant, i.e. few nanowires are formed for D < 15 nm and D > 45 nm (figure 9.8). A substrate temperature of 160 ºC is very close to molecular desorption temperature (167 ºC).This results in a considerable decrease of the thickness of the

underlying wetting layer on the particle patterned site and leaves nearly no film deposition on the reference bare SiO_2 site.

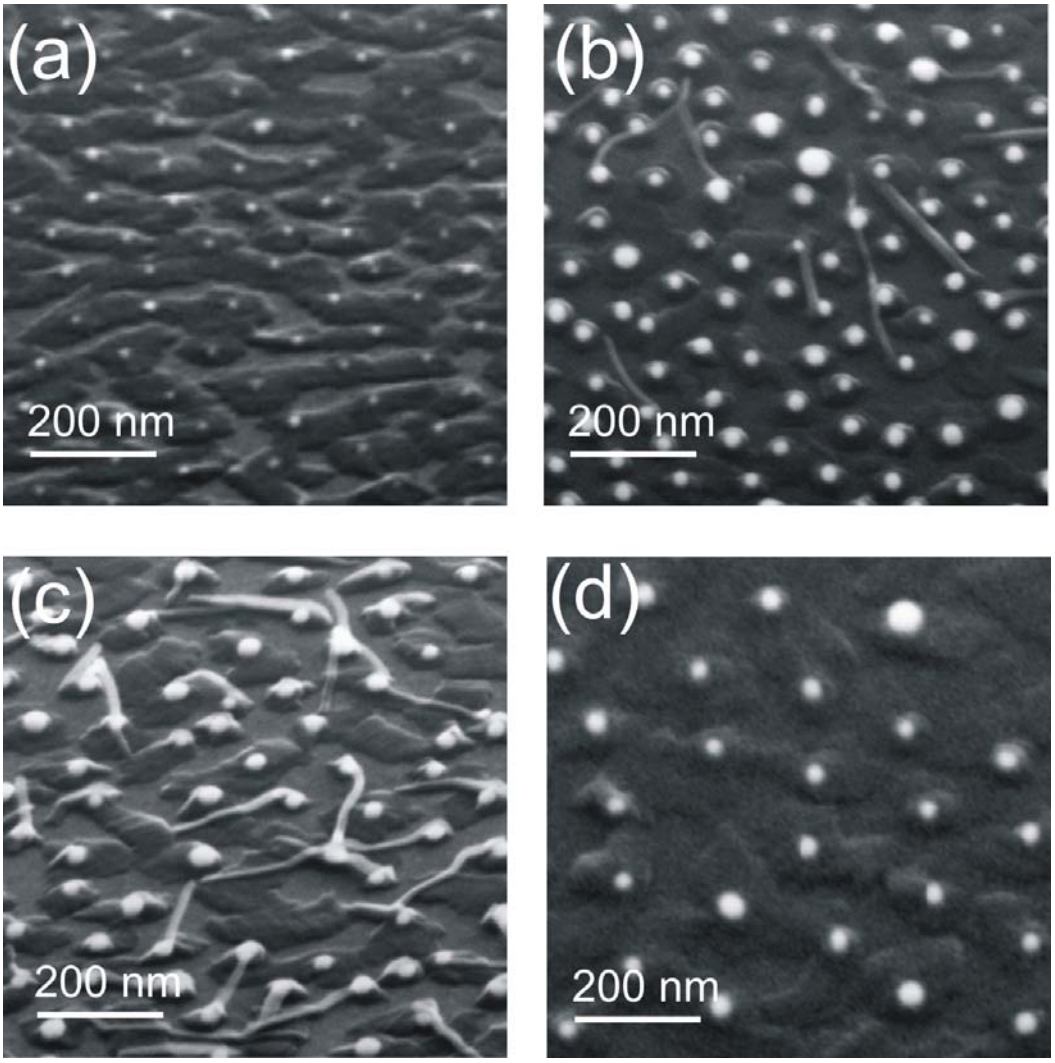

Figure 9.7: SEM images illustrating the growth of $F_{16}CuPc$ on Au nanoparticle arrays at 140 °C, which presents an obvious selective size range of Au nanoparticles for the formation of organic wires.

The temperature and Au nano-particle size selectivities of the $F_{16}CuPc$ nanowires are summarized in table 9.1. The observed temperature-dependent morphology gives clear evidence that the nanowire growth is a thermally activated process. The assembly of $F_{16}CuPc$ in uniform wires is apparently governed by thermodynamic forces, i.e. by the minimization

of surface energies (resulting in 20nm-width wires) together with kinetic parameters (nucleation at the Au nanoparticles is clearly mediated by surface and bulk diffusion).

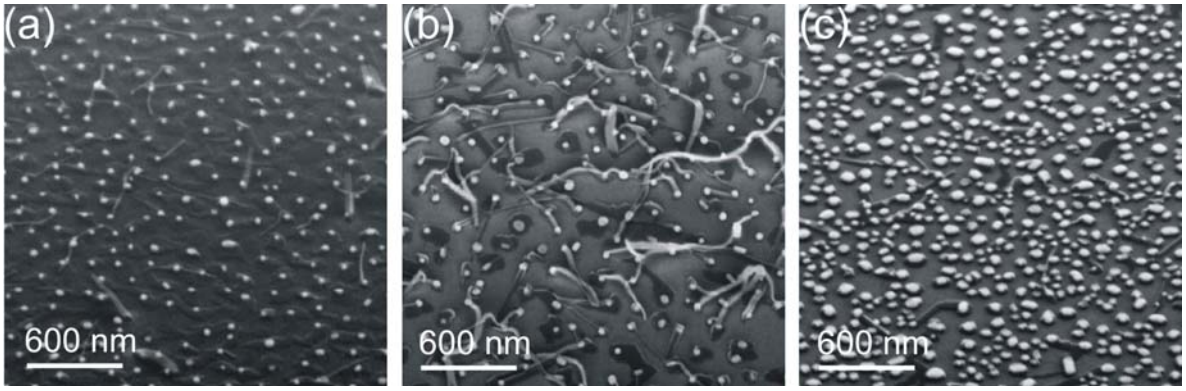

Figure 9.8: The growth of organic $F_{16}CuPc$ on Au nanoparticle arrays at 160 °C.

T_{sub} (°C)	35	120		140	160
D (nm)	---	25 - 35	> 35	20 - 30	15 - 35
Nanowires	no	single wires	multiple wires	single/multiple wires	single/multiple wires

Table 9.1: The temperature and Au nano-particle size selectivity of the $F_{16}CuPc$ nanowires.

9.1.3 Inhibition of the 1D selective growth of organic nanostructures by SAMs

We show that the 1D selective growth of organic $F_{16}CuPc$ nanostructures can be inhibited by fictionalization of SAMs. Among all the SAMs, the methyl-terminated SAMs OTMS molecule (CH_3-$(CH_2)_{17}$-Si(O-$CH_3)_3$) is widely used as the promoter for biomaterials. Adsorbed and self-assembled on the surface, OTMS exhibits a layer height of about 25 Å and a hexagonal in-plane packing structure with a lattice parameter of 4.9 Å. The resulting SiO_2 surface functionalized by OTMS reduces the surface energy from ~ 79 to ~ 20 mN/m and consequently influences the growth process of organic semiconducting thin films on top. By functionalizing the surface with OTMS, the selective growth behaviour of $F_{16}CuPc$ nanostructure on Au nano-particles can actually be inhibited. Figure 9.9 shows two SEM images of two organic $F_{16}CuPc$ thin films on self assembled monolayers of OTMS without

(a) and with (b) Au nanoparticles. The F_{16}CuPc thin film displays elongated crystalline morphology due to the dramatic reduction of the surface energy, in turn an enhancement of the surface diffusion length of the molecules. Because of the layer of OTMS, F_{16}CuPc elongated crystalline stripes ignore the local perturbation of the Au nanoparticles. The absence of the organic nanowires on OTMS functionalized Au nanoparticles discloses that local surface energy or the strong electrostatic interaction are prerequisites for the growth of the organic nanowires. This observation also suggests an efficient way to tune the growth of organic nanowires. As the elongated F_{16}CuPc stripes are highly crystalline, the one connecting two Au nanoparticles can act as a one step fabricated OFETs without domain boundaries. However one faces the challenge of the separation of individual OFETs to allow the alternately switch.

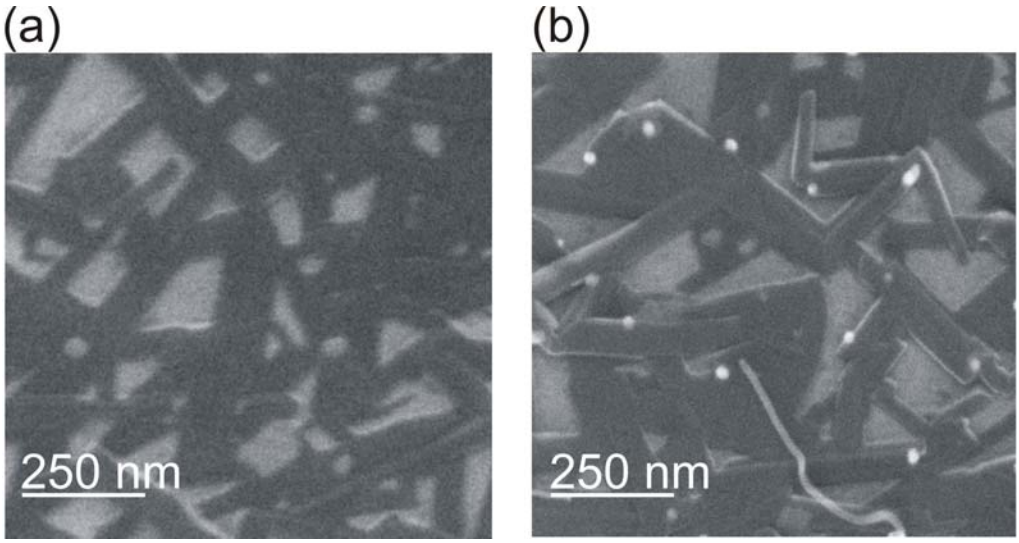

Figure 9.9: (a) SEM image of the organic thin film of F_{16}CuPc on self assembled monolayers of OTMS at 120 °C. (b) SEM image of the growth of organic on Au nano-particle arrays.

9.1.4 The growth behaviour of F_{16}CuPc on other substrates

F_{16}CuPc molecules demonstrate strong selective growth behavior on Au nanoparticles. However to exact elucidate the physical mechanism behind this, the structural and morphological knowledge of F_{16}CuPc grown on the two extreme ends, namely on single

crystal Au and on bare Si substrate, is necessary. Further more, F_{16}CuPc growth behaviour on other inorganic substrate analogies provides useful information.

We first give example of typical morphology and structure study of F_{16}CuPc on bare SiO_2. For a complete description, the reader is referred to chapter 5. Figure 9.10 (a) gives an AFM image of 200 Å F_{16}CuPc grown on SiO_2 at room temperature. The film exhibits an intrinsically anisotropic growth governed by the strong intermolecular coupling of electrons on adjacent molecules. The average roughness measured from larger images is ~ 1.1 nm. The sepcular X ray measurement of a thicker film (~ 220 Å) shows obvious Kiessig and Laue oscillations, the Bragg peak corresponds to a d-spacing of 14.39 Å characteristic of the standing-up configuration of the F_{16}CuPc film (figure 9.10 (b)).

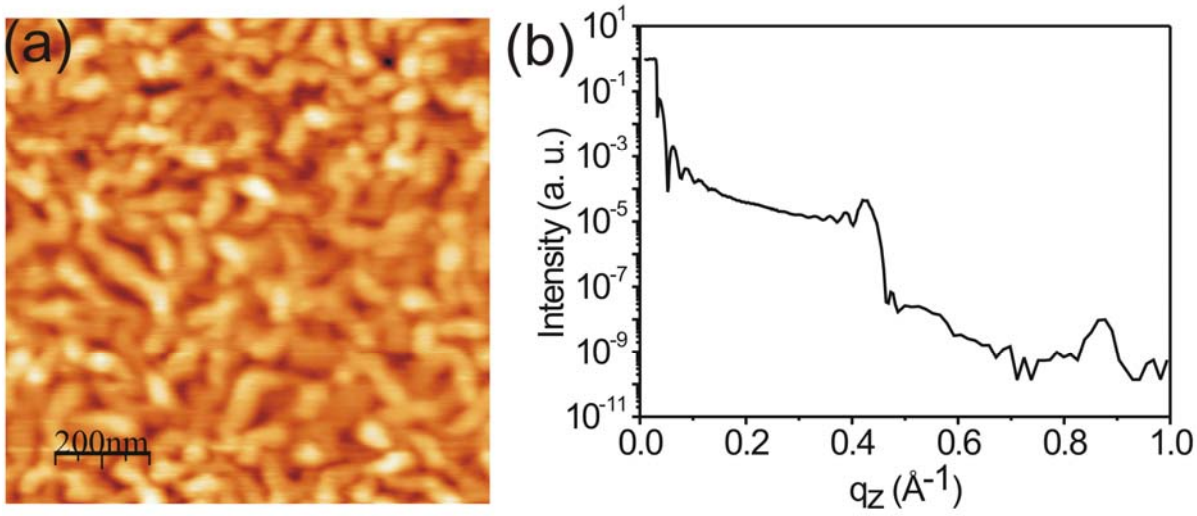

Figure 9.10: (a) AFM image of 200 Å F_{16}CuPc at RT. (b) X-ray measurement of a thicker film of 270 Å F_{16}CuPc at RT.

To study the formation of F_{16}CuPc on Au, around 150 Å F_{16}CuPc were deposited on a single crystal Au (111) substrate. Prior to the deposition, the Au single crystal was treated with combined circles of sputtering and annealing, details see chapter 5. By performing AFM measurement under UHV condition, we observed that F_{16}CuPc exhibits an island growth mode on Au (111) with a roughness ~ 30 Å, figure 9.11 (a). The domain size is ~ 100 nm. An atomic resolution image on one of the islands shows that the F_{16}CuPc molecules are essentially lying down on the surface and its Fourier transform gives the in-plane spacing of

a ~ b = 14.5 Å in agreement of the dimension of the planar molecule geometry. The X ray reflectivity measurement was performed with a six-circle high resolution X ray diffractometer. The reflectivity curve represents neither Kiessig nor Laue oscillation indicating a strong island growth mode consistent with the AFM measurements. The Bragg peak of F_{16}CuPc centred at q_z=1.999 $Å^{-1}$ corresponding to d = 3.143 Å in real space, characteristic the lying down molecular π-π spacing. The structure of F_{16}CuPc on bulk gold is characteristic for the interaction between electron rich metal and π orbitals of the organic semiconductor, which usually gives lying down configuration of the organic molecules on the substrates.

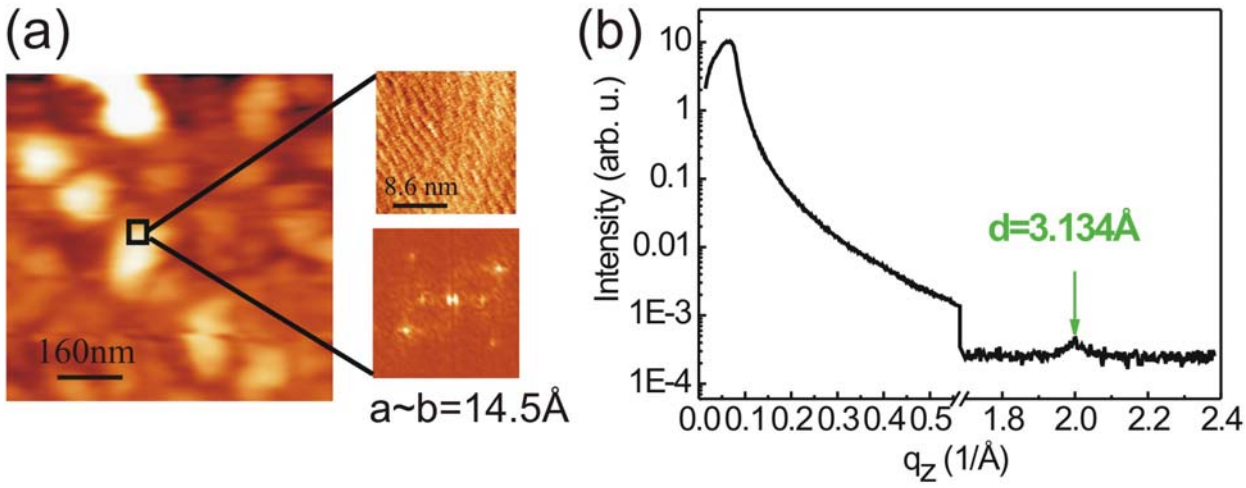

Figure 9.11: (a) AFM measurements of F_{16}CuPc grown on Au (111): island growth mode was observed. The atomic resolution image suggests that the F_{16}CuPc molecules are essentially lying down on the surface and its Fourier transform gives the in-plane spacing of a = b ~ 14.5 Å. (b) The X ray reflectivity measurement shows an out-of-plane spacing of d = 3.134 Å in agreement with the geometry observed by AFM.

We further investigated the growth of F_{16}CuPc on Si substrate with a (111) orientation to elucidate the effect of the substrate steps. Figure 9.12 (a) shows F_{16}CuPc on the triangle structure of a Si (111) surface, F_{16}CuPc homogenously covered the very rough Si (111) surfaces. If the Si (111) surface is functionalized with OTMS, typical stripe like crystalline emerges. It is interesting to see that the directions of these stripes are mainly along the two directions of the triangles and the length of the stripes is limited by the triangles. It is common to take advantage of the natural steps or other specific morphologies of the substrate

to guide the orientated growth of the thin film. By combing of the substrate morphology and the tenability of the substrate surface energy by self assembled monolayers, a vast variety of the controlled growth can actually be achieved.

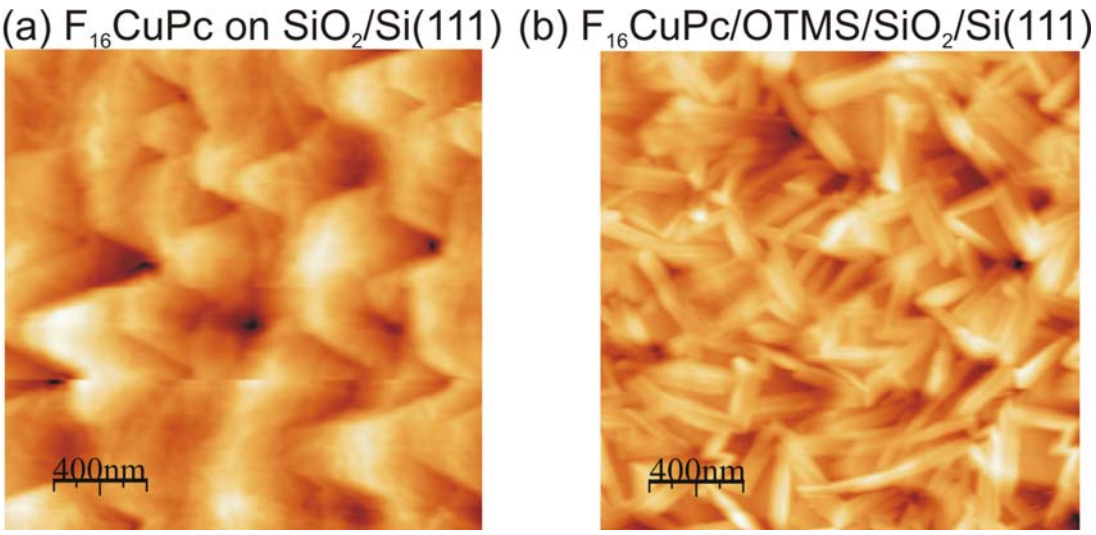

Figure 9.12: AFM morphologies of $F_{16}CuPc$ grown on different substrates (a) on SiO_2/Si (111) and (b) on OTMS functionalized SiO_2/Si (111) surface.

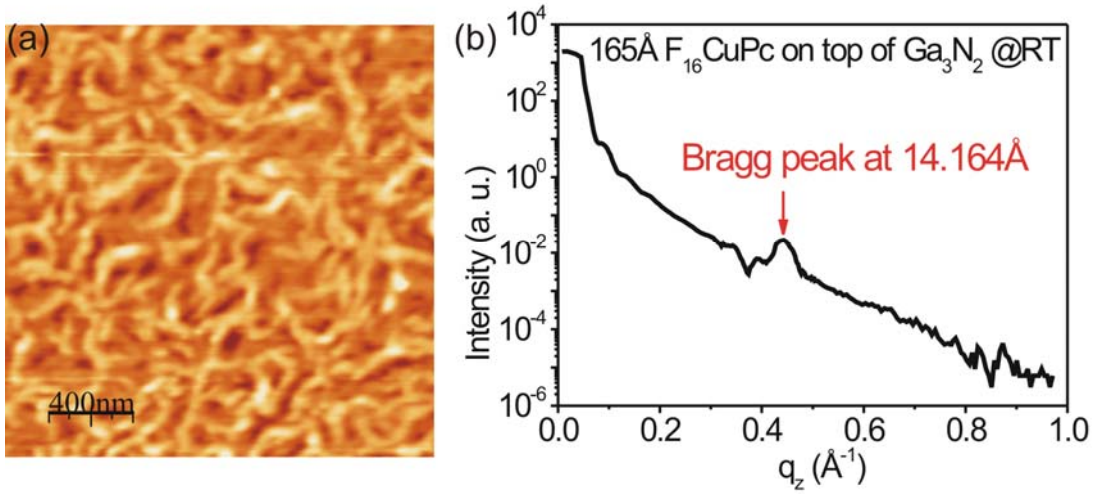

Figure 9.13: (a) AFM image of $F_{16}CuPc$ grown on Ga_3N_2 grown at room temperature. (b) X-ray specular measurement on the same sample.

Finally, we give one more example of $F_{16}CuPc$ on another inert substrate to emphasize the importance of the choice of the substrates on rich morphological changes. Figure 9.13 (a) shows an AFM image of 165 Å $F_{16}CuPc$ grown on Ga_3N_2, which displays very similar

morphology to that on SiO_2. The elongated worm-like structure has an average width of 16 nm and length up to 900 nm interconnected forming nets. The X-ray reflectivity measurement (Figure 9.13 (b)) gives a d-spacing of 14.16 Å, similar to that of $F_{16}CuPc$ on SiO_2.

9.1.5 Conclusion

In conclusion, we have demonstrated that the growth of uniform $F_{16}CuPc$ nanowires/nanotubes (diameter ~ 20-30 nm) with precise localization and packing density can be accomplished by the templates of Au nanoparticles. The dependence of the formation of the nanowires/nanotubes on substrate temperature and Au nanoparticle size is investigated. We are convinced that this simple and inexpensive strategy can be broadly applicable to other small aromatic molecules with strong intermolecular coupling between π - π orbitals. This provides us exciting systems to test fundamental questions about localization excitons and quantum transport in 1D organic structure. The fact that the $F_{16}CuPc$ nanowires assemble in a network connecting gold nanoparticles by the action of electrostatic forces, suggests promising avenues for the bottom-up fabrication of integrated organic circuits. The vertical growth of uniform $F_{16}CuPc$ nanowires (diameter ~ 20-35 nm) with precise localization and packing density can be accomplished by the templates of Au nanoparticles. $F_{16}CuPc$ nanowires can assemble in a network connecting gold nanoparticles. Extensive work of $F_{16}CuPc$ grown on Au single crystal, SiO_2 and other inert substrate was performed for comparison.

9.2 Growth from multilayer to single-crystalline islands of DIP by Self-Assembled Monolayers

9.2.1 Introduction

Over the past few years, growth of large organic single crystals for the fabrication of single crystal organic electronics attracted increasing attention. The advantage of single crystal

organic electronics over its thin film analogue is that single crystal provides defect free charge transport, no domain boundaries, and perfect ordering which improves the charge motility in magnitude. Organic molecular crystals hold the promise for the development of organic semiconductor materials. Self-assembled monolayers (SAMs) have emerged as effective means for tailoring the physical and chemical properties of the substrate's surface and thereby, to modify the growth of the organic films. The growth of single crystalline islands on patterned SAMs have recently be used to fabricate organic single-crystal field effect transistors with high performance [150]. The nucleation of crystals has been attributed to heterogeneous nucleation due to the high roughness of the SAM pattern. Moreover improved performance in OFETs has been reported by covering the gate dielectric with SAMs which has been attributed to reduction of traps at the channel [151-152].

In this section we show our study on growth and structure of DIP on amino terminated SAM, 3-aminopropyltriethoxysilane (APS, chain length ~ 11 Å) grown on SiO_2. We show that DIP films undergo an unexpected growth mode transition, exhibiting smooth 2D morphology in a nonequilibrium regime (at low substrate temperature) and 3D growth of micron-sized DIP single crystals at high temperature, which later will have potential applications in electronic devices.

9.2.2 Morphology and structure of DIP on APS SAMs

The as-grown APS films present an excellent quality: smooth and homogeneous with root mean square roughness ~ 1.4 Å, measured from AFM topographic images (figure 9.14 (a)). The as-grown film is hydrophilic, with a water contact angle of ~ 26.39° in agreement with the data reported in the literature. The thickness of the APS film has been determined by X-ray reflectivity data (figure 9.14 (b)). The data were fitted by a routine fitting algorithm (Parrat 32, L.G. Parrat, Phys. Rev. 95, 359 (1954)) with a three box model concerning the bulk Si layer, SiO_2 layer and APS layer. The electron density profile obtained from the fitted model is plotted in figure 9.12 (c).

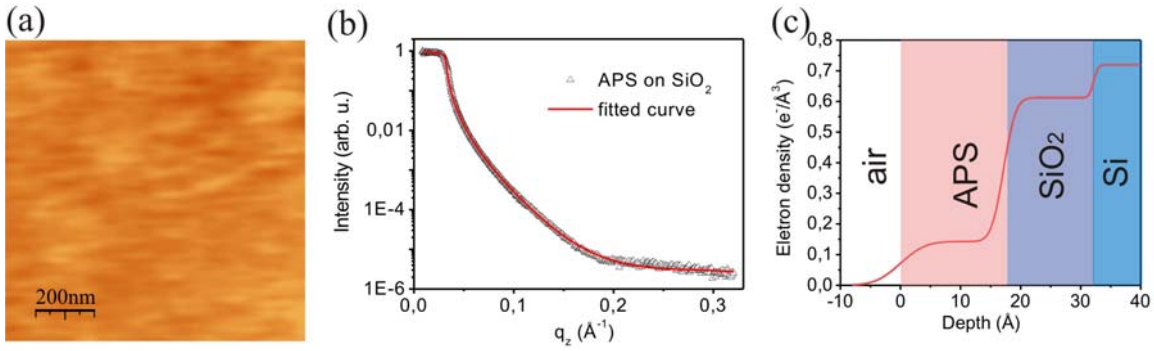

Figure 9.14: (a) AFM image of as prepared APS film on SiO_2, from which a roughness of ~ 1.4 Å can be derived. (b) XRD data together with the fit. (c) Electron density profile of APS on SiO_2.

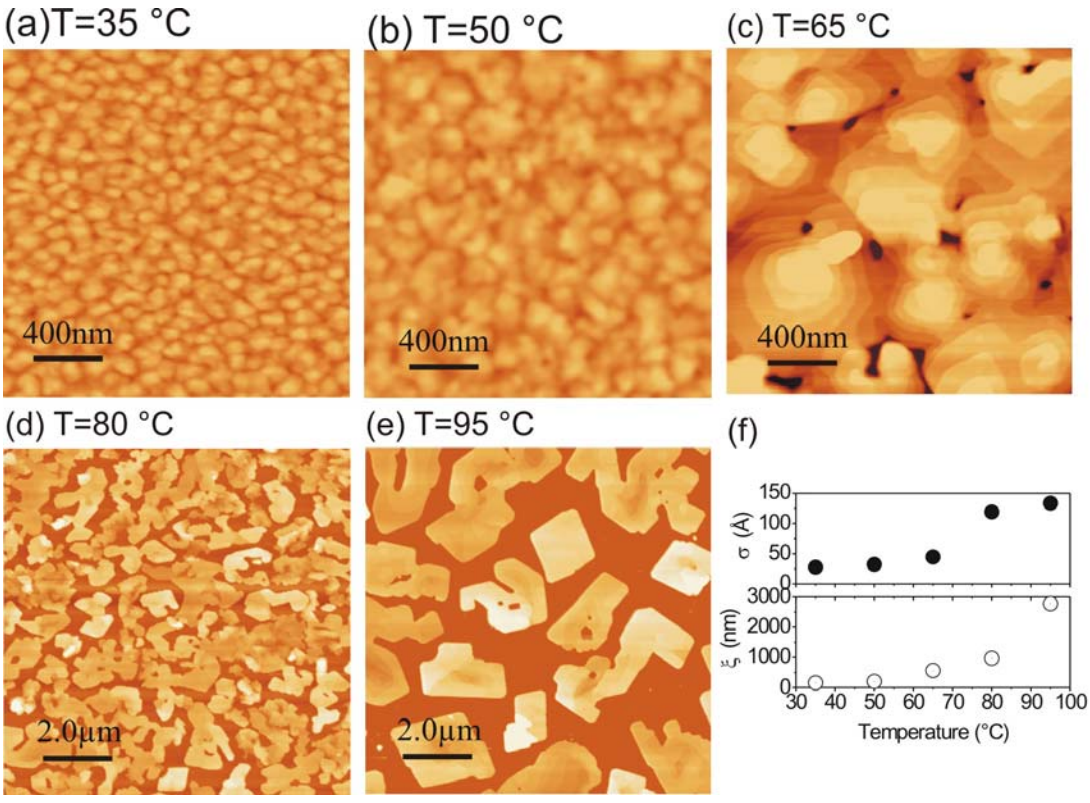

Figure 9.15: (a)-(e) AFM topographic images of DIP on APS at substrate temperature of 35 °C, 50 °C, 65 °C,90 °C and 95 °C. (f) Mean square roughness as a function of the temperature and lateral correlation length calculated from 2D power spectral density analysis.

The average electron density obtained from the fitted model for the APS film is 0.143 $e^-/Å^3$. However the film thickness of 17.16 Å, derived from the fit, is three times larger than the expected value for a monolayer assuming an upright configuration to the surface. For comparison, the thickness of amino-terminated layer from ~ 5 Å up to ~ 2 nm was reported [153-155]. By simply applying a high force on the cantilever (> 12 nN) to scratch a hole in the film of SAMs, a film thickness of 19±2 Å was obtained, confirming that APS films consist of triple monolayers.

After preparation, the substrates functionalized with APS were immediately transferred to the UHV growth chamber to avoid contamination, and further heated up to 120 °C for one or two hours to avoid water moisture before the growth. DIP films deposited at several substrate temperatures showed a strong evolution of the morphology. Figure 9.15 shows topographical AFM images of DIP films grown on SAMs of APS at different substrate temperatures. The deposition of DIP at room temperature results in smooth two-dimensional growth consisting of small grains. The film morphology is very similar to that found for DIP on bare SiO_2, which confirms that at room temperature the film growth is kinetically determined without significant influence of the substrate. At 50 °C, a slight enlargement of the grains (average grain size evolves from ~ 160 nm at room temperature to ~ 205 nm at 50 °C) was observed whereas deposition at 65 °C leads to the formation of mounds with pyramidal shape. Single molecular DIP terraces are clearly visible on the pyramids with a step height of 16.64 ± 1.29 Å, which is characteristic for upright standing DIP. By further increasing the deposition temperature to 90 °C, a morphology transition to pronounced 3D islanding emerges. In this case, the mounds and 3D islands coexist. At an increased temperature to 95 °C, i.e. near the equilibrium condition, solely 3D islands formed. The islands have a narrow vertical height distribution of 30-50 nm and lateral size distribution of 3-6 μm. No DIP film has been detected by scanning among the islands. In addition, the friction difference between the islands and the surrounding surface confirms the absence of a DIP wetting film. The morphology transition as a function of the growth temperature results in a sudden increase of the RMS and of the lateral correlation length ξ, from 200 nm at room temperature to about of 2700 nm at 95 °C (figure 9.15 (f)).

When the sample grown at room temperature was annealed to 95°C for 1.5 hours, no post-annealing effect was observed. Therefore the introduced thermal energy is not enough to

mobile the DIP for the transition towards a 3D morphology. The 3D islanding appears to be due to a dynamical aspect of the growth process itself.

The occurrence of polymorphism, i.e. coexistence of difference crystalline phases, is rather common in organic films with dependence on the growth temperature. XRD measurements, performed on the same samples shown above in figure 9.15. Figure 9.16 (a) shows the X-ray diffraction data in specular geometry, providing information of the structure perpendicular to the surface. The first-order Bragg reflection and higher order reflections are observed for all the samples (with variations of 1% for the samples that grew at higher temperature). The diffraction peaks correspond to distance between molecular layers of 16.66 Å, in agreement with terrace height measured by AFM and the structure observation on bare SiO_2. The XRD measurement of sample grown at 95 °C is lack of Kiessig oscillation indicating the island growth consistent with AFM observation. GIXD experiments have been performed for three of the films (figure 9.16 (b)) yielding the same in-plane structure. DIP films that grew at 95 °C show a pronounced narrowing of the peaks indicating the formation of larger in-plane crystallites. The in-plane X ray measurement is resolution limited for experimental sake. Nevertheless it can be estimated that the main domain size increases from 270 Å to > 700 Å as the deposition temperature is increased from 35 °C to 95 °C, consistent with the large crystalline observed by AFM.

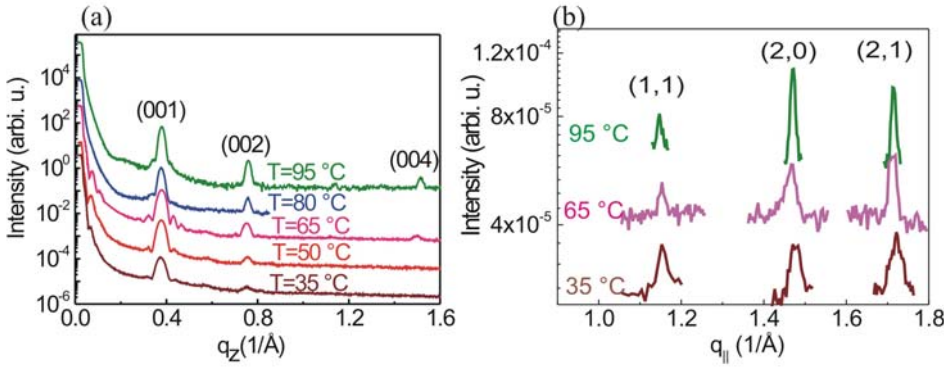

Figure 9.16: (a) X ray specular data for samples grown at different temperatures. The curves are shifted for the sake of clarity. (b) GIXD measurements for samples at substrate temperature 35°C, 65°C and 95°C.

Indeed, the faceted-like shape of the majority of DIP islands grown at 95ºC suggests the formation of single crystallites. By performing AFM molecular resolution imaging on the

islands, the DIP in-plane lattice structure is clearly observed. Measurements on different areas on the same island have been performed to determine whether one island consists of one or several orientated domains. Figure 9.17 shows an AFM image of one island and molecular resolution images taken on different islands. The equivalent lattice orientation of the DIP film in all the images indicates that the island are *single* crystalline. The lattice parameters obtained by Fourier transformation of the images have the dimensions of $(5.0 \pm 0.9$ Å$)*(5.0 \pm 0.9$ Å$)$, corresponding to the nearest distance between neighbouring DIP molecules, i.e along the [1,-1] or [1, 1] directions. The sides of the island is along the [0,1] and [1,0], [1,-1] or [1, 1] are observed in different islands. Thus the angles found between faces of DIP islands mainly have angles 90° or 60°-120° (along [1,-1]/[1,1] or [0,1]/[1,0] axis respectively). Considering a near equilibrium system, i.e. in a supersaturation condition, the shape of the crystal depends on specific surface free energies of different crystallographic orientations from a thermodynamic point of view in order to minimize the work of the formation of the crystal. The difference in surface energy for different DIP faces is probably small since, in our case, rich crystallographic faces are present.

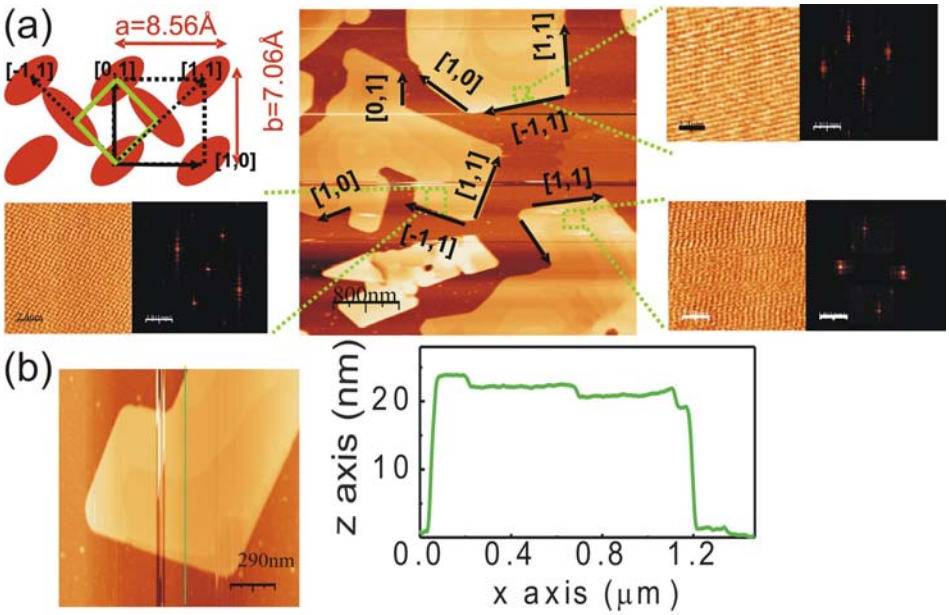

Figure 9.17: (a) The AFM image of one island grown at 95 °C. The molecular resolution images of one island. The images were measured from different terraces as shown in figure

and the inset shows the 2D Fourier transform of the images. (b) Topographic profile across the island.

Notice that SiO_2 covered by APS is supposed to favors the two-dimensional growth of the film due to a higher surface energy than SiO_2. In contrast to this prediction, we clearly observed a growth mode transition from a 2D film to island growth when going to near-equilibrium conditions (at high temperature). As reported in chapter 6, the growth of DIP on SiO_2 is of the above observed growth mode transition. Notice all the APS samples were stored in UHV for at least 3 hours and further heated up to 120 °C for one or two hours to avoid water moisture before the growth. Hence, the question that arises is whether the thermal treatment can have an impact on the SAMs of APS. The as-prepared APS samples were annealed at 120 °C for 1 hour, 5 hours and 24 hours respectively in UHV. AFM measurements performed under UHV condition without exposed to any impurities showed that the annealing induces bubbles-like structure leading to a considerable increase of surface roughness (figure 9.18). In addition, the contact angle of the APS film increased up to 69º (data summarized in table 1).

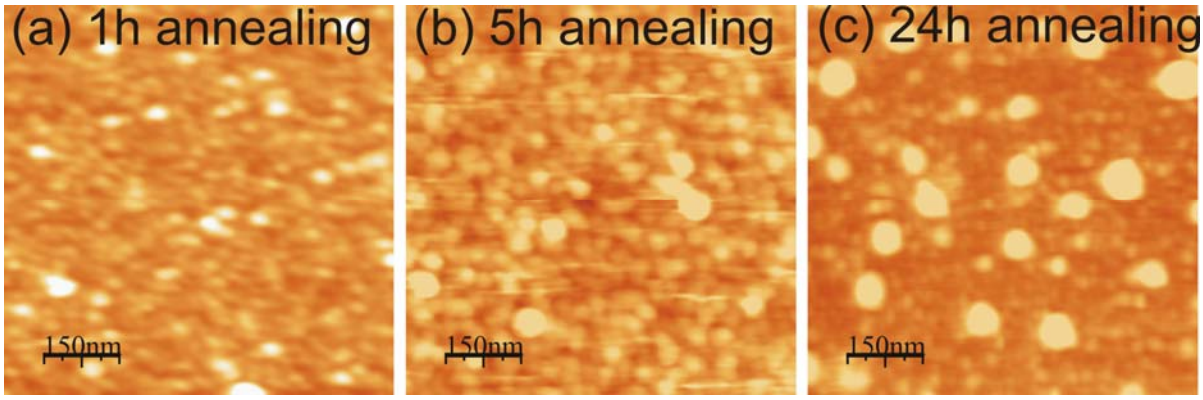

Figure 9.18: AFM images of APS film after different heating time: 1h (a), 5h (b), 24h (c).

APS film	freshly prepared	1h at 120°C	5h at 120°C	24h at 120°C
Contact angle (°)	26.39±0.45	50.39±0.97	59.92±1.39	67.76±0.79
RMS (Å)	1.4	6.2	9.2	12.1

Table 9.2: The contact angle measurements of APS film under different condition and corresponding roughness mean square calculated from AFM images.

Thus, these results unambiguously demonstrate that the APS film underwent morphological changes during the thermal treatment, which could be attributed to a dewetting of the two APS upper monolayers. The combined effect of increased roughness and decreased surface energy, promoting heterogeneous nucleation and higher molecular mobility, favoured 3D growth of DIP film at higher substrate temperature. Using SAMs as templates to functionalize the surface is rather common, whereas the effect of subsequent treatment on the SAMs before or during deposition of the organic thin films is rarely considered. However the change of physical and chemical properties of the SAMs, for instance, by aging effect, heating procedure or occurrence of possibly chemical reactions has un-neglected importance on the overlayer growth of organic thin films.

9.2.3 Conclusions

In conclusion, we have shown that thin films of DIP deposited on the APS terminated silicon wafers exhibit growth transitions from 2D growth to 3D growth at a deposition temperature of 90°. In spite of the different morphologies, X ray measurements reveal the same film structure. The transition gives rise to the formation of de-wetting film containing large high crystalline DIP islands. Molecular resolution images show that the islands are mono crystalline, with potential applications in electronic devices. Moreover, we emphasize the importance of the treatment of the APS before or during the growth. This growth mode transition of DIP film is clearly associated with the surface energy changes of the APS during the annealing of the substrates. We report a study on the growth of DIP, as example of organic semiconductor, on SiO_2 functionalized by an amina-terminated self-assembled monolayes (APS), by Atomic Force Microscopy and X-ray diffraction.

Due to insolubility of most high performance organic semiconductors, so far the majority of organic single crystal is manufactured by physical vapor transport, which suffers from a large variety of crystal size from tens of nanometer to several micrometers and further needs of transferring to build up devices. An alternative approach by choosing the suitable solution-processable organic materials is feasible but limits by few choices of organic materials and the crystal size grown by solution process are random and much smaller (limit by supersaturated solution concentration and volume transferred from the solution). We

demonstrate that the yielded DIP single crystals during the growth mode transition bearing potential applications for single-crystal field-effect transistors: The large micrometer size organic single crystal with well defined lateral separation are prefabricated OTFTs structures, one more step deposition of the electrodes result in real single organic crystal device without unexpected domain boundaries.

In addition, we emphasize the importance of the treatment of the APS before or during the growth: This growth mode transition of DIP film is clearly associated with the morphological and surface energy changes of the APS during the annealing of the substrates. Although using SAMs as templates to functionalize the surface is a rather common strategy today, the effect of subsequent thermal treatment before or during deposition of the organic thin films is rarely considered. This study shows that the change of physical and chemical properties of the SAMs by aging effect, heating procedure has important ramifications for the growth of organic thin films.

Chapter 10

Architecture design of organic-organic heterostructure

10.1 Introduction

Organic-organic heterostructure is the building block for modern rapid developed organic related electronics, for instance, organic solar cells, organic ambipolar transistors, OPV and OLEDs [156-160]. The first bilayer device that established the field of organic OPV was devised by Tang in 1986, which consisted of donor and acceptor layers deposited by sequential thermal vacuum sublimation of two small molecules. Unlike an inorganic photovoltaic device, efficient operation in an organic cell requires two semiconducting materials with a band-edge offset to split phonon-generated electron/hole pairs efficiently. The first bulk heterojunction solar cell was realized ten years later. This design allows for extraction of charges from a much larger volume of active material, increasing both light absorption and photocurrent. In single heterojunction cells, active organics normally direct contact to deposited electrode leading to quenching of excitons. The double or multiple heterojunction as an improved device architecture confines excitons within the active layers, thus allows substantially higher internal efficiencies to be achieved. Despite the rapid development of the electronics, the physical principles of the growth of the organic heterostructures and the relationship between the hetrostructal ordering and the device performance are in still in infancy.

In this chapter, taking advance of the in-situ X ray diffraction, by combining AFM measurements, we studied the structural and morphological properties of a few organic-

organic heterostructures. The systems under investigation include DIP-H_{16}CuPc, pentacene-PTCDI, H_{16}CuPc-F_{16}CuPc and F_{16}CuPc-pentacene. We aimed at understanding of the physics underlying the operation of single and multiple heterojunction, it is structural and ordering relationship.

The in-situ X-ray measurements were carried out either in-situ at ANKA synchrotron with a wavelength of λ = 1.2984 Å or at ESRF with a wavelength of λ = 1.54613 Å or ex-situ in house with a six circle high resolution diffractometer Cu (K_α) of λ = 1.5418 Å. The AFM measurements were performed with Nanotech in air. The substrate was held at certain temperature as experimental need during evaporation of films. All the organic molecules were thermally evaporated from Knudsen cells in sequence at a constant deposition rate of ~ 3 Å/min. Film thickness was monitored in-situ using a quartz crystal microbalance positioned near the substrate.

10.2 DIP and H_{16}CuPc heterostructure

The study of the bilayer structure DIP-H_{16}CuPc is motivated by recent study of DIP-F_{16}CuPc bilayers [161]. In the case of DIP on F_{16}CuPc heterostructure, DIP forms nanodots and a novel type of reconstruction of the underlying F_{16}CuPc film was revealed. The formation of the reconstructed F_{16}CuPc layer suggests a strong intermolecular interaction between DIP and F_{16}CuPc. In this part, instead of F_{16}CuPc, we used a close analog of F_{16}CuPc, H_{16}CuPc, to explore the interfacial properties of organic-organic heterostructure. The experiments were carried out at high and low substrate temperature respectively.

When deposited only 5 Å H_{16}CuPc on SiO_2 substrate, the in-plane Bragg reflection appears, corresponding to α phase H_{16}CuPc with lattice spacing of 12.295 Å, figure 10.1 (a) black curve. Upon DIP deposition, the in-plane structure of underneath H_{16}CuPc layer remains unchanged showing no structural rearrangement, which differs from the DIP-F_{16}CuPc heterostructure, where an obvious structural change of F_{16}CuPc layer were observed. The DIP thin film exhibits similar in-plane structure on an ultra-thin H_{16}CuPc film to that grown on bare Si. With increasing DIP coverage, the intensities of all the in-plane DIP peaks increase due to an increasing coverage. Moreover, the reflection peaks undergo a slightly shift: the lattice parameter develops from (a,b) = (8.578 Å, 6.783 Å) to (a,b) = (8.538 Å,

7.029 Å) with increasing DIP coverage from 20 Å (~ 1.2 ML) to 120 Å (~ 7.2 ML) respectively. The lateral domain size L exhibits similar value independent of the coverage (~ 155 Å), evidencing a similar morphology.

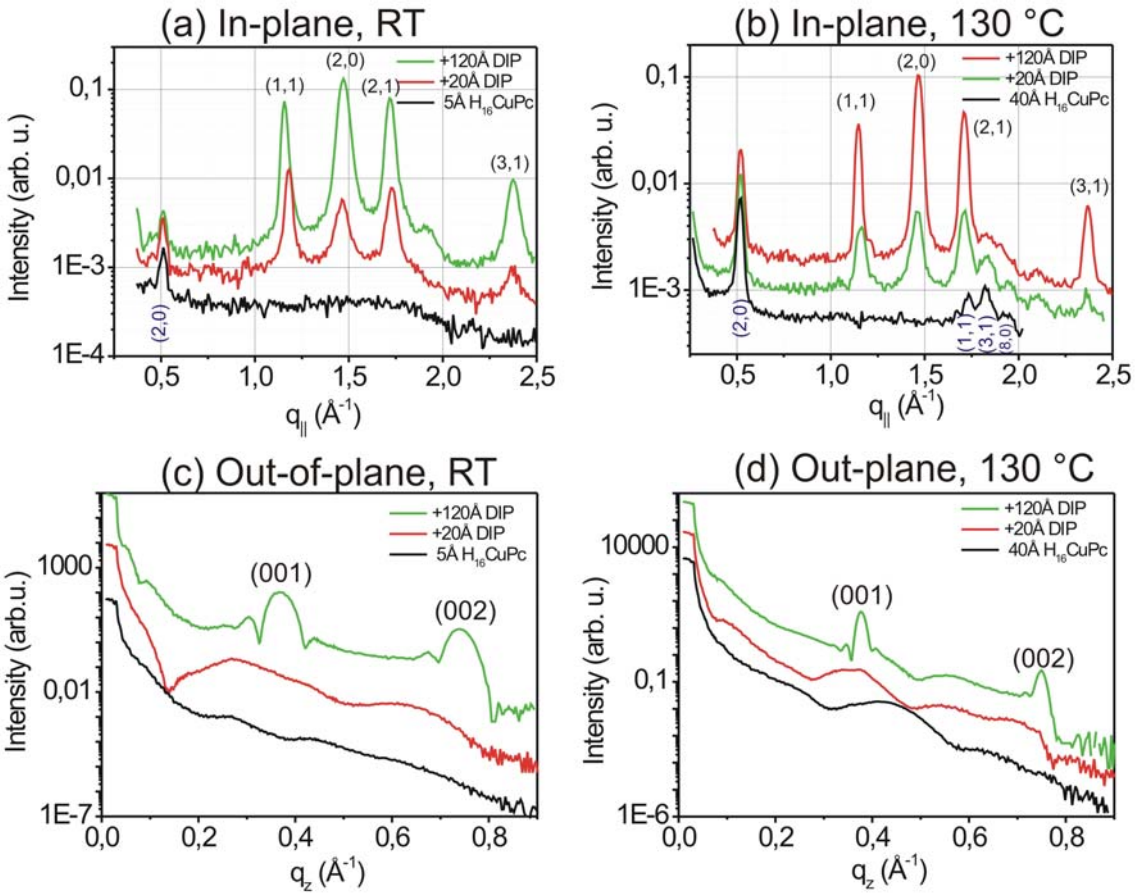

Figure 10.1: X ray in-plane and out-of-plane measurements of DIP and $H_{16}CuPc$ heterostructure at room temperature (a) (b) and 130 °C (c) (d) respectively.

We further performed the experiment at an increasing substrate temperature 130 °C, which is the optimized temperature for DIP growth. The $H_{16}CuPc$ film with 40 Å thickness shows ordering structure. The in-plane α phase lattice spacing is 12.153 Å, ~1 % compressed than the film grown at room temperature (notice increasing substrate temperature normally leads to an increase lattice parameter due to the thermal expansion). Respect to the in-plane measurements, three small peaks of $H_{16}CuPc$ film correspond to (1,1)/(1,0) at 3.62 Å, (3,1) at 3.45 Å and (8,0) at 3.23 Å can be observed, they are not visible in previous case due to very

thin H_{16}CuPc film, in turn, a low signal to noise ratio. The H_{16}CuPc structure is uninfluenced by present of DIP adlayer. The DIP in-plane Bragg reflections superimposed on H_{16}CuPc reflections are similar to those at substrate temperature 30 °C. Again a decrease of lattice parameter *a* and an increase of *b* were observed from (a,b) = (8.601 Å, 6.990 Å) to (a,b) = (8.565 Å, 7.129 Å) when increase DIP coverage from 20 Å to 120 Å. The structure changing of the DIP film on H_{16}CuPc could be an intrinsic character of DIP film when forming the interface with inert substrates. The early stage of growth of DIP on SiO_2 was discussed in detail in chapter 6 and we revealed a continuous structural change of in-plane lattice parameters with coverage. It is related to the interfacial interaction between SiO_2 and film, resulting to morphology transition from a layer-to-layer growth to rapid roughening growth.

The X ray reflectivity data up to the second Bragg peak at the substrate temperature 30 °C and 130 °C are shown in figure 10.1 (c) and (d) respectively. The H_{16}CuPc on Si has a very small mosaicity of 0.00662° at room temperature and 0.00685° at 130 °C, obtained from the rocking scan of the reflection. Independent of the substrate temperature the mosaicity upon deposition of DIP remains in the same order, indicating the well aligned molecule planes of the bilayers respect to the surface normal. When deposited DIP on H_{16}CuPc, DIP forms ordered film and the Bragg peak develops with increasing coverage. For the growth at room temperature, the interference fringes at low q value is clearly visible for a thick DIP/H_{16}CuPc bilayers, its period is slightly larger than the total film thickness (160 Å to 125 Å real) indicating a formation of islands with similar height on top of a smooth growth. The Bragg peak locates at $Q_z = 0.3699$ Å^{-1} corresponding to a standing-up configuration of DIP molecules with spacing 16.9854 Å, the obtained vertical domain size is ~177 Å. At a higher substrate temperature, the refection of DIP lacks of Kiessig fringes meaning a much rougher surface. The Bragg peak corresponds to DIP molecule with a d-spacing of 16.73 Å. Note the much narrower width, a vertical domain size of ~ 440 Å can be obtained, which is ~ 2.5 times larger than DIP thin film grown at room temperature. The lack of interference fringes and a very large vertical and lateral domain sizes evidence a SK growth mode. The lattice parameters and the corresponding domain sizes of DIP on H_{16}CuPc are summarized in table 10.1. For comparison, we list the corresponding lattice structures of DIP on bare SiO_2.

Another important issue is the growth mode. To monitor the growth mode of DIP thin film on H_{16}CuPc, we performed real time scan while DIP depositing on 40 Å H_{16}CuPc at room

temperature and the data is plotted in figure 10.2. The deposition rate is ~ 3 Å/min. The apparent oscillations up to 9 periods indicate a quasi layer-by-layer growth mode of DIP thin film. This observation is similar to the heterostructure of DIP/F_{16}CuPc, where a LBL growth mode was also reported.

	D (Å)	a (Å)	b (Å)	c (Å)	V (Å^3)	LD (Å)	VD (Å)	Mosaicity (°)
30 °C -CuPc	20	8.578	6.783	---	---	154.1	---	0.00681
	120	8.538	7.029	16.985	1018.86	162.6	176.7	0.00719
130 °C -CuPc	20	8.601	6.990	---	---	131.7	---	0.00686
	120	8.565	7.129	16.733	1021.69	191.2	436.9	0.00700
30 °C -SiO_2	10	8.621	6.763	---	---	143.6	---	---
	115	8.572	6.984	16.989	1017.08	198.8	231.1	0.00596
120 °C -SiO_2	10	8.641	6.807	---	---	174.3	---	---
	110	8.573	7.107	16.900	1021.56	225.1	178.1	0.00596

Table 10.1: Lattice parameters and the corresponding lateral, vertical domain size and mosaicity of the DIP on H_{16}CuPc (as –CuPc)or on SiO_2 (as –SiO_2) at different substrate temperatures.

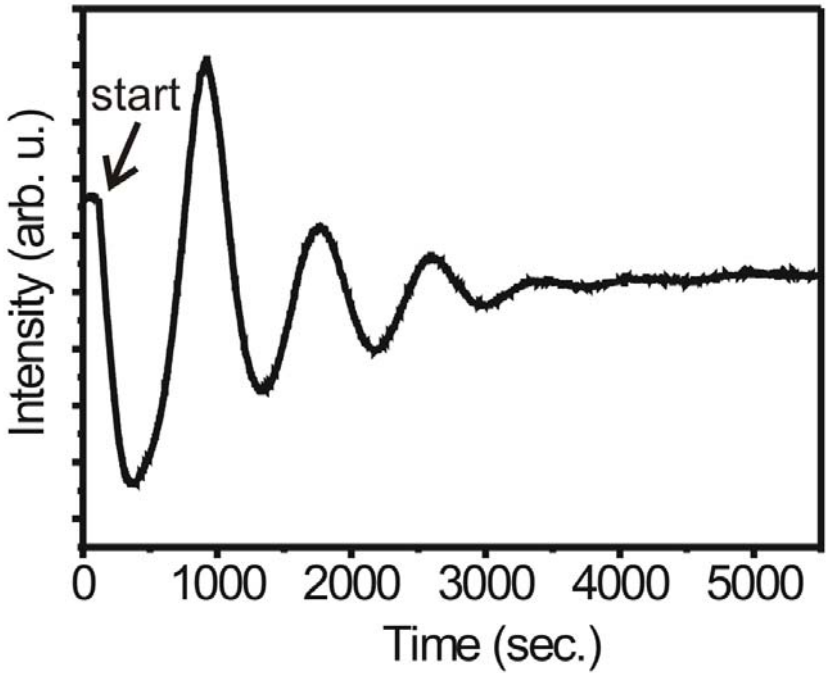

Figure 10.2: X ray time scan measurement of DIP on 40 Å H_{16}CuPc at RT.

For the growth mode of DIP thin film grown at high substrate temperature, we rely on the ex-situ AFM measurements. A series of samples were grown at the same condition as the X ray measurements, that is with increasing DIP coverage (10 Å, 30 Å, 60 Å and 110 Å) on top of 40 Å $H_{16}CuPc$ at growth temperature of 130 °C. AFM images show an SK growth mode consistent with X-ray measurements. DIP molecules form ordered organic dots with well defined size are summarized in Figure 10.3. Increasing the coverage initially increases the density of these dots and they grow in both vertical and lateral directions. Roughness mean square value as a function of the DIP thin film coverage is shown in figure 10.3 (e). The characteristic average size and height of DIP nano-dots are plotted in figure 10.3 (f) as triangle and star respectively. The formation of these dots is very similar to the bilayer structure of DIP on top of $F_{16}CuPc$. Considering the complex scenario of DIP growth on SiO_2, the structure change of DIP is difficult to attribute to the underneath layer, rather than its intrinsic behavior when grown on inert substrates. However, to figure out these issues clearly need more experimental and theoretical work. Recent report of STM study revealed that DIP and $F_{16}CuPc$ formed highly interacting H-F bonds when co-evaporation on Au or Cu single crystal [250]. The DIP and $H_{16}CuPc$ interact weakly through van der Waals force at the interfacial layer, therefore absence of the $H_{16}CuPc$ reconstruction. We summarize the growth modes of heterostructures of DIP/$H_{16}CuPc$, DIP/$F_{16}CuPc$ and DIP/SiO_2 in table 10.2, where by using a thin buffer layer, the growth mode is more kinetically driven and shows a transition from LBL to SK growth.

Growth mode	DIP on SiO_2	DIP on $F_{16}CuPc$	DIP on $H_{16}CuPc$
RT	LBL→SK	LBL	LBL
130 °C	LBL→SK	SK	SK

Table 10.2: Growth mode comparison of DIP grown on different substrates.

As a conclusion, in this section we studied the structure and growth mode of organic heterostructure DIP/$H_{16}CuPc$ on SiO_2. The heterostructure of DIP/$H_{16}CuPc$ shows similar growth mode transition to DIP/$F_{16}CuPc$ heterostructure from LBL (RT) to SK (130 °C) as detected by in-situ X-ray real time scan and ex-situ AFM measurements respectively. Unlike $F_{16}CuPc$, the structure of template layer $H_{16}CuPc$ remains the same upon the deposition of

DIP thin film due to weak van der Waals interaction between $H_{16}CuPc$ and DIP molecules. DIP thin film shows structural change as a function of thickness, which is also observed in the heterostructure DIP/$F_{16}CuPc$ and DIP grown on bare SiO_2.

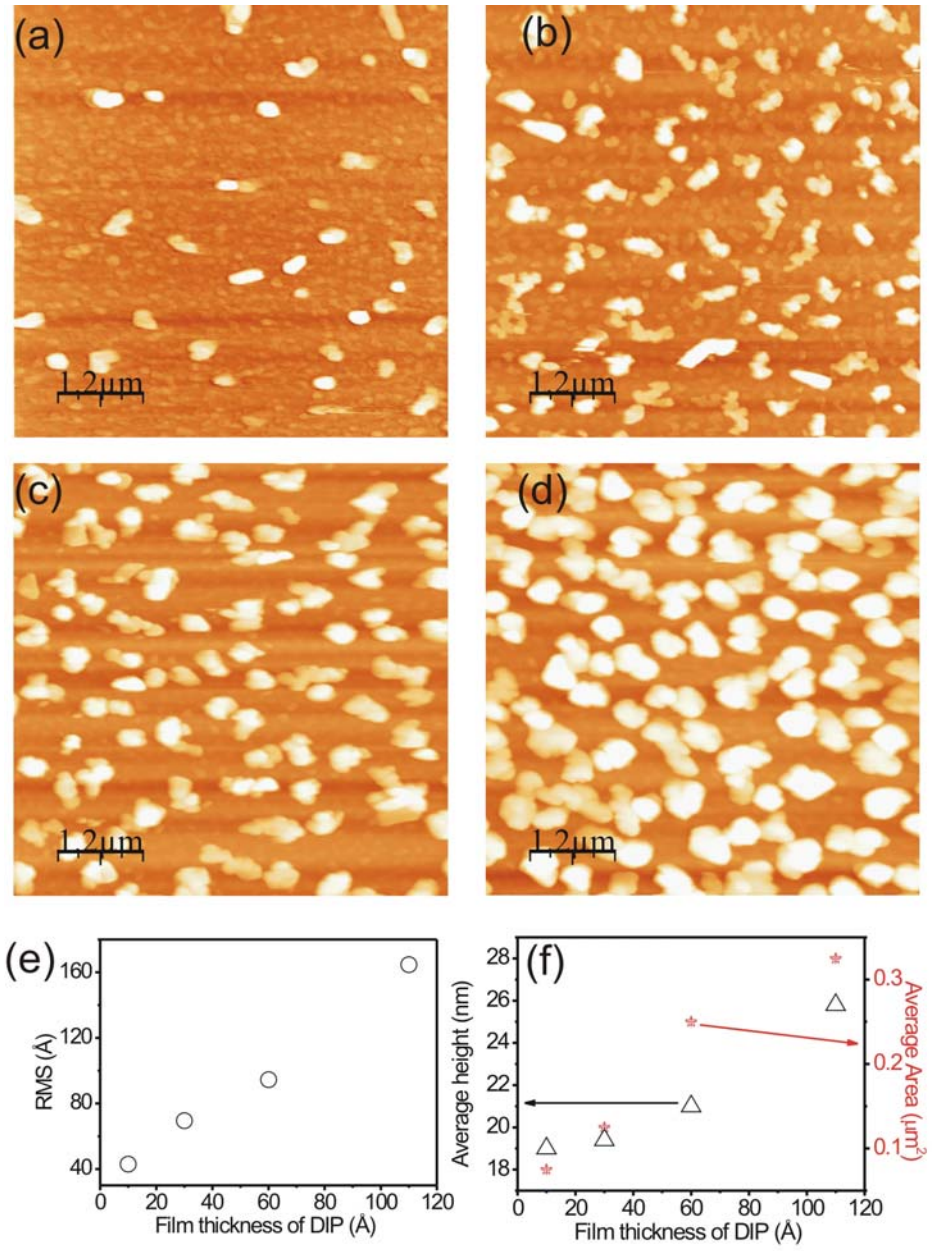

Figure 10.3: AFM images of increasing DIP coverage (a) 10 Å, (b) 30 Å, (c) 60 Å and (d) 110 Å on top of 40 Å $H_{16}CuPc$ template layer at 130 °C. (e) Evolution of the roughness mean square as a function of the DIP film thickness. (f) The average dots height and dot area as a function of the DIP thin film coverage.

10.3. F_{16}CuPc and H_{16}CuPc heterostructure

The bilayer structures of p-type H_{16}CuPc and it fluorinated analogue, n-type F_{16}CuPc form a donor/acceptor heterojunction with exciton separation at the heterointerface for application in photovaltacics devices. Moreover, OTFTs based on this heterostructure showed the ambipolar characteristics [162-163]. Belonging to phthalocynine group, H_{16}CuPc and F_{16}CuPc display many similarities: molecular shape, structure and charge carrier mobilities. In addition, it has been highlighted recently that the ambipolar characteristics has a strong correlation with relevant thickness of two active organic semiconductor layers. As structure and morphology are of crucial importance for high-performance ambipolar OFETs; and therefore a throughout understanding of the relationship between the structure ordering and film thickness is essential for producing controllable architectures. In this section, we performed in-situ X ray study of H_{16}CuPc/F_{16}CuPc and F_{16}CuPc/H_{16}CuPc heterostructures to find out acquired knowledge of these influences. Microstructure and ordering characteristics are intimately correlated to the thickness of underneath buffer layer. The formation of the interface layer is accompanied with structural reconstruction of the underlying organic film, which further affects ordering of the overlayer. By controlling deposition order and relative film thickness of the bilayers, we tuned the heterostructures from an amorphous film to an ordered one. We propose suggestion for optimization of performance of the practical devices.

Figure 10.4 shows X ray measurement in specular and grazing incident geometries of 100 Å thick F_{16}CuPc layer on top of H_{16}CuPc films with different thicknesses, i.e. 40 Å (3 ML), 150 Å (11 ML) and 600 Å (45 ML). H_{16}CuPc film on Si substrate shows highly crystallinity and its (002) out of plane Bragg peak locates at $q_z = 0.484$ Å^{-1}, corresponding to a layer spacing of nearly upright configuration 12.979 Å (a = 25.9577 Å). Unlike F_{16}CuPc, which shows a complex structure scenario grown on SiO_2 (a disordered interfacial layer → ~ 2 ML $\beta_{bilayer}$ → rearranged $\beta_{bilayer}$ then finally β phase above 14 ML with increasing film thickness), H_{16}CuPc exhibits single α structure phase with increasing coverage: 3 ML and 45 ML thick H_{16}CuPc films show the same in-plane structure. During deposition of F_{16}CuPc/H_{16}CuPc heterostructure, Kiessig fringes always reveal the whole film thickness of H_{16}CuPc

(+F_{16}CuPc), which evidences a smooth growth of both H_{16}CuPc on Si and F_{16}CuPc on top of H_{16}CuPc. F_{16}CuPc shows specular ordering on an ultra thin H_{16}CuPc film and its Bragg peak develops with increasing coverage, positioned at $q_z = 0.439$ Å^{-1}, corresponding to 14.31 Å (standing up molecule) in real space, similar to the previous work of F_{16}CuPc grown on bare Si wafer. The out-of-plane order of F_{16}CuPc overlayer suppresses with thicken H_{16}CuPc buffer layer. For a H_{16}CuPc film thickness of 11 ML, only a slight order of F_{16}CuPc film can be observed from asymmetric shape of H_{16}CuPc Bragg peak associating with a small intensity enhancement upon F_{16}CuPc deposition. No specularordered structure of F_{16}CuPc can be obtained for heterostructure 100 Å F_{16}CuPc on 600 Å H_{16}CuPc, which is a more ideal condition for F_{16}CuPc/H_{16}CuPc (the substrate influence can be neglected). Accompany with continuous disordering out-of-plane procedure of F_{16}CuPc, the Laue oscillation (coherently ordered film) reveals in Fig 10.4 (c) the sum film thickness of H_{16}CuPc (+F_{16}CuPc), in Fig 10.4 (b) H_{16}CuPc (+partial F_{16}CuPc) and H_{16}CuPc in Fig 10.4 (a) respectively. Distribution of normal vector (mocaicity) of the film can be probed by a rocking scan on the position of the (001) Bragg peak. Mocaicity is in the magnitude ~ 0.008° for single layer and bilayers deposition indicating an excellent microscopic alignment respect to the surface normal.

The in-plane structures were probed extensively by employing GIXD measurements, and the results is plotted in Fig 10.4 right part. H_{16}CuPc on bare Si substrate shows α phase with in-plane lattice parameter a = 24.10 Å, b = 3.70 Å, $\beta = 90.4°$ which are ~7 % and ~2 % less than the reported unit cell constants [164]. Besides the main peaks, the lattice spacing of 12.59 Å and 6.66 Å are also observed. No unit cell rearrangement of H_{16}CuPc was found by the presence of F_{16}CuPc overlayer. Deposition of F_{16}CuPc on top of H_{16}CuPc affects remarkable the X ray intensity of underneath H_{16}CuPc layer. A clear decrement of intensity of H_{16}CuPc (0,2,0) peak with increasing F_{16}CuPc coverage can be observed. The contribution from absorption of F_{16}CuPc capping layer on X ray intensity can be neglected since coefficient β of F_{16}CuPc is around 2.2×10^{-7} (calculated from ref. 64). Moreover, the absorption may decrease intensities of all peaks of H_{16}CuPc, which is not consistent with our experimental results: for thick H_{16}CuPc layer, the intensity of (0,2,0) peak decreases by 10 %, while those of (1,0,0) and (1,3,0) peaks enhance by 100% and 225 % after deposition of F_{16}CuPc. In addition, the enhancement of intensity is not due to the superposition of the Bragg peaks from the top F_{16}CuPc layer.

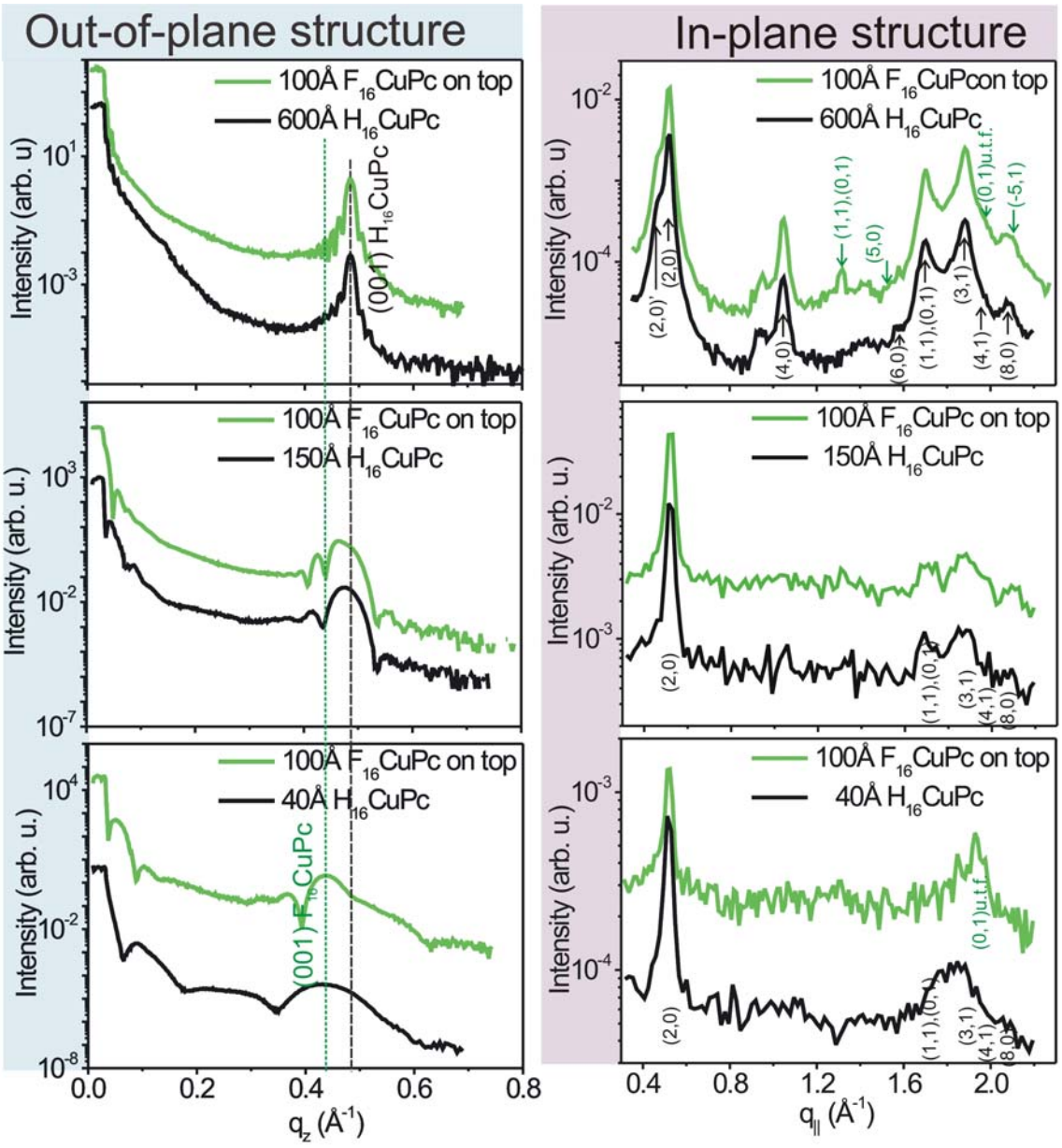

Figure 10.4: X ray specular measurements and X ray grazing incident measurements of 100 Å $H_{16}CuPc$ on $F_{16}CuPc$ buffer layers at RT.

Possible explanation lies on those $F_{16}CuPc$ molecules at the interfacial layer rearrange the underlying $H_{16}CuPc$ layer. The reconstructed $H_{16}CuPc$ molecules adopt new orientation without altering the shape of unit cell, but in turn bring out the intensity variations due to the changed structure factor. In contrast to general belief that the ordering of the thin film at the

interface rarely influenced by the crystalline morphology since most of these van der Waals bonded materials do not require lattice matching to form ordered structures, the rearrangement of molecule orientation within unit cell as a function thickness were observed experimentally in a few organic thin film systems, for instance, F_{16}CuPc and pentacene. Detailed analysis of the diffraction data discloses the impact of substrate on an ultra-thin H_{16}CuPc. Interaction between SiO_2 substrate and H_{16}CuPc film dominates in the first H_{16}CuPc layers and tends to remain the initial thin film structure of H_{16}CuPc, leadinf to a thinner interfacial layer, notice that the integrated intensity of (0,2,0) Bragg peak reduces to 55 % of initial intensity for the first capping layer of 50 Å thick, while monotonically decreases to 41.753 % and 34.906 % for the capping layer of 100 Å and 150 Å thickness, respectively. For an ultra-thick H_{16}CuPc film, the influence of substrate is weak and negligible and the effect of interfacial layer dominates: little in-plane ordering of F_{16}CuPc overlayer was observed and its out-of-plane ordering was suppressed with increasing thickness of underneath H_{16}CuPc film.

Figure 10.5 illustrates the heterostructure of inverted order, i.e. using F_{16}CuPc as template layer. F_{16}CuPc film on Si shows crystalline feature and its (001) out of plane Bragg peak corresponds to layer spacing of 14.3 Å (upright configuration) [64]. The development of out of plane structure shows similar tendency as its inverse analogue: Kiessig fringes always reveal the whole film thickness of H_{16}CuPc (+F_{16}CuPc) evidencing a smooth growth mode. F_{16}CuPc shows specular ordering on top of an ultra thin but not on a thick F_{16}CuPc buffer layer.

The in-plane structure of F_{16}CuPc film is similar to that reported before. By deposition of 100 Å H_{16}CuPc on an ultra thin and a thick templating F_{16}CuPc film respectively, H_{16}CuPc shows well ordered in-plane structure associating with a decreasing in-plane peak intensity of underneath F_{16}CuPc layer. The energy changing can be understood by same speculation: counterbalance between structure modification and influence of substrate results in of ~ 1 ML resident structure ordering for a 35 Å thick F_{16}CuPc film. Again a suppression of out-of-plane ordering was observed with increasing underneath buffer layer thickness.

To elucidate the structure changing, we employed further experiment on the thick films of heterostructures: sample a of F_{16}CuPc 480 Å on H_{16}CuPc 340 Å (Fig 10.6 (a)) and sample b of H_{16}CuPc 340 Å on F_{16}CuPc 480 Å (Fig 10.6 (b)). AFM images of a and b samples reveal

similar roughness, ~ 48 Å and ~ 40 Å respectively. In addition, small differences of morphologies are addressed: sample a shows elongated worm like domains; while sample b shows a round shaped small domains. Outstanding in-plane and out-of-plane ordering of F_{16}CuPc buffer layer and H_{16}CuPc overlayer was observed in sample a, in-plane Bragg peaks of F_{16}CuPc $(0,1)_{u.t.f}$ is clearly visible. And the two out-of-plane Bragg peaks at q_z=0.433 $Å^{-1}$ with halfwidth = 0.0254 $Å^{-1}$ and q_z = 0.484 $Å^{-1}$ with halfwidth= 0.0117 $Å^{-1}$ correspond to H_{16}CuPc with layer spacing of 12.98 Å (vertical domain size of ~ 248 Å) and F_{16}CuPc with layer spacing of 14.51 Å (vertical domain size of ~ 537 Å). However, for sample a only in-plane ordering of H_{16}CuPc is observed and heterostructure H_{16}CuPc/F_{16}CuPc only shows Bragg peak of H_{16}CuPc locates at q_z=0.479 $Å^{-1}$ with halfwidth of 0.0116 $Å^{-1}$ correspond to a layer spacing of 13.12 Å. Coincide with the in-situ X ray diffraction measurement from figure 10.4.

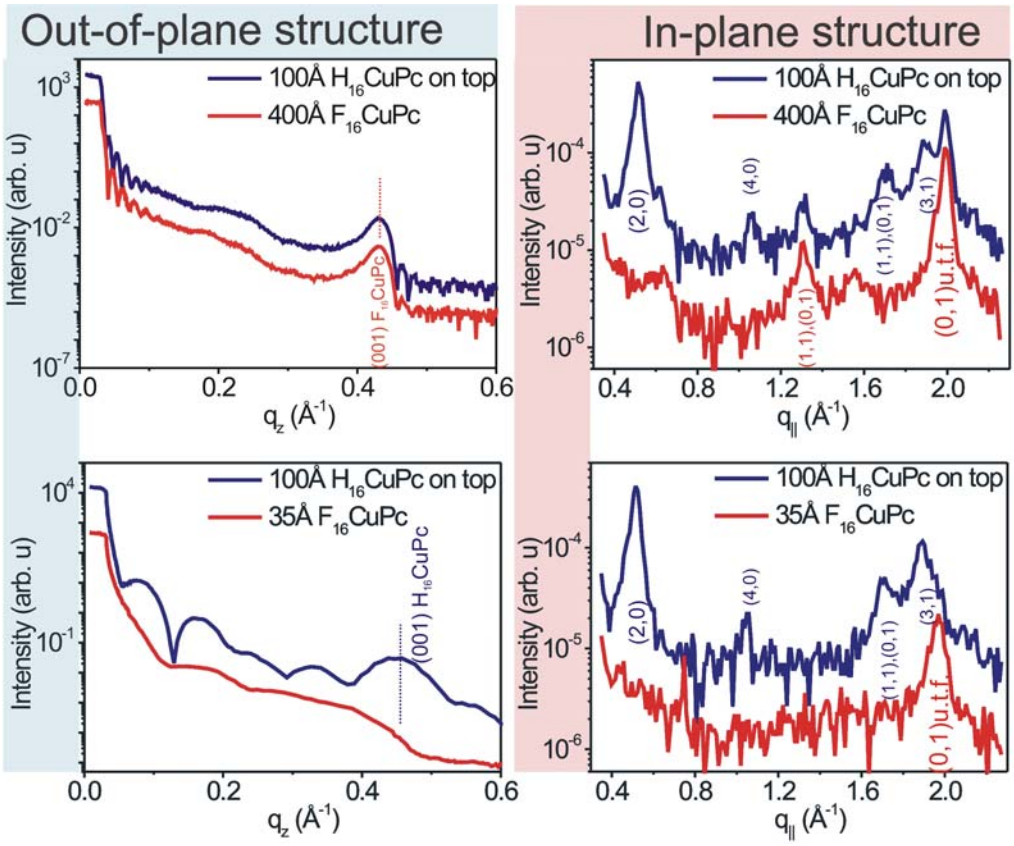

Figure 10.5: X ray specular measurements and X ray grazing incident measurements of 100 Å F_{16}CuPc on different thickness of H_{16}CuPc buffer layer at RT.

We present a schematic summary of the effect of the template layer on the ordering of the adlayer of heterostructure of $H_{16}CuPc/F_{16}CuPc$ and $H_{16}CuPc/F_{16}CuPc$ at room temperature (figure 10.7). From observed results, we suggest a thin $F_{16}CuPc$ buffer layer exhibits ordering structure which carry the potential to induce higher charge mobility in the design of organic electric devices. The change of OTFTs character from an N type to an ambipolar type by tuning the film thickness of $F_{16}CuPc$ has been previous reported by Wang et al in their study of heterostructure $H_{16}CuPc/F_{16}CuPc$, which may be closed related to the change of its structure ordering or the built up of interfacial layer.

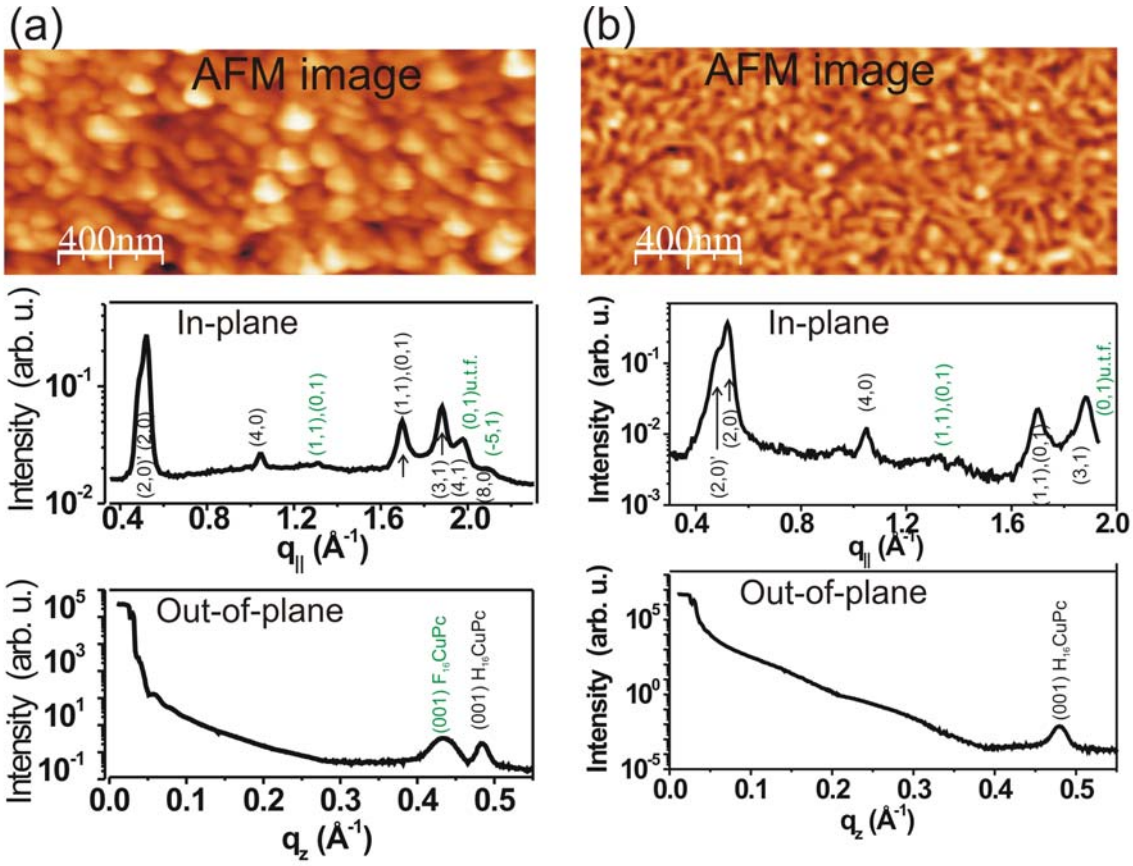

Fingure 10.6: AFM and X ray diffraction measurements of (a) 340 Å $H_{16}CuPc$ on 480 Å $F_{16}CuPc$ at RT and (b) 480 Å $F_{16}CuPc$ on 340 Å $H_{16}CuPc$.

As a summary, structure and ordering properties of organic-organic $F_{16}CuPc$ and $H_{16}CuPc$ heterostructures were investigated by combing in-situ X ray diffraction and AFM

measurements. We demonstrate that structure and ordering are strongly correlated with the component and thickness of underneath buffer layer. The observed phenomena can be explained qualitatively in terms of the formation of interfacial layer and the influence of the substrate. The formation of interfacial layer strongly affects further the structural and ordering properties of the overgrown layer. The present results suggest that in the architecture of F_{16}CuPc and H_{16}CuPc p-n junctions, a thin F_{16}CuPc film always introduces ordered structure of the heterostructure and should be chosen as buffer layer in design steps for optimization of the performance of OFETs.

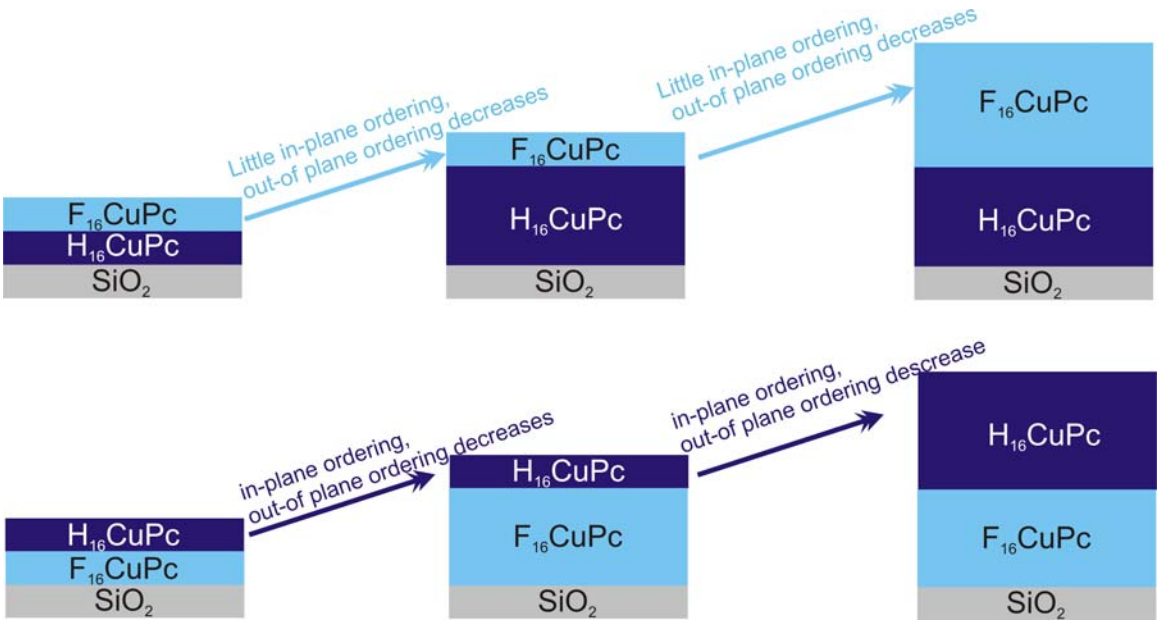

Fingure 10.7: Schematic summary of the effect of the template layer on the ordering of the adlayer of heterostructure of H_{16}CuPc/F_{16}CuPc and H_{16}CuPc/F_{16}CuPc at room temperature.

10.4. Pentacene and PTCDI heterostructure

In this section, we extend the study to the pentacene/PTCDI and pentacene/PTCDI heterostructures. We use SiO_2 and Al_2O_3 as substrates to explore the structure and the ordering properties.

10.4.1 On SiO_2

PTCDI deposited on SiO_2 substrate at room temperature shows in-plane ordering structure, the calculation from the positions of in-plane peaks gives an unit cell of a = 10.14212 Å, b = 4.82704 Å and θ = 66.94997°. The lattice parameters of PTCDI show small difference between a thin film (66 Å) and a thick one (400 Å), 0.6 %, 0.2 % and 0.1 % for a, b and θ respectively by using the value of the thick film as reference (figure 10.8). We conclude that PTCDI presents constant lattice parameters with increasing thickness within the error bar of thousand percentages. The d-spacing of the film derived from a thick film is at 20.577 Å.

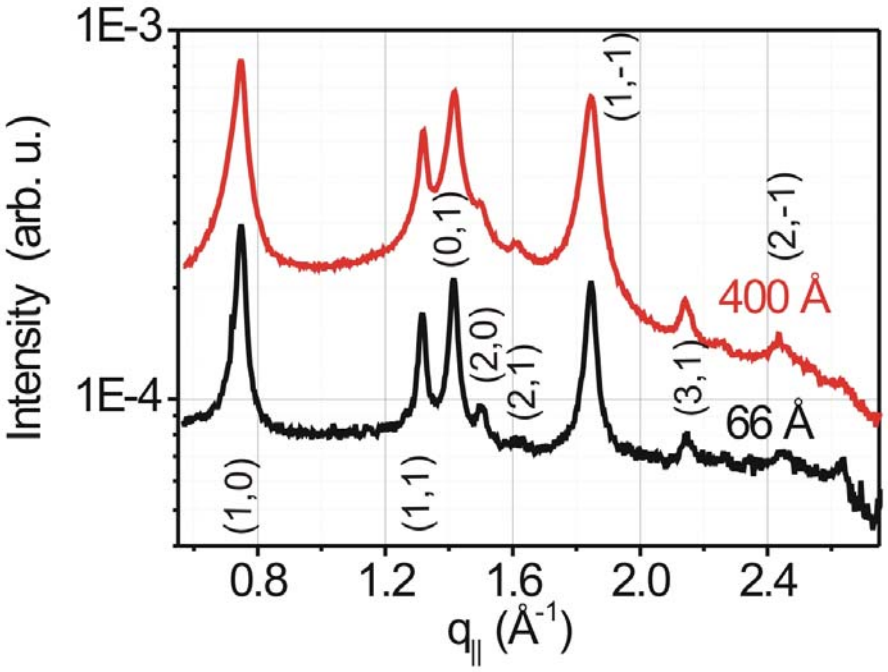

Figure 10.8: GIXD measurements of PTCDI as a function of coverage at substrate temperature of RT.

Figure 10.9 (a) black curve (the labels of different peaks shown underneath the curve) shows the GIXD measurements of 65 Å PTCDI deposited on SiO_2 substrate at room temperature. Depositing pentacene on top, the lattice parameters of PTCDI keep unchanged. The pentacene adlayer exhibits in-plane structure of a = 5.947 Å, b = 7.60 Å and θ = 89.01°, which is similar to that grown on bare Si (figure (a) red and blue curves). With increasing pentacene adlayer thickness, the intensities of pentacene continuous increasing, while the intensity of PTCDI layer decreases. The lateral domain size of pentacene of two step

depositions increases from ~ 480 Å to ~ 600 Å for 30 Å and 120 Å pentacene. The out-of-plane measurement shows no out-of-plane ordering of pentacene layer, figure 10.9 (b).

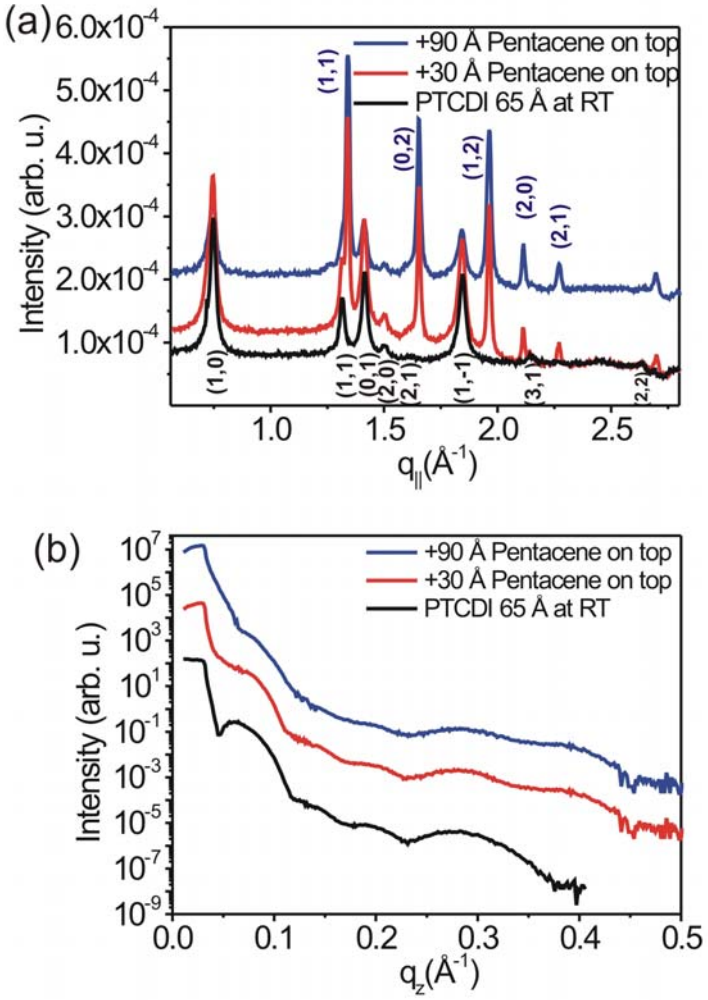

Figure 10.9: X ray measurements of organic heterostructure of pentacene on PTCDI by using SiO_2 as substrates (a) in-plane X ray measurements (b) specular X ray measurements.

By growing the samples at the same condition, we further performed ex-situ AFM measurements as complimentary method to check the growth mode. The results are summarized in figure 10.10. Pentacene forms homogenous small grains on PTCDI layers at room temperature. The AFM images in phase mode show the lack of pentacene wetting layer (figure 10.10 (a) and (b)) evidenced by pronounced friction difference. With increasing pentacene thickness from 30 Å to 120 Å, the film shows similar morphology and the grains

grow in lateral and vertical directions. The corresponding profile shows these small grains have an average height of ~ 15 nm and an average lateral size ~ 500 nm for a 30 Å thick pentacene layer. At a coverage of 120 Å pentacene, the grains have an average height of ~ 32 nm and an average lateral size ~ 1.1 μm. Figure 10.10 (c) summarizes the height distribution of the individual images, from which an increasing islands height from can be clearly disclosed (the height of the underneath PTCDI film is shifted as 0 nm). Figure 10.10 (d) gives the lateral distribution information of the islands.

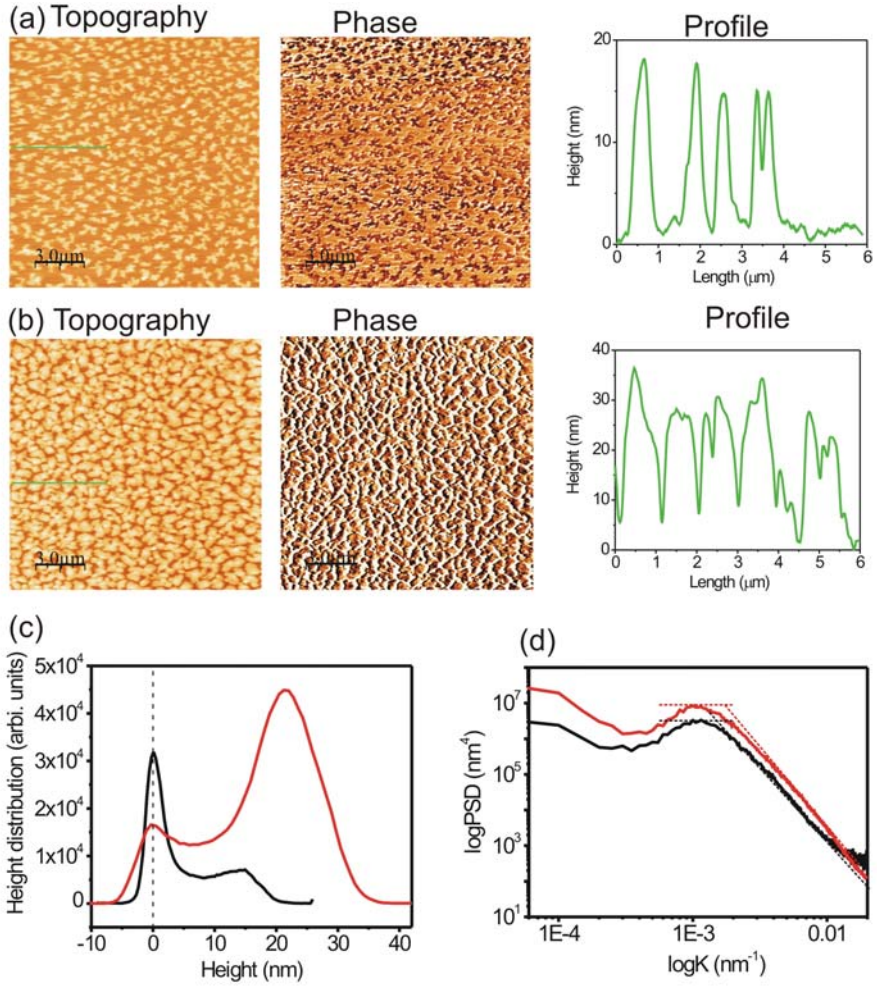

Figure 10.10: AFM topographical images (left) and the corresponding phase images (middle) of (a) ~ 30 Å and (b) ~ 120 Å pentacene on 65 Å PTCDI at room temperature. The profile corresponds to the green line are plotted as green lines on the right. Figure (c) shows the height distribution of the images (the average height of PTCDI is set as 0 nm). Figure (d) shows the lateral information of the images.

By increasing the substrate temperature while deposition of PTCDI, an increasing ordering of pentacene adlayer was observed. The X ray diffraction measurements of around 120 Å pentacene on a thin layer of PTCDI at 150 °C is plotted as figure 10.11. Pentacene has an in-plane lattice parameter of a = 5.947 Å, b = 7.601 Å, θ = 89.88°. The reflectivity Bragg peak of pentacene locates at 0.392 $Å^{-1}$, corresponding to a layer spacing of 16.029 Å, this value however is ~ 3 % larger than pentacene on SiO_2 substrates, which normally gives spacing of 15.566 Å. The complementary AFM data are summarized in figure 10.12.

Figure 10.12 (a) and (b) gives large size images of ~ 40 Å and ~ 120 Å pentacene on an untra-thin PTCDI layer (30 Å), from which we observe very similar morphology, thus the morphology of the PTCDI buffer layer essentially decide the subsequent pentacene adlayer. The zoom in images gives a detail morphology information, from which mount structure and coverage difference are clearly observed, figure 10.12 (c) and 10.12 (d). The formation of mound structure indicates an obvious improvement of the ordering from the small 3D domains to ordered mount-like structure, comparing of the pentacene thin films grown on the room temperature deposited PTCDI buffer layer. The terraces have obvious facets with the angle ~ 90°, ~ 60°, ~ 120°, which indicate the edges along the [1,1], [0,1], [1,0] and [1,-1] directions. The height profiles (figure 10.12(e) and (f)) between individual layers give a similar height of ~ 16 Å, consistent with the height of pentacene from X ray measurements.

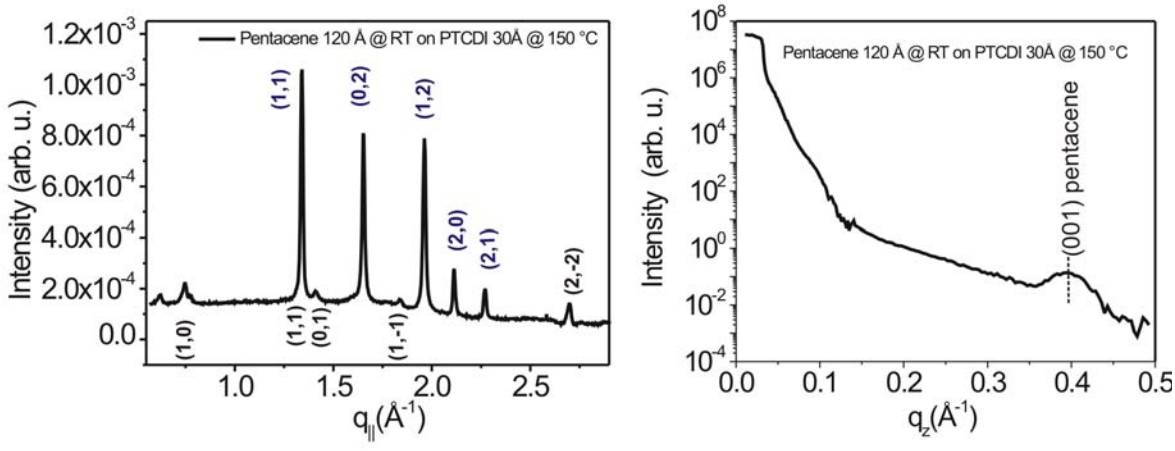

Figure 10.11: X ray diffraction measurements of deposition of around 120 Å Pentacene on a thin layer of PTCDI at 150 °C.

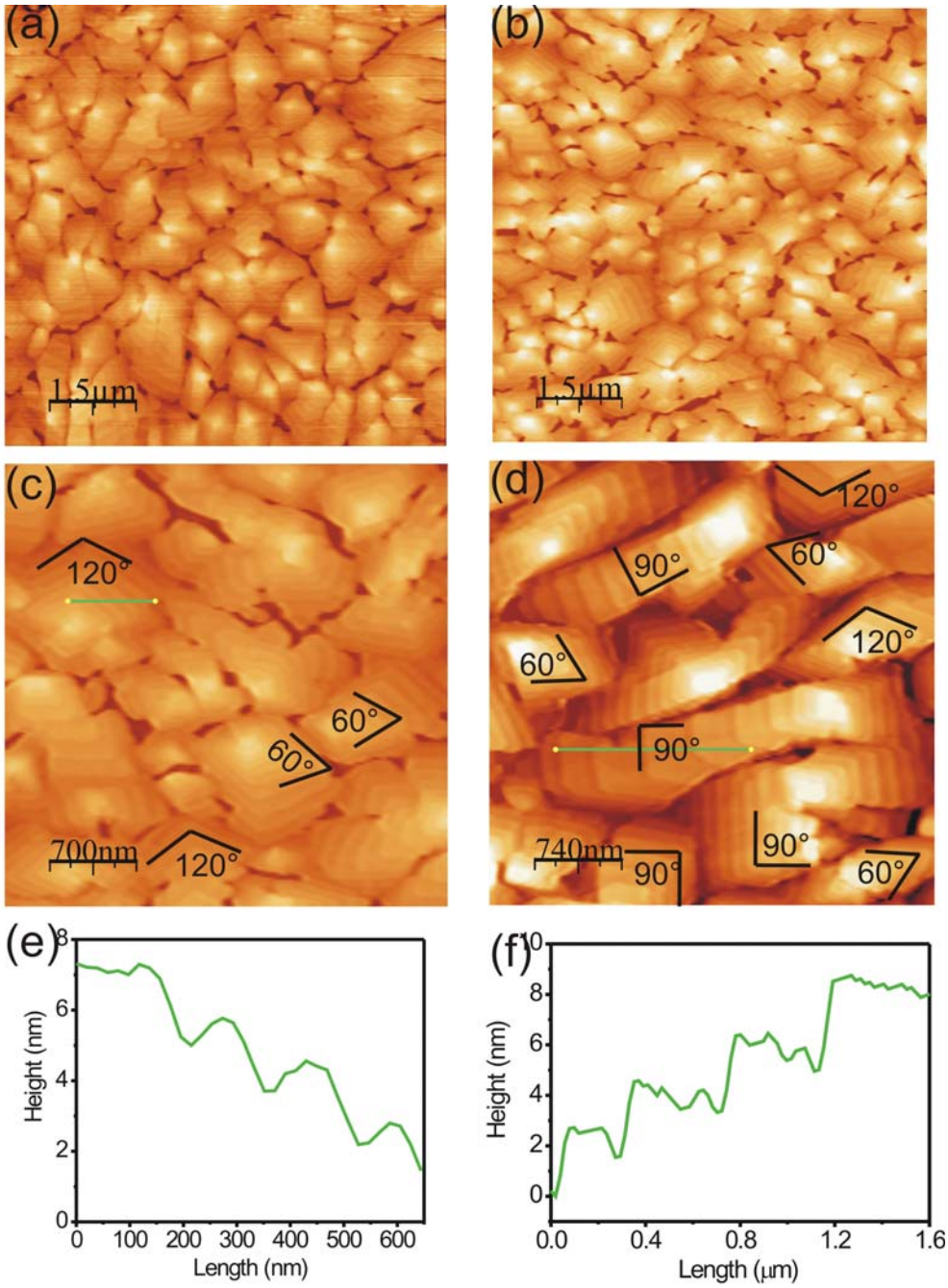

Figure 10.12: AFM images of (a) ~ 40 Å (a) or (b) ~ 120 Å pentacene thin film on ~ 30 Å PTCDI at 150 °C, which the morphology of the underneath PTCDI buffer layer guides the general morphology of subsequent pentacene adlayers; (c) and (d) are enlarged images, which shows the pentacene terraces with well defined angles of 90°, 60° or 120°; the monolayer height can be clearly indentified in the profile figures (e) and (f) respectively.

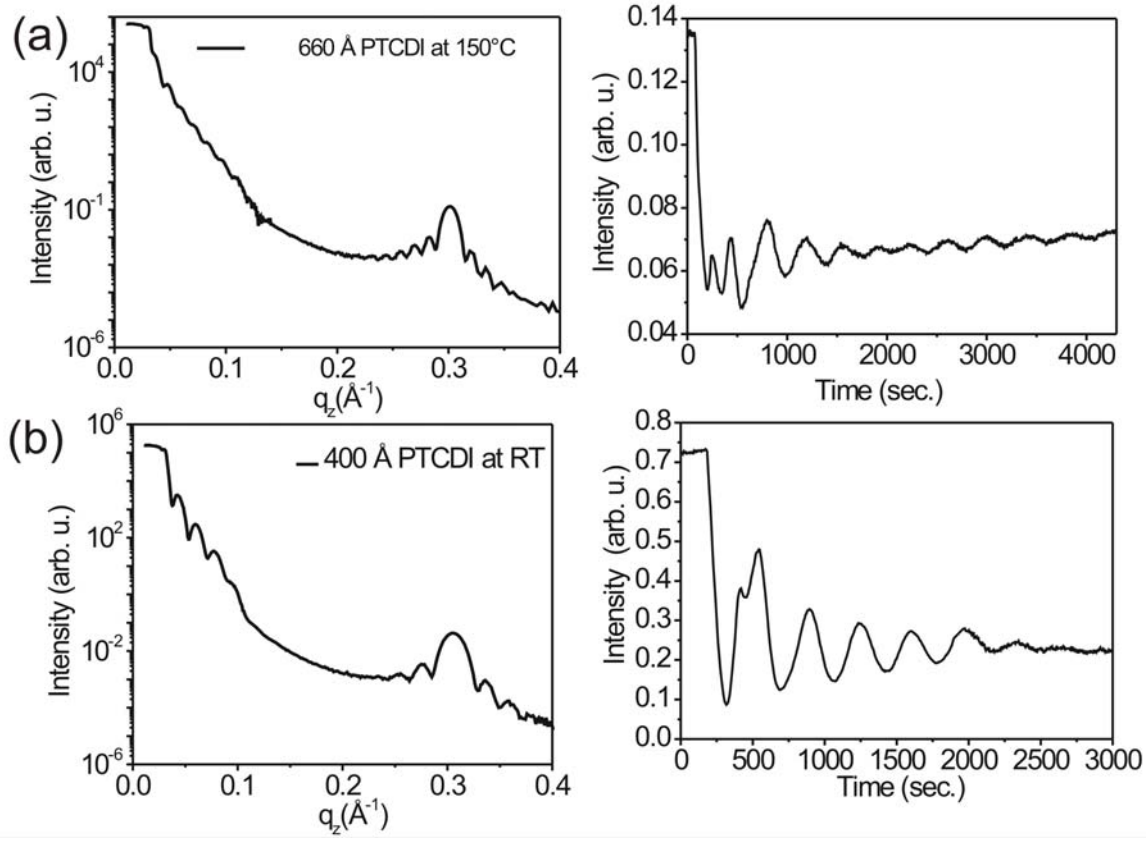

Figure 10.13: The X-ray reflectivity (a) and (b) real time (b) measurements of PTCDI grown at different substrate temperature. The real time measurement stopped only when no obvious oscillation can be observed, the film grown at 150 °C shows pronouns "layer-by layer" feature.

The deposition temperature of pentacene in both cases was fixed at room temperature, so the observed effect is only relative to the properties of the buffer layer. The morphologies of the PTCDI grown at RT and 150 °C are very similar (larger domains at higher substrate temperature). To test the morphology and structure difference of PTCDI buffer films we performed reflectivity and real time scan measurements. The growth mode difference of PTCDI thin film grown on different substrate temperature was monitored by in-situ real-time XRD measurements at the anti-Bragg point $q_z = \pi / d$, where d is d-spacing of PTCDI thin films. The anti-Bragg point of PTCDI grown on SiO_2 is lack of Kiessig oscillation, therefore ideal for probe the intensity difference. The scattered intensity is measured as a function of

the deposition time with a constant growth rate of 8 Å/min (~ 0.38 ML/min). The reference intensity is detected by constant intensity a few minutes before the real deposition. The measurement will be terminated once no obvious oscillation is observed. Figure 10.13 shows the quasi layer-by-layer growth is more pronounced of the PTCDI thin film grown at 150 °C on SiO_2, the oscillation is damped out until ~ 32 ML, while the film grown at room temperature until ~ 20 ML. This observation is consistent with more Kiessig and Laue oscillations of the reflectivity measurements at 150 °C.

By changing the deposition order, using pentacene as template layer, PTCDI shows well in-plane ordering, as illustrated by figure 10.14. The lattice parameters of underneath pentacene is a = 5.933 Å, b = 7.595 Å, θ = 89.89°. Upon deposition of PTCDI, pentacene's in-plane structure remains unchanged and PTCDI shows same lattice parameters as it has on SiO_2, the slight difference is listed in table 10.3. PTCDI shows excellent ordering on top of pentacene with Kiessig oscillation ~ 220 Å (sum the film thickness). The Bragg of PTCDI locates at 20.783 Å (q=0.30232 $Å^{-1}$) with a rocking scan of ~ 0.08°. The mocaicity of the PTCDI on pentacene however is one magnitude broader than it on bare SiO_2, indicating a less aligned structure. Consistly, the vertical domain size derived from the halfwidth of the Bragg peak is much smaller comparing to it on bare SiO_2.

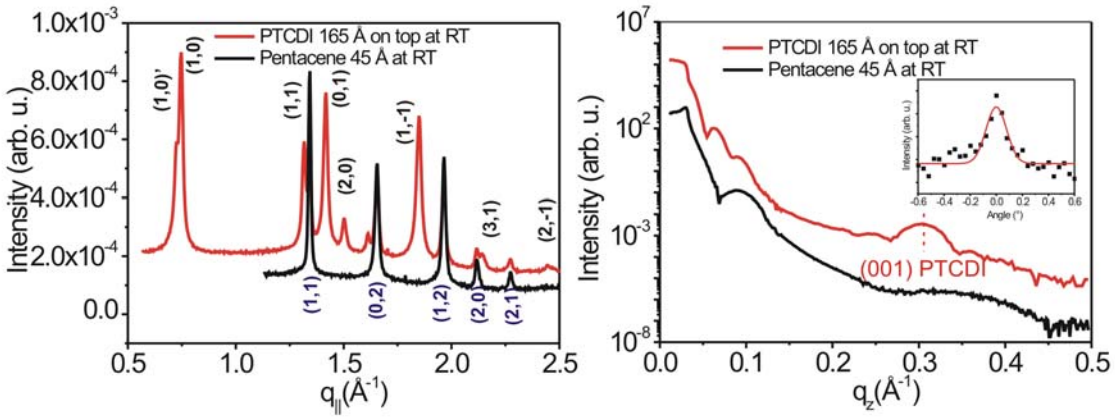

Figure 10.14: X ray diffraction measurements of deposition of PTCDI on top of pentacene at room temperature.

The corresponding AFM measurements are shown in figure 10.15, from which (a) shows 165 Å PTCDI on 45 Å pentacene and (b) shows same thickness of PTCDI on 235 Å pentacene. On a thin pentacene layer, PTCDI forms branch like structure while with

increasing pentacene coverage, these branch like structures considerably enlarge. Moreover in both case we notice the formation of highly ordered band structures on top of the branch like structure. In figure (a), the normal average length of these high crystalline band structure is ~1 µm and width of ~0.2 µm, in (b) a length of ~ 4 µm and width of ~0.3 µm can be derived.

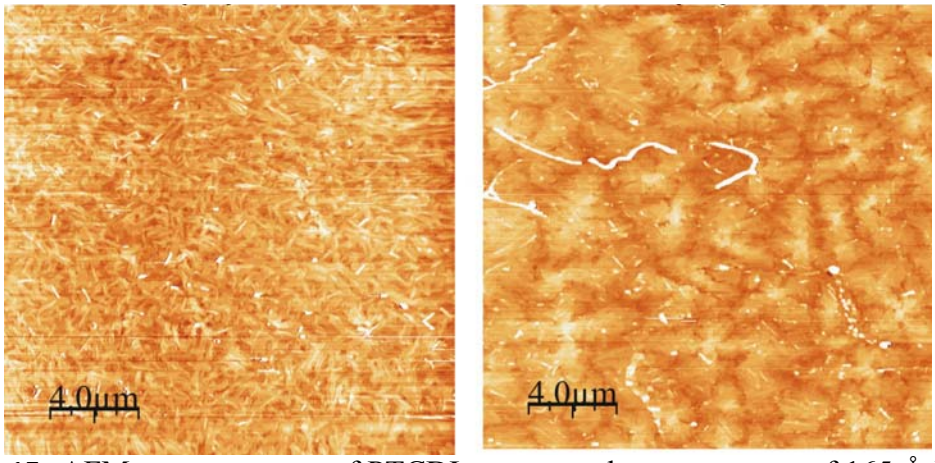

Figure 10.15: AFM measurements of PTCDI-pentacene heterostructure of 165 Å PTCDI on (left) 45 Å pentacene and (right) 235 Å pentacene at room temperature.

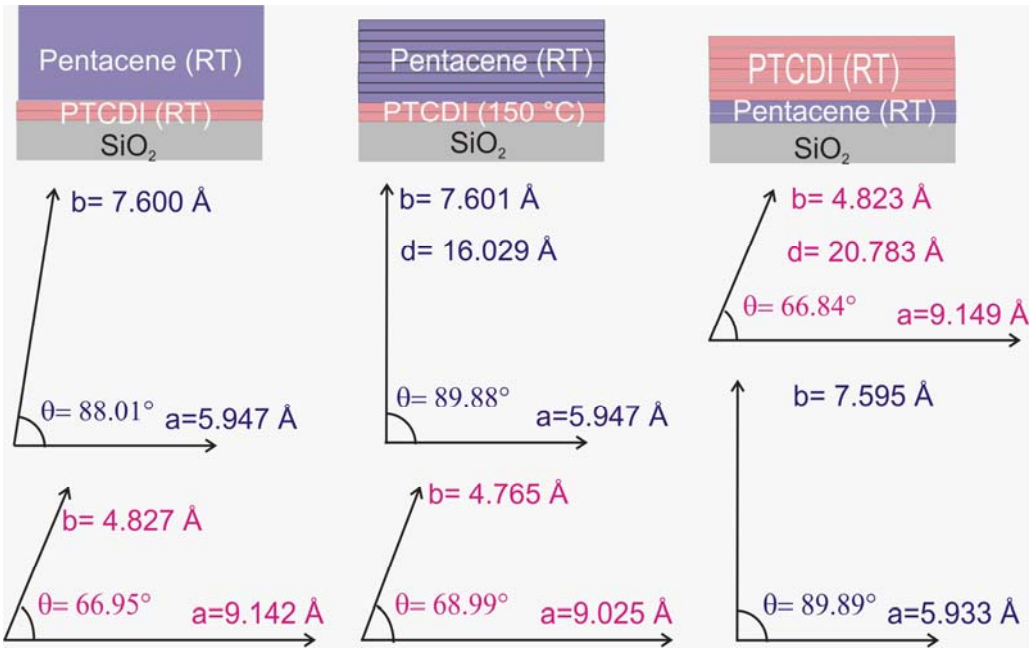

Figure 10.16: Schematic summary of the in-plane and out-plane structure of pentacene/PTCDI and PTCDI/pentacene heterostructures.

We summarize the structure of the heterostructure at all these 3 conditions and show as schematics in figure 10.16, the layering indicates the out-of-plane ordering. As we used thin template layers (thickness < 2 ML), the out-of plane Bragg peak of the buffer layer does not develop yet, however according to our results PTCDI and pentacene both shows out-of-plane ordering.

As a summary, the heterostructure composed of pentacene (RT)/PTCDI (RT) shows the worst ordering, pentacene adlayer shows little in-plane ordering and no out-of-plane ordering, coinciding with the bumped like structure observed by AFM. The heterostructures of pentacene (RT)/PTCDI (150 °C) however shows excellent structural ordering and mounds structures with well defined monolayer height. This is attributed to the higher structural ordering and larger domain size of the PTCDI buffer layer grown at 150 °C. The heterostructure of PTCDI (RT)/pentacene (RT) has also great structural ordering.

10.4.2 on Al_2O_3

By depositing organic molecules PTCDI and pentacene on Al_2O_3 $(11\bar{2}0)$, no orientation preference were observed despite the step structure of the substrate. At room temperature, the GIXD and specular X ray diffraction measurements showed that PTCDI (335 Å) thin film shows excellent ordering structure on Al_2O_3 (figure 10.17 (a) and (b) black curves). The Kiessig and Laue oscillations from the specular measurement reveal the whole film thickness indicating a smooth and coherent ordered growth of the film. The vertical and lateral domain sizes are ~ 338 Å and ~ 462 Å calculated from the halfwidth of Bragg peaks. A unit cell of a = 9.086 Å, b = 4.811 Å and θ = 66.98°, d = 20.849 Å can be derived from the Bragg peaks positions, therefore gives unit cell volume of 838.79 $Å^3$. Upon deposition of pentacene, the pentacene adlayer exhibits in-plane structure of a = 5.947 Å, b = 7.60 Å and θ = 81.01°, which is similar to that grown on bare Si. With increasing pentacene adlayer thickness, the intensities of pentacene continuous increasing, while the intensity of PTCDI layer decreasing. The lattice parameters of PTCDI keep unchanged with deposition of pentacene adlayer. The mosaicities of the pentacene and PTCDI films were performed by rocking scan at the Bragg peak position respectively. PTCDI film shows excellent alignment respect to the surface

normal on Al_2O_3 and unaffected upon deposition of pentacene. Figure 10.17 (c) I shows a misalignment of 0.00521° of the PTCDI film upon deposition of 240 Å pentacene, in the same magnitude as the film grown directly on the Al_2O_3. The pentacene film on top of PTCDI however shows a misalignment of ~ 1.14°, which is much higher than the film deposited directly on the Al_2O_3 substrate, indicating a less aligned structure to the surface normal.

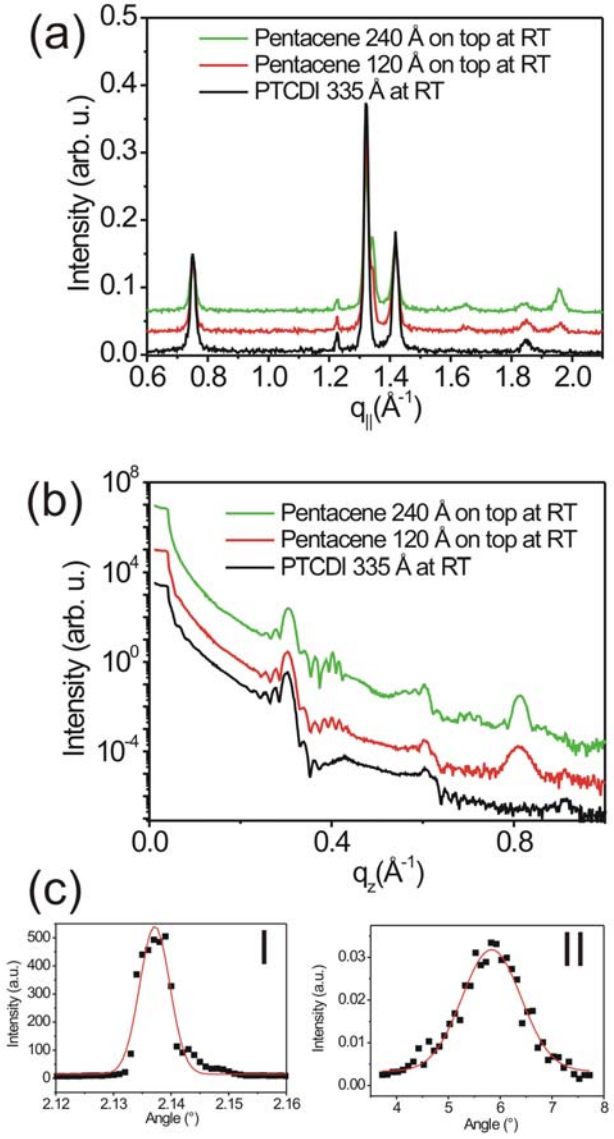

Figure 10.17: (a) The GIXD, (b) X-ray reflectivity and (c) X-ray rocking measurements of pentacene (RT)/PTCDI(RT) on Al_2O_3 (I) rocking of pentacene with halfwidth of ~ 0.00521° and (II) rocking of PTCDI with halfwidth of ~ 1.14°.

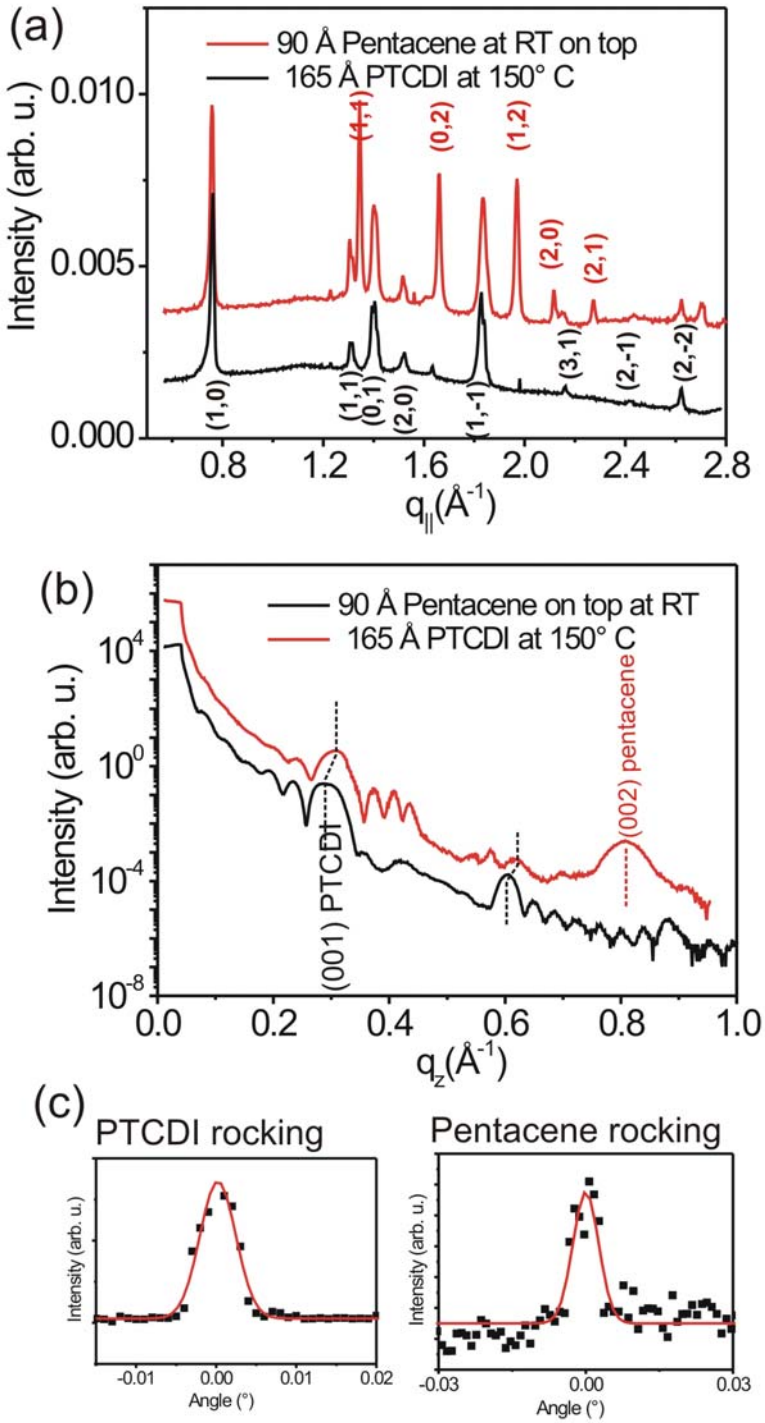

Figure 10.18: (a) The X-ray reflectivity, (b) GIXD and (c) X-ray rocking measurements of pentacene (RT)/PTCDI (150 °C) on Al_2O_3.

At 150 °C, PTCDI thin film on Al_2O_3 exhibits 2 unit cells, similar to that on SiO_2. The unit cell "I" has the parameters of a=9.135 Å, b=4.845 Å and θ=66.84°, while unit cell "II" has the dimension of a=9.008 Å, b=4.926 Å and θ=66.50°. The Bragg peak of the specular measurement is difficult to be fitted with 2 Gaussains, therefore gives a universal value of d ~ 20.812 Å. By performing similar experiments of the heterostructure pentacene (RT)/PTCDI (150 °C), i.e. after grew the PTCDI film at substrate temperature of 150 °C, the sample was cooled down to room temperature for the deposition of pentacene film, we observed an improved ordering of pentacene film. Figure 10.18 (a) shows in-plane measurements, the better ordering of pentacene film is confirmed by less pentacene film thickness and more enhanced intensity compare to the heterostructure pentacene (RT)/PTCDI (RT). The unit cell of pentacene calculated from the Bragg peak positions gives a= 5.938 Å, b= 7.68 Å, θ = 89.83° and d = 15.567 Å. Both pentacene and PTCDI shows great alignments, reflected by the small rocking angle as shown in figure 10.18 (c). Thus the better ordering of the Pentacene on PTCDI grown at higher temperature is unaffected by the properties of the two chosen substrates: SiO_2 and Al_2O_3.

Depositing pentacene thin film on Al_2O_3, the unit cell calculated from the Bragg peak positions gives a = 5.930 Å, b = 7.581 Å, θ = 89.98° and d = 15.440 Å, thus V = 694.11 $Å^3$. Figure 10.19 (a) black curve shows in-plane measurements of pentacene film, from which we suggest a better ordering of pentacene on Al_2O_3 than on PTCDI as less film thickness contributes more enhanced intensity compare to the heterostructure pentacene (RT)/PTCDI (RT). By depositing PTCDI adlayer on top, we reveal an ordered in-plane structure, but less ordering than PTCDI directly deposted on SiO_2 or Al_2O_3, figure 10.19 (b) red curve. Figure 10.20 (c) shows the rocking scan of the 2^{nd} Bragg peak of the pentacene. By depositing PTCDI film, the intensity of the rocking scan decreases while the halfwidth is not altered, which indicates less mass pentacene contributes to the out-of-plane structure ordering.

Figure 10.20 schematically summarizes the ordering and structure of pentacene and PTCDI heterostructures. The pentacene/PTCDI heterostructure shows both out-of-plane and in-plane ordering structure. In contrast, PTCDI thin film deposited on pentacene however shows little in-plane ordering and no out-of-plane ordering.

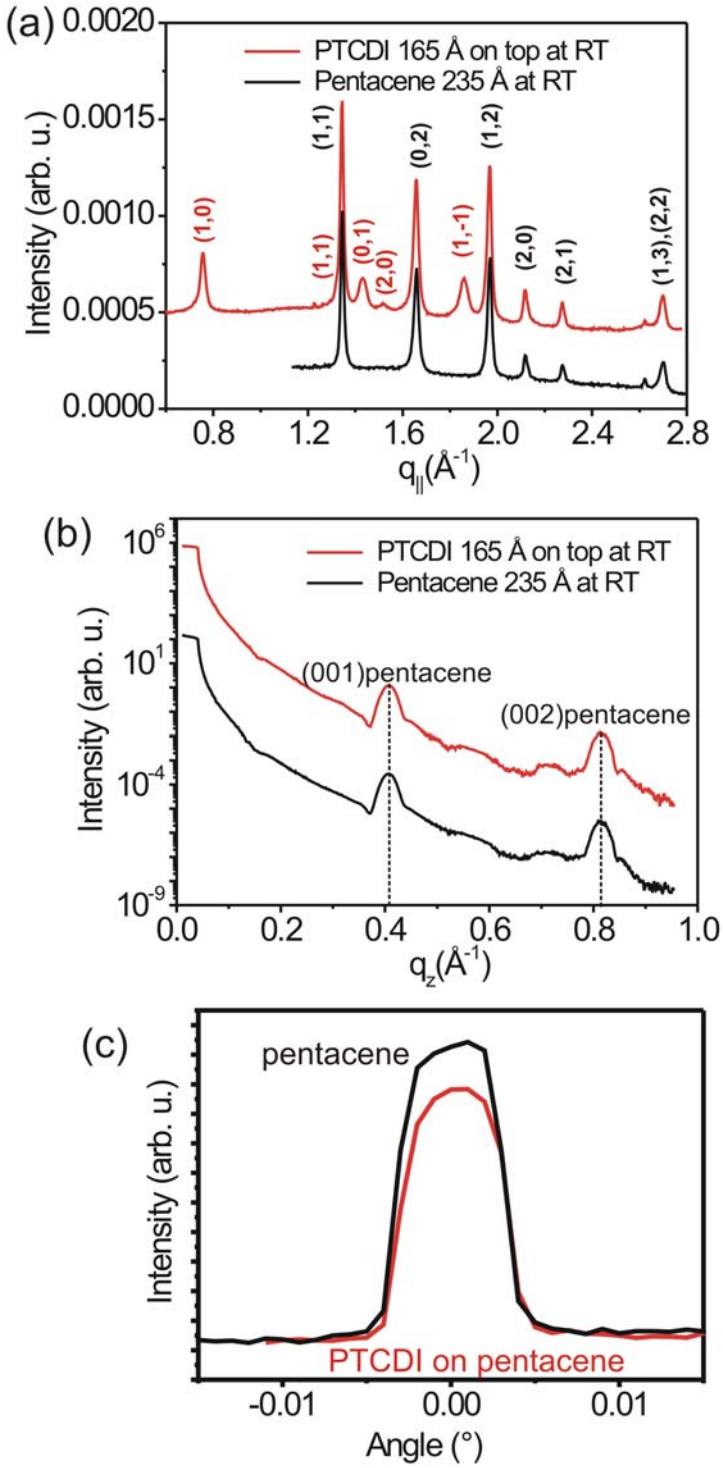

Figure 10.19: (a) The GIXD (b) X-ray reflectivity and (c) rocking measurements of heterostructure PTCDI (RT)/pentacene (RT) on Al_2O_3.

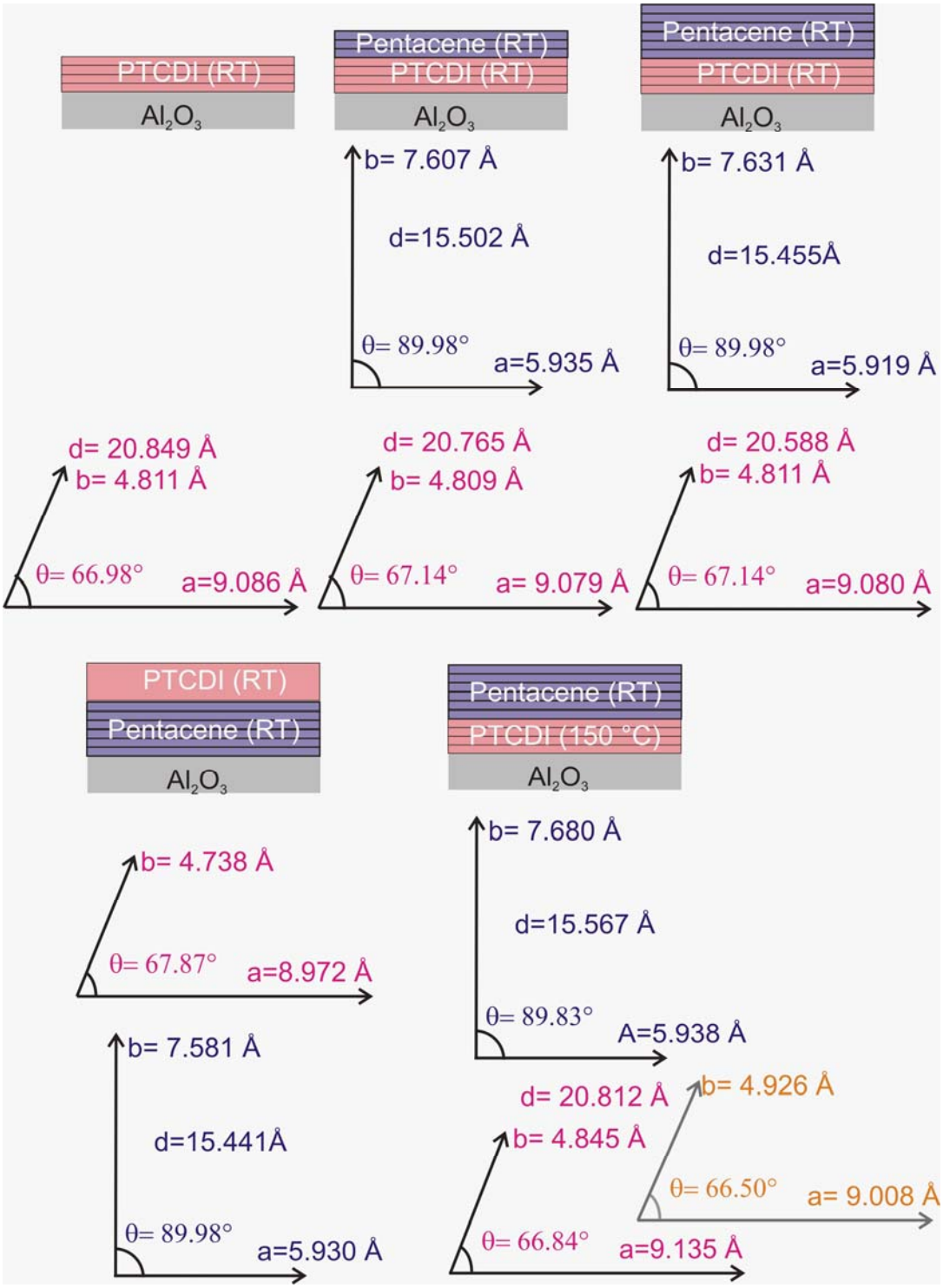

Figure 10.20: Schematic summary of the in-plane and out-plane structure of pentacene/PTCDI and PTCDI/pentacene heterostructures.

We summarize the structure of pentacene: on SiO_2 and Al_2O_3, the lattice parameter a, b and θ shows less than 0.08 % difference and therefore could considered to be the same. By using PTCDI grown at different substrate temperatures on SiO_2, no in-plane structure difference of pentacene is observed; however, pentacene grown on PTCDI at RT shows no out-of-plane ordering. Notice the Bragg peak of pentacene is at 16.03 Å, around 0.5 Å larger than all the other cases. By changing the buffer layer to PTCDI grown at different substrate temperatures on Al_2O_3, pentacene structure shows slightly difference: a = 5.938 Å, b = 7.680 Å and θ = 89.83° on PTCDI grown at 150 °C and a = 5.919 Å, b = 7.632 Å and θ = 89.99° at on PTCDI grown RT. The lattice parameters of pentacene are summarized in table 10.3.

Pentacene(RT)/	D (Å)	a (Å)	b (Å)	θ	A (Å^2)	d (Å)	VD (Å)	LD (Å)
/PTCDI (RT) /SiO_2	120	5.947	7.597	89.89	45.18	----	----	463
/PTCDI (150 °C)/SiO_2	120	5.947	7.601	89.88	45.20	16.029	153	490
/SiO_2	45	5.933	7.595	89.89	45.06	---	----	331
/Al_2O_3	235	5.930	7.581	89.98	44.96	15.440	278	300
/PTCDI (150 °C)/Al_2O_3	90	5.938	7.680	89.83	45.60	15.567	139	454
/ PTCDI (RT) /Al_2O_3	235	5.919	7.632	89.99	45.17	15.456	323	400

Table 10.3: Pentacene structure on different substrates.

We summarize all the calculated structure of PTCDI. PTCDI thin film exhibits 2 unit cells at a high substrate temperature of 150 °C, comparing to the unit cell of PTCDI at room temperature, the unit area A is ~ 2 % and unit cell volume is ~ 3.4 % larger might due to thermal expansion. Moreover, the film grown at 150 °C shows larger average domain size than the film grown at room temperature with vertical domain size increasing from 390 Å to 610 Å and lateral domain size from ~ 160 Å to 550 Å. By using organic blocking layer of pentacene on SiO_2 and Al_2O_3, we observe different structure and ordering of PTCDI. The PTCDI thin film shows in-plane ordering on pentacene layer but different lattice parameters: on pentacene film deposited on Al_2O_3, PTCDI exhibits a more compressive in-plane unit cell with a = 8.972 Å, b = 4.738 Å and θ = 67.87°, while on pentacene film deposited on SiO_2,

the unit cell has a dimension of a = 9.149 Å, b = 4.823 Å and θ = 66.84°. From specular X ray measurements, we notice that PTCDI shows no out-of –plane ordering on pentacene film deposited on Al_2O_3, but with Bragg peak locating at 20.783 Å on pentacene film deposited on SiO_2. When depositing PTCDI on top of F_{16}CuPc, PTCDI exhibits similar out-of-plane ordering and in-plane ordering on F_{16}CuPc grown on different temperature and different thickness.

PTCDI	D (Å)	a (Å)	b (Å)	θ (°)	A ($Å^2$)	d (Å)	VD (Å)	LD (Å)
(RT)/SiO_2	66	9.142	4.827	66.95	40.61	----	----	210
	400	9.127	4.821	67.03	40.51	20.577	389	160
(150 °C) /SiO_2	660	9.113	4.904	67.55	41.30	20.861	609	550
(RT)/Al_2O_3	335	9.086	4.811	66.98	40.23	20.849	338	462
(150 °C) /Al_2O_3	165	9.135	4.845	66.84	40.69	20.812	264	
		9.008	4.926	66.50	41.24			
(RT)/pentacene/ Al_2O_3	165	8.972	4.738	67.87	310.38	---	---	220
(RT)/pentacene/ SiO_2	165	9.149	4.823	66.84	40.57	20.783	203	300
(RT)/F_{16}CuPc/ SiO_2	86	9.126	4.904	67.62	41.38	20.920	341	360
(RT)/F_{16}CuPc/ SiO_2	137	9.100	4.905	67.51	41.24	20.857	521	420

Table 10.4: PTCDI structure on different substrates.

10.5 Conclusions

In this chapter we study the structure and ordering properties and growth mode of organic-organic heterostructures.

The heterostructure of DIP/H_{16}CuPc shows growth mode transition from LBL (RT) to SK (130 °C). Unlike DIP/F_{16}CuPc heterostructure, the structure of template H_{16}CuPc layer remains the same upon the deposition of DIP thin film due to weak van der Waals interaction between H_{16}CuPc and DIP molecules. DIP thin film shows structural change as a function of thickness, which is also observed in the heterostructure DIP/F_{16}CuPc and DIP grown on bare SiO_2.

For the organic-organic F_{16}CuPc and H_{16}CuPc heterostructures, we demonstrate that structure and ordering are strongly correlated with the component and thickness of underneath buffer layer. We suggest this is due to the formation of interfacial layer. The formation of interfacial layer strongly affects further the structural and ordering properties of the overgrown layer. The present results suggest that a thin F_{16}CuPc film always introduces ordered structure of the heterostructure and should be chosen as buffer layer in design steps for optimization of the performance of OFETs.

The heterostructure composed of pentacene (RT)/PTCDI (RT)/SiO_2 shows the worst ordering of pentacene adlayer: little in-plane ordering and no out-of-plane ordering, coinciding with the bumped like structure of pentacene observed by AFM. The heterostructures of pentacene (RT)/PTCDI (150 °C)/SiO_2 however shows excellent structural ordering of pentacene adlayer and mounds structures with well defined monolayer height. This is attributed to the higher structural ordering and larger domain size of the PTCDI buffer layer grown at 150 °C. The heterostructure of PTCDI (RT)/pentacene (RT)/SiO_2 exhibits great structural ordering. Pentacene (RT)/PTCDI (RT)/Al_2O_3 has little in-plane ordering but out-of-plane ordering of pentacene adlayer. The Pentacene (RT)/PTCDI (150 °C)/Al_2O_3 heterostructures exhibit great structure ordering and better alignment of pentacene thin film respect to the substrate normal. The heterostructure of PTCDI (RT)/pentacene (RT)/ Al_2O_3 has little in-plane and out-of-plane ordering of PTCDI adlayer.

Chapter 11 Summary

The aim of this thesis was to study the organic-inorganic (organic semiconductors with metals and insulators) and organic-organic (organic semiconductors with organic semiconductors) interfaces in variable architecture design for organic electronic devices such as OLEDs or OFETs.

For these purpose, we performed complementary techniques such as atomic force microscopy (AFM), scanning tunneling microscopy (STM), scanning electron microscopy (SEM), as well as in-situ and ex-situ X-ray diffraction (XRD). Different systems have been addressed, which comprise of the growth DIP on SiO_2 to address understanding of the growth process of organic semiconductors on dielectric materials; the self-assembly of DIP on copper metal surface to study the initial growth process of organic semiconductors on metal surfaces; the growth of one dimensional organic nanowires and nanotubes (F_{16}CuPc on Au nanoparticles) or the growth of the large microsize organic single crystals (DIP on APS) for the advanced organic electronics; and finally the growth of organic-organic heterostructures based on n-type F_{16}CuPc, PTCDI-C8 combined with p-type H_{16}CuPc, pentacene, DIP .

The studies devoted to the growth of DIP on SiO_2 have been performed with a special emphasis on the evolution of the structure and morphology in the early stages of DIP film growth on SiO_2. The morphological transition from layer-by-layer growth to rapid roughening of DIP films is a general phenomenon of the DIP thin film growth, ranging from far from equilibrium state to near equilibrium state. The van der Waals force interaction between the DIP molecules and the substrate lead to a layered growth mode. At the layer-by-layer growth regime, we studied carefully the 2D island size distribution, the island size and shape, their lateral correlation, thus gain insight into self-affine, scaling and fractal properties of the 2D islands. We disclose an Ostwald ripen process of the 2D islands grown at room temperature. Respect to the growth process, we reveal an Ostwald ripening process and a fast coalescence regime. The variation of diffusion length with the monolayer number is essential

governed by the interaction between the substrates and DIP film and the kinetically substrate temperatures. The onset of the growth mode transition from LBL growth to 3D islands increases with increasing substrate temperature, $\theta_{critical}$ ~ 3 ML at RT, $\theta_{critical}$ ~ 4 ML at 90 °C and $\theta_{critical}$ ~ 5 ML at 120 °C. In the rapid roughening regime, increasing substrate temperature leads to a shifting of $\theta_{critical}$ to lower β value, namely, β ~ 0.84 at RT, β ~ 0.80 at 90 °C, and β ~ 0.77 at 120 °C. A higher deposition rate leads to a higher $\theta_{critical}$ and higher β value. For the structural respect, SiO_2 causes the formation of a denser first layers of DIP films. In spite of amorphous character of the SiO_2 surface, the first DIP layer is under a compressive strain of ~ 3 % - 4 % along *a* lattice vector (relative to the relaxed structure of thin films) while only maximum ~ 0.8 % strain along *b* lattice vector. Upon further deposition, at 120 °C the in-plane structure of the whole films evolves continuously until a relaxed in-plane structure at $\theta_{critical}$, while at RT and 90 °C the structure of the films undergoes a sudden transition to the relaxed structure at $\theta_{critical}$. At 120 °C, accompany with the in-plane lattice revolution, the lattice spacing of DIP film continuously decrease from ~ 18 Å to 16.732 Å. The transition in morphology from layer-by-layer growth mode to rapid roughening is coincident with the transition in structure from a compressed in-plane structure to relaxed structure. The layer-by-layer to rapid roughening transition observed for DIP might be in essence SK growth as result from the energetic interplay with thickness.

We studied the self-assembly behavior of single molecules and (supra) molecular adsorbed at Cu (100) surface by performing scanning tunneling microscopy measurements in ultra-high vacuum conditions. An alternative step-by-step scenario was proposed involving formation of DIP 1D chains on the step edges and subsequent nucleation of two dimensional supramolecular nanostructures. We revealed an orientation preference nucleation of the organic molecules respect to the substrate orientation. We studied the molecular dynamics of the molecular clusters in percolation regime at 300 K, 240 K and 150 K. The cluster revolution with time at early stage of growth before coalescence suggest strongly mobile characteristic of the clusters at different temperatures. The substrate-molecule interaction leads to the observed 2D ordering patterns and further guides the epitaxial growth of the multilayers. The adsorbate-substrate interaction guides the orientation of the 2D pattering, the adsorbate-adsorbate lateral spacing is governed by weak van der Waals interactions. DIP

molecules are commensurate with the substrate and assemble into chiral domains, which is metalstable, a subsequent annealing results into more ordered domains.

By using the templates of gold nanoparticles, F_{16}CuPc forms uniform 1D nanowires/nanotubes. These nanowires/nanotubes show no dependence on nanoparticle size and adopts a universal diameter of 20-30 nm with precise localization on gold nanoparticles and packing density depending on the density of the gold nanoparticles. The formation of the nanowires/nanotubes has a sensitive selectivity of substrate temperature and Au nanoparticle size.

DIP thin films deposited on the APS terminated silicon wafers exhibit growth transitions from 2D growth to 3D growth at a deposition temperature of 80°. X ray measurements reveal the same film structure despite different morphologies at different deposition temperature. De-wetting film containing large high crystalline DIP islands forms above transition temperature. Molecular resolution images show that the islands are mono crystalline, with potential applications in electronic devices. The growth mode transition of DIP film is clearly associated with the surface energy changes of the APS during the annealing of the substrates. This study shows that the change of physical and chemical properties of the SAMs by aging effect, heating procedure has important impact for the growth of organic thin films.

We study the structure and ordering properties and growth mode of organic-organic heterostructures. We have determined thin film structure of all the investigated systems:

i) DIP/H_{16}CuPc heterostructure shows growth mode transition from LBL (RT) to SK (130 °C). The structure of template H_{16}CuPc layer remains the same upon the deposition of DIP thin film. DIP thin film shows structural change as a function of thickness, which is also observed in the heterostructure DIP/F_{16}CuPc and DIP grown on bare SiO_2.

ii) The structure and ordering of F_{16}CuPc/H_{16}CuPc and H_{16}CuPc/F_{16}CuPc heterostructures are strongly correlated with the deposition order and thickness of underneath buffer layer. We suggest the formation of an interfacial layer, which strongly affects further the structural and ordering properties of the adlayer. The present results suggest that a thin F_{16}CuPc film as buffer layer leads to the best ordering of the heterostructure structure, which should be chosen as buffer layer in design steps to gain better performance of OFETs.

iii) The pentacene/PTCDI and PTCDI/pentacene heterostructure series on SiO_2 and Al_2O_3 shows more complex scenarios. Pentacene (RT)/PTCDI (RT)/SiO_2 shows little in-plane

ordering and no out-of-plane ordering of pentacene adlayer, coinciding with the bumped like structure observed by AFM. In contrast, the heterostructures of pentacene (RT)/PTCDI (150 °C)/SiO_2 shows excellent structural ordering of pentacene adlayer and mounds growth with well defined monolayer height due to better templating LBL morphology and higher structural ordering of the PTCDI buffer layer grown at 150 °C. The heterostructure of PTCDI (RT)/pentacene (RT)/SiO_2 exhibits great structural ordering. Pentacene (RT)/PTCDI (RT)/Al_2O_3 displays little in-plane ordering but out-of-plane ordering of pentacene adlayer. The Pentacene (RT)/PTCDI (150 °C)/Al_2O_3 heterostructures show great structure ordering and better alignment of pentacene thin film respect to the substrate normal. The heterostructure of PTCDI (RT)/pentacene (RT)/ Al_2O_3 shows little in-plane ordering and no out-of-plane ordering of PTCDI adlayer.

List of figures

3.1 A photo of W.C. Röntgen who discovered X ray (left). The first X ray radiation graph (right) 5

3.2 The scattering from (a) an electron, (b) an atom, (c) a molecule and (d) a molecular crystal. 6

3.3 Schematic of the refraction of a multilayer 12

4.1 A schematic illustration of working principle of AFM The cantilever visualizes as a coil spring with its spring constant k directly affects the downward force exerted on the sample, which is positioned by tube piezoceramics position with high resolution. The laser is reflected by the cantilever to the photodiode to detect the deflection . . . 16

4.2 A schematic describes the Lennard-Jones force vs tip-sample distance . . . 18

4.3 A graph of a force-distance curve measured with AFM of DIP film on SiO_2 by using a Si_3N_4 cantilever with force constant of 0.1 nN/nm. (a) to (e) corresponds to the approach and retraction procedure 19

4.4 Energy level diagram for sample and tip. (a) Independent sample and tip. (b) Sample and tip at equilibrium, separated by small vacuum gap. (c) Positive sample bias electrons tunnel from tip to sample. (d) Negative sample bias electrons tunnel from sample to tip 23

5.1 Scheme of the orbitals and bonds for two sp^2-hybridised carbon atoms . . . 27

5.2 Molecular structure and dimension of di-indeno-perylene 28

5.3 Molecular structure of $H_{16}CuPc$ and $F_{16}CuPc$ 30

5.4 Typical crystal structures of planar phthalocyanines (a) and (b) the α-modification; (c) and (d) the β-modification. (a) and (b) represent the overlapping of neighbouring molecules within a molecular column. Both structures have herringbone type molecular pack-

ings. (from Hoshino et al.) 31

5.5 (a) Molecular structure of pentacene (b) up: crystal structure of bulk pentacene. down: The thin film structure of pentacene 33

5.6 Schematic of the structure and dimension of PTCDI-C_8 34

5.7 The three Growth modes layer-by-layer, layer-plus-island and island mode . . 36

5.8 Schematic of atomistic process of thin film growth 37

6.1 Three different MBE-UHV systems 41

6.2 AFM and STM systems 44

6.3 In-house 6 circle high resolution X-ray diffractometer 45

6.4 The synchrotron radiation facility at ANKA and ESRF 46

7.1 The typical features of (a) roughness σ as a function of t and (b) σ as a function of L and (c) ξ as a function of t for a layer-by-layer growth 53

7.2 Morphology of DIP thin film deposited on SiO_2 at the substrate temperature of RT. A layer-by-layer to 3D islanding is clear identified at a critical thickness of ~ 3 ML . 57

7.3 Morphological revolution of organic semiconductor DIP as a function of coverage grown at the 90 °C with deposition rate of 0.5, 2.0 and 3.5 Å/min 58

7.4 AFM images of morphological revolution as a function of coverage at 120 °C . . 59

7.5 The correlation length as a function of fraction layer coverage of DIP thin film grown at RT 61

7.6 Normalization of the island size distribution by the average size of the islands of DIP thin films grown at room temperature 61

7.7 Fractal analysis for DIP islands on SiO_2 at room temperature, in which plots (a) and (b) show the data of ~2000-3000 islands. The islands shape transition takes place at the critical area size of lnA ~ 14.2 $Å^2$ for the submonolayer and lnA ~ 15.5 $Å^2$ for the second and third layers 61

7.8 The island size distribution, the islands shape and the correlation length and ρ of DIP thin films grown at 90 °C with deposition rate of 0.5 Å/min and 2 Å/min . . 64

7.9 The incoming flux as a function of the nucleation density of DIP films with 0.33 ML coverage, the red curve is best fit and the green curve is the fitting by fixing i=2 . 65

7.10 (a) The selective islands images of coverage of 0.36 ML, 0.48 ML. (b) The PSD analysis, which shows different correlation length, roughness and roughness exponents of the

two films. (c) The different fractal shape of the two films 66

7.11 (a) and (b) the decreasing nucleation density with increasing coverage indicating a characteristic Oswald ripening regime 67

7.12 The islands density as a function of the substrate temperature for $\theta \sim 0.33$ ML . 68

7.13 Layer coverage as a function of film thickness in the 2D growth mode regime (a) at room temperature, (b) at 90 °C and (c) The roughness σ as a function of the film thickness in the 2D growth mode regime. The dotted line represents the behaviour of an ideal layer-by-layer growth 69

7.14 σ as a function of the film thickness. The square data are from room temperature, and the circle data for 90 °C and the star data for 120 °C. Two regimes can be observed below and above a certain threshold thickness, $\theta_{crit} \sim 3$ ML for RT, ~ 4 ML for 90 °C and ~ 5 ML for 120 °C. When the coverage exceeds the threshold thickness, a 3D growth mode regime is observed exhibiting a rapid roughening of the surface. The dash lines are the fits according to the scaling-law $\sigma \alpha (\theta - \theta_{crit})^{\beta}$, ($\beta = 0.84$ at RT and $\beta = 0.80$ at 90 and $\beta = 0.77$ at 120 °C respectively) 70

7.15 σ as a function of the film thickness at 90 °C for different deposition rate . . 71

7.16 The GIXD measurements of DIP at (a) RT, (b) 90 °C and (c) 120 °C. On the right, the calculated lattice parameters a and b are plotted as a function of the layer coverage. The shadows mark the morphology evolution separation of LBL growth and rapid roughening regimes, which take place accompanied with the strain relaxation at the same critical thickness 74

7.17 Specular X-ray reflectivity of three DIP films at different substrate temperature on SiO_2. The red curves are the fitting results by using Parratt formula 76

7.18 Specular X-ray reflectivity of the DIP films as a function of increasing film thickness at the substrate temperature of 120 °C on SiO_2. The dashed arrows red curves are guided for depicting the shifts of the Bragg peak positions (circles data cited from [64]) . . 78

7.19 Specular X-ray reflectivity of DIP films on SiO_2 as a function of coverage at substrate temperature of 120 C. The black curves are the fitting results by using Parratt formula, while the colored lines are XRD data, the curves are shifted for the clarity sake. . 79

8.1 STM image of the initial stage of DIP deposition with a deposition time of ~ 3 min (17 min for full layer coverage). The molecules are preferentially adsorbed along the step

edges forming single-row chains 84

8.2 (a) Molecular clusters starting from the upper and lower step edges. (b) Small molecular clusters on the large terraces 85

8.3 (a)-(i) STM images of dynamical behavior of organic clusters on the same area of one of large terrace of Cu (100) at room temperature (continuous scan with time interval of ~ 1 min) 86

8.4 (a)-(f) STM images of dynamical behavior of organic clusters on the same area of one of large terrace of Cu (100) at 240 K. The images have a size of 32 nm*32 nm. (Continuous scan on the same area, the interval time is 1 min per scan) 87

8.5 (a)-(j) STM images of dynamical behavior of organic clusters on the same area of one of large terrace of Cu (100) at temperature of 150 K. (Continuous scan on the same area, the interval time is 1 min per scan). The images have a size dimension of 25*37 nm. 88

8.6 The plots of the cluster sizes vs the statistical number of the clusters along different orientations of the substrate (a) at 300 K (b) at 240 K and (c) at 150 K . . . 89

8.7 Initial stage of DIP deposition with a deposition time of ~ 3 min (17 min for full layer coverage). The STM image shows large flat terraces without molecules, while the molecules are preferentially adsorbed along the step edges. (b) and (c) High resolution STM images of 1D molecular chains with illustrations showing the molecular orientations. 90

8.8 (a)-(j) STM images of dynamical behavior of organic clusters on the same area of one of large terrace of Cu (100) at 220 K. (Continuous scan on the same area, the interval time is 1 min per scan). The images have a size dimension of 40*80 nm . . . 91

8.9 (a)-(d) STM images of dynamical behavior of organic clusters on the same area of one of large terrace of Cu (100) at temperature of 150 K. (Continuous scan on the same area, the interval time is 1 min per scan) 92

8.10 (a) to (d) STM images showing the coexistence of liquid phase and solid phase of DIP and the continuous shrink of the liquid phase to solid phase, the black open circles mark the noticeable changing sites. The time interval from (a) to (c) is two minutes and from (c) to (d) is 1 min 93

8.11 Monolayer coverage of DIP on Cu (100) (a) on large terraces (b) on step edges . 94

8.12 The four different domain orientations labeled as “A”,”B”,”C” and “D” with a full layer coverage of DIP on Cu (100) on large terraces (deposition time is 17 min). The insects show the schematics of real space model of the corresponding adsorption geometry . 94

8.13 The arrangement of organic DIP on Cu (100) surface after annealing at 50 °C for 3 hours (a) on large terraces (b) on step edges 94

9.1 SEM image of the Au nanoparticle array on bare SiO_2. The separation L between the gold nanoparticles and the particle D are external control parameters. The gold nanoparticles adopt a hexagonal pattern on the surface 100

9.2 (a) A schematic figure illustrates the growth procedure of organic semiconductor $F_{16}CuPc$ molecules on the template of gold nanoparticle arrays. The part of substrate without Au nanoparticle arrays is used as reference. (b) SEM image taken on the boundary (yellow dotted line) between the gold template and bare SiO_2 showing the high selective growth of nanowires 101

9.3 SEM image illustrating the vertical growth of $F_{16}CuPc$ wires on top of the gold nanoparticles with a diameter of 20-25 nm 102

9.4 SEM images illustrating the influence of the Au particle size on the nanowire formation. Single nanowires emerge from Au nanoparticles when the size exceeds a critical diameter of D* = 20 nm. The width of the $F_{16}CuPc$ wires is independent of the particle size. The substrate temperature is 120 °C 103

9.5 SEM image depicts the Au nano-particle size effect of the formation of the organic $F_{16}CuPc$ wires (T_{sub} = 120 °C) 103

9.6 SEM images illustrating the growth of organic $F_{16}CuPc$ on Au nanoparticle arrays at room temperature, despite of increasing nanoparticle size, the formation of organic $F_{16}CuPc$ nanowires is rarely observed. The images have a size dimension of 600 nm x 1000 nm 104

9.7 SEM images illustrating the growth of $F_{16}CuPc$ on Au nanoparticle arrays at 140 °C, which presents an obvious selective size range of Au nanoparticles for the formation of organic wires 105

9.8 The growth of organic $F_{16}CuPc$ on Au nanoparticle arrays at 160 °C . . 106

9.9 (a) SEM image of the organic thin film of $F_{16}CuPc$ on self assembled monolayers of OTMS at 120 °C. (b) SEM image of the growth of organic on Au nano-particle arrays

. 107

9.10 (a) AFM image of 200 Å F_{16}CuPc at RT. (b) X-ray measurement of a thicker film of 270 Å F_{16}CuPc at RT 108

9.11 (a) AFM measurements of F_{16}CuPc grown on Au (111), island growth mode was observed. The atomic resolution image suggests that the F_{16}CuPc molecules are essentially lying down on the surface and its Fourier transform gives the in-plane spacing of a = b ~ 14.5 Å. (b) X ray reflectivity measurement shows an out-of-plane spacing of d = 3.134 Å in agreement of the geometry observed by AFM 109

9.12 AFM morphologies of F_{16}CuPc grown on different substrates (a) on SiO_2/Si (111) and (b) on OTMS functionalized SiO_2/Si (111) surface 110

9.13 (a) AFM image of F_{16}CuPc grown on Ga_3N_2 grown at room temperature. (b) X-ray specular measurement on the same sample. 110

9.14 (a) AFM image of as prepared APS film on SiO_2, from which a roughness of ~ 1.4 Å can be derived. (b) XRD data together with the fit. (c) Electron density profile of APS on SiO_2 113

9.15 (a)-(f) AFM topographic images of DIP on APS at substrate temperature of 35 °C, 50 °C, 65 °C,80 °C and 95 °C. (g) Roughness mean square as a function of the temperature and lateral correlation length calculated from 2D power spectral density analysis . 113

9.16 (a) X ray specular data for samples grown at different temperatures. The curves appear shifted for the sake of clarity. (b) GIXD measurements for samples at substrate temperature 35°C, 65°C and 95°C 115

9.17 (a) The AFM image of one island grown at substrate temperature 95 °C. (b) Topographic profile across the island. The red dashed lines correspond to the height of single molecular terraces. (c) The atomic resolution images of one island, the images were measured from different terraces as shown in figure 4(a). The inset shows the 2D Fourier transform of the images 116

9.18 AFM images of APS film after different heating time 1h (a), 5h (b), 24h (c) . 117

10.1 X ray in-plane and out-of-plane measurements of DIP and H_{16}CuPc heterostructure at room temperature and 130 °C respectively 122

10.2 X ray time scan measurement of DIP on 40 Å H_{16}CuPc at RT . . . 124

10.3 AFM images of increasing DIP coverage (a) 10 Å, (b) 30 Å, (c) 60 Å and (d) 110 Å on top of 40 Å H_{16}CuPc template layer at 130 °C. (e) Evolution of the roughness mean square as a function of the DIP film thickness. (f) The average dots height and dot area as a function of the DIP thin film coverage 126

10.4 X ray specular measurements and X ray grazing incident measurements of 100 Å H_{16}CuPc on F_{16}CuPc buffer layers at RT 129

10.5 X ray specular measurements and X ray grazing incident measurements of 100 Å F_{16}CuPc on different thickness of H_{16}CuPc buffer layer at RT . . 131

10.6 AFM and X ray diffraction measurements of (a) 340 Å H_{16}CuPc on 480 Å F_{16}CuPc at RT and (b) 480 Å F_{16}CuPc on 340 Å H_{16}CuPc 132

10.7 Schematic summary of the effect of the template layer on the ordering of the adlayer of heterostructure of H_{16}CuPc/F_{16}CuPc and H_{16}CuPc/F_{16}CuPc at RT . . 133

10.8 GIXD measurements of PTCDI as a function of coverage at substrate temperature of RT 134

10.9 X ray measurements of organic heterostructure of pentacene on PTCDI by using SiO_2 as substrates (a) in-plane measurements (b) specular measurements . . 135

10.10 AFM topographical images (left) and the corresponding phase images (middle) of (a) ~ 30 Å and (b) ~ 120 Å pentacene on 65 Å PTCDI at room temperature. The profile corresponds to the green line are plotted as green lines on the right. Figure (c) shows the height distribution of the images (the average height of PTCDI is set as 0 nm). Figure (d) shows the lateral information of the images 136

10.11 X ray diffraction measurements of deposition of around 120 Å Pentacene on a thin layer of PTCDI at 150 °C 137

10.12 AFM images of (a) ~ 40 Å (a) or (b) ~ 120 Å pentacene thin film on ~ 30 Å PTCDI at 150 °C, which the morphology of the underneath PTCDI buffer layer guides the general morphology of subsequent pentacene adlayers; (c) and (d) are enlarged images, which shows the pentacene terraces with well defined angles of 90°, 60° or 120°; the monolayer height can be clearly indentified in the profile figures (e) and (f) respectively 138

10.13 The X-ray reflectivity (a) and (b) real time (b) measurements of PTCDI grown at dif-

ferent substrate temperature. The real time measurement stopped only when no obvious oscillation can be observed, the film grown at 150 °C shows pronouns “layer-by layer” feature 139

10.14 X ray diffraction measurements of deposition of PTCDI on top of pentacene at room temperature 140

10.15 AFM measurements of PTCDI-pentacene heterostructure of 165 Å PTCDI on (a) 45 Å pentacene and (b) 235 Å pentacene at room temperature. . . . 141

10.16 Schematic summary of the in-plane and out-plane structure of pentacene/PTCDI and PTCDI/pentacene heterostructures 141

10.17 (a) The GIXD, (b) X-ray reflectivity and (c) X-ray rocking measurements of pentacene (RT)/PTCDI(RT) on Al_2O_3 (I) rocking of pentacene with halfwidth of ~ 0.00521° and (II) rocking of PTCDI with halfwidth of ~ 1.14° 143

10.18 (a) The X-ray reflectivity, (b) GIXD and (c) X-ray rocking measurements of pentacene (RT)/PTCDI (150 °C) on Al_2O_3. 144

10.19 (a) The GIXD (b) X-ray reflectivity and (c) rocking measurements of heterostructure PTCDI (RT)/pentacene (RT) on Al_2O_3 146

10.20 Schematic summary of the in-plane and out-plane structure of pentacene/PTCDI and PTCDI/pentacene heterostructures 147

List of Table

5.1 DIP lattice parameters of single crystals or thin films 28

5.2 H_{16}CuPc lattice parameters of single crystals or thin films . . . 31

5.3 F_{16}CuPc lattice parameters of single crystal or thin films on SiO_2 . . 32

5.4 Lattice parameters of pentacene single crystal and it on SiO_2 . . . 33

7.1 The layer coverage percentage of the 3rd layer and the 4th layer of DIP grown at room temperature 69

7.2 In-plane lattice parameters and calculated strain as a function of the coverage. $^1\delta$ a= Δ a/a*100% and $^2\delta$ b= Δ b/b*100% calculated relative to the lattice parameters for a DIP film with highest coverage 75

7.3 The thickness, deposition rate, electron density and roughness of DIP films prepared at different substrate temperatures, from fitting the XRD curves by the Parratt algorithm 77

7.4 The fitting results of the first Bragg reflectivity and the second Bragg reflectivity bying Gaussian formula. The mociacity is given by the half-width of the rocking curve fitted by Gaussian formula. The d-spacing is calculated by using the position of the second Bragg peak and the average domain size by its half-width of the second Bragg peak 77

7.5 The fitting results of the X ray reflectivity data, the fit is with 3 box model including a thin film layer and a layer of SiO_2 and bulk Si 79

8.1 The dynamical and static characterization of clusters at substrate temperature of 300K, 240 K and 150K. $\overline{i(t)}$ means average size of a single cluster size fluctuate with time, $\overline{\Delta i(t)}$ is average cluster size change per min; $\bar{i}$ is the average cluster size, σ is its derivative 89

8.2 The matrixes of four typical domains of DIP correspond to lattice parameters $\begin{bmatrix} \vec{a}_{0-11} \\ \vec{a}_{011} \end{bmatrix}$ of Cu substrate 96

9.1 The temperature and Au nano-particle size selectivity of the $F_{16}CuPc$ nanowires 107

9.2 The contact angle measurements of APS film under different condition and corresponing roughness mean square calculated from AFM images . . 117

10.1 Lattice parameters and the corresponding lateral, vertical domain size and mosaicity of the DIP on $H_{16}CuPc$ (as –CuPc) or on SiO_2 (as –SiO_2) at different substrate temperatures 124

10.2 Growth mode comparison of DIP grown on different substrates . . 125

10.3 Pentacene structure on different substrates 148

10.4 PTCDI structure on different substrates 149

Bibiography

[1] G. Horowitz, Adv. Mater. 10, 365 (2001).

Organic field-effect transistors.

[2] C. D. Dimitrakopoulos and D. J. Mascaro, IBMJ. Res. & Dev. 45, 11 (2001).

Organic thin-film transistors: A review of recent advances.

[3] W.P. Wu, W. Xu, W.P. Hu, Y.Q. Liu, D.B. Zhu, Front. Chem. China 4, 357 (2006).
Progresses in organic field-effect transistors and molecular electronics.

[4] L. Jason, R, Mark, M, Stefan; Z.N. Bao, J. Macrom. Sci, Polymer reviews, 46, 79 (2006).

Optimizing the Thin Film Morphology of Organic Field Effect Transistors: The Influence of Molecular Structure and Vacuum Deposition Parameters on Device Performance.

[5] J. T. Mabeck and G.. G. Malliaras, Ana and Bioananlytical Chemistry, 384, 343 (2006).

Chemical and biological sensors based on organic thin-film transistors.

[6] Th. B. Singh and N. S. Sariciftci, Annu. Rev. Mater. Res. 36, 199 (2006).

Progress in plastics electronics devices.

[7] H. E. Katz Electroanalysis, 16, 1837 (2004).

Chemically Sensitive Field-Effect Transistors and Chemiresistors: New Materials and Device Structures.

[8] G. Witte and C. Wöll , J. of Mater. Res. 19, 1889 (2004).

Growth of aromatic molecules on solid substrates for applications in organic electronics.

[9] D. A. Pardo, G. E. Jabbor, and N. Peyghambarian, Adv. Mater. 12, 1249 (2000).

Application of screen printing in the fabrication of organic light-emitting devices.

[10] R. Sprengard, K. Bonrad, T.K. Daeubler, T. Frank, V. Hagemann, I. Koehler, J. Pommerehne, C.R. Ottermann, F. Voges and B. Vingerling, Proceedings of SPIE, Organic Light-Emitting Materials and Devices VIII, 173 (2004).

OLED devices for signage applications: a review of recent advances and remaining challenges.

[11] D. Sweatman, Microelectric enginnering research conference (2001).

Organic Devices: A Review.

[12] J. Shinar, NY: Springer-Verlag (2004). ISBN 0-387-95343-4.

Organic Light-emitting Devices: A Survey.

[13] S. Miyata and H. S. Nalwa, Gordon and Breach Science Publishers, Amsterdam (1997).

A Review of: "Organic Electroluminescent Materials and Devices".

[14] A. P. Kulkarni, C. J. Tonzola, A. Babel, and S. A. Jenekhe Chem. Mater. 16, 4556 (2004).

Electron transport materials for organic light-emitting diodes.

[15] Z.G. Li and H. Meng, Taylor and Francis CRC Press (2006).

Organic light-emitting materials and devices.

[16] P. Peumans and S. R. Forrest, Appl. Phys. Lett. 79, 126 (2001).

Very-high-efficiency double-heterostructure copper phthalocyanine/C_{60} photovoltaic cells.

[21] H. Dosch, Springer Tracts in Modern Physics vol.126. Springer, Heidelberg, (1992).

Critical Phenomena at Surfaces and Interfaces.

[22] G. Bauer and W. Richter, Springer-Verlag, Berlin, (1996).

Optical Characterization of Epitaxial Semiconductor Layers.

[23] J. Daillant and A. Gibaud, (Springer, Berlin, 1999).

X-ray and neutron reflectivity: principles and applications.

[24] B. E. Warren. Addison-Wesley, New York, 1990.

X-Ray Diffraction.

[25] Jens Als-Nielsen and Des McMorrow. John Wiley & Sons, Ltd, (2000).

Elements of Modern X-ray Physics.

[26] M. Tolan, Vol. 148 of Springer Tracts in Modern Physics (Springer, Berlin, 1999).

X-Ray Scattering from Soft-Matter Thin Films.

[27] E. Hecht and A. Zajac. Addison-Wesley, Mass., (1974).

Optics.

[28] R. M. A. Azzam and N. M. Bashara. North-Holland, Amsterdam, (1977).

Ellipsometry and Polarized Light.

[29] L. G. Parratt, Physical Review 95, 359 (1954).

Surface Studies of Solids by Total Reflection of X-Rays.

[30] T.R. Albrecht, S. Akamine, T.E. Carver, and C.F. Quate, J. Vac. Sci. Technol. A 8, 3386

(1990).

Microfabrication of cantilever style for the atomic force microscope.

[31] T.R. Albrecht, P. Grütter, D. Horne, and D. Rugar, J. Appl. Phys. 69, 668 (1991).

Frequency modulation detection using high-Q cantilevers for enhanced force microscope sensitivity.

[32] G. Binnig, C.F. Quate, and Ch. Gerber, Phys. Rev. Lett. 56, 930 (1986).

Atomic force microscope.

[33] J.H. Hoh, and P.K. Hansma, Trends Cell Bio. 2, 208 (1992).

Atomic force microscopy for high-resolution imaging in cell biology.

[34] S. Sarid, Oxford,U.K.: Oxford University Press, 1994.

Scanning Force Microscopy.

[35] G. Meyer, and N.M. Amer, Appl. Phys. Lett. 57, 2089 (1990).

Simultaneous measurement of lateral and normal forces with an optical beam deflection atomic force microscope.

[36] C.A.J. Putman, B.G. De Grooth, N.F. Van Hulst, and J. Greve, J. App. Phys. 72, 6 (1992).

A detailed analysis of the optical beam deflection technique for use in atomic force microscopy.

[37] O. G. Frank, and G. Nicolas, Phys. Rev. B 43, 4728 (1991).

Roles of the attractive and repulsive forces in atomic-force microscopy.

[38] A.L. Weisenhorn, P.K. Hansma, T.R. Albrecht, and C.F. Quate, Appl. Phys. Lett. 54, 2651 (1989).

Forces in atomic force microscopy in air and water.

[39] Lennard-Jones and J. E. Cohesion., Proceedings of the Physical Society, 43, 461 (1931).

Cohesion.

[40] R. Pérez, M. C. Payne, I. Štich, and K. Terakura, Phys. Rev. Lett. 78, 678 (1997).

Role of covalent Tip-Surface Interactions in noncontact Atomic Force Microscopy on Reactive Surfaces.

[41] R. Pérez, M. C. Payne, I. Štich, and K. Terakura, Phys. Rev. B. 58, 10835 (1998).

Surface-tip Role interactions in noncontact atomic-force microscopy on reactive surfaces: Si(111).

[42] R. Pérez, I. Štich, M. C. Payne, and K. Teakura, Appl. Sur. Sci. 140, 320 (1999).
Chemical interactions in noncontact AFM on semiconductor surfaces: Si(111), Si(100) and GaAs(110).
[43] N. Sasaki, and M. Tsukada, Appl. Sur. Sci. 140, 339 (1999).
Theory for the effect of the tip-surface interaction potential on atomic resolution in forced vibration system of non-contact AFM.
[44] J. P. den Hartok, Springer-Verlag, Berlin, 2nd ed. (1952).
Mechanische Schwingungen.
[45] B. Anczykowski, D. Krueger, Fuchs, H., Phys. Rev. B 53, 15485 (1996).
Cantilever dynamics in quasinoncontact force microscopy: Spectroscopic aspects.
[46] R. García, and A. san Paulo, Phys. Rev. B 61, R13381 (2000).
Dynamics of a vibrating tip near or in intermittent contact with a surface.
[47] G. Binnig, H. Rohrer, C. Gerber, and E. Weibel, Appl. Phys. Lett. 40, 178 (1982).
Tunneling through a controllable vacuum gap.
[48] G. Binnig, H. Rohrer, C. Gerber, and E. Weibel, Phys. Rev. Lett. 49, 57 (1982).
Surface studies by scanning tunneling microscopy.
[49] G. Binnig, and H. Rohrer, Reviews of Modern Physics 59, 615 (1987).
Scanning Tunneling Microscopy--from Birth to Adolescence.
[50] J. Golovchenko, Science 232, 48 (1986).
The Tunneling Microscope: A New Look at the Atomic World.
[51] R. J. Hamers, *Annu.* Rev. Phys. Chem. 40, 531 (1989).
Atomic-resolution surface spectroscopy with the scanning tunneling microscopy.
[52] J. Bardeen, Phys. Rev. Lett. 6, 57 (1961).
Tunneling from a many-particle point of view.
[53] J. Tersoff, and D. R. Hamann, Phys. Rev. Lett. 50, 1998 (1983).
Theory and application for the scanning tunneling microscope.
[54] J. Tersoff, and D. R. Hamann, Phys. Rev. B. 31, 805 (1985).
Theory of the scanning tunneling microscope.
[55] T. Müller, VeeCo report (2007).
Scanning Tunneling Microscopy: A Tool for Studying Self-Assembly and Model Systems for Molecular Devices.

[56] M. Pope and C.E. Swenberg, Oxford University Press, Oxford (1999).
Electronic Processes in Organic Crystals and Polymers.
[57] H. Klauk, Wiley, Weinheim (2006).
Organic Electronics: Materials, Manufacturing, and Applications.
[58] A. Facchetti, Materials Today, 10, 28, (2007).
Semiconductors for organic transistors.
[59] J. von Braun and G. Manz, Patent-Nr.: 595 024: (Deutsches Reichspatentamt, Berlin, 1934).
Verfahren zur Herstellung von Kondensationsprodukten des Fluoranthens.
[60] I. C. Lewis and L. S. Singer, Carbon, Pergamon Press Ltd., Great Britain, 5, 373 (1967).
Further electron spin resonance studies of the pyrolysis of aromatic hydrocarbons.
[61] J. Paum, S. Hirschmann, W. Frey, and N. Karl, submitted (2005).
[62] A. Hoshino, S. Isoda, and T. Kobayashi, J. Cryst. Growth 115, 826 (1991).
Epitaxial growth of organic crystals on organic substrates polynuclear aromatic hydrocarbons.
[63] M. Heilig, M. Domhan, and H. Port, J. Luminescence 110, 290 (2004).
Optical properties and morphology of thin diindenoperylene films.
[64] A. C. Dürr, Ph.D. thesis, Max-Planck-Insitut für Metallforschung - Institut für Theoretische und Angewandte Physik der Universität Stuttgart, Stuttgart, (2002).
Growth and structure of DIP thin-films and Au-contachts on DIP thin-films.
[65] A. C. Dürr, F. Schreiber, K. A. Ritley, V. Kruppa, J. Krug, H. Dosch, and B.Struth, Phys. Rev. Lett. 90, 016104 (2003).
Rapid roughening in thin film growth of an organic semiconductor (Diindenoperylene).
[66] R. Strohmaier, J. Petersen, B. Gompf, and W. Eisenmenger, Surf. Sci. 418, 91 (1998).
A systematic STM study of planar aromatic molecules on inorganic substrates: I. Submolecular image contrast.
[67] A. C. Dürr, N. Koch, M. Kelsch, A. R uhm, J. Ghijsen, R. L. Johnson, J.-J. Pireaux, J. Schwartz, F. Schreiber, H. Dosch, and A. Kahn, Phys. Rev. B 68,115428 (2003).
Interplay between morphology, structure and electronic properties at diindenoperylene-gold interfaces.

[68] N. Karl, in Charge Carrier Mobility in Organic Molecular Crystals, Vol. 41 of Springer Series in Materials Science, edited by R. Farchioni and G. Grosso, Springer, Berlin, Chap. 3 (2001).

[69] N. Karl, Synth. Met. 133-134, 649 (2003).

Charge-carrier transport in organic semiconductors.

[70] M. Münch, Ph.D. thesis, Universität Stuttgart, Stuttgart, 2001.

[71] J. Blochwitz, M. Pfeiffer, T. Fritz and K. Leo, Appl. Phys. Lett. 73, 729 (1998).

Low voltage organic light emitting diodes featuring doped phthalocyanine as hole transport material.

[72] C.C. Leznoff and A.B.P. Lever, vol.3**,** VCH, New York (1993).

Phthalocyanines, Properties and applications.

[73] N.B. Mc Keown, Cambridge University Press, Cambridge (1998).

Phthalocyanine Materials.

[74] P. H. Lippel, R. J. Wilson, M. D. Miller, Ch. Wöll and S. Chiang, Phys. Rev. Lett. 62, 171 (1989).

High-Resolution Imaging of Copper-Phthalocyanine by Scanning-Tunneling Microscopy.

[75] B. N. Achar and K. S. Lokesh, Journ. of S. S. Chem., 177, 6,1987 (2004).

Studies on polymorphic modifications of copper phthalocyanine.

[76] F.H. Moser and A.L. Thomas, Reinhold, New York (1963).

Phthalocyanine Compounds.

[77] F.H. Moser, A.L. Thomas, Vols. 1 and 2, CRC Press, Boca Raton, FL, (1983).

The Phthalocyanine.

[78] J. M. Robertson, J. Chem. Soc. 615 (1935).

An X-Ray Study of the Structure of the Phthalocyanines. Part I. The Metal Free, Nickel, Copper, and Platinum Compounds.

[79] J. M. Robertson, J. Chem. Soc. 1195 (1936).

An X-ray study of the phthalocyanines. Part II. Quantitative structure determination of the metal-free compound.

[80] A. C. Brieva, T.E. Jenkins, D.G. Jones, F. Strössner, D.A. Evans and G.F. Clark , J. of Appl. Phy. 99, 073504, (2006).

Internal structure of copper II-phthalocyanine thin films on SiO_2/Si substrates investigated by

grazing incidence x-ray reflectometry.

[81] I. Biswas, H. Persert, M. Nagel, M.B. Casu, S. Schuppler, P. Nagel, E. Pellegrin and T. Chassé, THE JOURNAL OF CHEMICAL PHYSICS 126, 174704 (2007).

Buried interfacial layer of highly oriented molecules in copper phthalocyanine thin films on polycrystalline gold.

[82] D. G. de Oteyza, E. Barrena, S. Sellner, J. O. Osso, and H. Dosch, Journal of Physical Chemistry B 110, 16618 (2006).

Structural rearrangements during the initial growth stages of organic thin-films of $F_{16}CuPc$ on SiO_2.

[83] D. G. de Oteyza, PHD thesis, Max Planck Institute für Metallforschung, Stuttgart, 2006.

Fluorinated copper-phthalocyanines in model systems for organic electronic devices.

[84] Y.Y. Lin, D. J. Gundlach, S. F. Nelson, T. N. Jackson, IEEE Electron Device Lett., 18, 606 (1997).

Stacked pentacene layer organic thin-film transistors with improvedcharacteristics.

[85] C. D. Dimitrakopoulos, P. R. L Malenfant, Adv. Mater. 14, 99 (2002).

Organic thin film transistors for large area electronics.

[86] N. Karl, Synth. Met., 133, 649 (2003).

Charge carrier transport in organic semiconductors.

[87] G. Horowitz, Adv. Mater., 10, 365 (1998).

Organic Field-Effect Transistors.

[88] S.E. Fritz, S.M. Martin, C.D. Frisbie, M.D. Ward and MF Toney, J. Amer. Chem. Soc, (2004).

Structural Characterization of a Pentacene Monolayer on an Amorphous SiO_2.

[89] B. Campbell, J. Monteath Obertson and J. Trotter Acta Cryst., 14, 705, (1961).

The Crystal and Molecular Structure of Pentacene.

[90] D. Holmes, S. Kumaraswamy, , A. Matzeger and K. P. C. Vollhardt, Chem. Eur. J. 5, 3399, (1999).

On the Nature of Nonplanarity in the [N]Phenylenes.

[91] I. P. M. Bouchoms, W. A. Schoonveld, J. Vrijmoeth and T. M. Klapwijk, Synthetic Metals 3, 175, (1999).

Morphology identification of the thin film phases of vacuum evaporated pentacene on SiO_2

substrates.

[92] T. Minakata, H. Imai, M. Ozaki and K. Saco, J. Appl. Phys. 72, 5220, (1992).

Structural studies on highly ordered and highly conductive thin-films of pentacene.

[94] DJ Gundlach, TN Jackson, DG Schlom and SF Nelson, Appl. Phys. Lett. 74, 3302, (1999).

Solvent- induced phase transition in thermally evaporated pentacene films.

[94] C. C. Mattheus, A. B. Dros, J. Baas, G. T. Oostergetel, A. Meetsma, J. L. de Boer and T. T. M. Palstra, Synth. Met. 138, 475 (2003).

Identification of polymorphs of pentacene.

[95] C.C. Mattheus, A.B. Dros, J. Baas, A. Meetsma, JL de Boer and TTM Palstra. Acta Cryst. C57, 939-941. (2001).

Polymorphism in pentacene.

[96] I. P. M. Bouchoms, W. A. Schoonveld, J. Vrijmoeth, T. M. Klapwijk, Synth. Met. 1999, 104, 175.

Morphology identification of the thin film phases of vacuum evaporated pentacene on SiO_2 substrates.

[97] D. Knipp, R. A. Street, A. Volkel, J. Ho, J. Appl. Phys. 93, 347 (2003).

Pentacene thin film transistors on inorganic dielectrics: Morphology, structural properties, and electronic transport.

[98] S. E. Fritz, S. M. Martin, C. D. Frisbie, M. D. Ward, and M. F. Toney, J. Am. Chem. Soc. 126, 4084 (2004).

Structural Characterization of a Pentacene Monolayer on an Amorphous SiO_2 Substrate with Grazing Incidence X-ray Diffraction.

[99] T. Kakudate, N. Yoshimoto and Y. Saito, Mater. Res. Soc. Symp. Proc. Vol. 965 Materials Research Society, 0965-S12-52, (2007).

In-Plane Structure and Polymorphism of Pentacene Thin Films.

[100] J. S. Wu and J. C. H. Spence, Journal of applied crystallography, 37, 78 (2004).

Electron diffraction of thin-film pentacene.

[101] P. R. L. Malenfant, C. D. Dimitrakopoulos, J. D. Gelorme, L. L. Kosbar, and T. O. Graham, Appl. Phys.Lett. 80, 2517 (2002).

N-type organic thin-film transistor with high field-effect mobility based on a N,N'-dialkyl-3,4,9,10-perylene tetracarboxylic diimide derivative.

[102] R. J. Chesterfield, J. C. McKeen, C. R. Newman, C. D. Frisbie, P. C. Ewbank, K. R. Mann, and L. L. Miller, J. Appl. Phys. 95, 6396 (2004).

Variable temperature film and contact resistance measurement on operating n-channel organic thin film transistors.

[103] E. Hädicke, and F. Graser: Acta Cryst. C42, 189 (1986).

Structures of Eleven Perylene-3,4:9,10-bis(dicarboximide) Pigments.

[104] C. W. Struijk, A. B. Sieval, J. E. J. Dakhorst, M. van Dijk, P. Kimkes, R. B.M. Korhorst, H. Donker, T. J. Schaafsma, S. J. Picken, A. M. van de Craats, J. M. Warman, H. Zuilhof, and E. J. R. Sudho1lter, J. Am. Chem. Soc. 122, 11057 (2000).

Liquid Crystalline Perylene Diimides: Architecture and Charge Carrier Mobilities.

[105] T. Krauss, Diplom thesis, University Stuttgart, May, 2006.

Structure and morphology of organic oilms of PTCDI-C on silicon dioxide.

[106] S. A. CHAMBERS Surface Science reports, (2000).

Epitaxial growth and properties of thin film oxides.

[107] K. Reichelt, Vacuum. Vol. 38, 12, 1083 (1988).

Nucleation and Growth of Thin Films.

[108] Zhenyu Zhang and Max G. Lagally, Science, 276, 5311, 377 (1997).

Atomistic Processes in the Early Stages of Thin-Film Growth.

[109] N. Kaiser, Appl. Opt. 41, 3053 (2002).

Review of the Fundamentals of Thin-Film Growth.

[110] J A Venables, G D T Spiller and M Hanbucken, Rep. Prog. Phys. 47 399 (1984).

Nucleation and growth of thin films.

[111] http://www.omicron.de

[112] http://www.jeol.com

[113] http://www.nanotec.es

[114] http://www.veeco.com

[115] Angströmquelle Karlsruhe GmbH (ANKA); Institute for Synchrotron Radiation, Karlsruhe, Germany.

http://hikwww1.fzk.de/anka/.

[116] ID10B Troïka II, multi-purpose, ESRF,Grenoble, France.
http://www.esrf.fr/UsersAndScience/Experiments/SCMatter/ID10B/.
[117] European synchrotron radiation facility (ESRF), Grenoble, France.
http://www.esrf.fr
[118] Z. Bao, J. A. Rogers and H. E. Katz, J. Mater. Chem., 9, 1895 (1999).
Printable organic and polymeric semiconducting materials and devices.
[119] G. Witte, C. Woll, J. Mater. Res. 19 (7), 1889 (2004).
Growth of aromatic molecules on solid substrates for applications in organic electronics.
[120] F. Yang, M. Shtein and S. R. Forrest, *Nat. Mat.*, 4, 37 (2005).
Controlled growth of a molecular bulk heterojunction photovoltaic cell.
[121] S. Kobayashi, T. Nishikawa, T. Takenobu, S. Mori, T. Shimoda, T. Mitani, H. Shimotani, N. Yoshimoto, S. Ogawa, Y. Iwasa, Nat. Mat., 3, 317 (2004).
Control of carrier density by self-assembled monolayers in organic field-effect transistors.
[122] C.W. Chu, S.H. Li, C.W. Chen, V. Shrotriya, and Y. Yang Appl. Phys. Lett. **87**, 193508 (2005).
High-performance organic thin-film transistors with metal oxide/metal bilayer electrode.
[123] M. Shtein, J. Mapel, J. B. Benzinger, S. R. Forrest, Appl. Phys. Lett. 81, 268 (2002).
Effects of film morphology and gate dielectric surface preparation on the electrical characteristics of organic-vapor-phase-deposited pentacene thin-film transistors.
[124] J. Veres, S. Ogier, G. Lloyd , D. de Leeuw, Chem. Mater., 16 (23), 4543, 2004.
Gate insulators in organic field-effect transistors.
[125] S.C. Lim, S. H .Kim, J. H. Lee, M. K. Kim, D. J. Kim, T. Zyung, Synth. Met., 148, 75 (2005).
Organic thin-film transistors on plastic substrates.
[126] H. Klauk, U. Zschieschang, J. Pflaum, M. Halik, Nature, 445, 745 (2007).
Ultralow-power organic complementary circuits.
[127] D. J. Gundlach, J. A. Nichols, L. Zhou, and T. N. Jackson, Appl. Phys. Lett., 80, 2925 (2002).
Thin-film transistors based on well-ordered thermally evaporated naphthacene films.
[128] D. Knipp, R. A. Street, A. Völkel, and J. Ho, J. Appl. Phys., 93, 347 (2003).

Pentacene thin film transistors on inorganic dielectrics: Morphology, structural properties, and electronic transport.

[129] X. Liu, S. H. Mohamed, J. M. Ngaruiya, M. Wuttig, T. Michely, J. Appl. Phys. 93, 4852 (2003).

Modifying the growth of organic thin films by a self-assembled monolayer.

[130] D.G. de Oteyza, E. Barrena, J. O. Osso, H. Dosch, S. Meyer, J. Pflaum, Applied Physics Letters, 87, 183504 (2005).

Controlled enhancement of the electron field-effect mobility of $F_{16}CuPc$ thin-film transistors by use of functionalized SiO_2 substrates.

[131] R Ruiz, B Nickel, N Koch, LC Feldman, RF Haglund, A. Kahn, F. Family and G. Scoles, Phys. Rev. Lett. 91, 136102 (2003).

Dynamic Scaling, Island Size Distribution, and Morphology in the Aggregation Regime of Submonolayer Pentacene Films.

[132] J.W. Evans, P.A. Thiel and M.C. Bartelt, Surf. Sci. Rep. 61, 1 (2006).

Morphological evolatuion during epitaxial thin film growth: Formation of 2D islands and 3D mounds.

[133] S. M. Jordan, R. Schad, D. J. L. Herrmann, J.F. Lawler, and H. van Kempen, Phys. Rev. B, 58, 13132 (1998).

Quantitative assessment of STM images of Fe grown epitaxially on MgO(001)using fractal techniques.

[134] B. Müller, L. Nedelmann, B. Fischer, H. Brune, J. V. Barth and Klaus Kern, Phys. Rev. Letter, 80, 2642 (1998).

Island Shape Transition in Heteroepitaxial Metal Growth on Square Lattices.

[135] K.-F. Braun, D. Farias, S. Fölsch, K.-H. Rieder, Surface Science 454, 750 (2000).

Fractal growth of LiF on Ag(111) studied by low-temperature STM.

[136] J. Krug, Physica A, 4, 647 (2004).

Power laws in surface physics: the deep, the shallow and the useful.

[137] J. Krug and P. Meakin Phys. Rev. Lett. 66, 703 (1991).

Kinetic roughening of Laplacian fronts.

[138] J. Krug and M. Rost Phys. Rev. B 60, R16334 (1999).

Linear theory of unstable growth on rough surfaces.

[139] P. Šmilauer and M. Kotrla, Europhys. Lett. **27,** 261 (1994).
Kinetic Roughening in Growth Models with Diffusion in Higher Dimensions.
[140] S. Kowarik, A. Gerlach, S. Sellner, F. Schreiber, L. Cavalcanti, and O. Konovalov, Phys. Rev. Lett. 96, 125504 (2006).
Real-time observation of structural and orientational transitions during growth of organic thin films.
[141] W. Auwarter , A Weber-Bargioni , A Riemann , A Schiffrin , O Groning , R Fasel , JV JV Barth, J. of Chem. Phys. 124 (19), 194708 (2006).
[142] M Oehzelt, L Grill, S Berkebile, G Koller, FP Netzer and MG Ramsey, Chemphychem, 8, 1707 (2007).
The molecular orientation of para-sexiphenyl on Cu(110) and Cu(110) p(2x1)O.
[143] GM Whitesides, JP Mathias, and CT Seto, Science 254, 1312 (1991).
Molecular self-assembly and nanochemistry: a chemical strategy for the synthesis of nanostructures.
[144] E. Barrena, D.G. de Oteyza, H. Dosch and Y. Wakayama, ChemPhysChem 8, 1915-1918 (2007).
2D Supramolecular Self-Assembly of Binary Organic Monolayers.
[145] P.D. Yang, Y.Y. Wu and R. Fan, International Journal of Nanoscience, 1,1 (2002).
Inorganic semiconductor nanowires.
[146] Y Wu, H Yan, M Huang, B Messer, JH Song and P Yang, Chemistry - A European Journal, 8, 1260 (2002).
Inorganic Semiconductor Nanowires: Rational Growth, Assembly, and Novel Properties.
[147] R.S. Wagner and W.C. Ellis, Applied Physics Letters. 4, 89 (1964).
Vapor-liquid-solid mechanism of single crystal growth.
[148] Karan, D.; Mallik, B. Chem. Phys. Letters**,** 434, 265 (2007).
Copper phthalocyanine nanoparticles and nanoflowers.
[149] R. Glass, M. Arnold, J. Bluemmel, A. Kueller, M. Moeller and J.P. Spatz, Advanced Functional Materials 13, 569 (2003).
Micro-Nanostructured Interfaces Fabricated by the Use of Inorganic Block Copolymer Micellar Monolayers as Negative Resist for Electron-Beam Lithography.
[150] A. L. Briseno, S. Mannsfel, M.M. Ling, R. J. Tseng, S.H. Liu, C. Reese, M.Roberts, Y.

Yang, F. Wudl and Z. Bao, Nature, 444, 913 (2006).

Patterning organic single-crystal transistor arrays.

[151] Y. Iwasa, H. Asanuma, H. Shimotani, T. Takenobu, T. Nishikawa and J. Takeya, Molecular Crystals and Liquid Crystals, 455, 277 (2006).

Organic Single Crystal Transistors: Interface Modification with SAMs and Double Gate Structure.

[152] B.H. Hamadani, D.A. Corley, J.W. Ciszek, J.M. Tour, D. Natelson, Nano Lett. 6, 1303-1306 (2006)

Controlling charge injection in organic field-effect transistors using self-assembled monolayers.

[153] A. Hozumi, Y. Yokogawa, T. Kameyama, H. Sugimura, K. Hayashi, H. Sugimura, K. Hayashi, H. Shirayama, O. Takai, J. Vac. Sci. Technol. A, 19, 1812 (2001).

Amino-terminated self-assembled monolayer on a SiO_2 surface formed by chemical vapor deposition.

[154] P. Martin, S. Marsaudon, L. Thomas, B. Desbat, J.P. Aime´, B. Bennetau, Langmuir, 21, 6934 (2005).

Liquid Mechanical Behavior of Mixed Monolayers of Amino and Alkyl Silanes by Atomic Force Microscopy.

[155] M.H. Hu, S. Noda, T. Okubo, Y. Yamaguchi and H. Komiyama, Appl. Surf. Sci, 181, 3-4, 21 (2001).

Structure and morphology of self-assembled 3-mercaptopropyltrimethoxysilane layers on silicon oxide.

[156] R.H. Ye, M. Baba, K. Suzuki and K. Mori, Solid State Electronics, 52, 60 (2008).

Fabrication of highly air-stable ambipolar thin-film transistors with organic heterostructure of F_{16}CuPc and DH-α6T.

[157] S.D. Wang, K. Kanai, Y. Ouchi and K. Seki, Organic Electronics, 7, 457 (2006).

Bottom contact ambipolar organic thin film transistor and organic inverter based on C_{60}/pentacene heterostructure.

[158] P. Damlin, C. Kvarnström, A. Nybäck, M. Käldström and A. Ivaska, Electrochimica Acta, 51, 606027 (2006).

Electrochemical and spectroelectrochemical study on bilayer films composed of C_{60} and poly(3,4-ethylenedioxythiophene) PEDOT.

[159] M. Oehzelt, R. Resel, C. Suess, R. Friedlein and W. R. Salaneck, J. Chem. Phys. 124, 054711 (2006)

Crystallographic and morphological characterization of thin pentacene films on polycrystalline copper surfaces.

[160] B.J. Chang, J. H. Park, K. H. Lee, Y. C. Kim, J-W Yu and J. K. Kim, Current Applied Physics, 6, 658 (2006).

Characteristics of emissive bilayers in electrophosphorescent organic light-emitting diode.

[161] D. G. de Oteyza, T. N. Krauss, E. Barrena, S. Sellner, H. Dosch, and J. O. Ossó, Applied Physics Letters 90, 243104 (2007).

Towards controlled bottom-up architectures in organic heterostructures.

[162] R.B. Ye, M. Baba, Y. Oishi, K. Mori, K. Suzuki, Appl. Phys. Lett. 86, 253505 (2005).

Air-stable ambipolar organic thin-film transistors based on an organic homostructure.

[163] J. Wang, H. Wang, X. Yan, H. Huang and D. Yan, Appl. Phys. Lett. 87, 093507 (2005).

Organic heterojunction and its application for double channel field-effect transistors.

[164] M. Ofuji, K Inaba, K. Omote, H. Hoshi, Y. Takanishi, K. Ishikawa and H. Takezoe Jpn. J. Appl. Phys. Vol 44, 5467(2002).

Grazing Incidence In-Plane X-Ray Diffraction Study on Oriented Copper Phthalocyanine Thin Films.

Acknowledgements

Though only my name appears on the cover of this dissertation, a great many people have contributed in one way or another to the completion of this thesis.

At first place, I thank Prof. Helmut Dosch, I am greatly indebt to him for giving me the opportunity of working under such excellent experimental conditions. I really appreciate his helpfulness, his kindness and his insightful thought-provoking comments and constructive criticisms at different stages of my research. I am grateful to him for holding me to a high research standard and enforcing strict validations for each research result, and thus teaching me how to do research. I thank Prof. Wachstrup for admission of being my co-advisor, who has been always there to listen and give advice. I am deeply grateful to him for the long discussions. I acknowledge the financial support of IMPRS. I have to give a special mention for the support given by Dr. Libuda, as a coordinator of this program; he is who always thinks of our students and supports us.

My deepest gratitude is to Dr. Esther Barrena. I have been amazingly fortunate to have an advisor who gave me the freedom to explore on my own and at the same time the guidance to recover when my steps faltered. Esther taught me how to question thoughts and express ideas. Her patience and support helped me overcome many crisis situations and finally finished this dissertation. I give all the best wishes to her new family with David and little Yuan.

A lot of thanks go to Dimas for his help in the lab and during the beamtimes, where also Tobias, Dipak, Claudia, Oriol were once gave me a hand. Thanks the impressive helpfulness of Ralph Weigel for solving all the possible technical problems, also Nikolei Kasper, for their help for our measurements in ANKA. I acknowledge the technical support of Bernd Struth when measuring in the ESRF at ID-10B.

I specially thank Janos, Roland Roth and Ayse for proofreading of this thesis, for encouraging the use of correct grammar and consistent notation in my writings and for

carefully reading and commenting on countless revisions. Thanks Jonathan Heidkamp and Felix Maye for the help of the German in the first chapter.

I am also grateful to the former or current organic group members: Dimas, Stephan, Tobias, Dipak, Claudia, Yi, Ayse, Evolina, Monamie, Ajay, for the good time we have had inside and outside the lab. Thanks to the technicians of the Dosch department, who make our life much easier: Frank Adams, Annette Weisshardt, Taufan Zimmer, Stefan Weber, Ernst Günther, Longinus Raschke and Peter Schützendübe. I would like to acknowledge Dr. Andreas Stierle, Dr. Harald Reichert, Dr. Hubert Zajonz for numerous informal discussions that helped me improve my knowledge in the area and enrich my ideas. I thank Frau Sussdorf, she is the one of best secretaries I ever seen and I appreciate that she sends me all the brochures or information of programs or films about china. Thanks to all Dosch department members for the good time we have had inside the institute, in the movie nights, in Ringberg and Volksfest excursions.

Particularly, I would like to acknowledge Wakayama-san for giving me the opportunity of internship in NIMS in Japan. Thanks also to Yumi Hirose for helping with the administration, and to Toyohiro Chikyow, Yoma Nakayama, Takahiro Nagata, Kenji Ohmori, Miho Nakayama and all the other department colleagues. Thanks to all the friends there JingYang Wang, WenLong Wang, ChuYi Zhi and their wives for making my stay in Japan so joyful.

My sincere gratitude also goes to all my friends who made my stay in Stuttgart so enjoyable, Fu LiWei, Liu Xiong, Wang LiJuan, Yang XiaoPing, Wang Lei, Qiu ZhiJian, Cai HangFeng and so many others. Many friends have helped me stay through these years. Their support and care helped me overcome setbacks and stay focused on my graduate study. I greatly value their friendship and I deeply appreciate their belief in me.

At last, but still importantly, none of this would have been possible without the love, concern, support, and patience of my family all these years. I would like to express my heart-felt gratitude to my family.